Resistive Non-Volatile Memories Characteri-zation by Conductive Atomic Force Micros-copy (C-AFM) in Ultra-High Vacuum Environment

Amit Kumar Singh

Communauté UNIVERSITÉ Grenoble Alpes

THÈSE

Pour obtenir le grade de

DOCTEUR DE LA COMMUNAUTÉ UNIVERSITÉ GRENOBLE ALPES

Spécialité : NANO ELECTRONIQUE ET NANO TECHNOLOGIES

Arrêté ministériel : 25 mai 2016

Présentée par

Amit Kumar SINGH

Thèse dirigée par **Martin KOGELSCHATZ**, MCF, Université Grenoble Alpes
et codirigée par **Serge BLONKOWSKI**, STMicroelectronics
préparée au sein du **Laboratoire Laboratoire des Technologies de la Microélectronique**
dans **l'École Doctorale Electronique, Electrotechnique, Automatique, Traitement du Signal (EEATS)**

Caractérisation des Mémoires Non-Volatiles Résistives par Microscopie à Force Atomique en mode Conduction (C-AFM) sous Ultravide

Resistive Non-Volatile Memories Characterization by Conductive Atomic Force Microscopy (C-AFM) in Ultra-High Vacuum Environment

Thèse soutenue publiquement le **24 juin 2019**,
devant le jury composé de :

Monsieur LAMBERT ALFF
PROFESSEUR, UNIV. TECH. DE DARMSTADT - ALLEMAGNE, Rapporteur
Monsieur BRICE GAUTIER
PROFESSEUR, INSA LYON, Rapporteur
Monsieur ALAIN SYLVESTRE
PROFESSEUR, UNIVERSITE GRENOBLE ALPES, Président
Madame CLAUDIA WIEMER
CHARGE DE RECHERCHE, CNR IMM AGRATE UNIT, Examinateur
Monsieur MARTIN KOGELSCHATZ
MAITRE DE CONFERENCES, UNIVERSITE GRENOBLE ALPES, Directeur de thèse
Monsieur SERGE BLONKOWSKI
INGENIEUR, ST MICROELECTRONICS CROLLES, Co-directeur de thèse

UNIVERSITÉ GRENOBLE ALPES

DOCTORAL THESIS

Resistive non-volatile memories characterization by conductive atomic force microscopy (C-AFM) in ultra-high vacuum environment

Author:
Amit Kumar SINGH

Supervisor:
Serge BLONKOWSKI
Guillaume AUDOIT
Martin KOGELSCHATZ

Abstract

Title: *Resistive non-volatile memories characterization by conductive atomic force microscopy (C-AFM) in ultra-high vacuum environment.*

Memories are the fundamental for any electronic system we interact with in our daily life and are getting more and more important day by day in our present era. Non-volatile memory (NVM) technologies play a fundamental role in the micro-electronics industry. The growing functionalities and performance of the electronic products such as digital cameras, smart phone, personal computer, solid state hard disk and many more, need continues improvement of its features.

Floating gate-based Flash technology is the main NVM technology used extensively in market these days. Nevertheless, Flash technology presents many problems making further scaling impossible. In this context, there are many other memory technologies emerging and interest in new concepts and materials to go beyond the Flash technology is growing. Innovative approaches other than displacing and trapping electrons like in Flash memories have been investigated.

Resistive non-volatile memories based on two terminal devices, in which an active material is sandwiched between two electrodes have been investigated. The main idea of using this kind of structure and material is to use a specific physical mechanism allowing to switch it between two different resistive states for information storage.

For example, in oxide based random-access memory (OxRAM), a conductive filament is grown inside the oxide layer, linking the two electrodes. By creation and disruption of this filament, two different resistance states can be generated. Another example is the phase change random-access memory (PCRAM), in which a chalcogenide material with the ability to change its phase between a high resistive amorphous and a low resistive crystalline state is used. These two emerging memory technologies (OxRAM & PCRAM) are the most studied ones nowadays and can potentially replace the current Flash technology.

Over the last few years OxRAM has been widely investigated due to many advantages like good scalability, long data retention time, fast read & write speed and low power consumption. The main benefit is that it is compatible with Back-end of line fabrication. In MIM structures for OxRAM, forming and disruption of the nanometer sized conductive filament is commonly accepted as the physical phenomenon for the switching, but still a debate is going on to understand the nature and characteristics of the conductive filament. Also, many studies have been done to evaluate the scaling capability of OxRAM and PCRAM.

Hence, in this thesis work we studied mechanisms related to the conductive filament based resistive switching at nanoscale. To do the electrical characterization, a new technique using conductive atomic force microscopy (C-AFM) in ultra-high

vacuum is proposed. The impact of different AFM tip materials (which is used as top electrode), different bottom electrode materials and the compliance current effect in two different regimes (in nA and in μA) are investigated. It is found that in the case of HfO_2 based OxRAM, the filament is formed by Ti diffusion from the bottom electrode through the oxide layer. The switching is due to the disruption of the filament in the vicinity of the tip explaining the effect of the tip nature on the High resistance current. The results are in good agreement with device characteristics and could be reproduced by modeling. Also, phase transition in phase change materials for PCRAM is investigated for $Ge_2Sb_2Te_5$ (GST-225) and Ge rich GST. It was found that the phase transition from amorphous to crystalline is possible at nanoscale. Finally, the threshold for GST-225 is observed at values nearer to those observed on devices than former observations with standard C-AFM.

Keywords: *Non-Volatile Memories, OxRAM, PCRAM, Conductive atomic force microscopy (C-AFM), Nanoelectronics, Microelectronics, Ultra-high vacuum, Electrical characterization, Filament, Simulation.*

Resumé

Titre: *Caractérisation des mémoires non volatiles résistives par microscopie à force atomique en mode conduction (C-AFM) sous ultravide.*

Les mémoires sont à la base de tout système électronique avec lequel nous interagissons dans notre vie quotidienne et deviennent de plus en plus important jour après jour à notre époque. Les technologies de mémoire non volatile (NVM) jouent un rôle fondamental dans l'industrie de la microélectronique. Les fonctionnalités et les performances croissantes des produits électroniques tels que les appareils photo numériques, les téléphones cellulaires, les ordinateurs personnels, les disques durs, etc., nécessitent une amélioration continue de ses fonctionnalités.

La technologie Flash à grille flottante est la principale technologie NVM utilisée sur le marché actuellement. Néanmoins, la technologie Flash pose de nombreux problèmes rendant tout redimensionnement impossible. Dans ce contexte, de nombreuses autres technologies de mémoire sont en train d'émerger et l'intérêt pour les nouveaux concepts et matériaux allant au-delà de la technologie Flash ne cesse de croître. Des approches innovantes autres que le déplacement et le piégeage des électrons comme dans les mémoires Flash ont été étudiées.

Des mémoires résistives non volatiles basées sur deux types de dispositifs, dans lesquelles un matériau actif est pris en sandwich entre deux électrodes, ont été étudiées. L'idée principale d'utiliser ce type de structure et de matériau est d'utiliser un mécanisme physique spécifique permettant de le basculer entre deux états résistifs différents pour le stockage d'informations.

Par exemple, dans la mémoire à base d'oxydes (OxRAM), un filament conducteur est développé à l'intérieur de la couche d'oxyde, reliant les deux électrodes. En créant et en interrompant ce filament, deux états de résistance différents peuvent être générés. Un autre exemple est la mémoire à changement de phase (PCRAM), dans laquelle un matériau à base de chalcogénure capable de changer de phase entre un état amorphe à haute résistance et un état cristallin à faible résistance est utilisé. Ces deux technologies de mémoire émergentes (OxRAM & PCRAM) sont les plus étudiées et peuvent potentiellement remplacer la technologie Flash actuelle.

Les mémoires OxRAM ont été largement étudiées au cours des dernières années en raison de leurs nombreux avantages, tels qu'une bonne évolutivité en matière de réduction de taille, une longue rétention, une vitesse de lecture et d'écriture rapide et une faible consommation d'énergie. Le principal avantage est leur compatibilité avec la fabrication en back end. Dans les structures MIM pour OxRAM, la formation et la rupture d'un filament conducteur de taille nanométrique sont communément acceptées comme étant le phénomène physique de la commutation, mais un débat est toujours en cours pour comprendre la nature et les caractéristiques du filament conducteur. De plus, de nombreuses études ont été réalisées pour évaluer le potentiel de réduction des dimensions des mémoires OxRAM et PCRAM. Par

conséquent, dans cette thèse, nous étudions les mécanismes liés à la commutation résistive à base de filaments conducteurs à l'échelle nanométrique. Pour effectuer la caractérisation électrique, une nouvelle technique utilisant la microscopie à force atomique en mode conduction (C-AFM) sous ultravide est proposée. L'influence du matériau de la pointe AFM (utilisés comme électrode supérieure), du matériau de l'électrode inférieure et l'effet du courant limite dans deux régimes différents (en nA et en μA) sont étudiés. Il ressort de notre travail que dans les mémoires OxRAM à base de HfO_2, le filament est créé par diffusion de Ti de l'électrode inférieure à travers l'oxyde. D'après le travail présenté dans cette thèse, la commutation résistive est due à la rupture du filament au voisinage de la pointe expliquant l'effet dû à la nature de la pointe sur le courant à haute résistance. Les résultats sont en bon accord avec ceux obtenus sur des dispositifs et ont pu être reproduits par un modèle. En outre, la transition de phase dans les matériaux pour PCRAM est étudiée pour le GST riche en Ge et le GST-225. Il a été constaté que la transition de phase dans les matériaux à changement de phase est possible à l'échelle nanométrique. Enfin, le champ électrique de seuil observé dans le cas du GST-225 est bien plus proche des valeurs mesurées sur dispositifs que celles obtenues avec un CAFM standard.

Mots-clés: *Mémoires non volatiles, OxRAM, PCRAM, Microscopie à force atomique conductrice (C-AFM), nanoélectronique, microélectronique, ultravide, caractérisation électrique, filament, simulation.*

Acknowledgements

Firstly, I would like to express my sincere gratitude towards my supervisors Serge BLONKOWSKI, Martin KOGELSCHATZ and Guillaume AUDOIT for the continuous support of my Ph.D study and related research, for their patience, motivation, and immense knowledge. Their guidance helped me in all the time of research and writing of this thesis. I could not have imagined having a better advisor and mentor for my Ph.D study. I would also like to thank all my jury members.

A very special thanks to Olga CUETO for being a constant support always and helping me understand the COMSOL simulation part of this research project. I thank her for her patient guidance, useful critiques and answering my incessant queries. I would like to thank Constantin MATEI for performing SEM-EDX measurements with me. I would also like to thank Tristan DEWOLF for TEM analysis. I would like to thank Chiara SABBIONE and Gabriele NAVARRO for providing the samples.

My sincere thanks also goes to all the lab members, who provided me an opportunity to join their lab as PhD student, and who gave access to the laboratory and research facilities. Without their precious support it would not be possible to conduct this research. I would like to thank my fellow doctoral students for their feedback, cooperation and of course friendship.

I would like to thank my friends for accepting nothing less than excellence from me. Last but not the least, I would like to thank my family: my parents and to my brothers for supporting me spiritually throughout writing this thesis and my life in general.

Contents

List of Figures

List of Tables

Introduction

Non–volatile memory technologies are an important part of the microelectronics industry as they are the fundamental for any electronic system we interact with in our daily life. The growing market of the electronics for example digital cameras, smart phone, personal computer, solid state hard disk and many more, need continues improvement in performance and in functionalities.

For many decades flash technology is the main NVM technology used extensively in all electronics but many problems are arising for further scaling and in performances. Because of these problems, it is necessary to look for alternative solution which can replace flash technology as main NVM memory. Many new emerging non-volatile memories has been studied based on new concepts and new materials which can replace the current flash technology. Innovative approaches other than displacing and trapping electrons like in Flash memories have been investigated.

Magnetic random-access memory (MRAM), ferroelectric random-access memory (FeRAM), Oxide based random-access memory (OxRAM) and phase change random-access memory (PCRAM) are some of emerging resistive non-volatile memory which can potentially replace the Flash technology. These kinds of memories are generally based on two terminal devices, and have an active material sandwiched between two electrodes. The main idea of using this kind of structure and material is to use a specific physical mechanism allowing to switch it between two different resistive states for information storage.

For oxide based random-access memory (OxRAM), generally a conductive filament is grown inside the oxide layer, linking the two electrodes due to which two stable state can be generated by creation and disruption of the conductive filament. For the phase change random-access memory (PCRAM), a chalcogenide material is used which can change its phase between a high resistive amorphous and a low resistive crystalline state. These are the two emerging memory technologies which are being studied a lot these days and are showing better performance in terms of read and write speed and also have low power consumption. Many research teams are working to improve the performances and to understand the mechanism behind the switching clearly. The switching mechanism in OxRAM is still a debatable topic and many theories have been provided.

In this thesis, we will study these two different technologies (OxRAM & PCRAM) to understand the mechanism behind switching at nanoscale and to see the scalability by using conductive atomic force microscopy (C-AFM) in ultra-high vacuum. A detailed study for HfO_2 based OxRAM will be presented showing effects on resistive switching due to different bottom electrode material, different AFM tip material and compliance currents by performing electrical characterization. For PCRAM, a study based on $GeSbTe$ (GST) material will be presented. Electrical characterization will be performed to see the phase change.

In chapter 1, a general overview of non-volatile memory technologies will be presented. Different technologies will be briefly discussed and will be compared to each other in terms of improvements. After providing a brief overview of all the volatile and non-volatile memory technologies, a comprehensive review will be provided for OxRAM and PCRAM. Different materials, their performance and challenges as well as different switching mechanisms provided in literature will be discussed in detail for both technologies. In the end a state of art will be presented for the motivation of this thesis work.

In chapter 2, different experimental techniques used to study these memory technologies will be presented. As C-AFM is used as probe station to characterize them, a general overview of atomic force microscopy will be discussed. Also, different C-AFM tips used for electrical characterization of memories as well as different AFM scanning techniques will be discussed. All the characterization will be done in ultra-high vacuum, so the setup will also be presented briefly. A brief overview of scanning electron microscope (SEM) and SEM-EDX (energy-dispersive X-ray spectroscopy) will also be presented as these techniques will be used to characterize the C-AFM tips after having used them for performing the electrical characterization.

Chapter 3 is focused on HfO_2 based OxRAM. Resistive switching in this kind of memory will be presented and its dependence on compliance current will be discussed. First of all, a general study to know the nature of switching behavior (bipolar, unipolar or non-polar) will be performed. Once the switching nature for different HfO_2 based samples determined, a detailed study will be performed in two different compliance current regimes, the nA and the μA range. In both regimes, I-V characteristics will be studied to determine the impact of compliance current on memory effect and the ON state conductance. The results obtained by C-AFM will be compared to device characteristics. To understand the experimental results, an analytical model of filament growth in nA regime will be discussed. A more detailed study in μA regime will be presented in chapter 4.

In chapter 4, a detailed study of resistive switching in high compliance current regime (μA) for HfO_2 based OxRAM will be presented. First of all, the effect of C-AFM tip material (PtSi and full diamond) on resistive switching will be discussed as AFM tips are used as top electrode. Also, the effect of tip radius will be discussed as the tip-sample contact area depends on it. Full diamond tips will be blunted to increase their diameter from 10-20 nm to around 100 nm in order to study its impact. I-V characteristics with sharp and blunt tips will be compared. Also, topographical study will be performed in order to see the deformation on the HfO_2 surface after electrical characterization. SEM-EDX study will be performed to see the chemical composition of the tip before and after the electrical characterization. A brief TEM analysis of the deformation (hillocks) of the HfO_2 surface will be done in order to know its composition. The impact of bottom electrode material on resistive switching will also be studied. All the results obtained by C-AFM will be compared to 1T1R devices in terms of conductance. In the end, effect of polarity on forming and resistance switching will also be discussed. A model based on metallic filament growth will be discussed and will be compared to the experimental results.

Chapter 5 is focused on PCRAM memory. A brief introduction about phase change in phase change materials will be provided. Different phase change materials studied will be discussed. By using C-AFM setup, phase change from amorphous to crystalline will be studied in GST-225 and Ge rich GST. Analytical models

for On-state (crystalline state) and off state (amorphous state) conductance will be discussed. Also, a finite element method approach for phase change in GST-225 will be given. In the end, experimental results obtained by C-AFM will be compared with these models.

Finally, a general conclusion of this work, summarizing the main results will be provided. Also, the highlights and the perspectives of this research for both technologies studied will be given.

Chapter 1

Memory Landscape and Emerging Technologies

In this chapter, an overview of different memory technologies is provided. They will be briefly discussed and compared in terms of their strengths and areas for improvement. This chapter is focused on emerging non-volatile memories especially oxide resistive random-access memories (OxRAM) with an emphasis on HfO_2 as the active layer and phase change memories (PCM) with an emphasis on GST as chalcogenide material. This chapter will comprehensively review OxRAMs and PCM from materials point of view to their performance and the physical mechanisms behind their operation. Different mechanisms given in literature for Oxide based Random access memory will also be discussed briefly.

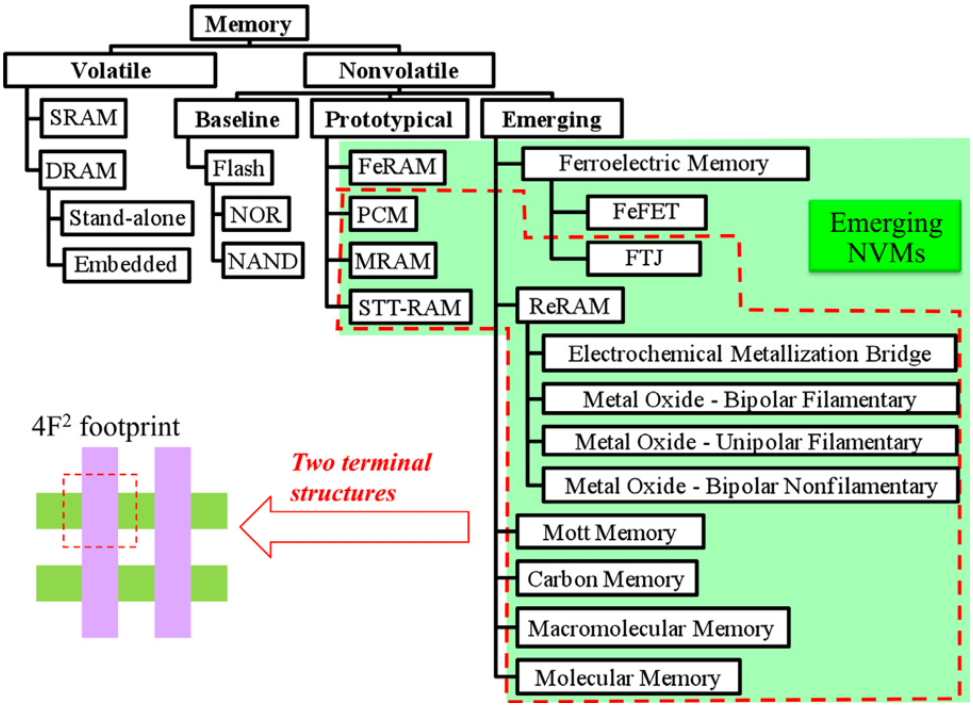

FIGURE 1.1: Overview of different memory technologies[1]. $4F^2$ represents the cell dimension where F is the minimum feature size.

1.1 Overview of memory technology

Normally, memory technologies are divided into two main categories according to their ability to maintain the information without supply voltage, Volatile memories and non-volatile memories. Two different technologies for Volatile memories are well known which are the Static random-access memory (SRAM) and the Dynamic random-access memory (DRAM). Volatile memories lose their data when power is turned off, non-volatile memories don't. There are many different technologies which belong to the non-volatile group like Flash, NOR, NAND and some emerging technologies like, RRAM, PCM, MRAM, etc. An overview of memory technologies is shown in figure 1.1. The memory cell dimension is generally presented in terms of F^2 where F is the minimum feature size. The minimum feature size (F) is the size or the width at which a transistor or any type of device on the silicon surface can be drawn at.

1.1.1 Volatile Memories

Static random-access memory

The word static indicates that the information stored in the memory does not have to be refreshed periodically. However, data is lost when power is switched off due to the volatile nature. SRAMs generally use a matrix of six transistors and no capacitors to store information (shown in figure 1.2). They present very fast Read/write speeds (1ns/1ns) and excellent endurance[2]. However, they are expensive and have low density integration because of their larger feature size ($24F^2$)[2]. They are generally used as cache in computer systems. This type of memory has low power consumption.

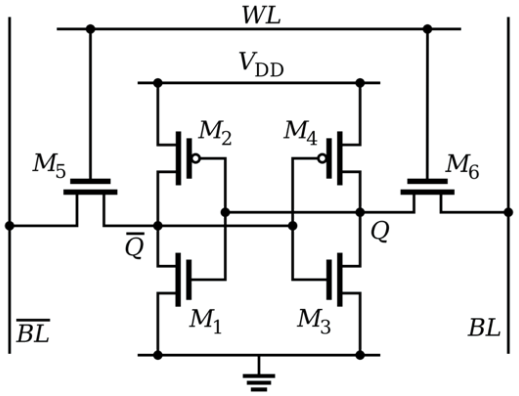

FIGURE 1.2: A typical cell structure of SRAM memory.

Dynamic random-access memory

DRAM, unlike SRAM, must be refreshed in order to maintain their data. This is done by placing the memory on a refresh circuit that rewrites the data several hundred times per second. DRAM is used for most memory systems because it is cheap and small. DRAMs consist of one transistor and one capacitor (1T1C) to store information as shown in figure 1.3. The presence of charge at the terminals of the capacitor corresponds to Logic "1" while Logic "0" corresponds to the absence of charge. Due

to its smaller feature size (6-8F^2)[2], this technology is cheap and presents a very high integration density level with very excellent endurance. DRAMs are generally used as main memory in computer RAMs. DRAM consumes more power and is slower compared to SRAM. A Micron Technology MT4C1021 DRAM integrated circuit is shown in figure 1.4.

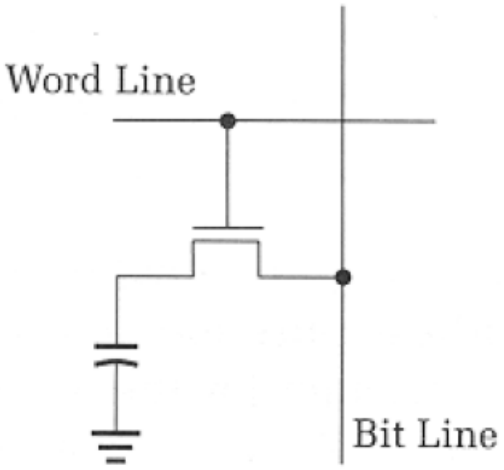

FIGURE 1.3: A typical cell structure of DRAM memory.

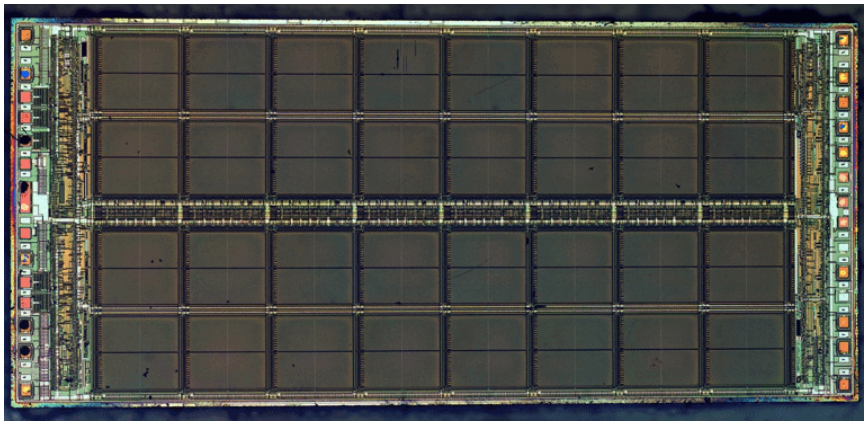

FIGURE 1.4: A die photograph of the Micron Technology MT4C1021 DRAM integrated circuit.

1.1.2 Nonvolatile memories

These kinds of memory technology do not lose data after turning off the power like SRAM and DRAM. Over past few decades, Flash is often used as the non-volatile memory. This memory technology benefits from the traditional scaling of semiconductor industry allowing the high-density integration for mass production. However, the scaling limit is approaching to end due to serious problems such as floating gate interface, lower coupling ratio, leakage current due to thinner oxide layer, short channel effect and low electron charge in the floating gate[3]. After these limitations became critical in flash technology, some new technologies are needed which can scale down without having any effect of the problems discussed for Flash. Hence,

alternative solutions are being discovered referred as emerging non-volatile memories[1;4–6]. There are many different kinds of emerging non-volatile memories such as Ferroelectric random-access memory (FeRAM), Magnetic random-access memory (MRAM), Phase change random access memory (PCRAM) or simply phase change memory (PCM), Conductive bridge random access memory (CBRAM) and oxide based random access memory (OxRAM). Some of them are already commercially available in market like PCM and MRAM. All these memories will be discussed briefly in next section. A comparison of different memory type cell structures is presented in figure 1.5.

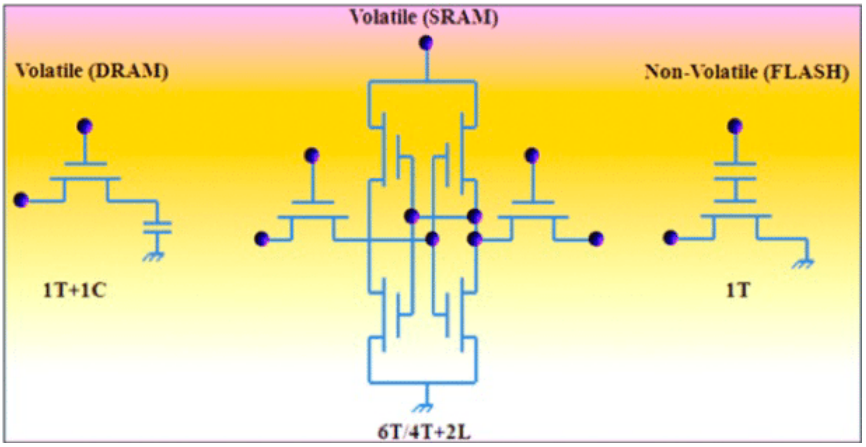

FIGURE 1.5: Comparison of different cell structures for different types of memory technology[4].

1.2 Emerging nonvolatile memory technologies

1.2.1 Flash

Flash memory is a nonvolatile storage device that can be erased and reprogrammed. Flash memory was developed from electrically erasable programmable read only memory (EEPROM). There are two different types of Flash memory based on logic gates, NAND and NOR Flash memory. The internal characteristics of different types of flash memory cells exhibit characteristics similar to the corresponding gates. The NAND type is primarily used in main memory, memory card, USB flash drives, solid state drives for general storage and transfer of the data. The NOR type is used as a replacement for the older EPROM and alternative to certain kind of ROM applications.

In 1967, Kahng et al. presented the floating gate and its application for memory in their paper[7]. Flash memory was invented by Dr Fujio Masuoka while working in Toshiba in 1980. Mausoka et al. presented the invention at the IEEE 1984 International Electron device meeting held in San Francisco[8;9]. Intel first commercialized the NOR type Flash memory chip in 1988.

Flash memory cell[10] is a typical floating gate MOS transistor, and this floating gate (FG) is completely surrounded by dielectric or oxide layer, and electrically governed by a capacitively coupled control gate (CG)[4;11]. This floating gate is electrically isolated from the control gate and the channel by two dielectric layers: control oxide and tunnel oxide. Being electrically isolated, the floating gate acts as the

storing electrode of the cell. When a positive voltage is applied to the control gate, electrons are injected into the floating gate through the tunnel oxide via Fowler-Nordheim (FN) tunneling. The Logic state is represented by the charging level. The neutral or positively charged state is associated with logic state "1" and the negatively charged state corresponds to logic state "0".

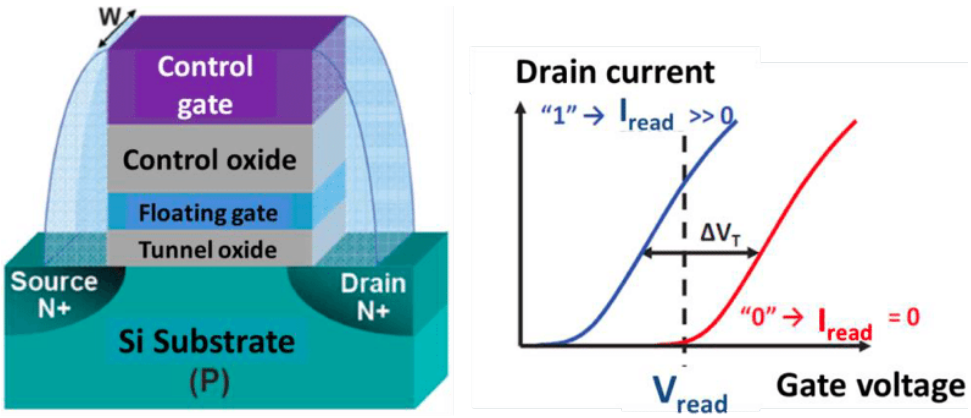

FIGURE 1.6: (left) Basic structure of Flash memory cell (right) Example of corresponding IV characteristics; adopted from[12].

Flash has two different kind of architectures based on gate, NOR and NAND arrays, which are named after the resemblance to the pull-down networks in the corresponding CMOS logic gates. In the NOR array, cells are organized in a parallel architecture, aiming at a direct access of each cell, which is connected to its bit line through a dedicated drain contact enabling the device to achieve random access. Because of this parallel architecture the performance is better for NOR. This configuration enables the short-read times required for random access microprocessor instructions. NOR flash is ideal for lower density, high speed-read applications.

NAND flash was developed as an alternative optimized for high density data storage, giving up random access capability in a trade of smaller cell size. This was done by creating memory cells connected in series and organized into memory strings, trading off read/write random speed for a higher integration density and, thus, a lower cost per bit[13–15]. So, NAND flash is ideal for low cost, high density and high-speed program/erase application. The architecture comparison between NAND and NOR flash is given in figure 1.7.

Over past years many improvements were done in flash technology. Flash technology has been scaled down in order to meet the requirement of reduced feature size and large memory. Intel started the mass production of 32-layed NAND chips as shown in figure 1.8. When reaching the scaling limit of transistors, some alternative technologies have to be developed. Even after a remarkable development in the field of flash, it is believed that scaling beyond 22nm node will be challenging and serious physical problems will appear[17]. In order to have 10-year data retention, the tunnel and control oxide need to be thick enough to prevent charge loss. But scaling down the thickness of tunnel oxide will affect this requirement. The primary concern is that stress Induced leakage current (SILC) affects the device reliability and its amplitude increases when reducing the oxide thickness[18]. Also,

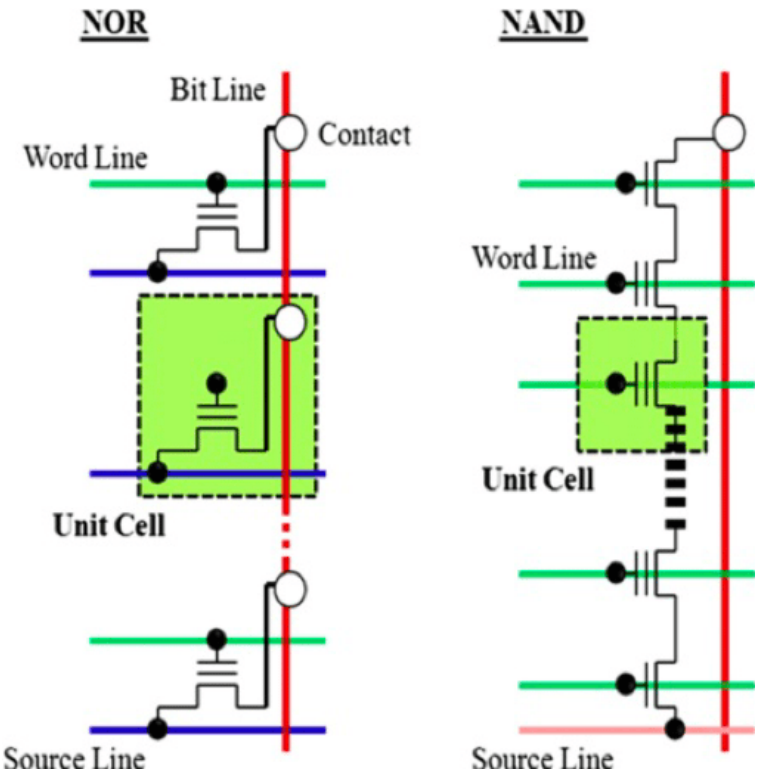

FIGURE 1.7: Comparison of NOR Flash array and NAND Flash array architectures[4].

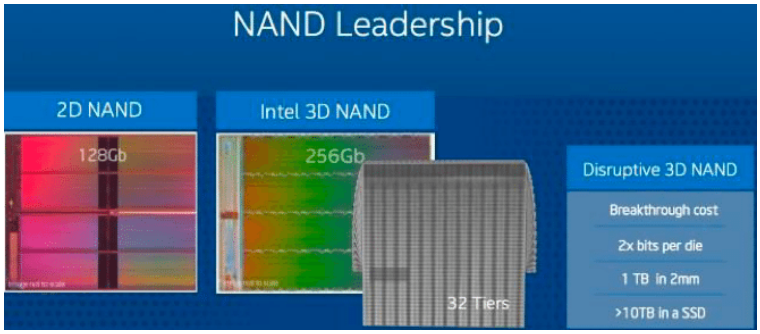

FIGURE 1.8: 32-layer 3D NAND Flash produced by Intel[16].

few electron phenomena may be an ultimate intrinsic limit in the scaling of Flash memories[19].

Currently, an extensive research is going in the field of memory and it is not easy to predict which technology will win the race. Even though there are many technologies which are showing the great interest in the field of memory and will be discussed in coming sections.

1.2.2 FeRAM

Ferroelectric random access memory[20;21] (FeRAM) is a type of non-volatile memory which uses ferroelectric layer as a capacitor to store the data. It uses the ferroelectric effect for the storage mechanism. It is polarized by applying external electric field and remains polarized even if the external electric field is removed. This type of polarization is called remanent polarization. Due to this polarization characteristic,

FeRAM does not lose any data if the power is removed from it. When the direction of the applied field is reversed, the polarization of the ferroelectric material changes its direction and hence, it can update the new data. Polarization is a phenomenon due to the ionic displacement of atoms of ferroelectric crystal structure.

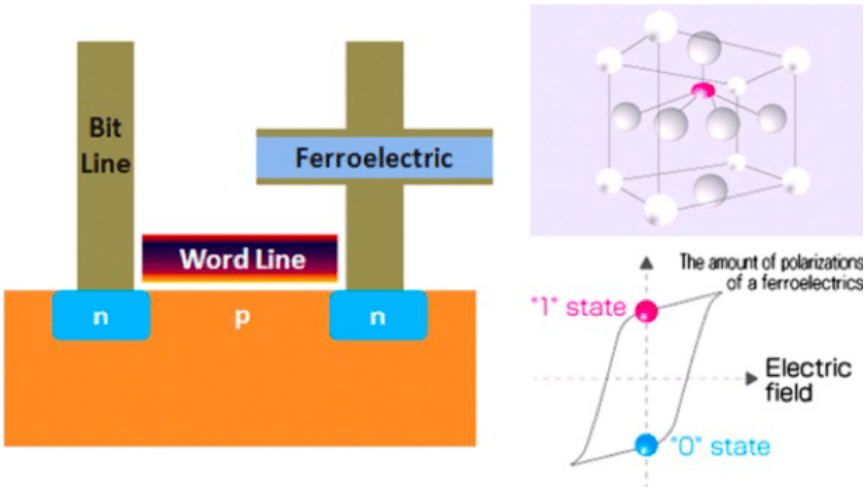

FIGURE 1.9: On left hand, the basic structure of a FeRAM cell is shown. On top right crystal structure of ferroelectric and on bottom right an electric polarization-electric field hysteresis curve are also shown[4].

Therefore, FeRAM is a superior memory that has fast speed of reading and writing the data. It has low power consumption among other semiconductor memories[22] and higher operation speed compared to DRAM[23;24]. So, it is a fast memory that can endure a high number of cycles (for example 10^{14})[25]. The idea of ferroelectric memory was first given by Bell Laboratory in 1955. In 1980, a FeRAM in which data is stored by polarization direction in ferroelectric capacitors and read out by using reverse polarization direction was proposed[26]. A FeRAM memory cell has the same structure as a DRAM cell and consists of a transistor and a capacitor, but in this case the FeRAM cell contains a capacitor with a ferroelectric dielectric.

This kind of memory is fabricated by depositing a film of ferroelectric material in crystalline form between two electrode plates to form a capacitor. This structure is similar to that of the DRAM capacitor. It is important that the ferroelectric films should have high remanent polarization, low leakage current, low coercive field. Low operating voltage is reached because of the low coercive field which also helps in faster switching speed and better fatigue resistance. Today's FeRAM uses lead zirconate titanate (PZT); other materials are being considered. FeRAM are extensively studied. Even after FeRAM has achieved a level of commercial success, with the first devices released in 1993[27]. Since 2011 there are new promising development with HfO_2 based materials which present ferroelectricity[28].

1.2.3 MRAM

Magnetic Random access memory is also nonvolatile memory[29] but it works on magnetic field unlike other nonvolatile memories like flash which work on charge storage. It uses a magnetic element having a magnetoresistance effect in a memory cell. Magnetoresistance effect is a phenomenon which happens when a magnetic

field is applied to magnetic material and its electrical resistance is changed in accordance with the direction of its magnetization.

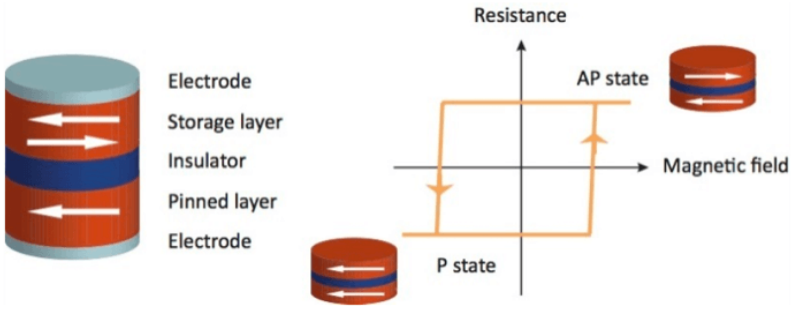

FIGURE 1.10: Simple structure of a magnetic tunnel junction is shown in the left side and variation in resistance with magnetic field is shown in the right side with two different magnetic states, the parallel one and the anti-parallel one[30].

The basic MRAM cell element consists of a magnetic tunnel junction (MTJ) as shown in figure 1.11. Magnetic field induced magnetic switching was first employed in the early realization of MTJ based MRAM[30–32]. These MTJs are composed of three different layers. One layer is insulating layer which is sandwiched between two magnetic layers, called free magnetic layer[33] and fixed magnetic layer. Electrons in MTJs which are spin polarized by magnetic layer traverse the dielectric barrier through tunneling[34] when a bias is applied. These MTJs devices have low resistance when the magnetic moment of the free magnetic layer is parallel to the fixed magnetic layer and have high resistance state when they are in antiparallel state.

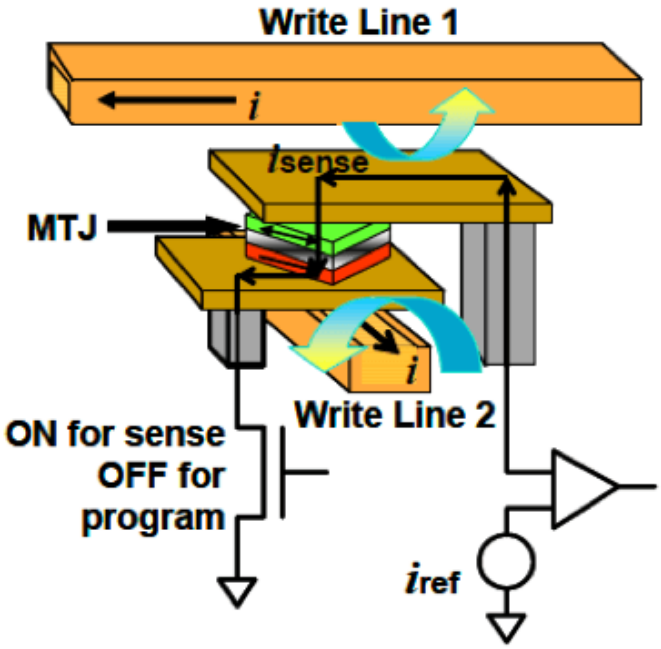

FIGURE 1.11: Schematic of 1-transistor, 1-MTJ cell.

Early MRAM devices had problems due to very high write currents necessary

to induce the magnetic field for switching, but with the development in the field of MRAM, the write current level[35] decreased. For example, devices based on STT-MRAM (Spin transfer torque-MRAM)/MRAM have high endurance and high-performance characteristics (high speed, low voltage) which makes them good candidates for embedded applications. On the other hand, MRAM has low integration density compared to Flash or DRAM[35] and its scalability beyond the 20nm node still remains to be demonstrated[36].

1.2.4 CBRAM

One of non-volatile memory is conductive-bridging random access memory (CBRAM)[37;38] which is based on metal ion transport and redox reactions to form a persistent conducting filament in a high resistance film between two electrodes. The switching is based on formation and dissolution of this metallic filament in the material under external bias. CBRAM consists of an inert electrode like platinum, iridium, gold or tungsten and the other electrode can oxidize such as copper or silver. This effect may be reversed to return the device to a high resistance state. These two electrodes are separated by a solid electrolyte or oxide material[39;40]. Memory Switching using a Ag dendrite in a Ag-doped As_2S_3 film in a $Ag/As_2S_3/Mo$ structure is reported by Hirose et al.[41] in 1976. The On state is achieved by applying a positive bias at the oxidizable anode resulting in the redox reaction driving the positive silver ions to the inert cathode if the electrode is of silver. Due to this effect, a filament of metal rich clusters is formed leading to a conductive bridge between the electrodes. By applying the opposite voltage, the filament can be dissolved breaking the conductive bridge between the electrodes.

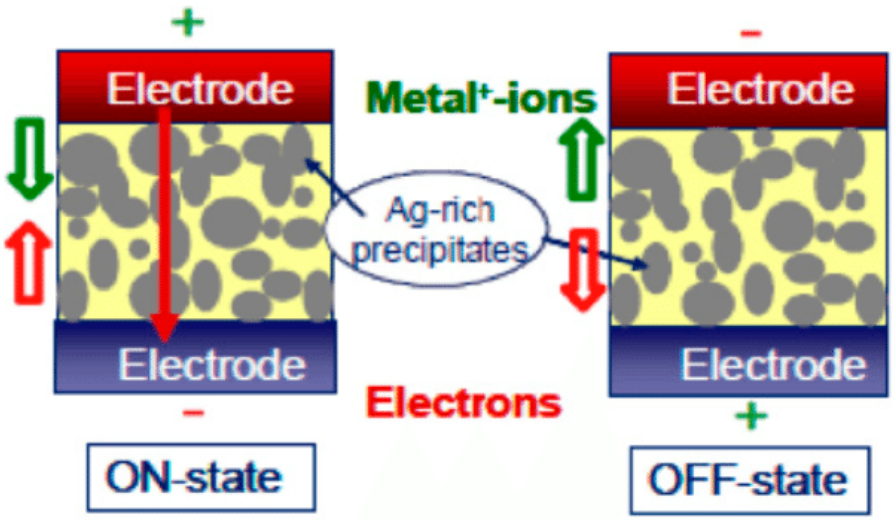

FIGURE 1.12: Schematic illustration of the CBRAM switching mechanism[42].

The CBRAM memory is also known as programmable metallization cell (PMC). In 1999, Kozicki et al.[43] reported a programmable metallization cell (PMC) device using metal-doped chalcogenide films. PMC devices are also called electrochemical metallization cell (ECM)[44;45], atom switch[46], or CBRAM[42;47].

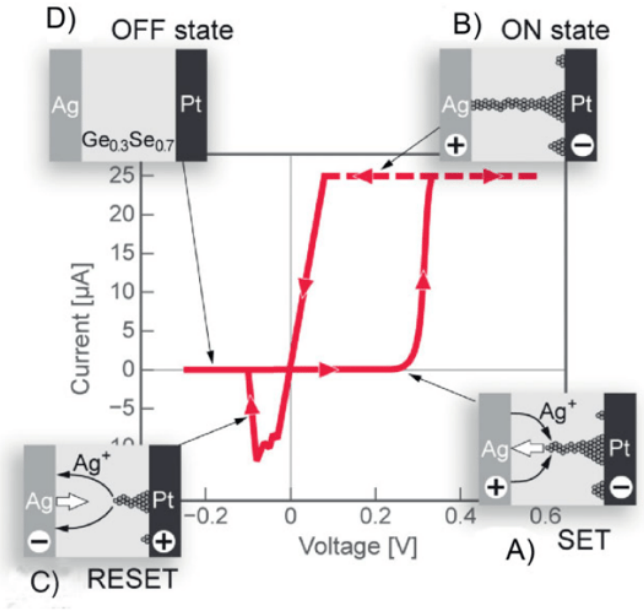

FIGURE 1.13: Typical I-V characteristic of Ag/Ag-Ge-Se/Pt electrochemical metallization cell. Adopted from reference[48].

1.2.5 PCRAM

Phase change memory (PCM) or Phase change random access memory (PCRAM) is the most matured technology among the emerging non-volatile memories. Phase change memory is based on the phase change of the active material. Generally, chalcogenide materials are used as a phase change material. Chalcogenide materials are in amorphous phase initially and can change the phase to crystalline by applying a bias. The on state corresponds to the low resistance state due to crystalline phase and the Off state to the high resistance state of the amorphous state. A schematic structure for PCM is presented in figure 1.14. This type of memory will be discussed in more detail in section 1.4.

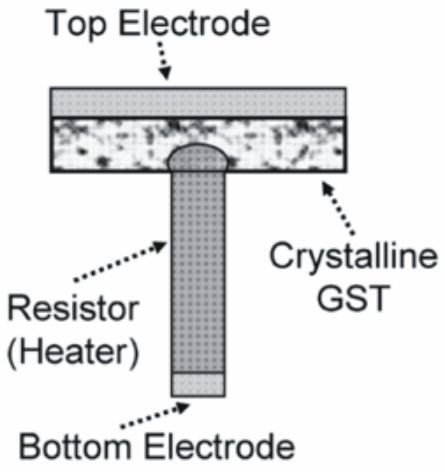

FIGURE 1.14: Schematic of a PCRAM cell[49].

Type	SRAM	DRAM	NOR FLASH	NAND Flash	MRAM	PCRAM	FeRAM	RRAM
Cell elements	6T	1T1C	1T	1T	1(2)T1R	1T1R or ID1R	1T1C	1T1R or ID1R
Cell	Latch	Stack/ trench capacitor	Floating gate/ change trap	Floating gate/ change trap	Magneto resistance	Phase change	Polarization change	Resistance change
Minimum / cell size nm^2	$140F^2$	$6F^2$	$10F^2$	$5F^2$	$20F^2$	$4F^2$	$22F^2$	$4F^2$
Write/ erase time	0.3 ns/0.3ns	<10 ns/<10 ns	1 ms/10ms	1ms/0.1ms	10 ns/10 ns	20 ns/50 ns	10 ns/10 ns	5 ns/5ns
Endurance (cycles)	$>3 \times 10^{16}$	$>3 \times 10^{16}$	$>10^5$	$>10^5$	$>3 \times 10^{16}$	$>10^8$	$>10^{14}$	$>10^{10}$
Application	Cache	Main memory	Storage	Storage	Storage	Storage	Storage	Storage/ Main memory

TABLE 1.1: Comparison of conventional and emerging memories. The data is taken from reference[50]. 1D1R is one diode and one resistor unit cell.

1.2.6 OxRAM

Oxide based random access memories (OxRAM) belong to resistive random-access memories (RRAM) and are also well known emerging non-volatile memories. An intensive research is going on for OxRAM. OxRAM has a high switching speed, low power consumption and is scalable. The basic structure of OxRAM is MIM (metal/insulator/metal). When a bias is applied a filament is formed inside the oxide layer connecting the two electrodes changing the resistance state. When the two metal electrodes are not connected through a filament, it is in high resistance state (HRS) which is also known as off state. When the two electrodes are connected through a filament, the low resistance state is achieved, this state is also known as On state. OxRAM will be discussed in detail in section 1.3.

A comparison is provided for all the volatile and non-volatile memories discussed in previous sections in table 1.1. Cell structure, minimum cell size, write and erase time as well as the number of endurance cycles for different memory technologies are presented in the table 1.1.

1.3 Oxide based random access memory

The resistive switching effect has been studied for more than 40 years. In 1962, Hickmott et al.[51] reported resistive switching for the first time in the I-V characteristic of five metal oxide metal structures: SiO_x, Al_2O_3, Ta_2O_5, ZrO_2 and TiO_2. The switching time[51] was evaluated to be less than 0.5 μs. Still the mechanism of resistive switching was unclear. In 1964, Gibbons et al.[53] reported a study on NiO, where they believed that the switching is due to the formation and rupture of a Nickel filament in NiO thin film which is sandwiched between two electrodes. In 1967, Simmons et al.[54] reported the pioneering study discussing the use of this resistive switching for memory application[55]. In 1970, fast switching of resistance in $Al/SiO_x/Au$ structure was shown by Dearnaley et al.[56] and they concluded that the reason was an electronic effect rather than the filament formation and rupture. Also, a paper published by Chua et at.[57] on "Memristor-the missing circuit element" contributed to this field. ' Many studies have been done over the years on non-volatile memories from the 1960s to the beginning of the 21st century[58;59] and a 64-bit perovskite oxide-based ReRAM memory was fabricated by Zhuang et al.[60] in 2002 by using a 0.5 μm CMOS process. In 2004 a group from Samsung Advanced Institute of Technology reported binary transition metal oxide-based ReRAM and successfully demonstrated RRAM operation below 3V and 2mA, 10^6 set/reset operations and 10^{12} reading cycles[61]. A paper title "Missing memristor found" triggered the intensive development in RRAM[62]. Since then, great achievement had been reported in the field of RRAM by Unity[63], SanDisk/Toshiba[64], Micron/-Sony[65] and IMECAS[66]. Also, TSMC announced in 2017 a new plan to start the production of embedded RRAM chips in 2019 based on 22-nm process. A roadmap for OxRAM is shown in figure 1.15.

1.3.1 Basic Operation of OxRAM

As discussed in the previous section, the resistive switching mechanism in OxRAMs is still under debate. C. Cagli et al.[67] studied the switching in HfO2 based OxRAM devices. They did several experiments to demonstrate that the switching is driven by creation/disruption of a conductive filament (CF). They reported the resistance

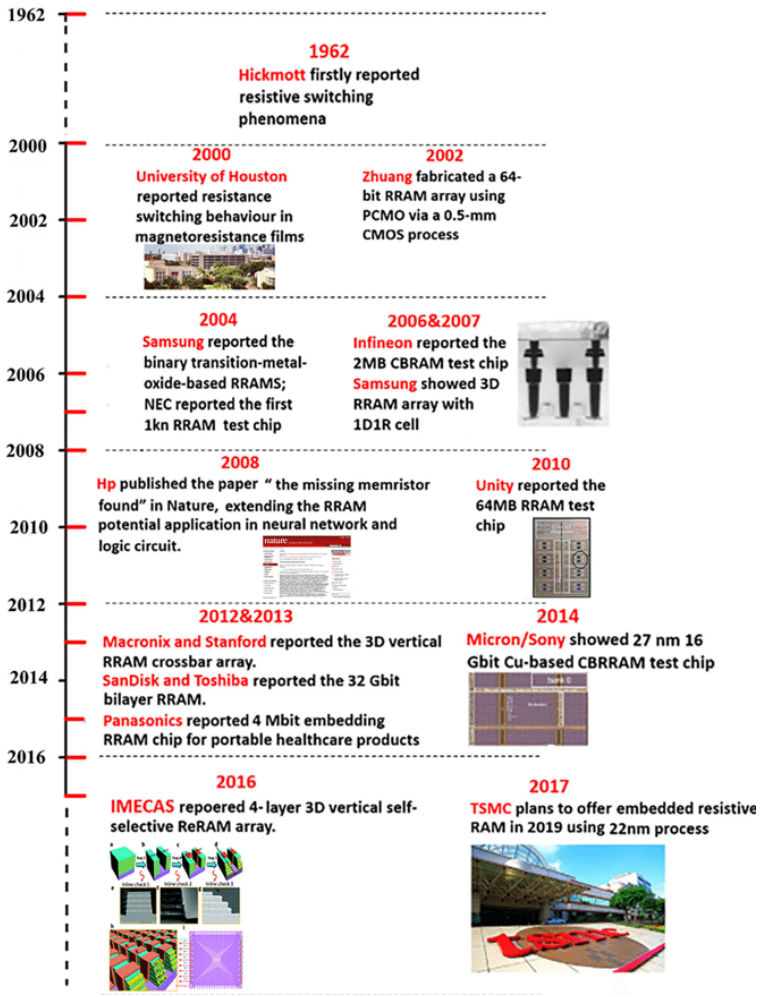

FIGURE 1.15: Historical timeline of RRAM development from 1962 to 2017. Adopted from [52].

variation as a function of cell dimension as shown in figure 1.16. As it can be seen, there is no influence of cell dimension on the resistance in low resistance state (LRS) or On state, but the resistance should decrease with increasing the cell dimension according to the cross sectional area law. This clearly indicates that switching is driven by creation/disruption of a conductive filament. Also, there is small fluctuation in high resistance state (HRS) or off state. These fluctuations may be due to tunneling enhanced by partially disrupted filaments with different lengths. According to the independence of resistances to devices area, C. Cagli et al. suggested that the switching is due to the creation and disruption of the filament. So, in this thesis, we will verify this assumption by using C-AFM measurements at nanoscale.

In pristine state, the resistance of the oxide layer is very high and it needs to be preconditioned before resistive switching. To precondition the resistance of pristine oxide an operation called forming is done. Forming is current controlled breakdown of the oxide layer which creates a conductive path with low resistance called conductive filament (CF) inside the oxide layer connecting the two electrodes.

Once the conductive filament is formed, the resistance across the electrodes decreases rapidly. When forming the filament, the current is limited to a value called

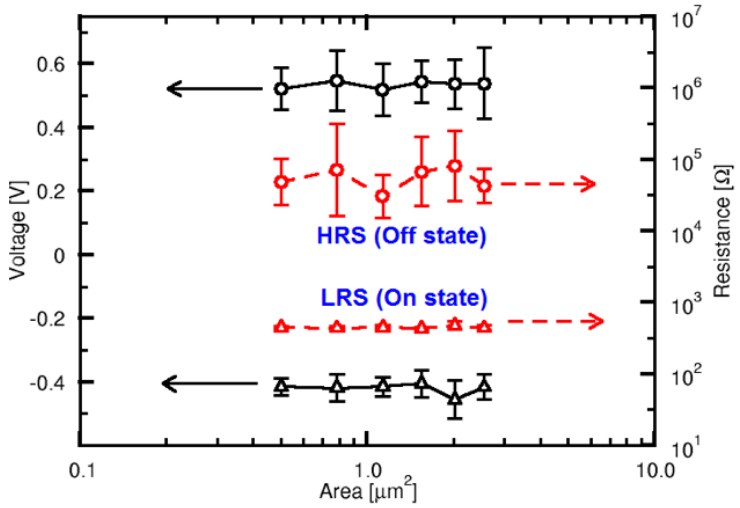

FIGURE 1.16: Dependence of cell dimension on the resistance in on and off state (right coordinate axis)[67].

compliance current (Ic) in order not to destroy the device permanently. When studying the characteristics of devices, this compliance current is fixed by a semiconductor parameters analyzer for 1R devices and by a field effect transistor for 1T1R devices.

By applying higher bias after forming, the filament can be ruptured or disrupted. Once the conductive filament is ruptured the device comes back to high resistance state. This process is known as RESET. Then, by applying a bias, the filament can be created completely again and the device is back in low resistance state. This process is known as SET. Forming, Set and Reset operations are shown in figure 1.17. When the filament connects the electrodes, the memory cell is in the on state (SET) or logic state "1" and when the filament is ruptured, the memory cell is in the off state (RESET) or logic state "0".

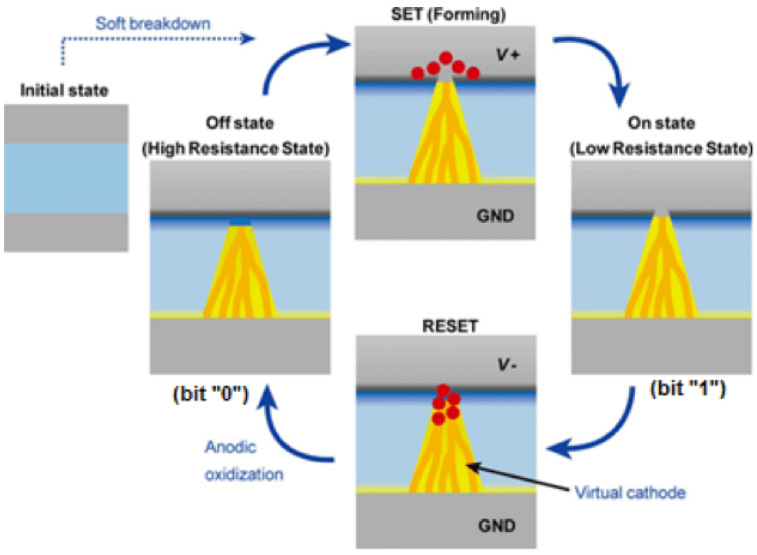

FIGURE 1.17: Different steps for RRAM operation showing forming of the conducitve filament, SET and RESET[68].

Different switching behaviours have been observed for OxRAM depending on

the polarity known as unipolar and bipolar resistive switching. When the same bias is applied to form the conductive filament and to rupture it in order to SET and RESET the state, it is called unipolar behaviour. On the other hand, when different polarities are used to SET and RESET the filament in order to change the state from high resistance state to low resistance state or vice versa, it is called bipolar switching behaviour. For bipolar switching, the same polarity is used for forming and SET process. In figure 1.18, different switching behaviours can be seen.

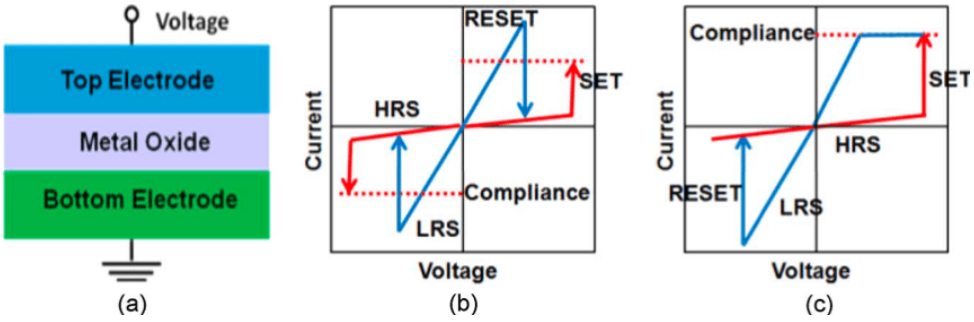

FIGURE 1.18: (a) Basic structure of OxRAM or RRAM with metal-insulator-metal configuration, (b) Unipolar switching behaviour in an OxRAM device and (c) Bipolar switching behaviour in an OxRAM device[69].

In figure 1.19, switching I-V characteristic for bipolar OxRAM is presented. When a bias is applied to pristine oxide, the first resistive switching happens at the so-called forming voltage leading to the low resistive state. To rupture the filament to RESET it, opposite polarity is applied. The voltage when the current starts decreasing is known as reset voltage (V_{RESET}). At V_{RESET} the filament is ruptured changing the resistance state from LRS to HRS.

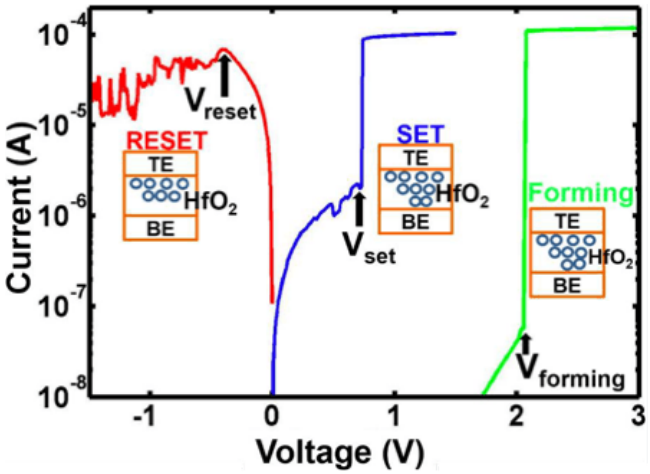

FIGURE 1.19: I-V characteristic for a bipolar OxRAM device showing forming, SET and RESET steps[70].

Before the SET process, the current increases slowly with increasing voltage and at the set voltage (V_{SET}) it increases abruptly reaching the compliance current immediately. At V_{SET}, the conductive filament is completley formed and both electrodes are connected through the filament changing the state from HRS to LRS.

1.3.2 Materials

Many different binary metal oxides have been studied for RRAM or OxRAM with most of the metals belonging to transition metals. In 1962 Hickmott et al.[51] had studied five different oxide films including SiO_x, Al_2O_3, Ta_2O_5, ZrO_2 and TiO_2 with a large negative resistance in the current voltage characteristics. Since then, a large number of materials has been found and investigated exhibiting resistive switching (RS) behavior, which can be categorized into binary oxides, ternary and

Storage medium	Switching mode	ON/OFF ratio	Operation speed (set;reset)	Endurance
Binary Oxides				
AlO_x[71–73]	Unipolar, bipolar	$>10^6$	<10ns;<10ns	$>10^4$
SiO_x[74;75]	Unipolar, bipolar	$>10^7$	<100ps;<100ps	$>10^8$
TiO_x[76–79]	Unipolar, bipolar	$>10^5$	<5ns;<5ns	$>2 \times 10^6$
CrO_x[80]	Bipolar	$>10^2$	<4μs;<5μs	$>6 \times 10^4$
MnO_x[81;82]	Unipolar, bipolar	$>10^4$	<100ns;<200ns	$>10^5$
FeO_x[83;84]	Bipolar	$>10^2$	<10ns;<10ns	$>6 \times 10^4$
CuO_x[85–87]	Unipolar, bipolar	$>10^5$	<50ns;<50ns	$>1.2 \times 10^4$
NiO_x[53;88–90]	Unipolar, bipolar	$>10^6$	<10ns;<20ns	$>10^6$
ZnO_x[91;92]	Unipolar, bipolar	$>10^7$	<5ns;<5ns	$>10^6$
GeO_x[93;94]	Unipolar, bipolar	$>10^9$	<20ns;<20ns	$>10^6$
ZrO_x[95–97]	Unipolar, bipolar	$>10^6$	<10ns;<20ns	$>10^6$
NbO_x[98]	Unipolar, bipolar	$>10^8$	<100ns;<100ns	$>10^7$
MoO_x[99]	Unipolar, bipolar	>10	<1μs;<1μs	$>10^6$
HfO_x[100–106]	Unipolar, bipolar	$>10^5$	<300ps;<300ps	$>10^{10}$
TaO_x[107–110]	Unipolar, bipolar	$>10^9$	<105ps;<120ps	$>10^{12}$
MgO_x[111]	Unipolar, bipolar	$>10^5$	–	$>6 \times 10^2$
Ternary and more complex Oxides				
$LaAlO_3$[112;113]	Bipolar	$>10^4$	–	$>10^2$
$SrTiO_3$[114;115]	Bipolar	$>10^5$	<5ns;<5ns	$>10^6$
$BaTiO_3$[116;117]	Unipolar, bipolar	$>10^4$	<10ns;<70ns	$>10^5$
$BiFeO_3$[118;119]	Unipolar, bipolar	$>10^5$	<50ns;<100μs	$>10^3$
Chalcogenides				
Cu_2S[120]	Bipolar	$>10^6$	<100μs;<100μs	$>10^5$
GeS_x[121]	Bipolar	$>10^5$	<50ns;<50ns	$>7.5 \times 10^6$
Ag_2S[122;123]	Bipolar	$>10^6$	<200ns;<200ns	–
Ge_xSe_y[124]	Bipolar	$>10^6$	<100ns;<100ns	$>3.2 \times 10^{10}$
Nitrides				
AlN[125–128]	Unipolar, bipolar	$>10^3$	<10ns;<10ns	$>10^8$
SiN[129–131]	Unipolar, bipolar	$>10^7$	<100ns;<100ns	$>10^9$
Others				
$a-C$[132;133]	Unipolar, bipolar	$>3 \times 10^2$	<50ns;<10ns	$>10^3$
$a-Si$[77;134]	Bipolar	$>10^7$	<5ns;<10ns	$>10^8$
AgI[135;136]	Bipolar	$>10^6$	<50ns;<150ns	$>10^5$

TABLE 1.2: Different materials used for RRAM switching in literature.

more complex oxides, nitrides, amorphous-silicon/carbon and some organic materials[137] with specific application in the field of flexible electronic devices[138]. All

the materials used for RRAM are shown in table 1.2. Among all these some of binary metal oxides like TaO_x, TiO_x, AlO_x, NiO and HfO_2 have gained more interest.

Yang et al.[139] studied the resistive switching based on TaO_x. Top electrode of Ta and bottom electrode of Pt is used for the MIM structure. They have reported 1×10^{10} switching cycles. They used pulses of 1 μs with +1.9 V for SET and -2.2 V for Reset. The corresponding current voltage characteristic can be seen in figure 1.20.

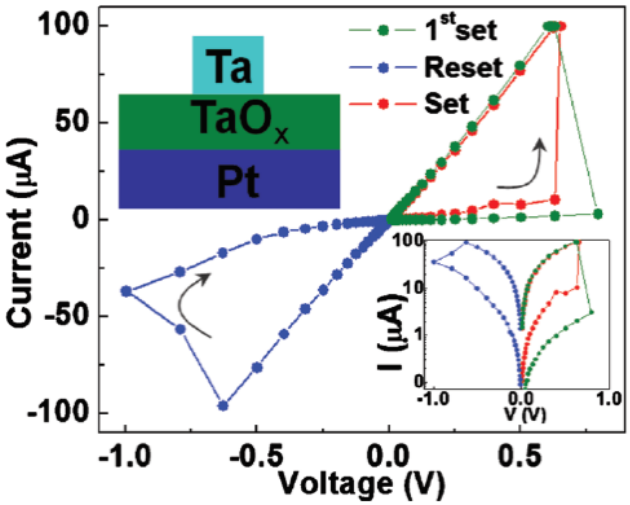

FIGURE 1.20: I-V characteristic Pt/TaOx reported by Yang et al.[139].

Park et al.[76] studied TiO_x based RRAM for multi bit operation. They investigated the mechanism using $Ir/TiO_x/TiN$ structure. The characteristics they obtained are shown in figure 1.21.

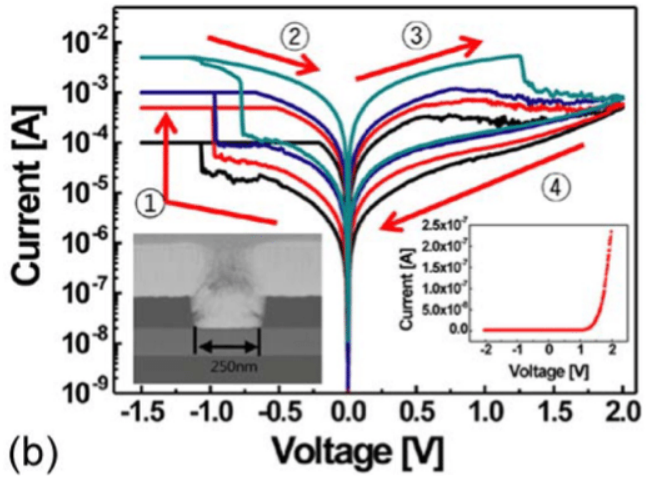

FIGURE 1.21: I-V characteristic TiOx based RRAM reported by Park et al.[76].

Yoshida et al.[140] studied high speed resistive switching in $Pt/TiO_2/TiN$. They showed an excellent endurance over 2×10^6 cycles. Voltage pulse of 5ns at -1.9V was used for set and 5ns at 2.9V for reset. I-V characteristic obtained by Yoshida et al are shown in figure 1.22.

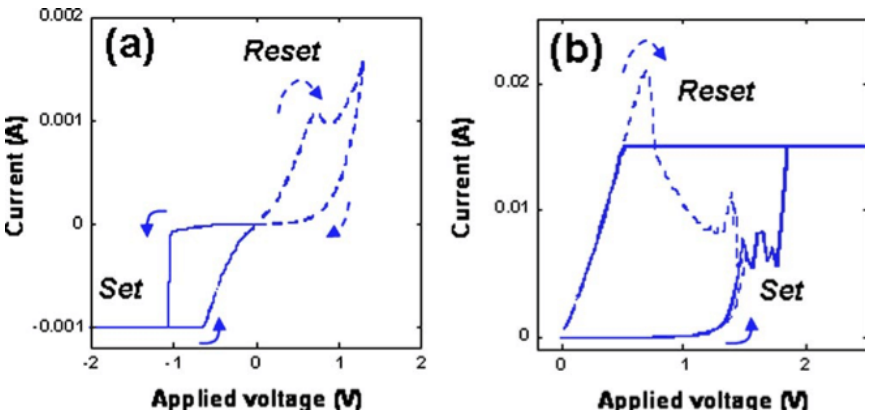

FIGURE 1.22: I-V characteristic Pt/TiO2/TiN reported by Yoshida et al.[140].

Many different groups worked on NiO film as oxide layer for resistive memory. Yoshida et al.[141] showed bipolar resistive switching in $Rh/NiO/Pt$ structure. Ielmini et al.[142] and Huang et al.[89] also presented their work on NiO based resistive switching.

HfO_2 is one of the most adopted metal-oxide for resistive switching. It has been intensively studied by many groups, companies and research laboratories. It is also compatible with CMOS back end of line process which makes it more attractive. Hou et al.[143] demonstrated the switching for devices in sub-10nm range. Zhao et al.[144] recently reported 2nm ultrathin HfO_2 layer sandwiched between Pt and TiN electrodes for 3D integration. High endurance (>10^8 cycles)[145], low voltage[145;146], very good data retention[144;147] and excellent device yield[148] have been presented for HfO_2 based RRAM devices. Hence HfO_2 is the best suitable and investigated among other binary metal oxides. In this thesis work, we will also adopt HfO_2 for resistive switching studies.

1.3.3 Electrode material effect on switching behavior

Top and bottom electrodes exhibit the effect of work function, oxygen affinity, electronegativity and inter-diffusion. Many noble metals such as Pt, Au and Ru have been used as electrode material. Also, Ti, TiN, TaN, Al have been used as electrode. Yang et al.[149] studied Cu_2O layer with top electrode of Pt combined with various bottom electrodes. It was concluded in the paper that when Ohmic or Schottky contact is formed to create high enough electric field across the Cu_2O layer, resistive switching behavior is induced. Many reports showed the effect of top and bottom electrode material on the RS behavior of RRAM. An overview is given in table 1.3.

As can be seen in table 1.3, it is a general trend that switching behavior of the memory cell depends on the electrode materials. When a top electrode is oxygen reactive metal like Ti, the switching is mostly bipolar. When both top and bottom electrode are symmetrical and less reactive with oxygen then the memory cell shows unipolar or non-polar behavior. When unipolar and bipolar switching is found for the same system, this behavior is called non-polar switching behavior. RRAM device performance depends on the choice of the electrode material making its characteristic influenced by stack composition. There are many studies going on to completely understand the origin of the unipolar and bipolar switching in RRAM. By changing the electrode materials for the same oxide, the switching behavior can be changed.

Bottom Electrode	Oxide Material	Top Electrode	Switching Behavior
Pt[150]	ZrO_2	Ti	Unipolar
Pt[95;150]98,152	ZrO_2	Pt	Unipolar
Pt[95]	ZrO_2	Ti	Bipolar
TaN[151]	$TaO_x/Ta_2O_{5-\delta}$	Ir	Bipolar
Pt[152]	TaO_x/Ta_2O_{5-x}	Pt	Bipolar
Pt[139;153]	TaO_x	Pt	Bipolar
TiN[154]	HfO_2	Ti/TiN	Bipolar
TiN[155]	HfO_2	AlCu/TiN	Bipolar
TiN[156]	HfO_2	Ti/TiN	Bipolar
TiN	HfO_2	Pt	Unipolar/Bipolar
Pt[157]	HfO_2	Au	Unipolar
Pt[158]	HfO_2	Pt	Unipolar
Pt[78]	TiO_2	TiN	Bipolar
Pt[159;160]	TiO_{2-x}/TiO_2	Pt	Bipolar
Pt[62;161]	TiO_2	Pt	Bipolar
Pt[162;163]	TiO_2	Pt	Unipolar
Pt[164]	TiO_2	Ru	Unipolar
Nobel Metal[61]	NiO	Nobel Metal	Unipolar
Pt[158;165]	NiO	Pt	Unipolar

TABLE 1.3: Different materials used for top and bottom electrode in MIM structure for RRAM in literature.

So the electrode material has an impact on switching behavior and not only the oxide material[69]. Cagli et al.[67] reported that when a top electrode is changed from Pt to Ti in the case of a HfO_2 oxide layer, the switching is also changed from unipolar to bipolar.

1.3.4 Switching mechanisms

Resistive switching mechanism has been observed for many binary oxide materials. Mostly a filamentary resistive switching is reported for this kind of oxides sandwiched between two metal electrodes. Filamentary resistive switching is the widely accepted switching mechanism[166–169]. The remaining questions are then the nature of the conductive filament and the formation mechanism. The most common assumptions are that the conductive filament consists of oxygen vacancies, metal ions or a mixture of both metal and oxygen ions. Possible filaments which switch the device to LRS presented in literature are Metallic nano-bridges[91], oxygen vacancies (V_O^{2+} s) composed conductive channels[170], dislocations[171] and a trail of metallic islands[134]. A distinct feature of filament-type resistive switching is that the resistance in LRS is independent on device area as reported by Zhang et al.[82] and Yang et al.[81] for MnO_x films and by Cagli et al.[67] for HfO_2 films. In addition, the cross section of the filament determines the scaling limit. In general, RRAM devices need to be preconditioned for resistive switching through the operation of forming. Forming is a stochastic process which is still not well understood leading to the formation of a conductive filament through the oxide layer. There are several studies done to understand the formation of filament in binary metal oxides for RRAM in literature.

Identification of the grain boundaries (GB) in HfO_2 as constituting leakage paths that ultimately transform into the CF during the forming process is reported by Bersuker et al.[168] which is consistent with GB assisted filament formation reported by Lanza et al.[172].

Zhao et al.[173] explained the forming process in a $Pt/TiO_2/Pt$ stack through the formation of oxygen ions and oxygen vacancies at the anode. The oxygen vacancies migrate towards the cathode and grow into a cone-shaped CF of Ti_4O_7 with the larger side of the cone at the cathode. The O ions are removed from the oxide and chemisorbed at the grain boundaries of Pt electrode near the anode interface.

Jeong et al.[174] also worked on similar stack of $Pt/TiO_2/Pt$ and elaborates on the Ti ions. The Ti ions in the oxygen deficient regions might be reduced to fulfil the local charge neutrality by capturing electrons from the cathode. These reduced valence states of Ti ions can form a metallic phase with the oxygen vacancies in the form of $TiO_{2-n/2}$ for approximately n > 1.5. According to Waser et al.[175], this conductive $TiO_{2-n/2}$ forms a sort of "virtual cathode" that moves towards the anode.

The majority of the models do not consider or mention the possible migration/diffusion of the metal electrode into the oxide layer during the CF formation. In the case of $TiN/HfO_2/Ti$ based RRAM, this scenario may not be completely excluded as is proposed by Privitera et al.[176] working on $TiN/HfO_2/Ti$ devices through the experimental EELS-STEM technique. Some of well-known mechanisms are explained briefly below:

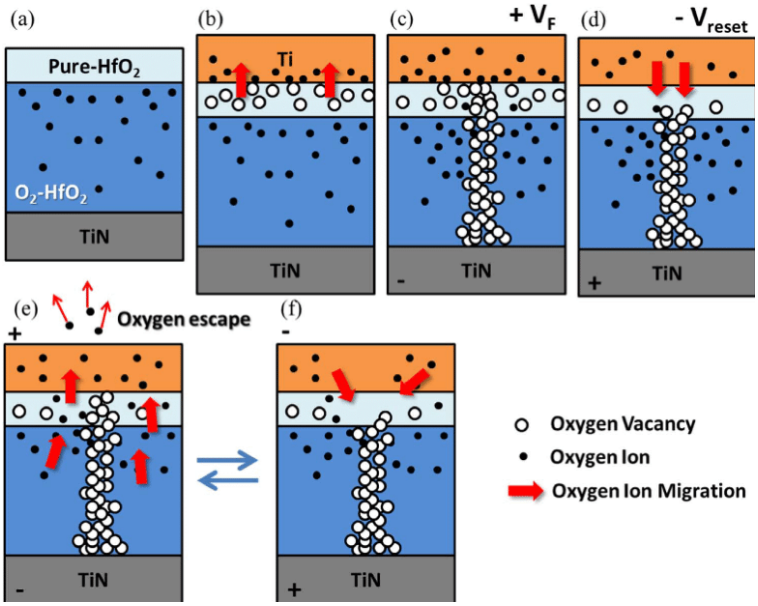

FIGURE 1.23: Schematic description of the RS mechanism of the device. (a) Before and (b) after the Ti top electrode deposition. (c) CF grows from TiN to Ti electrodes under a positive forming voltage applied to it. (d) A negative voltage is applied on it to rupture the CF. (e) CF formation and some oxygen ions release during set process. (f) CF ruptures during reset process[177].

Switching based on oxygen ion migration

Most of resistive switching behaviors are assumed to be due to the oxygen ion migration between the electrodes, that is, the resistive switching layer, leading to form a conductive filament[178]. This switching process due to oxygen ion migration is as shown in figure 1.23. As explained above, there is a current controlled breakdown of the dielectric layers leading to oxygen ion drift to the anode interface due to the high electric field. For a memory cell in the LRS, the current flows through the CFs in the bulk oxide. During the reset process, oxygen ions migrate back to the bulk to recombine with the oxygen vacancies and return the memory cell to the HRS.

Switching based on Metal ions migration

When a filament is formed by redox reaction in RRAM, it is called an electrochemical metallization cell (ECM) or conductive bridge (CB) cell or programmable metallization cell (PMC). In this kind of memory, a thin film of solid electrolyte is sandwiched between an electrochemically active metal electrode such as Cu, Ag or Ni and an electrochemically inert electrode such as Pt, Au, W or Ir. In this kind of memory, generally electrochemical redox process is accepted to be responsible for the resistive switching. Here the set is due to the electrochemical formation of metallic filaments in the ion-conducting electrolyte and reset is due to the dissolution of the metallic filament.

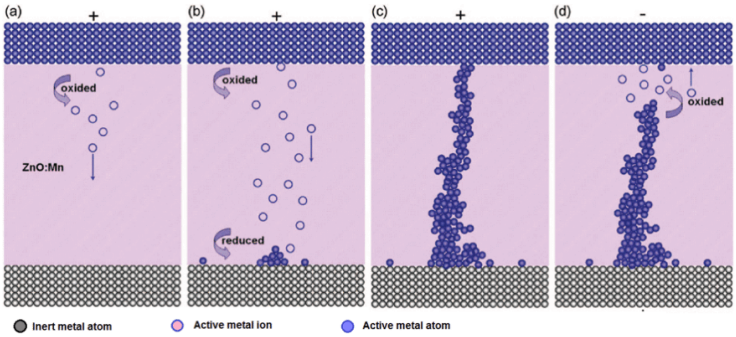

FIGURE 1.24: A schematic diagram for mechanism of resistive switching effects in ECM cell: (a) Electrochemically active metal atoms oxidize to ions at the anode, and then the active metal ions migrate to the cathode and deoxidize therein; (b) Precipitations of active metal atoms at the electrochemically inert electrode leading to the formation of a highly conductive filament in the cell; (c) When the polarity of the applied voltage is reversed, an electrochemical dissolution of the filament takes place, resetting the system into HRS[91].

When a positive voltage is applied on the electrochemically active metal it is oxidized at the interface, which can be described as $M \rightarrow M^{z+} + ze-$, where M^{z+} represents the metal cation. The mobile metallic cations migrate through the solid electrolyte layer towards the electrochemically inert electrode where they are reduced by the electrons flowing from the cathode, i.e., $M^{z+} + ze- \rightarrow M$. The successive active metal atom accumulation at the cathode leads to a growth of the metal filament, which finally reaches the anode to form a highly conductive filament, and switches the device to LRS. When a negative voltage is applied on the active electrode, an

electrochemical dissolution takes place in the weakest part of the filament, and reset process occurs bringing the system back into HRS. The whole process is shown schematically in figure 1.24.

Switching based on thermochemical reaction

In thermochemical reaction based switching, the forming and set are due to the thermal decomposition of storage media leading to the forming of a conductive filament and the reset is due to the thermal melting of this conductive filament[48]. Because of the joule heating, this type of switching is independent of electric polarity and can show both unipolar and bipolar modes for RRAM. Thermochemical reaction dominated switching behavior has been recently shown in $Pt/NiO/Pt$[179–181], $Pt/CoO/Pt$[182] and $Pt/TiO_2/Pt$[182;183]. Many attempts have been made to confirm the composition of these metallic CFs. They should compose of sub oxide or even metal atoms.

Park et al.[184] examined the switching in NiO_x films by HR-TEM and electron energy loss spectroscopy (EELS) and they reported that the conductive filament in NiO_x is composed of Ni atoms which are located at the grain boundaries. It was confirmed by Hwang et al.[185] that the conductive filament in TiO_2 is composed of Ti_nO_{2n-1} which is also called Magnéli phase and they grow from the cathode to the anode with their thinnest part near the anode. Chen et al.[186] reported a real time formation and rupture of filament in ZnO by using in situ TEM and showed that the conductive filament is composed of Zn dominated ZnO_{1-x}.

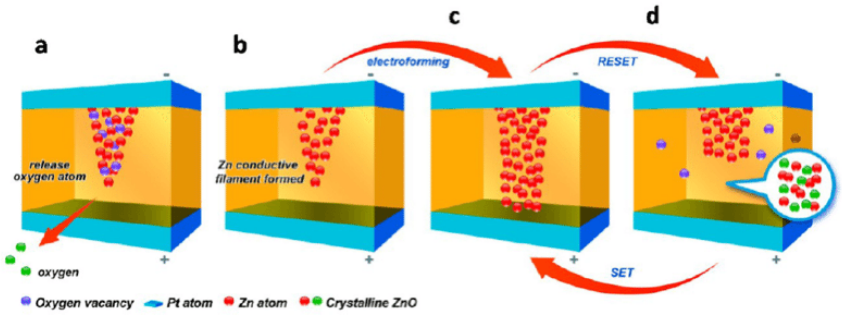

FIGURE 1.25: Schematic diagram for the mechanism of resistive switching in $Pt/ZnO/Pt$ devices. (a) The release of oxygen gas O_2 leads to the oxygen vacancies in the bulk of ZnO. (b) The migration of the mobile oxygen vacancies toward the cathode (oxygen ions O^2 towards the anode) and the rearrangement of Zn-dominated ZnO_{1x}. (c) The precipitation of Zn atoms to form a conductive filament. (d) The rupture of the filament. When the energy of Joule heating enhances the thermochemical reaction, the filament will rupture and change back to ZnO. Due to the migration of oxygen ions, the ReRAM resets back to the off state. Text and figure are adopted from reference[186].

All these experimental results presented above can be explained by using an universal model for thermochemical reaction dominated non polar switching by Kim et al.[187]. Detailed mechanism for thermochemical reaction based switching behavior for p-type semiconductors like NiO and n-type semiconductor like TiO_2 can be found in the article presented by Kim et al.[187] and Pan et al.[188].

1.3.5 Conduction Mechanism

Intensive research has been performed to understand the properties of conductive filament in literature by studying the temperature dependence of the device state and by using some other techniques such as complex impedance spectroscopy and low frequency noise measurement. In low resistance state the conduction is mostly observed Ohmic but the origin is still under discussion. Some of possible electron conduction mechanisms in high resistance state are Schottky emission, F-N tunneling, direct tunneling, Poole-Frenkel tunneling, space charge limited current (SCLC) and trap assisted tunneling (TAT). Various oxide RRAM devices can have different conduction mechanisms depending on the dielectric properties (band gap or trap energy level, etc.), the properties of the interface between the oxides and the electrodes (interfacial barrier height), the fabrication process conditions (annealing temperature, annealing ambient, etc.).

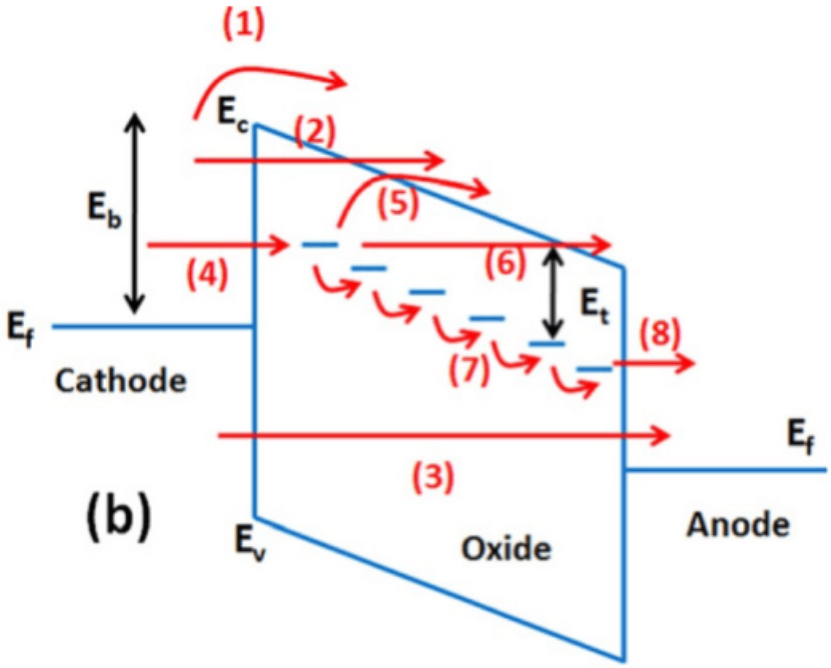

FIGURE 1.26: Schematic of the possible conduction mechanism in TiN/HfOx/Pt stack: (1) Schottky emission; (2) Fowler-Nordheim (F-N) tunneling; (3) direct tunneling; (4) tunneling from cathode to traps; (5) emission from trap to conduction band, which is essentially the Poole-Frenkel emission; (6) F-N like tunneling from trap to conduction band; (7) trap to trap tunneling; and (8) tunneling from traps to anode. Adopted from reference[189].

1.4 Phase change random access memory (PCRAM or PCM)

Phase change memories are a type of emerging nonvolatile memories. They use the ability of phase change materials to change phase between amorphous and crystalline state to store information. Chalcogenides are the mostly used materials because of their phase transition property. They are semiconducting glasses made of

the elements of sulfur, selenium, tellurium, germanium and antimony. The first concept of amorphous to crystalline phase transition of chalcogenide materials to store information was given by S R Ovshinsky[190] in the 1960's. The concept of a non-volatile PCM, based on the properties of the chalcogenide alloys, came out at the beginning of 1970's[191]. In these devices, the memory element is a variable resistor which is composed of chalcogenide material. The resistance of the device depends on the state of the phase. If the material is amorphous, the resistance is very high (RESET state). On the other hand, when the material is in crystalline state the resistance is low (SET state). This change of phase is accomplished by current induced Joule heating. The RESET is achieved by applying a large and short current pulse (see figure 1.27), raising the temperature of the chalcogenide material above the melting point. The melt chalcogenide then quenches into the glass state during the abrupt fall of the reset pulse. The SET is achieved by applying a smaller and longer current pulse and heating the glass above the crystallization temperature and activating the nucleation and growth of the crystalline phase[192].

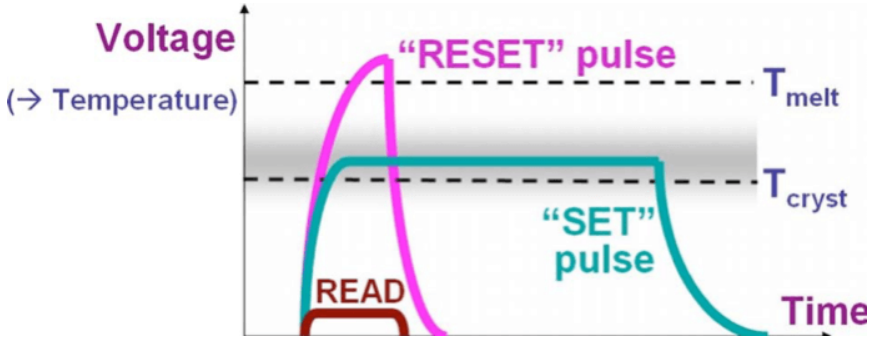

FIGURE 1.27: Programming for read, set and reset for PCM devices[193].

An important property of the phase change material is threshold switching[194–197]. Without this property, the PCM would not be a feasible technology. When the PCM is in high resistance state, extremely high voltage would be required to deliver enough power to heat the material above the crystallization temperature. However, when a voltage above the threshold voltage Vt is applied to the phase change material in amorphous state, the high electric field increases the electrical conductivity. This effect is still not completely understood but few studies have shown that it is attributed to a complex interplay between trapped charge, device current and local electric field1[194;198]. With this sudden high electrical conductivity, a large current start flowing, resulting in heating of the material. When this current is sufficient to heat the sample above the crystallization temperature but below the melting temperature, the material is switched into crystalline state. This threshold effect makes the device switching into crystalline state with an applied voltage of a few volts, despite the high resistance of the device in the reset state without voltage applied.

1.4.1 The PCM Cell Structure and its switching mechanism

The Phase change memory cell is a two terminal device. A memory cell structure is shown in figure 1.28a. The active phase change material is sandwiched between the top metal electrode and the resistive plug which is also called heater. When an electric pulse is applied, the current at the interface of the heater and the GST leads to joule heating of the mushroom shaped volume of the GST, which changes its state.

The functionality of the PCM is based on the resistance change due to the phase change, between amorphous and crystalline. When the material is in crystalline state the overall resistance of the device is low which corresponds to the SET, or logic 1. When the material is in amorphous state the resistance of the device is very high, which corresponds to the RESET state, or logic 0.

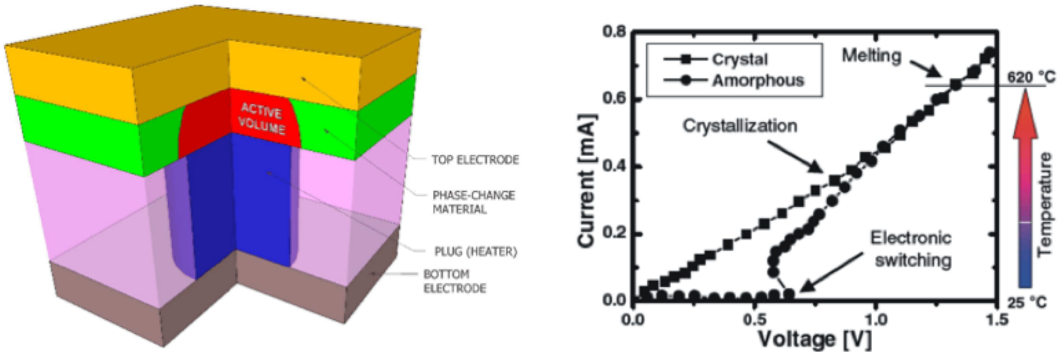

(A) (B)

FIGURE 1.28: (a) Schematic of a general PCM cell[199] (b) I-V characteristic of a PCM cell showing the amorphous and crystalline phase[200].

A typical PCM cell and its I-V characteristic are shown in figure 1.28b. As shown in figure 1.27, to RESET the device, a RESET pulse consisting of a higher amplitude for short duration in the range of tenths of nanoseconds, which can raise the temperature above the melting temperature of GST, is applied and followed by a sharp trailing edge quenching the material into the amorphous state. This is called RESET operation. To SET and to change the phase to crystalline again, a current pulse with duration in the range of hundreds of nanoseconds but with lower amplitude is applied which again heats the cell resulting in temperature rise above the crystallization temperature but below the melting temperature.

1.4.2 Phase Change Materials

Mostly, chalcogenides are used as phase change material because of the strong electrical and optical contrast between the crystalline and amorphous phase, fast crystallization and high crystallization temperature. The alloys along the pseudo-binary line between Sb_2Te_3 and $GeTe$ with the composition of $(GeTe)_m(Sb_2Te_3)_n$ have been studied intensely[202] and used for PCM devices. Other materials along the pseudo binary line between GeTe and Sb were studied[203], starting from $Ge_2Sb_1Te_2$. A tertiary phase diagram for $Ge-Sb-Te$ with popular alloys for phase change material is present in figure 1.29.

$GeTe$[204] is one of the first examples of chalcogenide material presented in the literature which demonstrated a reproducible and controllable phase transition from a low resistive, crystalline and high reflective state, to a high resistive, amorphous state. At room temperature, the crystalline phase has the structure of rhombohedrally distorted Te super lattice phase with some of the Ge atoms misaligned[205]. $GeTe$ is still largely investigated because of its high crystallization speed[206–208]. The melting temperature for GeTe is around 725°C[209] and its crystallization temperature (see figure 1.30) is around 180°C[210].

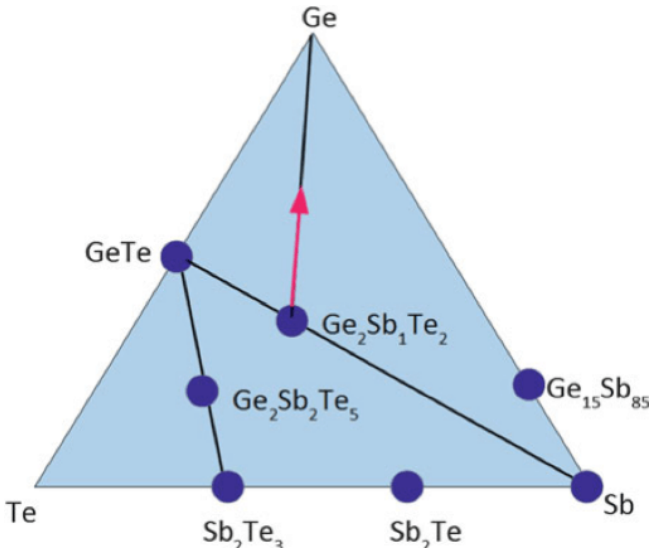

FIGURE 1.29: Tertiary $Ge-Sb-Te$ phase diagram with some popular phase change alloys highlighted. The red arrow indicates the trend of adding Ge to $Ge_2Sb_1Te_2$ alloys[201].

$Ge_2Sb_2Te_5$ (GST-225) is the most common and most studied phase change material[211]. It has been studied since 1990s because of its long-term stability at ambient temperature and its fast crystallization speed. Before, it was selected and studied for

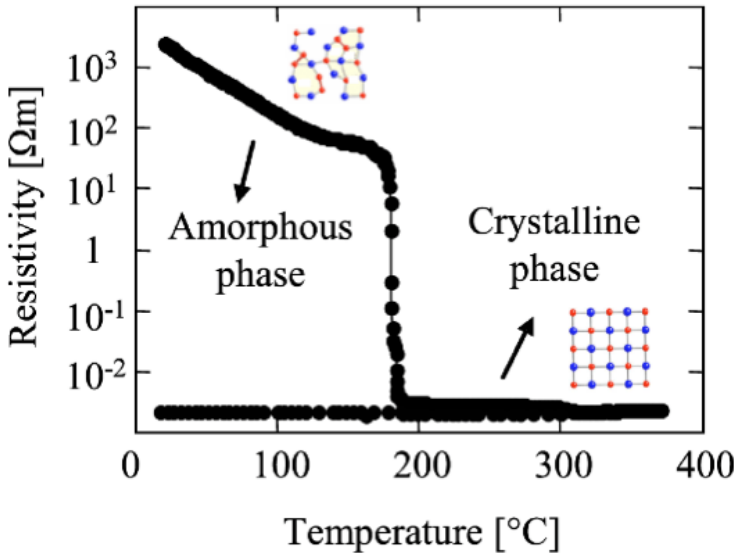

FIGURE 1.30: Resistivity as a function of the temperature for $GeTe$ phase change material[199].

optical disk storage because of its fast crystallization speed and high optical contrast. It is also the material mostly used in PCRAM these days. But there are some properties which are not suitable for PCRAM applications and doping has been used to modify its properties according to the requirement. The most popular dopant is nitrogen which leads to fine grain size, higher crystallization temperature, and higher resistivity in both, the amorphous and crystalline phases[212–214]. The crystallization

temperature for GST-225 is around 150°C, while the melting temperature is around 660°C[215].

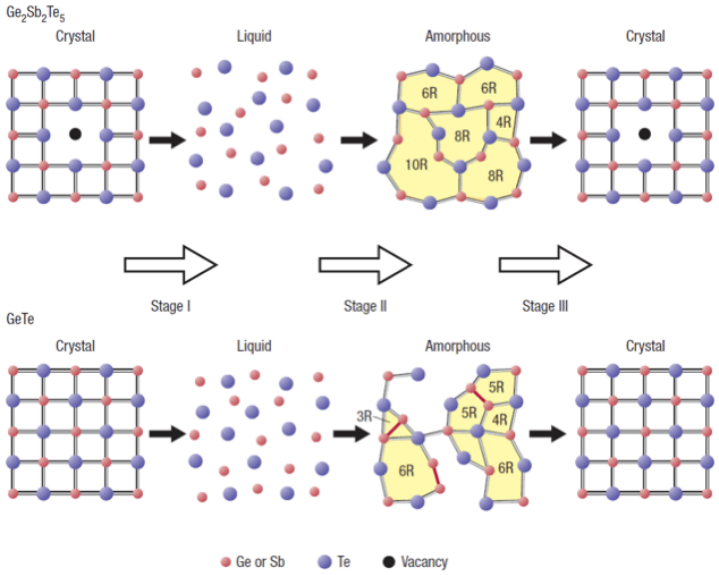

FIGURE 1.31: Schematic representation of phase transformation during the record and erase process for $Ge_2Sb_2Te_5$ and $GeTe$[208].

Many different phase change materials have been developed[216–218] and the choice of available materials can be further increased by doping[219–221]. Materials such as doped $Ge_{15}Sb_{85}$[222] and doped Sb_2Te[219] have also been used in PCRAM cells. Also $Ge_1Se_1Te_2$[223], $AgSbSe_2$[224], $Sb-Se$[225], $Ag-In-Sb-Te$[226] and some variant of$Sb-Te$[219;227] are used for phase change materials. Also Ge-rich $Ge_xSb_yTe_z$ materials have been recently developed with improved crystallization temperature and have been proven to guarantee the data retention in extended temperature range for automotive application[228].

1.5 Conductive atomic force microscopy for resistive memories

The main motivation of this thesis work is to understand the scalability for OxRAM and PCRAM and also to understand the possible mechanism leading to resistive switching. To understand these effects, it is necessary to do the study at nanoscale. With current lithography, it is difficult to fabricate electrodes in the nm range. So, to overcome this problem many groups started using conductive atomic force microscopy (C-AFM) to do the electrical characterization considering C-AFM as probe station. C-AFM tips can serve as nano-electrodes allowing to study the switching effect at nanoscale.

1.5.1 For OxRAM

To provide in-situ information about the formation and rupture of the filament, the use of characterization tools with high resolution are necessary. The most widespread techniques for nanoscale electrical characterization are scanning tunneling microscope (STM) and conductive atomic force microscope (CAFM). There are many groups

which are already using C-AFM to study OxRAM at nanoscale. The diameter of the filament was found to be in the range of nm with this technique.

Chen et al.[229] observed cyclic resistive changes in Nb-doped $SrTiO_3$ using scanning tunneling microscope. In STM the tip is not in contact with the sample, so the current is due to the tunneling between the tip and the sample adding a resistive component. This problem can be solved by using atomic force microscopy (AFM), as the tip is in contact with the sample. Trapatseli et al.[230] used conductive AFM

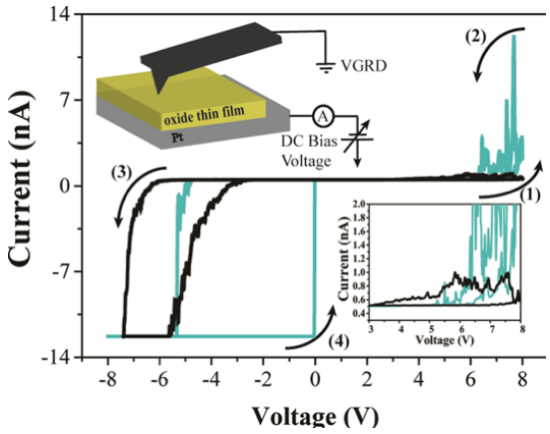

FIGURE 1.32: 1-V characteristic of TiO2-x (black curve) and TiOx (blue curve) thin films obtained by C-AFM[230]

to investigate the switching threshold in TiO_x layers. They used conductive Pt/Ir coated Si tips as a top electrode for MIM structure. They used a compliance current of 12.5 nA in order to prevent tip damage. They studied the I-V behavior as shown in figure 1.32 for two different titanium layers, TiO_{2-x} (in black) and TiO_x (in blue). They find out that I-V characteristics are showing asymmetric bipolar switching behavior for both films.

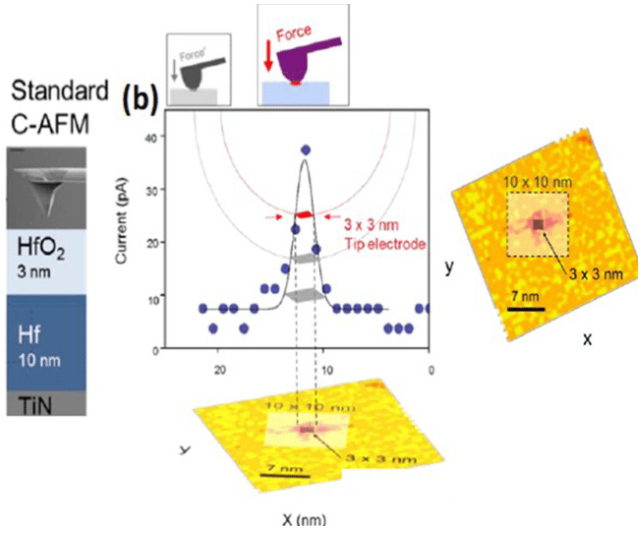

FIGURE 1.33: The C-AFM tip is placed in contact with HfO_2 layer and a tip-surface contact area of $3 \times 3nm^2$ is achieved by the precise control of the load force applied to the tip by Hou et al.[231].

Hou et al.[231] studied the multimode resistive switching at nanoscale in HfO_2 layer by using C-AFM. They studied the switching in the area of $3 \times 3nm^2$ (figure 1.33). Electrical bias was applied on the bottom electrode of TiN while the Pt tip was grounded. They explained the filament conduction in the framework of a low defect quantum point contact (QPC) theory.

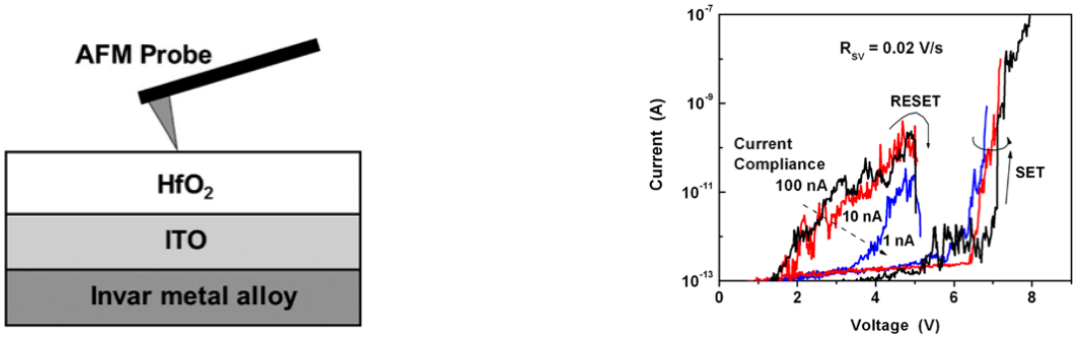

(A) (B)

FIGURE 1.34: (a) Schematic diagram of the $HfO_2/ITO/Invar$ RRAM structure with an AFM Pt/Ir tip as the top electrode. (b) Typical nanoscale I-V characteristics of the $HfO_2/ITO/Invar$ structure observed by Wu et al.[232].

Wu et al.[232] also studied the effect of compliance current and voltage sweep rate on the resistive switching in $HfO_2/ITO/Invar$ structure by using C-AFM as shown in figure 1.34. Invar is a binary alloy of 64% iron and 36% nickel. They reported unipolar resistive switching behavior when a Pt/Ir AFM tip is used as the top electrode.

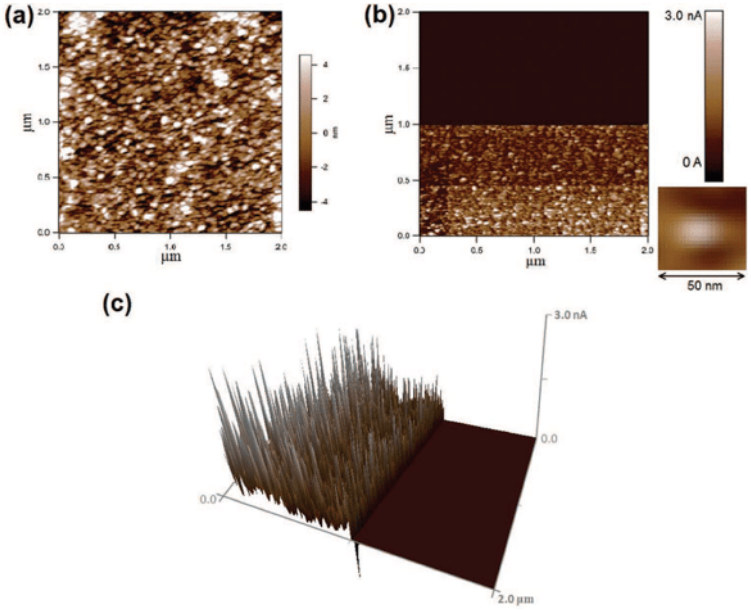

FIGURE 1.35: C-AFM mediated surface conductivity modifications of the TiO_2 thin film. (a) Topography (b) Current map. The surface is more insulating with 5V (upper region) and more conducting with +5V (lower region) surface, compared to surface in pristine state. One conducting spot is shown on the lower right corner. (c) Current mapping image in 3D of the same area[233].

Du et al.[233] studied the resistive switching in TiO_2 films by using conductive atomic force microscopy. They used a 20nm thick layer of TiO_2 and Pt as bottom electrode. Also, a Pt coated silicon tip as top electrode was used. They applied a +/- 5V bias on an area of $2 \times 2\mu m^2$ at 1Hz. They recorded the current mapping images and found out that more conducting surface was observed with positive bias and more insulating surface was observed with negative bias as shown in figure 1.35(b). For positive bias, a large number of nano-spots were observed and these spots mark the conductivity paths that connect the bottom electrode with the AFM tip. A 3D view for these spots is presented in figure 1.35 (c). They called these nano-spots multiple nano-filaments.

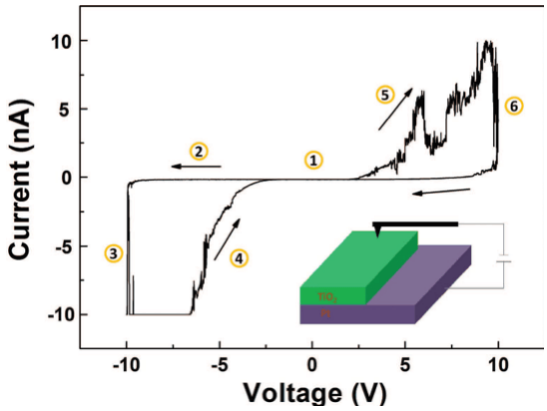

FIGURE 1.36: I-V characteristic measured by CAFM on a TiO_2/Pt surface, at a voltage sweep by C-AFM observed by Du et al.[233].

Also, they explained that the switching mechanism is related to charge injection and attributed to the migration of oxygen ions under an electric field. They introduced filament interface model combining both filamentary and interfacial effect to elucidate the observed phenomenon. I-V characteristic presented by Du et al. is shown in figure 1.36.

Hou et al.[143] presented Sub 10 nm low current resistive switching behavior in HfO_2 stack. They compared I-V behavior obtained for a 1T1R device and the characteristic obtained by C-AFM as shown in figure 1.37. They showed that the low current resistive switching characteristics are enhanced by the downscaling of the device to sub-10nm. They introduced a tip induced cell which is in good agreement with 1T1R cell. The full diamond tip which is used as the top electrode was blunted in order to mimic the dimension of the electrode used for devices.

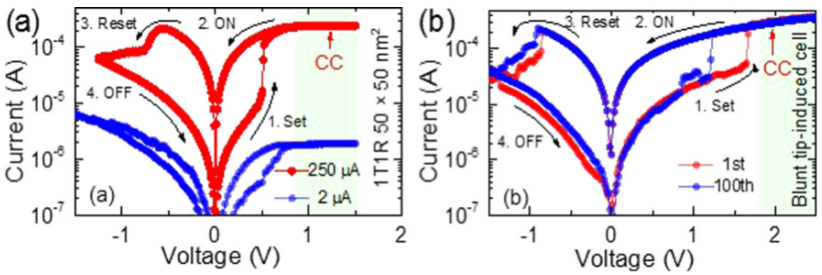

FIGURE 1.37: (a) RS I-V curves of a $50 \times 50nm^2$ $TiN/HfO_2/Hf/TiN$ device in the 1T1R cell with 250 μA compliance current (b) RS I-V curves of the $blunt - tip/HfO_2/Hf/TiN$ tip-induced cell, the 1st (red trace) and the 100th (blue trace), as presented by Hou et al.[143].

Diokh et al.[234] also studied 1T1R devices with 10nm HfO_2 layer thicknesses as Hou et al. It can be seen in figure 1.37(a) and figure 1.38 that the On-state conductance is similar for both Hou et al. and Diokh et al for 1T1R device. It can also be seen that the I-V measurements performed by Hou et al using CAFM (figure 1.37(b)) show a similar On-state conductance compared to the 1T1R devices studied by both groups. So, it can be concluded that the I-V characteristics by C-AFM are comparable to the results obtained on devices. The area of the 1T1R device used by Hou et al is $50 \times 50nm^2$ and for Diokh et al. is $1 \times 1\mu m^2$, so it can be concluded that there is no effect of the cell dimension on the On-state conductance as the conductance is due to a conductive filament as explained in section 1.3.1. From all these studies presented in this section, it can be seen that the scaling of the OxRAM is possible and C-AFM is a very useful tool to study OxRAM memories at nanoscale.

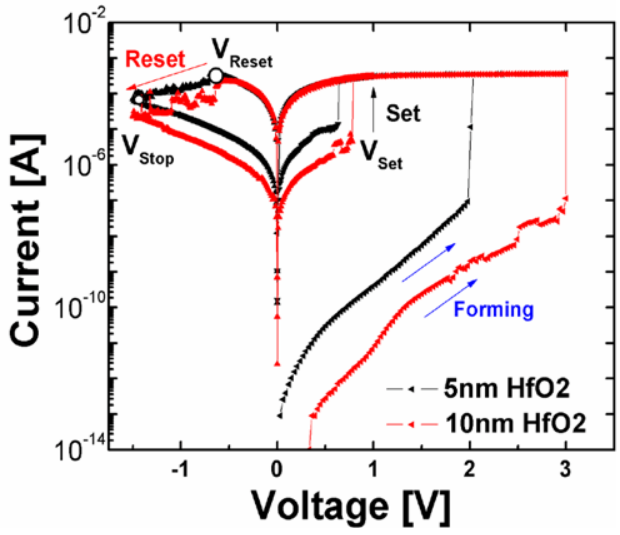

FIGURE 1.38: Typical I-V curves of HfO_2 based 1T1R device with a device area of $1 \times 1\mu m^2$ [234].

1.5.2 For PCRAM

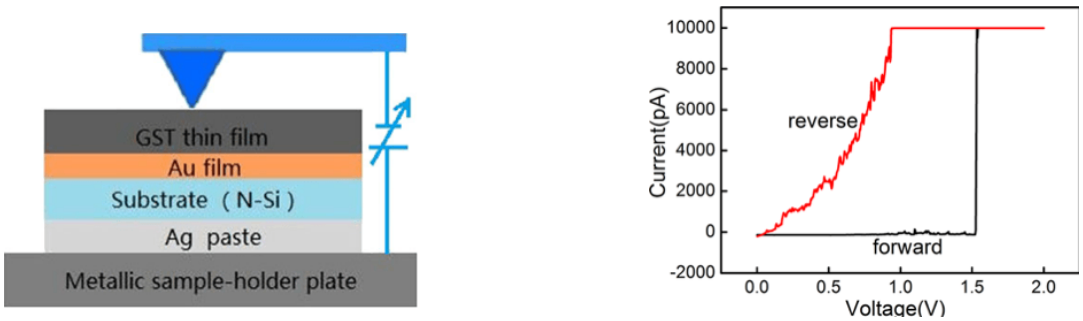

(A) (B)

FIGURE 1.39: (a) Schematic diagram of GST-based structure using C-AFM Current–voltage spectroscopy of amorphous GST films obtained by Yang et al.[235].

Recently, many studies related to phase change material have been made to disclose the material properties at nanoscale[235–240]. H.Kado and T. Thoda have reported nanometer-scale recording in an amorphous $Ge_1Sb_2Te_4$ film by locally changing the electrical property with a C-AFM tip[241].

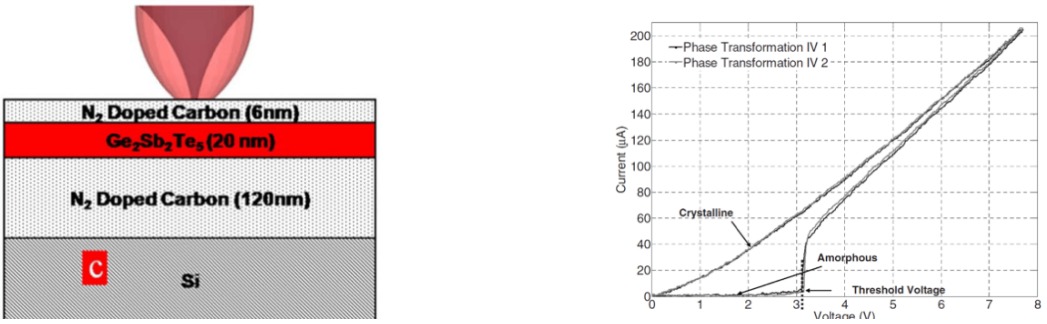

(A) (B)

FIGURE 1.40: (a) Schematic cross section of the phase-change stack used in the experiments by Bhaskaran et al. (b) Current-voltage plot for two phase transformation curves on the unpatterned stack as shown in figure (a) from the amorphous to the crystalline phase obtained with an encapsulated tip[242].

Yang et al.[235] performed characterization of GeSbTe phase change material by using C-AFM to observe nanofilament formation (see figure 1.39). They showed an electrical threshold switching. When the applied voltage exceeded the threshold voltage, conductive nanofilaments with average size of 15-60 nm were reported.

Bhaskaran et al.[242] also studied phase transformation at nanoscale in $Ge_2Sb_2Te_5$ using encapsulated tips (see figure 1.40). By using PtSi conductive tips they demonstrated the creation of nanoscale crystalline dots on an amorphous film of $Ge_2Sb_2Te_5$.

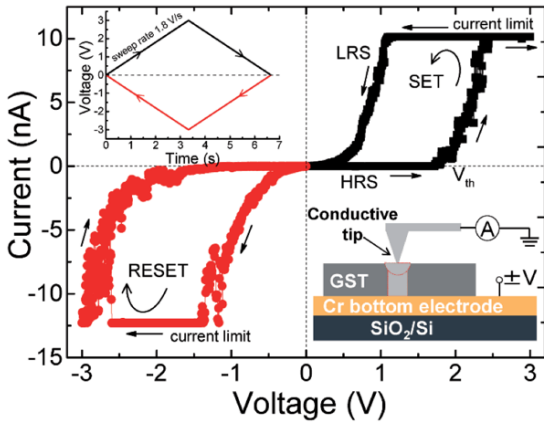

FIGURE 1.41: Switching behavior of the combined PC/RRAM device. Measured I–V characteristic of $GST/Cr/SiO_2/Si$ arrangement with PtIr-coated C-AFM tip (diameter is 20 nm) as top electrode by Sun et al.[243]

Tanaka et al.[244] studied the smallest (10nm) phase change marks in amorphous and crystalline $Ge_2Sb_2Te_5$ films. They used both STM and AFM techniques to study

the phase transition in GST and suggested that AFM is more suitable for producing the nanoscale marks obtaining the diameter of 10nm.

Sun et al.[243] presented bipolar electrical switching of $Ge_2Sb_2Te_5$ phase change material at nanoscale by using the C-AFM. I-V characteristics are shown in figure 1.41.

1.6 Conclusion

All these studies at nanoscale for OxRAM and PCRAM presented behavior of switching. But most of the studies were done in ambient conditions. At ambient conditions, there can be electrochemical reactions or capillary effects at the contact between the tip and the sample which can change the electrical characteristics. It is then necessary to do the electrical characterization in better controlled conditions. In this thesis, we will introduce and assess a nanoscale characterization methodology in ultra-high vacuum to study resistive switching at nanoscale. This methodology will be applied to HfO_2 based OxRAM in two regimes (low and high compliance currents) and phase change material (GST-225 and Ge rich GST).

Chapter 2

Experimental Techniques

2.1 Atomic Force Microscopy

2.1.1 Introduction & Basic Principle

In 1981, Gerd Binning & Heinrich Rohrers invented the scanning tunneling microscope (STM)[245] at IBM Zurich and for this they earned the Nobel Prize in Physics in 1986. The scanning tunneling microscope has become a useful tool to investigate metal and semiconductor surfaces at atomic scale. The only limitation of STM is that it requires the sample to be conductive. In 1986 Gerd Binning, Calvin Quate and Christoph Gerber[246] found a way to characterize non-conductive surfaces and proposed a new type of microscope. Instead of using tunneling current between the STM tip and the sample, they suggested to measure the force between tip and sample on atomic scale. The atomic force microscope (AFM) is composed of a mechanical profilometer, using a mechanical spring to sense the force and the STM, using the piezoelectric transducers for scanning. One year after proposing the AFM, Binning et al. presented the first atomic resolution on graphite. In the same year Albrecht et al.[247] showed the atomic resolution on insulator (Boron Nitride) for the first time. After all these milestones in the history of AFM the development of the instrument continued. Insulator, Organic materials[248], biological macromolecules[249;250], polymers[251;252] ceramics and glass are the other examples investigated by using AFM. Apart from being applied to different material, the instrument was improved continuously. New detection method, sensor preparation and incorporation of the microscope for different environments like liquid[253], vacuum and low temperature[254] are the examples for various modifications of the instrument undergone.

The basic principle of atomic force microscope is to measure the force or to measure the interactions between the tip and the sample surface. Which leads to the creation of many new scanning probe microscope techniques such as STM/AFM, AFM/MFM (Magnetic Force Microscopy), AFM/FFM (Friction Force Microscopy) to provide the opportunity to characterize a single nm sized spot and therefore gain more information than by a separate application of single method.

The development of commercial STM and AFM for conductive materials as well as for insulating materials attracted not only physicist or chemist but also biologist, electrochemist and mechanical engineer. Sample can be prepared without any specific requirement in ambient condition. The instrument characterizes the morphology of sample such as roughness or height distributions.

In STM or AFM the tip is attached to the cantilever-type sensing. When AFM tip comes near the surface many forces are playing role between them and because of these forces there is deflection of the cantilever. Surface images are taken by scanning

the sample surface by using the tip and digitizing the deflection of cantilever or the z movement of the piezo as the function of lateral position x,y. Two force regimes are distinguished, first one contact mode and another non-contact mode.

In non-contact mode the distance between tip and surface is around 10-100 nm. There are many different kinds of forces present between tip and sample in non-contact mode like van der Waals, electrostatic, magnetic or capillary forces which can be sensed and can give information about the surface topography, distribution of charge, magnetic domain wall information or liquid film deposition.

In contact mode the separation distance is in the order of angstrom. In this mode the repulsive force allows to scan the surface with higher resolution. Also, the frictional force, elasticity or plasticity can be detected in appropriate condition. Also tapping mode is widely used for AFM measurements. This mode allows a high-resolution topographical image for the sample which can get easily damaged or loosely hold to the substrate. This mode overcomes the problem associated with the friction, electrostatic force or adhesion. Tapping mode imaging is used in ambient air by oscillating the cantilever at or near the resonance frequency using piezoelectric crystal. This mode prevents the tip from sticking to the surface and causing damage during scanning, unlike non-contact and contact modes, it has sufficient oscillation amplitude to overcome the tip sample adhesion forces.

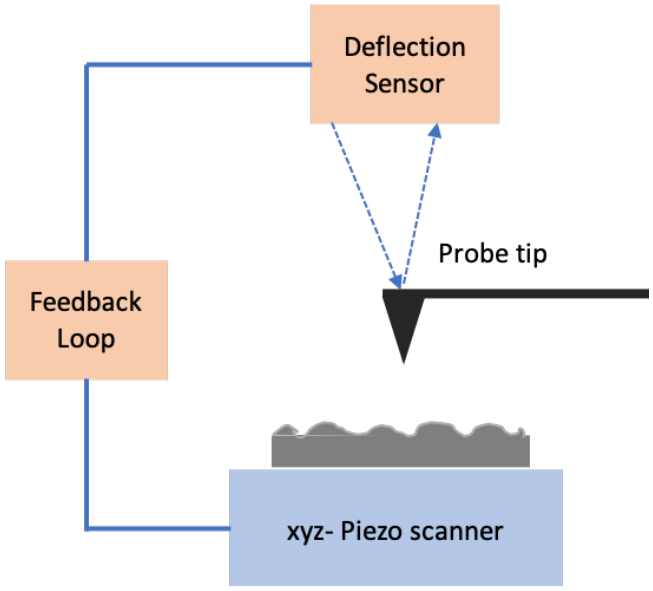

FIGURE 2.1: Basic illustration of Scanning Tunneling Microscope / Atomic Force Microscope.

2.1.2 AFM tips

Normally the tips used for atomic force microscopy are composed of silicon. The fabrication of the tip and cantilever is done from a single block from a wafer. The silicon wafer is thus etched in succession to obtain a cantilever of few micrometers and to form a tip at its end. To facilitate handling and mounting tips, a large silicon "holder" is kept at the base of the cantilever. The mapping of marketed AFM tip is given in Figure 2.2.

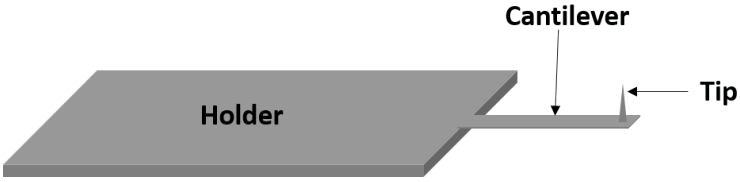

FIGURE 2.2: Schematic diagram of commercialized atomic force microscopy tip.

Depending on the force that we want to detect and on detection mode, it is necessary to adopt the suitable tip. Many commercial tips are available for different needs. Here we want to do the electrical measurements for switching studies, so it is necessary to use a conductive tip. To obtain good electrical conductivity these silicon tips are coated with a conductive coating. Many different kinds of coatings such as Pt/Ir alloy, Cr/Pt, gold, PtSi or boron doped diamond are used to make it conductive. For the electrical measurement we need to make the contact between tip and sample. So, we need tips which have good electrical and thermal conductivity and strong mechanical resistance to wear.

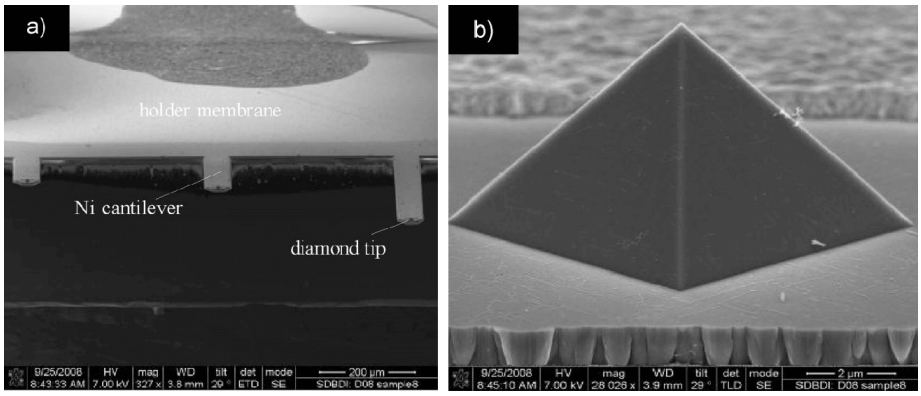

FIGURE 2.3: SEM image of (a) all the three cantilevers with different length present for boron doped full diamond, (b) pyramidal shape boron doped full diamond tip. Figure taken from reference[255].

Here we used many different kinds of commercially available conductive tips. We used silicon tip coated with Platinum Silicide (PtSi). The cantilever is also coated with PtSi. The spring constant is around 2.8 N/m for this tip and commercially available by Nanosensors. The other tip used is Boron doped full diamond tip. These tips are made from solid boron doped polycrystalline diamond in a pyramidal shape[255;256]. To enable high electrical conductivity, the diamond tip is highly doped with boron (10^{21} at/cm^3). The measured resistance of the tip on a metal surface range from 500 Ω to 100 kΩ. This value also depends largely on the size of the nano-contact. Every holder has three cantilevers with distinct spring constants from 3 N/m to 27 N/m. Ni cantilevers are mounted on a metalized Si chip. In which a pyramidal shape crystal of boron doped diamond is used as tip. These tips have good electrical conductivity because of high boron doping. In addition, unlike a metal coating, the diamond has a higher melting temperature (at high pressure 20 GPa diamond can be heated upto 2500°C and can withstand temperature of 3000°C and above) that allows it to resist to high current densities. This tip was developed by IMEC.

In Figure 2.3 we can see the fabricated probe imaged by scanning electron microscope (SEM) at low magnification[255]. It can be seen that all the three cantilevers have different length and because of this have different spring constant.

2.1.3 Surface Contact Area

For electrical measurements, the tip/sample contact surface is an extremely important parameter because the measured current is directly proportional to the contact area. It is therefore essential to be able to estimate the contact area accurately. A method is given by Landau[257] to calculate the contact area with the model of the Hertz contact theory[258;259] which makes it possible to determine the contact surface area between two spheres. When the two materials come into contact, deformation is created at the spheres giving rise to the creation of a contact surface rather than a single point. The contact area S_c can then be calculated by:

$$S_c = \pi\left(\frac{F_r R}{K}\right)^{2/3} \tag{2.1}$$

With,

$$R^{-1} = \frac{1}{R_1} + \frac{1}{R_2} \tag{2.2}$$

$$\frac{1}{K} = \frac{3}{4}\left(\frac{1-\gamma_1^2}{E_1} + \frac{1-\gamma_2^2}{E_2}\right) \tag{2.3}$$

In equation 2.1, F_c represents the applied force, in equation 2.2 R_1 and R_2 are the radius of the two spheres, in equation 2.3, γ_1 and γ_2 are the Poisson coefficients of the two materials and $E_{1,2}$ are Young modulus. In our case, the AFM tip is modeled

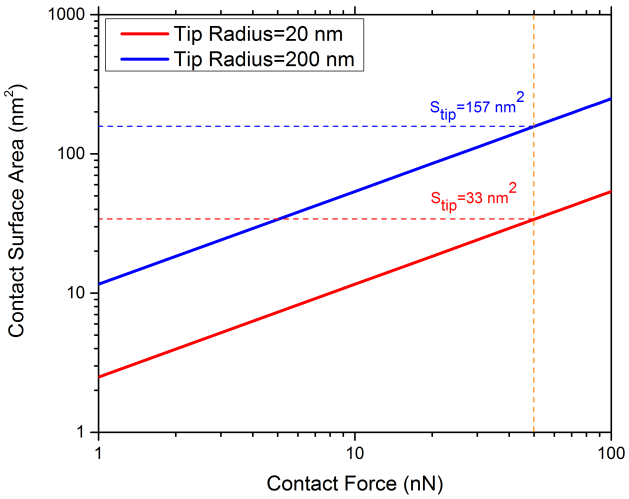

FIGURE 2.4: Contact surface area between tip and sample as a function of bearing force (contact force) for two different tip radii (20nm and 200nm). The calculation for contact surface area values are done at 50nN contact force.

by having the radius of sphere R_{tip}, corresponding to the radius of curvature of the tip while the sample was considered as plane so with an infinite radius of curvature. Our study focused mainly on the oxide and chalcogenide materials, and simulations were performed using specific elastic constants for the sample and diamond. Figure 2.4 shows the estimation of the tip/sample contact area in the case of diamond tips as a function of the bearing force (contact force).

In figure 2.4 we can see the dependence of the contact surface area on the radius of curvature of the tip. Extrapolation of the contact surface area was made for a radius of curvature of 200 nm as shown in figure 2.4. To take into account the diamond structure and the possibility that a single crystal of the tip is in contact with the sample, we also extrapolated the contact surface for a radius of curvature of 20 nm. All the mappings and electrical measurements were carried out for a low contact force of 50nN, so that there is no modification on the surface of the sample. For such contact force, the contact surfaces area extracted are 157 nm^2 for a radius of curvature of 200 nm and 33 nm^2 for 20 nm.

2.1.4 AFM in ultra-high vacuum

The AFM used during our work is an Omicron atomic force microscope (Figure 2.5) which is operated under ultra-high vacuum (UHV) (10^{-9} torr or 1.3×10^{-12} bar). In this type of instrument, the sample and the tip are placed on a platform that is levitated by means of a magnet system in order to minimize vibrations coming from surrounding. Ultra-high vacuum reduces the sensitivity of AFM to thermal drift and significantly reduces particulate contamination and moisture. Finally, for the realization of surface scans, the AFM Omicron moves the sample using hard piezoelectric devices which have the advantage of being more stable than soft piezoelectric once but reduce the maximum scan area to $5 \times 5\mu m^2$ only. All these characteristics give the device a very high stability in terms of measurements.

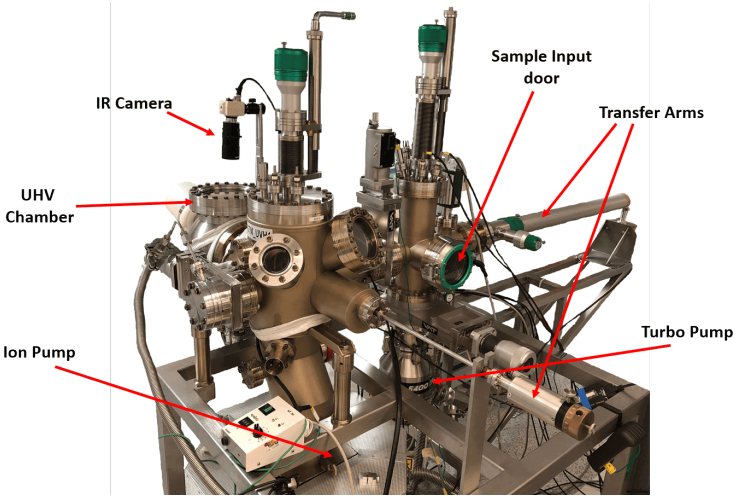

FIGURE 2.5: Omicron Atomic force microscopy setup in ultra-high vacuum.

The major drawback of UHV concerns the insertion and sample preparation time, which is generally ten times longer than in the case of AFM operation in air. The main motivation to use UHV despite its constraints is to remove any residual moisture in the air and remove the electrochemical effects. In fact, in the air or even

under a secondary vacuum, the moisture is present at the tip/sample contact to form a meniscus of water. The height of the meniscus increases with the surrounding humidity rate as shown in Figure **??**.

The presence of this meniscus of water affects the characteristics particularly when using the conductive mode. The application of voltage by the tip causes electrochemical reactions which can disturb the measurements[260]. The AFM under UHV allows to overcome this meniscus.

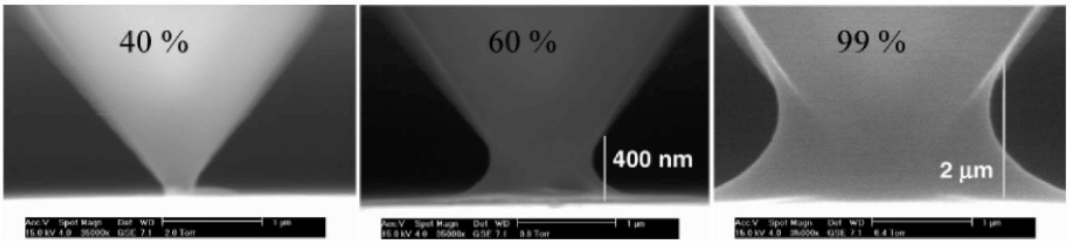

FIGURE 2.6: Evolution of the height of meniscus of water with percentage of humidity observed by MEB[261].

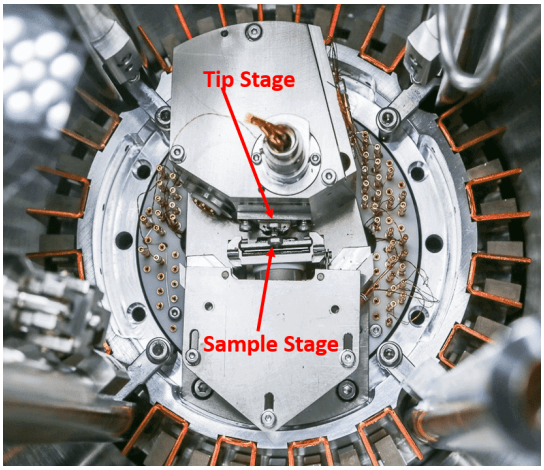

FIGURE 2.7: AFM sample stage and tip stage in ultra-high vacuum.

In order to introduce samples and tips into the ultra-high vacuum, the AFM Omicron® is composed of successive chambers of decreasing pressure. The samples are first placed in an airlock chamber, which is then pumped to a pressure of 10^{-3} *Torr* through a primary pump and then up to 10^{-7} *Torr* with the help of turbo pump. The samples are then moved using the transfer arms to the ultra-high vacuum chamber where the pressure is kept at 10^{-9} *Torr* by an ion pump. To do the measurement, the sample is placed on the sample stage as shown in the figure 2.7 by using the different transfer arms.

2.1.5 Calibration of AFM Tips

The conductive tips are attached to a metal tip holder using (Figure 2.8) an electrically conductive adhesive glue (silver epoxy) to facilitate their transfer into the AFM. The detection of the deviations of the cantilever is done by using the beam of LED reflecting on the back side of the cantilever.

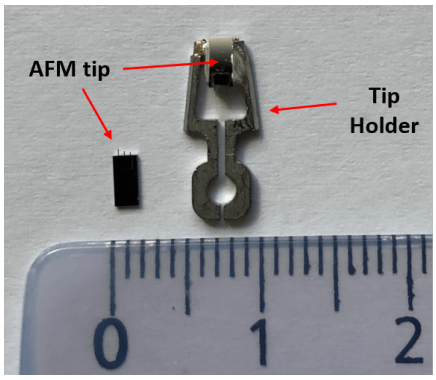

FIGURE 2.8: A full diamond AFM tip glued to the tip holder (right side) and a pristine full diamond AFM tip on left side.

After introducing the tip into the UHV, it is necessary to adjust the position of the beam on the cantilever as well as the reflection of the beam on the center of the four-quadrant photodetector. This adjustment is possible by electronically controlling the position of the two mirrors shown in Figure 2.9. With this system, a first visual adjustment is made to place the beam on the cantilever supporting the tip. Then, the position of the beam on the cantilever must be optimized. However, the resolution of the microscope is very sensitive to this position and can be considerably improved if the beam is reflected from the end of the cantilever as shown in Figure 2.10 (blue beam). When the cantilever bends, the deviation of the red ray is much smaller than that of the blue ray which reduces the sensitivity in the case of the red beam.

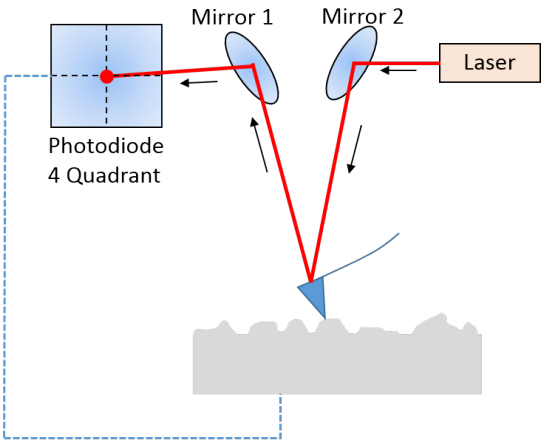

FIGURE 2.9: Schematic diagram of operation of the AFM in contact mode.

To refine this setting the tip is excited at its resonance frequency and the beam deflection amplitude is measured on the four-quadrant detector (Figure 2.9). By repeating this operation for different positions of the beam on the rear face of the cantilever, the position is identified for which the resonance amplitude is maximum, which corresponds to the best setting of the beam. Also, to be sure that the beam is reflected from the cantilever and not from some other place, resonance frequency is calculated at different amplitude.

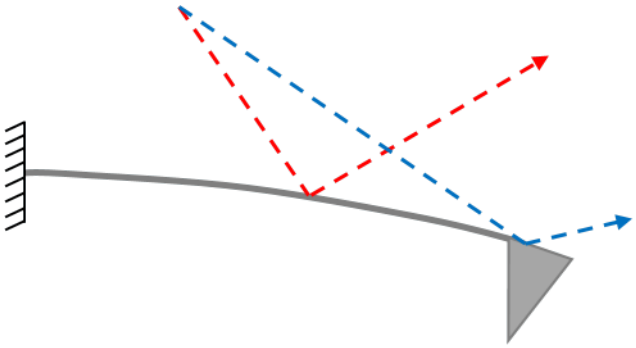

FIGURE 2.10: Schematic diagram showing the influence of beam positioning on sensitivity.

When the tip is excited in vacuum, the tip/cantilever system can be linked to a forced and damped harmonic oscillator of mass m whose oscillations are governed by non-linear second order differential equation:

$$m\frac{d^2z(t)}{dt} + \frac{m\omega_o}{Q}\frac{dz(t)}{dt} + kz(t) = F_o cos(\omega_d t) \tag{2.4}$$

In equation 2.4, F_o and ω_o respectively represent the excitation force and the excitation angular frequency, $z(t)$ corresponds to the variation of the tip/sample distance with respect to the equilibrium position of the tip, Q is the quality factor of the tip, k the stiffness constant (or spring constant) of the cantilever and wo the resonance angular frequency. The resolution of equation 2.4 allows determining the evolution of the height of the peak z(t)=A (ω_d) $\times$ cos(ω_dt+ϕ) as a function of the excitation frequency f_d with $A(f_d)$ the amplitude of oscillation given by:

$$A(f_d) = \frac{A_o}{\sqrt{(f_d^2 - f_o^2) + (\frac{f_d f_o}{Q})^2}} \tag{2.5}$$

where A_o depends on the excitation amplitude and fo is the resonance frequency.

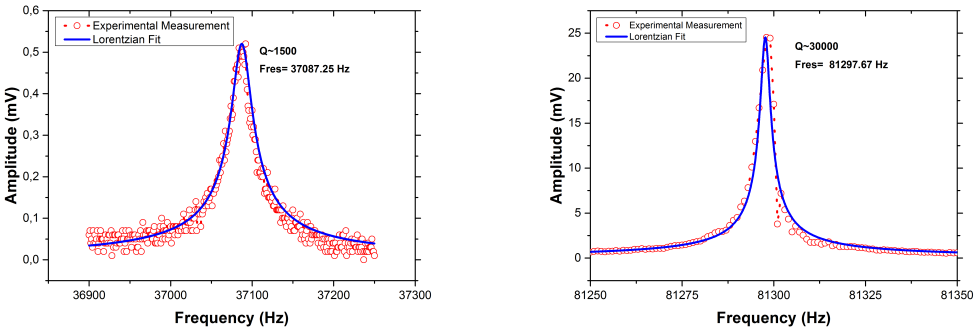

(A) (B)

FIGURE 2.11: Measurement of the amplitude as a function of the excitation frequency applied to the cantilever and calculation for Resonance Frequency curve for (A) Boron Doped full Diamond tip, (B) PtSi tip

The resonance curves in this study are performed under UHV, the tip is very little subject to friction forces and the quality factor thus obtained for diamond tips is about five times higher than that obtained in air ($Q_{UHV} = 1500$ and $Q_{Air} = 300$). Figure 2.11a shows a typical resonance curve of a diamond tip and PtSi tip. The quality factor Q in vacuum for PtSi tip ($Q_{UHV} = 30000$) is much larger than full diamond tip ($Q_{UHV} = 1500$). This is because of the difference in the spring constants of the cantilever for different tips.

Once the position of the light beam on the cantilever optimized, the tip can be brought into contact with the sample. As mentioned before, the contact is established with a force of 50 nN so as not to damage the oxide layer and also not to lose the contact after few measurements. The determination of the contact force is carried out by converting the voltage detected by the four-quadrant detector in newton (N) during the bending of the cantilever. In order to determine the interaction force between the tip and the sample as a function of the elongation of the piezoelectric actuator, approach/retract curves are recorded. An example is shown in figure 2.12. The stiffness constant of the tip indicated by the supplier is 15 nN/nm. The blue

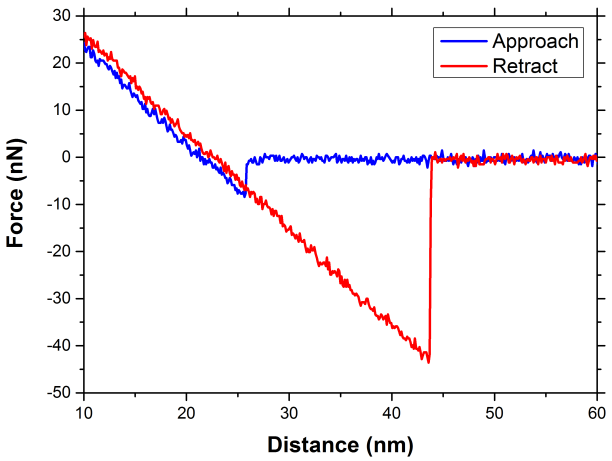

FIGURE 2.12: Approach / retract curve for an AFM tip. The approach is shown in blue, when the tip is close enough to the surface, it comes into contact with the sample. The withdrawal is shown in red. A greater force must be applied to detach the tip from the surface. This force curve is taken by using full diamond tip on HOPG.

curve represents the approach of the tip (A). In this approach, the tip-sample contact is initiated in (B) by a contact jump due to Van der Waals forces acting as an attractive force between the sample and the AFM tip. Once the contact is established, when the ceramic reduces the height of the lever, the deflection of the tip and the applied force increase linearly (C). On removal (D) shown in red, various adhesion forces act on the tip, so a higher force is needed to remove it from the sample (E).

After the calibration step, it is necessary to check the conductive properties of the tips used. For this, I-V measurements are performed on a highly conductive sample of graphite or HOPG (Highly Ordered Pyrolytic Graphite). To be used as upper electrodes of MIM structures, the tips must have a metallic characteristic, i.e. ohmic characteristic as shown in figure 2.13a. For a new tip, the ohmic current makes it possible to record a resistance of the tip of the order of a few hundred Ohms. When

the tip is used too much, we can see the non-linearity in current as shown in figure 2.13b. This loss of conductive properties may be due to loss of the conductive coating or contamination of the tip by dust during repeated scans of the sample surface.

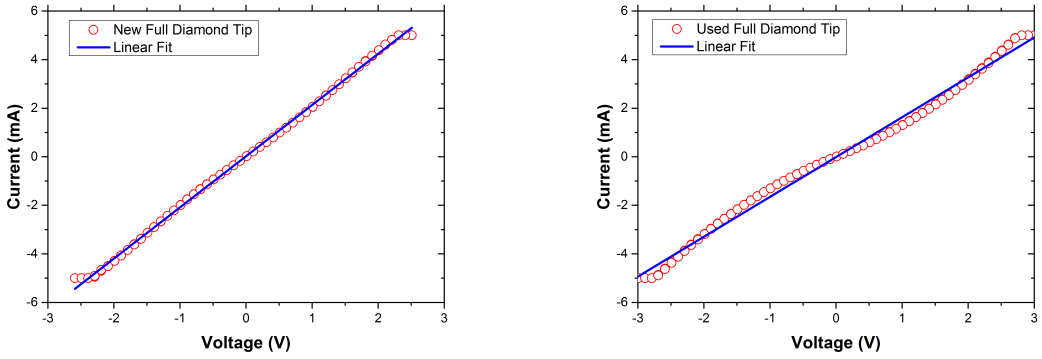

(A) (B)

FIGURE 2.13: I–V characteristics measured on HOPG sample by using full diamond tip for (a) new tip ($R_{tip} \approx 460\Omega$), (b) tip after using it for 2 months ($R_{tip} \approx 460\Omega$). We can see the non-linearity in the I-V characteristic for used tip

For the reproducibility and the reliability of the electrical measurements that we will realize, it is necessary to preserve the conductive capacities of the tip throughout the study. Indeed, the non-linearity behavior of the current observed during the degradation of the tip can lead to a shift of the voltages actually applied to the sample[262]. For reproducibility and reliability of measurements, it will be important to regularly check the electrical characteristics of the tip on HOPG sample.

2.1.6 Sample Preparation

The samples studied in this thesis work are produced by CEA Leti for resistive memory layers. These layers are developed on a full wafer of 200mm or 300mm. Ox-RAM samples consist of two different bottom electrodes. One sample is a Si sub/(TiN (50nm)/HfO_2(5 nm) stack and the other one is a Si sub/TiN (50 nm)/Ti (10 nm)/HfO_2(5 nm) stack. TiN and Ti layers were deposited by physical vapor deposition (PVD) and the HfO_2 layers by atomic layer deposition (ALD). For PCM sample, the sample details are given in chapte 5. The Omicron AFM does not have a loading chamber for whole wafers, so the first preparation step is to cleave samples with a size of $1 \times 1cm^2$ compatible with the AFM sample holders as shown in figure 2.14. To avoid being subjected to the variations generated during the oxide deposition, the samples are taken from the central part of the wafer. To ensure electrical contact, the samples are then fixed on sample holders using silver epoxy glue. This technique is well suited to the case of high current density electrical measurements. Also contact on the side of the sample were also confirmed by sticking the epoxy on the side wall of the sample. The sample holder thus makes it possible to manipulate the sample within the ultra-vacuum by using the transfer arms present in the AFM Omicron setup. Finally, to remove any trace of moisture and organic impurities on the sample, sometime it undergoes degassing at 125°C for 1 hours under a pressure of $10^{-7}Torr$.

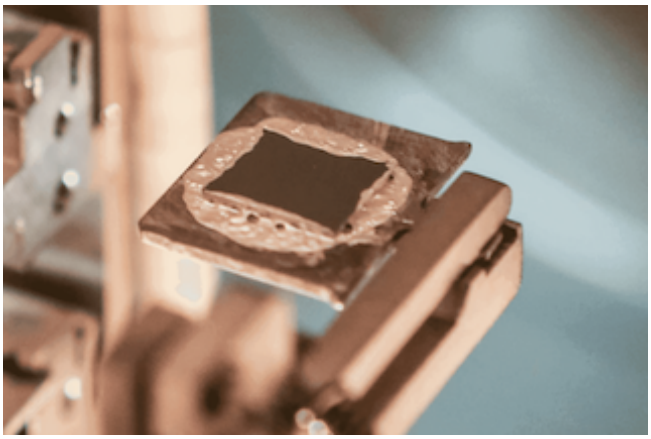

FIGURE 2.14: Sample holder where sample is glued to it using silver epoxy.

2.2 Measurement with AFM

The conductive mode atomic force microscope can be used to perform both topographic measurements of the sample surface and to perform the electrical characterizations of the oxide layers. The different types of measurement used in this study will be discussed in coming section.

2.2.1 Topography Characterization

In order to characterize the surface of the oxides physically, the thickness variations are measured by doing surface scans in contact mode. The software used for the image processing (Gwyddion) allows to rebuild the 3D images of the studied surface. Figure 2.15 shows an example of AFM topography obtained for a $1x1\mu m^2$ scan in contact mode with a full diamond tip on $HfO_2(5nm)$ sample.

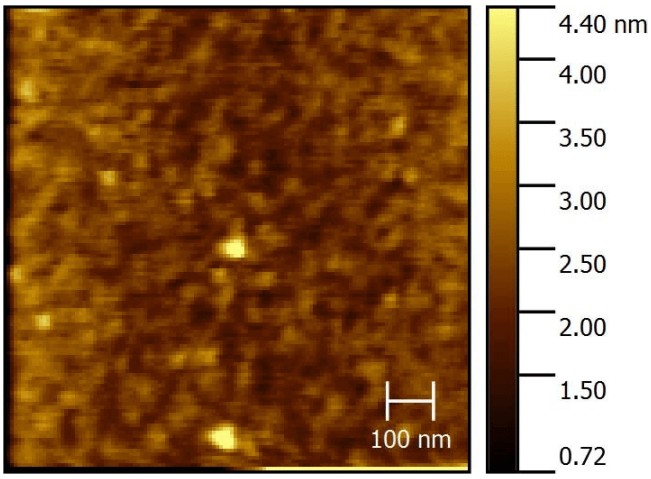

FIGURE 2.15: Topographical image taken by AFM for HfO_2 sample using full diamond tip.

The variations in thickness measured in the case of the oxides studied in this thesis are of the order of one nanometer for micrometric surfaces, which testifies to

their uniformity. The Gwyddion software is also able to calculate the RMS (Root Mean Square) value of roughness according to the formula

$$R_q = \sqrt{\frac{1}{N}\sum_{j=1}^{N}(Z_j - Z_m)^2} \tag{2.6}$$

In equation 2.6 Z_m and Z_j define the average height of the scanned surface and the height measured at the point j, N corresponds to the number of points measured.

This value describes the standard deviation of the distribution of measured thicknesses. Thus, the lower the RMS value, the more uniform the oxide thickness will be. Finally, the software makes it possible to obtain a statistical evaluation of the thicknesses measured over the entire surface in the form of a histogram. It has been shown that variations in thickness can be reproduced by a normal law[263].

2.2.2 Electrical Characterization

Contact mode is used to make the electrical measurements. Tip is in contact with the sample and a constant contact force is applied throughout the measurements. In our setup the tip stage is fixed so we can only move the sample stage. To make the contact, the sample stage is first moved towards the tip by using the remote control manually. The movement can be seen on the screen through the camera which is attached to the window of the UHV chamber next to AFM setup. The sample movement makes the cantilever vibrate by mechanical coupling which can be seen on the oscilloscope as variation of the signal of the four-quadrant detector. When the sample is close to the tip, an automatic approach is started in order not to destroy the tip. Once the tip is in contact, it is ready to make the electrical measurements. A Keithley with sub femtometer is connected to the AFM tip and the sample. As soon as the tip and sample are in contact, voltage is applied by using Keithley and current is measured by the same Keithley. By using a LabView program the current voltage characteristic can be stored. Also, LabView program permits to modify different parameters while measuring like voltage ramp speed, compliance current and also the applied voltage.

To do electrical measurement a voltage ramp is applied. This ramp can or cannot have effect on the I-V characteristic of the sample. Voltage ramp speed can be changed by selecting different step size of voltage. All this can be done in the LabView program. Different voltage step sizes were used like $0.1V$ which gives a ramp speed of $0.125V/s$. Other than then $0.1V$, $0.05V$ and $0.01V$ steps were used. We tried I-V measurement with different ramp speed to see the effect of ramp speed on its characteristic. Although we did not find any effect of ramp speed on the characteristic.

AFM is a tool now widely used in microelectronics laboratories. The reliability of the oxides at the nanoscopic scale was one of the first subjects to use C-AFM[264;265] and remains a highly studied subject[266;267]. Studies have shown the effectiveness of AFM in statistical studies and reproducibility with times for electrical breakdown[268;269]. Numerous studies have demonstrated the need to work under vacuum in order to obtain reliable measurements[270] and to prolong the life of AFM tips[260] by avoiding redox reactions.

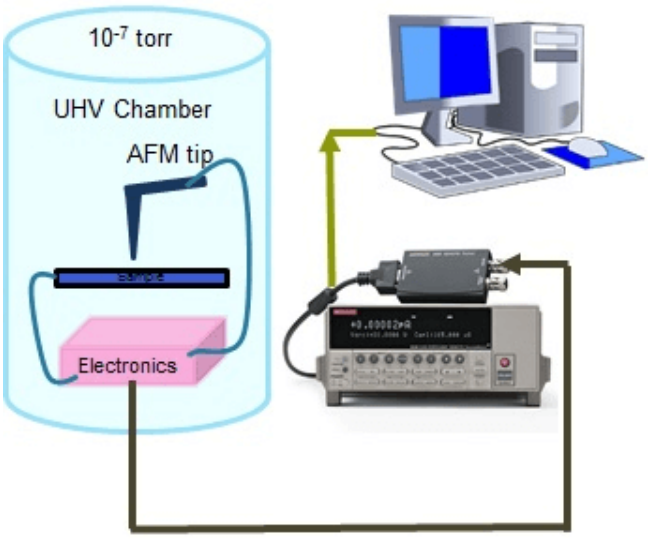

FIGURE 2.16: A basic AFM unit inside ultra-high vacuum chamber connected to Keithley for electrical measurement.

Many studies have focused on the use of C-AFM to study electrical conduction through oxides. In 1995, a first study on SiO_2 confirms the presence of Fowler Nordheim type conduction in I-V characteristics[271]. Using this leakage current, Frammelsberger[258] and Olbrich[272] shows that it is possible to determine the oxide thickness using the Fowler Nordheim current measured by C-AFM. During this study, various advanced materials are used and the authors extract the work functions for each type of tip.

Various studies are undergoing for resistive memories also. Studies for resistive switching in Oxide based random access memory (OxRAM)[273] and in Phase change memory (PCM)[274] by using AFM have been done. Various groups have shown the resistive switching at nanoscale.

The main motivation of using C-AFM is to characterize the oxide layer and phase change materials at nanoscale, as the AFM tip can be used as nanometric top electrode of MIM structure. Few studies have been done with top electrode in the nanometric range[275;276]. Also few similar kind of studies were done by using C-AFM by some groups[267;273;277–280] but most of them are done in ambient conditions

2.3 Scanning Electron Microscope

2.3.1 Introduction and Basic Principle

The scanning electron Microscope (SEM)[281] is used to observe the surface of the samples. When fine electron beam is irradiated on a sample specimen, secondary electrons are emitted from the specimen surface. A topographical study of the sample can be done by scanning the electron probe over the surface and acquisition of an image from the detected secondary electrons. Accelerated electrons in SEM carries significant kinetic energy and this energy is dissipated in the form of various signals produced during the electron interaction with the sample when the incident electron is decelerated in the solid sample. These signals include many different types, like secondary electrons (used to produce the topographical image), backscattered

electron, diffracted back scattered electrons (used to determine the crystal structure and orientation on minerals), photons (characteristic X ray that is used for elemental analysis), visible light and heat. Mostly secondary electrons and backscattered electrons are used for topography studies of the sample. A scanning electron mi-

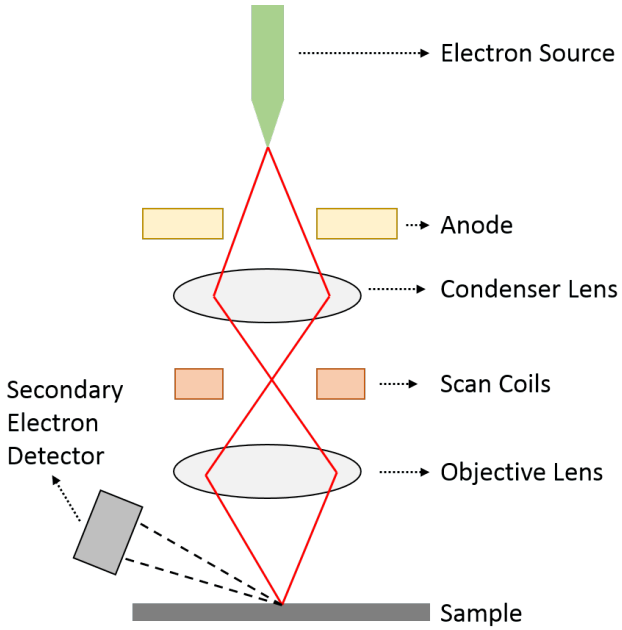

FIGURE 2.17: Basic unit of a scanning electron microscope.

croscope based on secondary emission of electrons was developed at RCA laboratories in New Jersey by Zwyorkin et al in 1942[282]. The SEM is composed of electron optical system to produce electron beam, a sample stage, a secondary electron detector to collect the secondary electrons and an image display unit. The electron optical system consists of an electron gun, condenser lens and objective lens to produce electron beam, a scanning coil to scan the electron probe and some other components. Whole system is kept under vacuum.

In our case scanning electron microscope is used to study the AFM tip morphology. SEM images were taken for the new tip and after using the tip. Also, to know the tip diameter after blunting the tip.

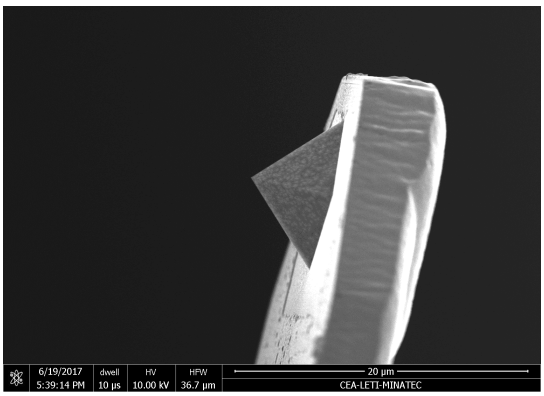

FIGURE 2.18: A SEM image of a new full diamond tip.

2.4 SEM EDX

2.4.1 Introduction and Basic Principle

As discussed in the last section, when an electron hits the sample it produces various signals. X-ray is one of them. The x-ray is generated in two steps in SEM. First when an electron beams hits the sample surface it transfers its energy to the atom of the sample and then this energy can be used by the electron of the atoms to jump to a

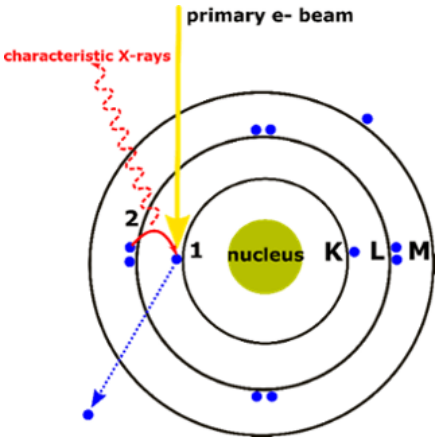

FIGURE 2.19: Schematic diagram for production of X-Ray.

higher energy shell or can be knocked off from the atom. If this happens the electron leaves behind a hole and these holes have positive charges. Now in second step this positive charge hole attracts the negatively charged electron from a higher energy shells. When an electron from higher energy shell recombines with hole of the lower energy shell, the energy difference of this transition can be released in the form of X-Ray. So, this energy of X-Ray is the characteristic of the energy difference between two shells. It depends on the atomic number, which is a unique property of every element. So, in this way we can identify the elements that exist in the sample.

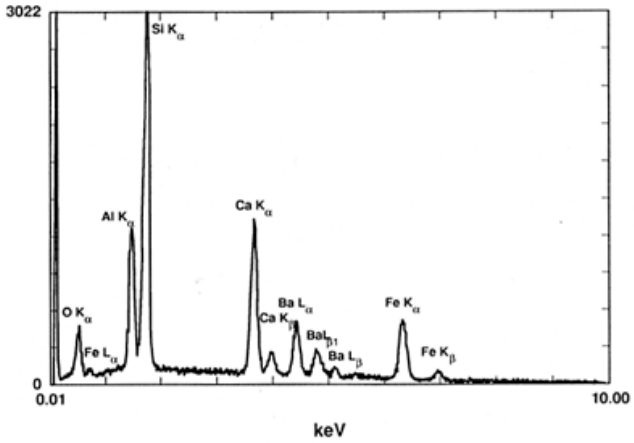

FIGURE 2.20: EDX spectrum of multi-element glass (NIST K309) containing O,AL,Si,Ca,Ba and Fe (Goldstein et al: 2003)[283]

X-Ray are electromagnetic radiation just like light and can consist of photons. It can be detected by a system called silicon drift detectors (SSDs). These kind of detectors are better for better resolution and faster analytical capabilities compared to

conventional Si(Li) detectors. These detectors are placed much closer to the sample at an angle and have ability to measure the energy of the incoming photons. These photons are in the X-ray range. The data generated by the EDX analysis consist of spectra with peaks corresponding to all the different elements that are presents in the sample. A typical EDX spectrum is shown in figure 2.20.

We studied many different AFM tips by using the SEM EDX to know the composition of a new tip and also to study the change in composition after making the electrical measurements with AFM tip.

2.5 Conclusion

Atomic force microscopy in conductive mode is widely used these days for electrical characterization at nanoscale. Nowadays Conductive AFM is used to study resistive memories at nanoscale to understand the switching effect by using the tip as top electrode. At device level, it is difficult to understand the phenomena occurring inside the layers when the electrical resistance switches because of many filament formations under the micrometer sized top electrode. So, it is difficult to know the exact property of the single filament. But with the help of C-AFM it is possible to get the information about the single filament because of AFM tip size in nm scale which we used as the top electrode. Also, the filament width size is more or less similar to tip diameter which means you can have single filament under the tip where tip is making contact with the sample. Also, different setups of AFM like for low temperature permits to study the effect of temperature on switching.

On the other hand, the use of such tool requires great attention to all the parameters that may affect the measurement results such as contact force between tip and sample, the physical and electrical characteristics of the tip, etc. In the following, all the measurements presented were carried out under a pressure of 10^{-7} to 10^{-9} Torr, at ambient temperature, using boron doped full diamond tip whose metallic characteristics were checked regularly on HOPG. Also, a change in pressure value can affect the electrical measurements because it would lead to a change in the tip-sample contact area which would impact the current value.

In the next chapters, we will discuss in more details the resistive switching studies done on different materials by Conductive AFM and suggest a switching mechanism. All measurements will be repeated many times to verify the reproducibility and to obtain statistical descriptions of the events. Also, we will analyse the tip material composition before and after doing electrical measurements by using SEM EDX.

Chapter 3

Impact of Compliance Current on Resistive Switching in OxRAM

3.1 Introduction

Generally, a simple OxRAM consists of a metal/insulator/ metal (MIM) structure[284], and by applying electrical bias, the resistance can be changed as discussed in chapter 1. The mechanism of resistive switching is still under intensive debate, but migration of oxygen ions under an electrical bias[160] to form a conductive filament is the widely accepted mechanism. The formation and rupture of this conductive filament results in a significant change in current flow. HfO_2 [105;143;177;231;285–290] is the most attractive material because of its CMOS compatibility and use as a high-k gate insulator for advanced CMOS technology.

The main motivation of using conductive atomic force microscopy (C-AFM) is to characterize the oxide layer at the nanoscale, as the AFM tip can be used as the nanometric top electrode for the MIM structure. Few studies have been done with the top electrode in the nanometric range[291;292]. Also, few similar kinds of studies were done by using C-AFM by some groups[143;166;233;285;290;293;294] but most of them are done in ambient conditions.

In this chapter, a preliminary study about OxRAM switching behavior will be done. Also, different parameters like SET and RESET voltages as well as on-state and off-state conductance will be studied. It is nowadays well known that the compliance current Ic fixes the value of the On-state conductance. It has already been shown that, at least on the OxRAM stacks under study here, the On-state conductance is proportional to the compliance current during the forming process. For 1T1R devices this relation is given by $G_{on} = V_c^{-1}.I_c$ with $V_c \sim 0.35V$. It is then attempting to explore the validity or the limit of this relation. The C-AFM in UHV is useful to accomplish this task. This is a motivation to study the switching effect in HfO_2 based sample by using the C-AFM from low compliance current (in the range of nA) to high compliance current (in the range of μA). A detailed model will also be discussed for the low compliance current. Switching model at high compliance current will be discussed in the next chapter.

3.2 Experimental Observations

3.2.1 Switching Behavior based on polarity

As discussed in the introduction part about the switching in the OxRAM, here we will do the basic studies to see the switching at a given compliance current. We will

see if the sample has the OxRAM characteristic or not. Two different AFM tips (PtSi and full diamond tip, for details see chapter 2) are used as top electrode to study the sample here. The voltage was applied on the sample and the AFM tip was grounded. To do these studies, electrical characterization was performed on each sample with both tips at two different compliance currents. PtSi tip is used at $100\mu A$ compliance current and full diamond tips at $400\mu A$ for forming process.

First of all, the measurements were done to know the behavior of the switching, because OxRAM switching can be bipolar, unipolar or non-polar. As we can see in table 3.1, the TiN/HfO_2 sample with both (PtSi &Full Diamond) is showing bipolar switching, which means that the SET and RESET are occurring for different polarities. For $TiN/Ti/HfO_2$ sample, the switching is non-polar. This sample is showing both bipolar and unipolar characteristic. All the different parameters obtained for both samples with both tips are presented in table 3.1.

Another study with different forming, SET & RESET procedures in different polarities is done to see if there is any effect of the polarity on the switching behavior. First of all, forming process to form the filament inside the oxide layer was done at $100\mu A$ compliance current in negative bias on TiN/HfO_2 sample with PtSi tip, and positive bias was used to reset the filament. Again, negative bias is used to SET the filament. In another procedure the Forming and SET were performed in positive bias and reset was performed in negative bias. For both procedures, the forming, set and reset voltages are the same. But the On-state conductance is different. It is lower when the filament is formed with negative bias. The Off-state conductance is in the same range for both procedures. SET and RESET memory windows (ratio between and ON and OFF state current in set and reset polarity) are also the same and the order of magnitude is presented in table 3.1. SET or RESET window is the difference in the current between on state and off state. There was no difference in the switching nature with both procedures, it is bipolar in both cases.

Then, the same study was performed with full diamond tip but with $400\mu A$ compliance current. Forming voltage is not polarity dependent. Set voltage has a wide range from 2-6 V when the filament is formed in positive bias. Reset voltage is almost the same in both cases. On state conductance and off state conductance are similar in both different cases as well as the SET and RESET window. Also, there was no effect on switching nature and the same observations were made with PtSi tips.

Similar studies were done on the $TiN/Ti/HfO_2$ sample with both tips. In the case of PtSi tip, the forming voltage is lower than with full diamond tips, no matter in which polarity, the filament is formed. Set voltage and reset voltages are in the same range with both different tips. The On-state conductance is also similar for both tips. The only difference is in the off state conductance. The off-state conductance is lower by several orders of magnitude in the case of PtSi tip and the SET and RESET windows with PtSi are larger compared to full diamond tip. Those features will be extensively analyzed in the next chapter. The Overall aspect of the switching characteristics stays the same whatever the tip nature. This sample shows both bipolar and unipolar characteristic, which means it is non-polar in nature.

Sample	Top Electrode (AFM tip)	Forming, Set, Reset directions	I_C (μA)	V_F (V)	V_S (V)	V_R (V)	I_R (mA)	G_{on} (10^{-6} Ω^{-1})	G_{off} (10^{-6} Ω^{-1})	SET memory window	RESET memory window	Non-Polar	Bi-polar	Uni-polar
TiN/HfO_2	PtSi	F→-ve bias S→-ve bias R→+ve bias	100	5-6	1-9	2.5-3	2-3	839.94	3.15e-4	10^{3-5}	10^{7-8}	No	Yes	No
TiN/HfO_2	PtSi	F→+ve bias S→+ve bias R→-ve bias	100	5-6	1-7	2-3	1-3	2225.15	1.54e-4	10^{3}	10^{7-8}	No	Yes	No
TiN/HfO_2	Full Diamond	F→-ve bias S→-ve bias R→+ve bias	400	5-6	4-5	3-5	∼4	2258.47	6.25e-4	10^{4-5}	10^{7-8}	No	Yes	No
TiN/HfO_2	Full Diamond	F→+ve bias S→+ve bias R→-ve bias	400	5-6	2-6	2-3	∼4	1895.44	6.89e-4	10^{4-5}	10^{7-8}	No	Yes	No
$TiN/Ti/HfO_2$	PtSi	F→-ve bias S→-ve bias R→+ve bias	100	3-4	3-6	1.5-2	2-4	2773.82	2.61e-7	10^{7-8}	10^{10-11}	Yes	No	No
$TiN/Ti/HfO_2$	PtSi	F→+ve bias S→+ve bias R→-ve bias	100	3-4	3-6	1.5-2.5	2-4	2920.53	1.77e-6	10^{7-8}	10^{10-11}	Yes	No	No
$TiN/Ti/HfO_2$	Full Diamond	F→-ve bias S→-ve bias R→+ve bias	400	5	2-3	1.5-3	2-4	2043.97	133.34	$<10^{1}$	10^{1}	Yes	No	No
$TiN/Ti/HfO_2$	Full Diamond	F→+ve bias S→+ve bias R→-ve bias	400	4.5	4.5-7	2-4	1-2	2699.53	2.35e-5	10^{3}	10^{10-11}	Yes	No	No

TABLE 3.1: Primary study for switching in TiN/HfO_2 and $TiN/Ti/HfO_2$ sample with different tips. ($I_C \rightarrow I_{Compliance}$, $V_F \rightarrow V_{Forming}$, $V_S \rightarrow V_{SET}$, $V_R \rightarrow V_{RESET}$, $I_R \rightarrow I_{RESET}$)

3.2.2 Low Compliance current effect (in the range of nA)

After having determined the switching nature in both samples with different tips, the impact of compliance current on switching was studied in the 100nA-400nA range.

Let us discuss the characteristic for 100nA compliance current on TiN/HfO_2 sample with full diamond tip as shown in figure 3.1a. Same compliance current was fixed for both polarities. The voltage ramp is started from 0V to negative bias. In figure 3.1a, arrows and numbers are showing the direction of the ramp. So, we form the filament in the negative bias. The current increases abruptly around -3 to -5V,

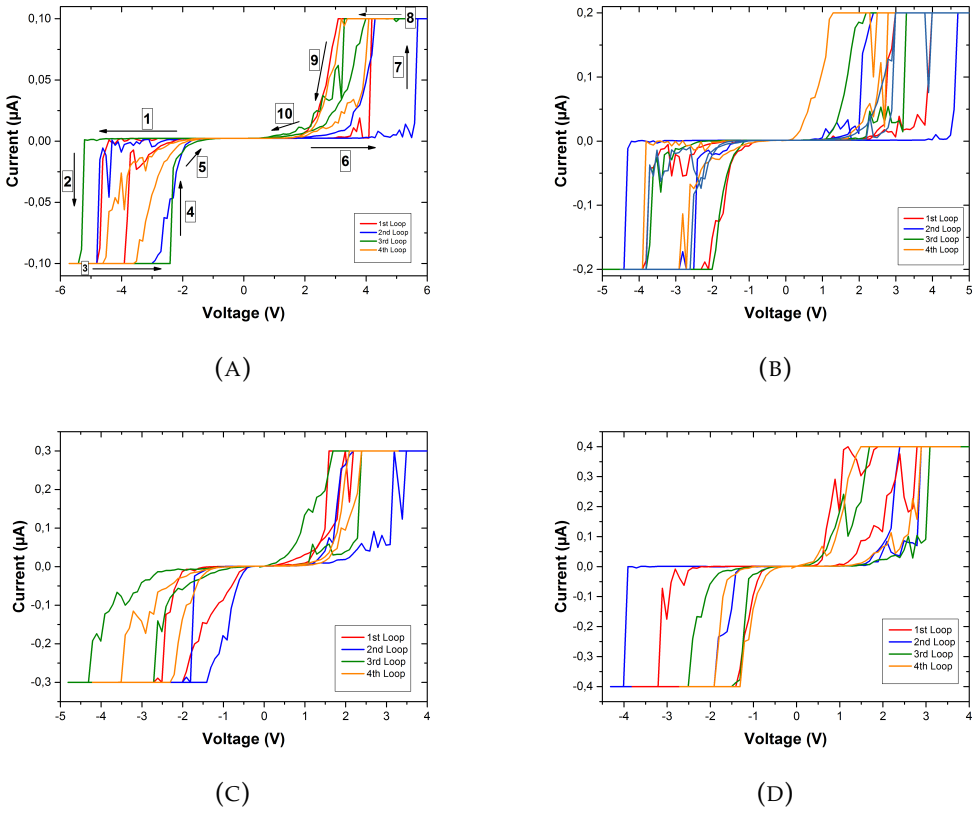

FIGURE 3.1: I-V characteristics at low compliance for TiN/HfO_2 sample with full diamond tip (a) at 100nA, (b) at 200nA, (c) at 300nA and (d) at 400nA.

until reaching the compliance current (arrow 1 and 2). Once the current reaches the compliance value, the direction of the voltage ramp is reversed and the current stays constant up to a voltage of around -2V (arrow 3). When the voltage drops below -2V, the current decreases exponentially and returns to the initial level around -1 V in most cases (arrow 4 and 5). The abrupt current rise beyond -3 to -4V corresponds to the filament formation that is normally used to initialize the memory to the low resistance state. As the ramp goes in positive bias the resistance stays high until 4V (arrow 6). Then, there is sudden increase and the current reaches the compliance value (arrow 7). After it reaches the compliance value the ramp is reversed and it stays in the low resistance state till around 2.5 V (arrow 8). After this voltage, the current starts decreasing exponentially and reaches the initial state around 1.5V (arrow 9). As we can see, for both polarities the same process is happening. The

current behavior of the second loop is identical. It means there is cycling without memory effect, in that sense that reversing the polarity changes the conductance values contrarily to typical OxRAM behavior.

The same measurements were done with 200nA, 300nA and 400nA but there was still no memory effect. In all the cases the current- voltage (I-V) characteristics are similar. The compliance current is too low here to form a completely grown filament inside the oxide layer. So, for absolute voltage values below 1 V, the current drops to almost zero in both polarities as one can see in figure 3.1. With every loop the breakdown voltage shifts to lower values.

The filament formation at all these compliance currents will be discussed in the discussion section by comparison with a model.

3.2.3 High Compliance current effect (in the range of μA)

As seen before, there was no memory effect observed at low compliance current (in the range of nA). So, we will analyze the switching at higher compliance current in the range of μA to determine the threshold for memory effect. First of all, an I-V characteristic was done with 300μA compliance current for both polarities in order to see if there is any memory effect. The corresponding I-V curve are shown in figure 3.2. The arrows and numbers are representing the direction of the ramp in figure 3.2a & 3.2b.

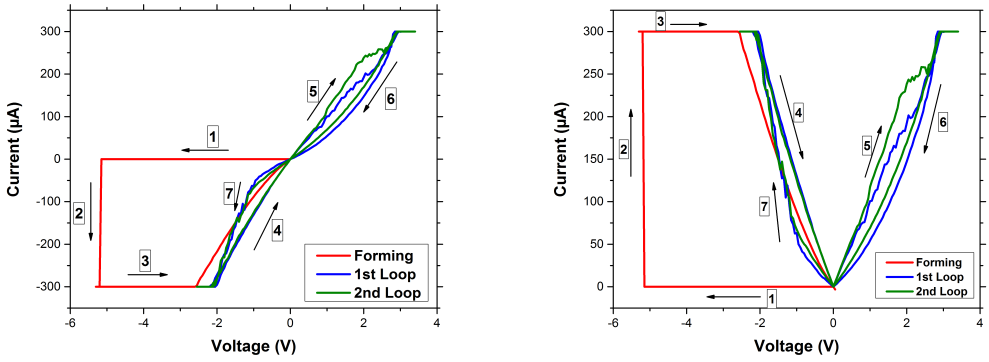

(A) (B)

FIGURE 3.2: I-V characteristics at high compliance (300μA) for TiN/HfO_2 sample with full diamond tip showing forming, SET and RESET for different loops. In fig (b) the absolute current is plotted for both polarities.

The negative voltage ramp is applied to form the filament inside the oxide layer. As one can in see in figure 3.2a, the current is in pA range until it reaches around -5 V and then there is sudden increase in the current reaching the compliance value (arrows 1 and 2). This breakdown in the oxide is due to filament formation. After current reaches the compliance limit the voltage ramp is reversed (arrow 3). After -2 V the current starts decreasing linearly which means the top electrode (AFM tip) and bottom electrode are connected through the filament (arrow 4). In figure 3.2b the absolute value of the current is plotted for both polarities.

When the voltage ramp in opposite bias was applied, the current starts increasing linearly till 1.8 V and then starts decreasing which means the filament is in the RESET state discontinuing the contact between the tip and the bottom electrode (arrow 5). Once again, when the current reaches the compliance limit the voltage ramp direction is reversed. As soon as the ramp is reversed the current starts decreasing non-linearly (arrow 6) and is lower than for increasing voltage (arrow 5), meaning that we start to see a little memory effect. Again, by applying negative bias, first the current increases slowly and around -1 V it starts increasing rapidly reaching the compliance limit, meaning that the filament connects the AFM tip and the bottom electrode completely again (SET), resulting in low resistance state (arrow 7).

So, we found that we start having the memory effect from the μA range on. Although the memory window is not large enough. Because of the limitation of the compliance current for the RESET, it is not possible to reset the filament completely.

The current necessary to RESET the filament depends on the forming step. Normally we need higher current density compared to the compliance current used for forming. By removing the limitation in compliance current value for positive voltages, we will have enough joule heating in order to reset the filament completely.

I-V characterizations were done at 10 μA, 50μA, 100μA, 200μA, 300μA, 400μA, 500μA & 600μA for both samples. Here we applied the same ramp as in the previous study (shown in figure 3.2) to begin with the same sweep direction as in literature as we are applying voltage on the sample with the tip grounded. So, we did the forming and SET in negative bias and RESET in positive bias.

Once the filament formation is done, positive bias is applied to reset the filament. Again, negative ramp is applied to Set the filament. Only SET and RESET characteristics are shown in figure 3.3. As can be seen in figure 3.3a, there is small SET and RESET in the I-V characteristics, which means that still the compliance current is not high enough to form the complete filament inside the oxide layer. But it was possible to observe the memory effect at 10μA. Although SET and RESET windows are smaller.

Again, in same way I-V characteristics were recorded for 50μA, 100μA & 200μA. As the compliance current is increasing the SET and RESET windows are increasing too. As can be seen in figure 3.3b, 3.3c & 3.3d, the RESET window is almost same in all the cases. SET voltage is varying from 1V to 2 V in all the three cases. The RESET voltage is in the range of 1.5V to 2.5V in all cases. This means that in the range of 50μA to 200μA, there is no effect of compliance current on the switching characteristics.

As the compliance current for set is increased further from 200μA to 300μA, the off-state conductance starts increasing. But the on-state conductance still gives non-linear behavior. Also, at 300μA and 400μA, the SET voltage is higher compared to the one obtained with the previous compliance current used as can be seen in figure 3.3e & 3.3f. At 50μA, 100μA & 200μA compliance current, the SET voltage was around 1V-2V but in the case of 300μA & 400μA, the SET voltage is around 2.5V – 3V. When a negative voltage ramp is applied to SET the filament, the current starts increasing and at a certain voltage, the current starts decreasing with increasing voltage. And at some voltage suddenly it reaches the compliance current setting the filament. This behavior will be explained in more detail in the next chapter.

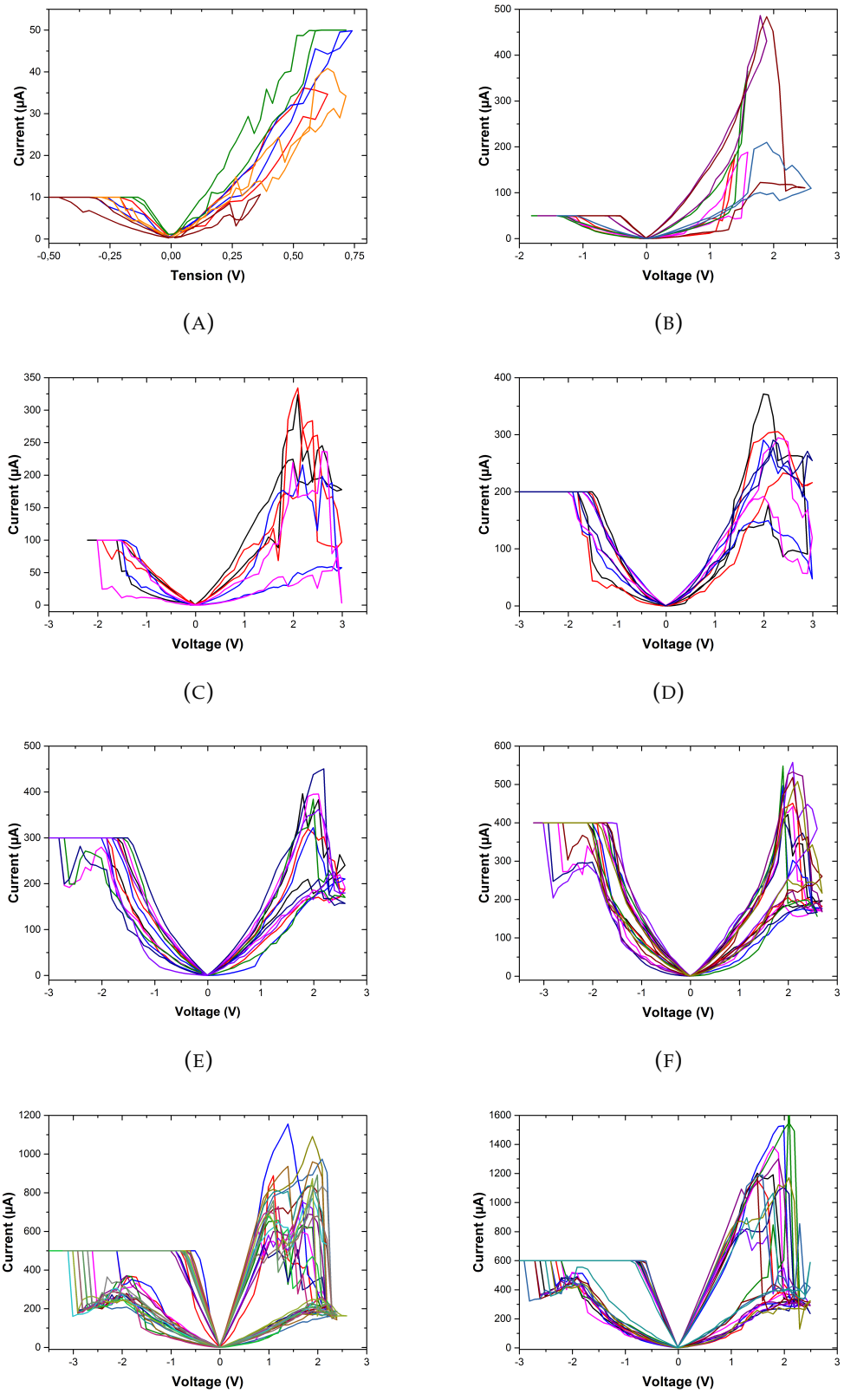

FIGURE 3.3: I-V characteristics at compliance current in the range of μA for TiN/HfO_2 sample with full diamond tip (a) at 10μA, (b) 50μA, (c) 100μA, (d) 200μA, (e) 300μA, (f) 400μA, (g) 500μA and (h) 600μA.

In figure 3.3g & 3.3h, once the compliance current is increased above 400μA to 500 μA & 600 μA, the on-state conductance becomes linear. It means that the filament is fully grown and the top electrode is completely connected to bottom electrode through filament. The SET voltage still stays high in the range of 2.5V-3V. The memory window gets better with increasing the compliance current. Also, at 500 μA & 600 μA the reproducibility of the I-V curve is getting better. All the loops for single measurement are almost similar.

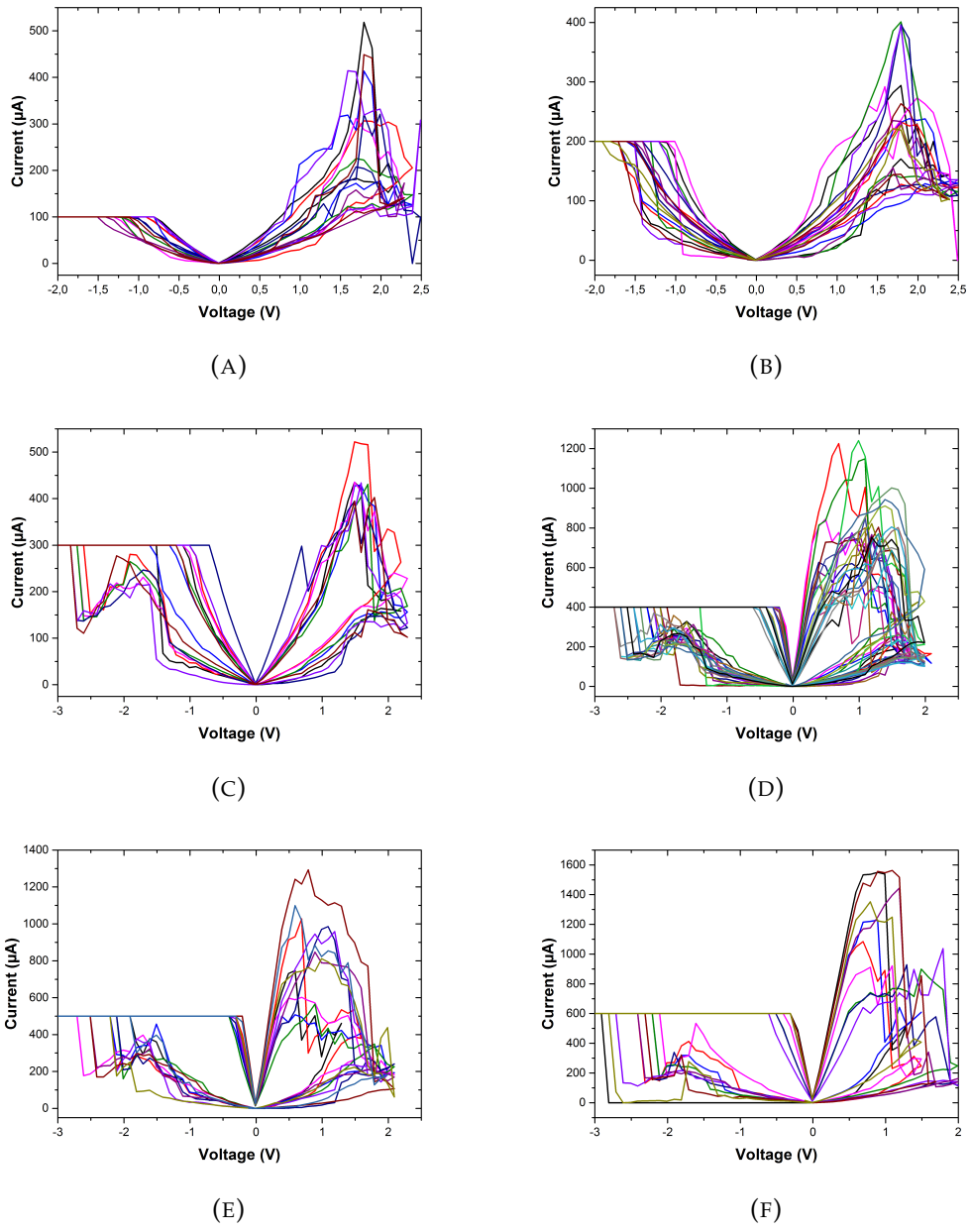

FIGURE 3.4: I-V characteristics at compliance current in the range of μA for $TiN/Ti/HfO_2$ sample with full diamond tip (a) at 10OμA, (b) 200μA, (c) 300μA, (d) 400μA, (e) 500μA and (f) 600μA.

Same study has been performed for $TiN/Ti/HfO_2$ sample as shown in figure 3.4. Low SET and RESET windows were observed at 100μA and 200 μA. The SET

and RESET voltage are in the range of 1-1.5 V and 1.5-2V respectively. Once the compliance current is increased from 200μA to 300μA, the I-V characteristic starts becoming reproducible. The SET voltage is increased to 2.5-3V. At 400μA, 500μA,

and 600μA, the I-V characteristics are reproducible and the SET voltage is almost similar in all the cases as well the RESET voltage. The on-state conductance is increasing with increasing compliance current and On-state is becoming more and more linear.

3.2.4 Threshold compliance current for full filament formation

Once the I-V characterizations were done at different compliance values, it is time to find out above which compliance current the on-state conductance is becoming linear and reproducible. As can be seen in the previous section that the on state was non-linear at 400μA and becoming linear at 500μA for TiN/HfO_2 sample. So, it is necessary to make some measurement in between 400μA to 500μA. So, to know the threshold compliance current (compliance current at which the on state is becoming linear), the I-V characterization was done at 450μA. As one can see in figure 3.5a, the SET and RESET were observed. The characteristics are similar to the one observed at 400μA. Still the on-state conductance is showing the non-linear behavior. So, the compliance current is increased again to 475μA and this time the characteristics are different than the one observed for 400μA and 450μA as can be seen in figure 3.5b. The on state is showing linear behavior and is higher now. I-V characteristics at 500μA (figure 3.5c) are similar to the one observed for 475μA. The I-V measurements were done at different positions on the sample to see if the characteristics are similar at 475μA, and it was observed that the I-V characteristics were reproducible.

On and Off state conductance is plotted in figure 3.6 for both samples. For TiN/HfO_2 sample, one can see in figure 3.6a that there is only small difference in on and off state conductance from 10μA to 400μA. At 450μA the difference between on and off state is getting higher and at 475μA the difference became really huge. For compliance currents higher than 450μA, the on-state conductance is around $8 \times 10^{-4}\Omega^{-1}$ and keeps increasing with increasing the compliance current. The off-state conductance stays almost similar in all the cases.

For $TiN/Ti/HfO_2$, this transition happens around 300μA. As it can be seen in figure 3.6b, the off state stays similar for almost all the compliance current values. The On-state conductance is a bit higher than the off-state conductance in the case of 100μA and 200μA. At 300μA, the difference became larger and on state conductance keeps increasing with increasing the compliance current.

The off-state current for both samples is almost similar in both cases. At 600μA, the off-state conductance for TiN/HfO_2 is around $2 \times 10^{-4}\Omega^{-1}$ and for $TiN/Ti/HfO_2$ around $1 \times 10^{-4}\Omega^{-1}$. The on state for TiN/HfO_2 is around $9 \times 10^{-4}\Omega^{-1}$ and for $TiN/Ti/HfO_2$ around $16 \times 10^{-4}\Omega^{-1}$ which is much larger than for the TiN/HfO_2 sample. It means that the presence of the Ti layer in the $TiN/Ti/HfO_2$ sample increases the on-state conductance. But there is not much effect of Ti layer on OFF state conductance. This will be discussed in more detail by comparison with a model in the next chapter.

In the $TiN/Ti/HfO_2$ case, one can see that G_{on} vs I_C characteristics obtained by C-AFM and on comparable devices have almost the same slope, whatever the device

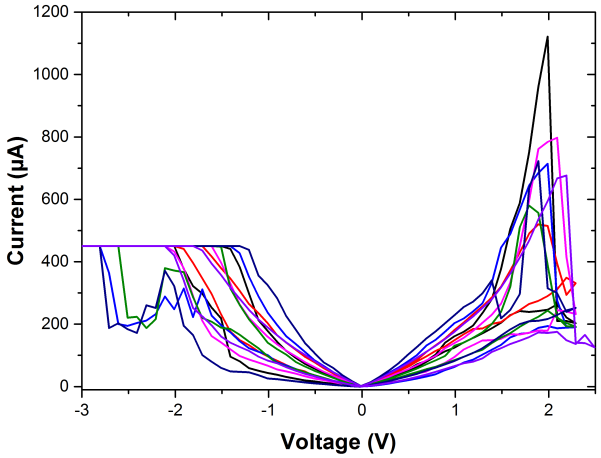

(A)

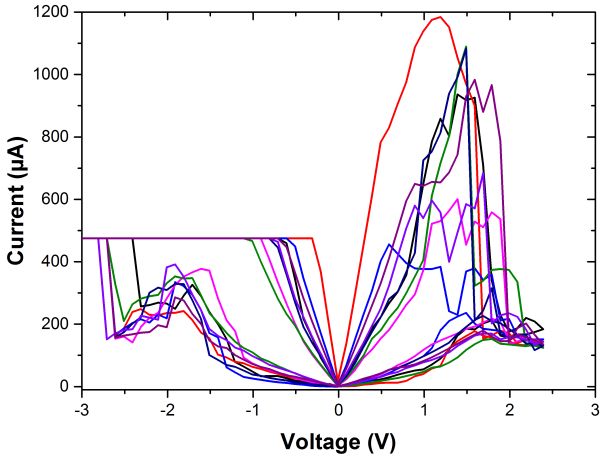

(B)

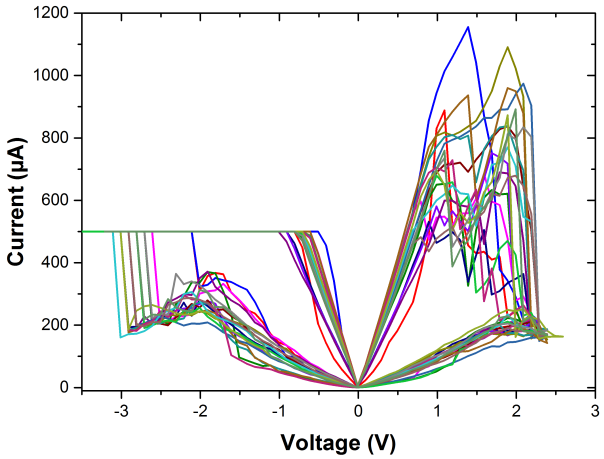

(C)

FIGURE 3.5: I-V characteristics for linear on state conductance for TiN/HfO_2 sample with full diamond tip (a) at 450μA, (b) 475μA and (c) 500μA.

area (nanometer to micrometer scale, if one excludes the 200μA point). This confirms the filamentary process and the interest in using UHV C-AFM. Below 100μA the number of conduction channels (N), involved in the quantum conductance ($G_{on} = Nq^2/h$) is very low ($N \leq 2$). It means that the thickness of the thinner part of the filament reaches the atomic size. It is then interesting to examine what happens in the case of the lower compliance. This will be discussed in the following part.

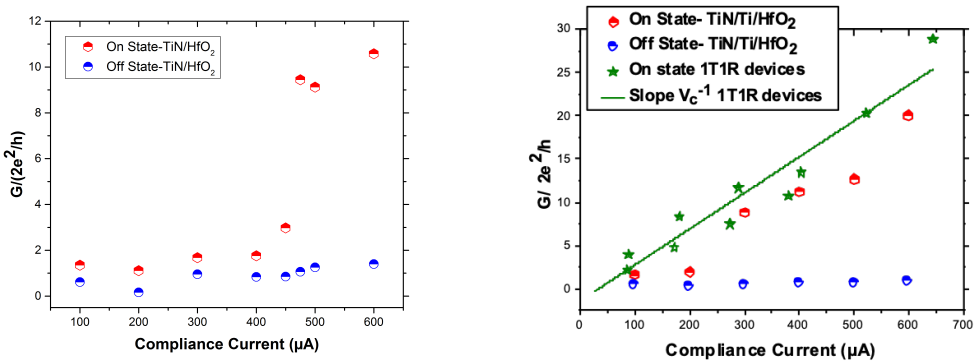

(A) (B)

FIGURE 3.6: On and off state conductance variation with compliance current for (a) for TiN/HfO_2 & (b) for $TiN/Ti/HfO_2$ and $1\mu m^2$ 1T1R ($TiN/Ti/HfO_2/Ti$) devices[286].

3.3 Discussion for Low Compliance (in nA range)

3.3.1 Filament Growth Model

The general overview of the filament model for OxRAM is given in the thesis of Romain Fossiac[295]. Firstly, filament growth model was given for phase change memories by Karpov et al.[296]. Here, we will describe the model based on formation of filament due to ion movement. We considered that the filament is growing from the bottom electrode side and the rate of the growth depends on the distance between the apex of the filament and the apex of the tip (as top electrode). Thus, the time dependence of the length of the filament, $I(t)$, follows the following differential equation:

$$\frac{dI(t)}{dt} = k_1(T_{ox} - l) - k_2 l \tag{3.1}$$

Where k_1 & k_2 are the growth characteristic ratess, l is the length of the filament and T_{ox} is the thickness of the oxide layer. This equation can be seen as one-dimensional growth equation. Moreover in ref[295], it was shown that the filament growth mechanism in HfO_2 was likely due to electric field assisted ionic drift mechanism.

Thus, growth characteristic rates for filament growth k_1 and for filament decay k_2 are given by:

$$k_1 = \frac{1}{\tau_o} exp\left(- \left(\frac{V_1 - 2qa_o \frac{V_{ox}}{T_{ox}}}{k_B T} \right) \right) \tag{3.2}$$

$$k_2 = \frac{1}{\tau_o} exp\left(- \left(\frac{V_2 + 2qa_o \frac{V_{ox}}{T_{ox}}}{k_B T} \right) \right) \tag{3.3}$$

Where τ_o is the characteristic time of atomic vibration in a lattice growth, a_o corresponds to atomic jump length, V_1 and V_2 are the activation energies for the growth and decay mechanism respectively, q is the charge, V_{ox} is the voltage across the oxide layer and T_{ox} is the thickness of the oxide layer. k_B is the Boltzmann constant and T is the temperature. The value for a_o is considered 1.6Å which corresponds to the ionic radius of the hafnium[297]. And τ_o is 10^{-12}s which corresponds to the characteristic time of vibration of atomic network in a solid[298].

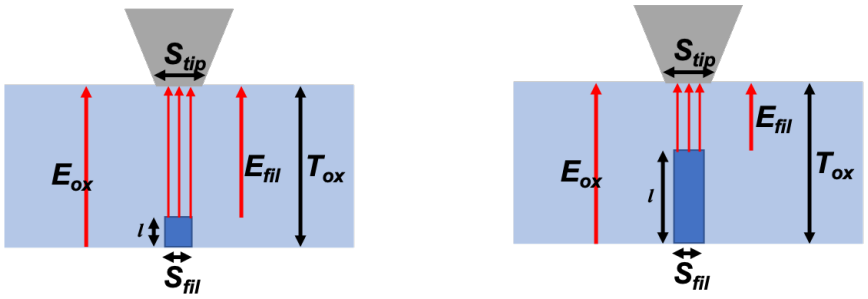

FIGURE 3.7: Filament growth inside oxide layer. The left figure is showing the filament in the beginning and right figure is showing the growth in the filament after reaching the compliance current.

By following the same approach as in reference[299], the overall current has two contributions: one between the filament and the AFM tip and another one through the whole oxide thickness between the AFM tip and the bottom electrode, which is negligible in our case. As it is sketched in figure 3.7, during the growth, the oxide thickness between AFM tip and filament is reduced, causing the increase in the electric field at the apex of the filament $E_{ox}(t)$, which can be described by:

$$E_{fil}(t) = \frac{V_{ox}}{T_{ox} - l(t, E)} \tag{3.4}$$

With

$$V_{ox} = V - V_d \tag{3.5}$$

Where V_d is the voltage applied by the external apparatus. As a result, the tunnel current from the filament increases as the electric field E_{fil} increases and the oxide thickness decreases. Thus, the filamentary current component increases with the growth of the filament. For the sake of simplicity, we will approximate the tunneling current in order to retrieve the Fowler-Nordheim tunneling when $V_{ox} > \phi_b$ (the

barrier height) and the direct tunneling when $V_{ox} < \phi_b$, where ϕ_b is the barrier height between filament and AFM tip. The tunnel current is given by (V>0):

$$I_t(V) = S_{fil}\frac{q^3}{8\pi h\phi_b}(E_{fil})^2 exp\Big[\frac{-8\pi\sqrt{2m_{eff}}\phi_b^{\frac{3}{2}}}{3qhE_{fil}}.\Big(1 - C(V_{ox})\Big(1 - \frac{qV_{ox}}{\phi_b}\Big)^{\frac{3}{2}}\Big)\Big] \quad (3.6)$$

Where E_{fil} is the electric field in between apex of the filament and the tip, $C(V_{ox})$ is a function which gives 1 when $qV_{ox} < \phi_b$ and zero otherwise, m_{eff} is the electron effective mass.

To take into account the external apparatus characteristic, one can consider that external apparatus is in series with the oxide sample and is behaving like a saturating transistor. This external apparatus is limiting the current. We propose to express this current (I_{lim}) in the external apparatus by:

$$I_{lim} = I_o tanh\Big(\frac{V_d}{V_{d0}}\Big) \quad (3.7)$$

Where I_o is the compliance current provided during experimental measurements. V_d is the voltage across the external apparatus and V_{d0} is the parameter to fit the curve to get I_{drain} vs V_{drain} transistor like characteristic as shown in figure 3.8.

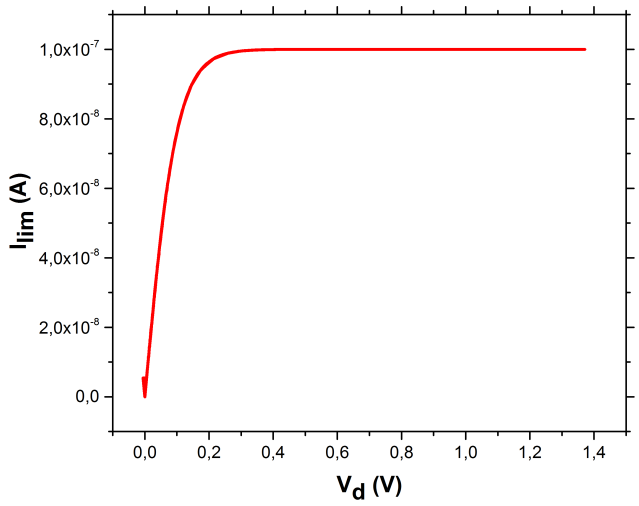

FIGURE 3.8: The characteristic of the external apparatus considered in equation 3.7.

As the external apparatus is in series with the tip and oxide sample, the current conservation reads,

$$I_{lim} = I_t \quad (3.8)$$

Thus, the voltage drop over the oxide V_{ox}, can be calculated by solving numerically

the following relation,

$$I_t(V_{ox}) = I_o tanh\Big(\frac{V - V_{ox}}{V_{d0}}\Big) \tag{3.9}$$

The numerical resolution of the equations 3.1, 3.5, 3.6 & 3.9 is self-consistent. Equation 3.6 allows to calculate the tunneling current and equation 3.1 allows to calculate the filament length inside the oxide layer. The parameter values used to model are given in table 3.2.

Symbol	Quantity	Values
T_{ox}	Oxide thickness	5 nm
τ_o	Characteristic time	10^{-12}s
ϕ_b	Barrier height	2.6/2.0 eV
a_0	Atomic radius	1 Å
l	Electron mean free path	12.5 nm
V_1	Energy well of position 1	1.025 eV (For 100nA- 275nA compliance current) & 0.95 eV For 300nA - 500nA compliance current)
V_1	Energy well of position 2	1.15 eV for all the compliance current

TABLE 3.2: Different parameters used for simulation to design the model for low compliance current.

3.3.2 Discussion & Model Comparison with experiments

The I-V characteristic at low compliance in nA range has been shown in section 3.2.2. One can see that there was no memory effect observed at low compliance in nA.

In figure 3.9 the experimental results are plotted with the simulated data calculated by using the model described in the previous section. One can see that the simulated data fits well with the experimental data. The model assumptions, i.e. that at lower compliance current the filament is not completely grown and the current is due to tunneling between the tip and the filament through oxide layer seems likely.

As explained, HfO_2 involves the migration of ions and there is reduction of the filament when the polarization is reversed. We were not able to have the memory effect at lower compliance current (in nA range) because the filament was not completely formed.

The simulation fits account well for the effect of compliance on current voltage characteristics at low compliance. As can be seen in the figure 3.9, the experimental data is plotted with the fit obtained by using the model discussed earlier. As the voltage is applied to the sample the filament starts growing and reached the maximum length of 3.84 nm for 100nA current compliance. With increasing the current compliance, the filament length is also increased which will be discussed in next paragraph in detail. But still compliance current in nA range is not enough to have a completely grown filament. Simulated fits are calculated for two consecutive loops to see the effect on the filament length.

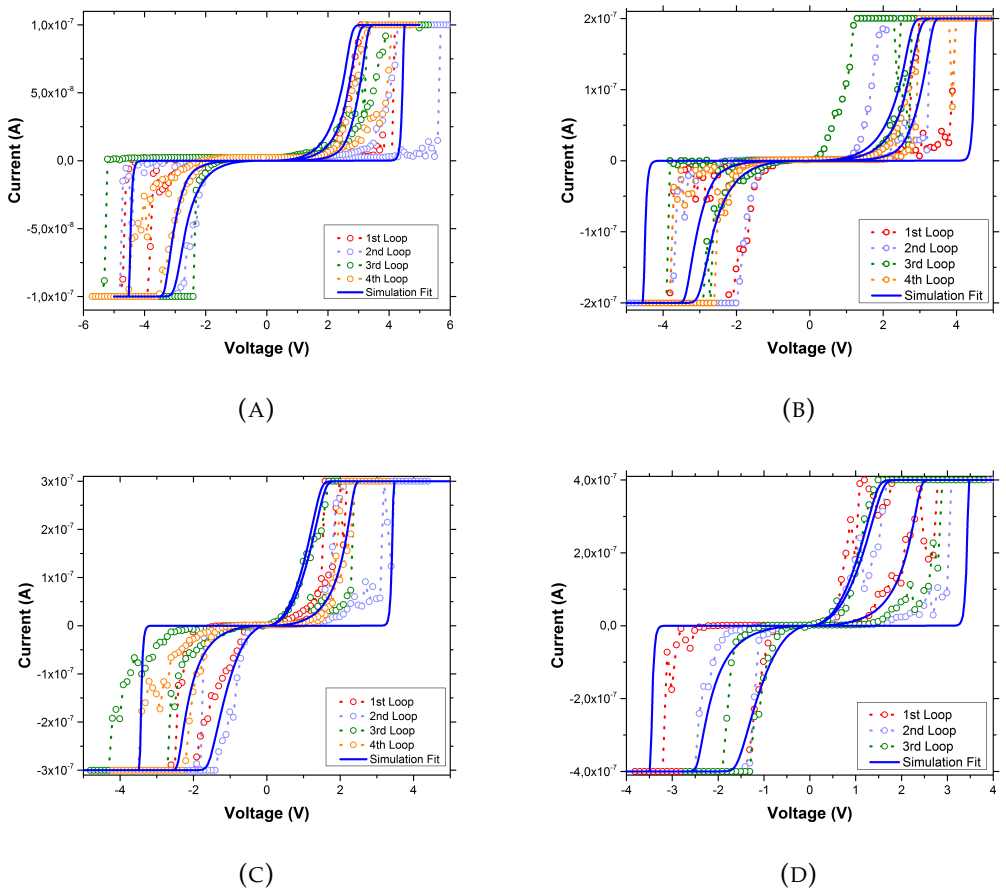

FIGURE 3.9: I-V characteristics at low compliance for TiNHfO2 sample with full diamond tip with simulated fits using the model designed for low compliance current (a) at 100nA, (b) at 200nA, (c) at 300nA and (d) at 400nA.

In figure 3.10, a detailed overview of filament growth with tip and voltage ramp is shown. The voltage ramp as a function of time can be seen in figure 3.10a. The filament length in the beginning is zero which means the voltage is not high enough to form a filament. After around 25s the filament starts growing, keeps growing until around 70s and its length stays the same till 100 s. When the voltage reaches its negative maximum, the filament decreases little bit. Here, filament growth is shown for two consecutive loops. Once the filament is formed, there is small variation of the length with the loop. In figure 3.10b, one can see that the filament length stays almost zero from 0 V to 2V for first loop and keeps increasing after 2 V until the voltage reaches the maximum voltage (5V) fixed for ramp. The filament keeps increasing even after reversing the ramp which means from +4V to +2V and stays the same from +2V to -4V. The filament starts decreasing after -4 V till it reaches the maximum limit (-5V) fixed for the voltage ramp. The filament keeps decreasing even after reversing the ramp from -5V to -4V and stays same till +2 V for the second loop. Same thing happens for the second loop for filament growth.

The filament growth was studied at different compliance currents as shown in figure 3.10c. The growth model for all the compliance currents is similar but the filament length is changing with the compliance current. Filament growth with respect to compliance current is plotted in figure 3.10d. It can be seen in the figure 3.10d that

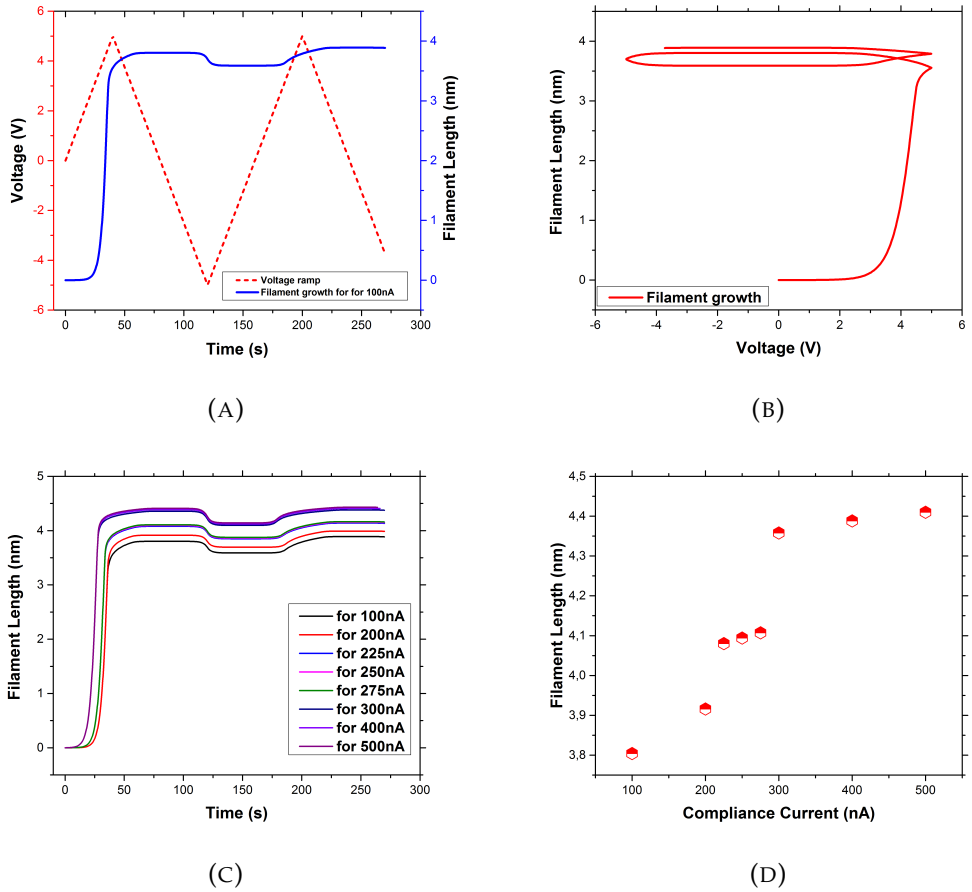

FIGURE 3.10: (a) Filament length evolution inside the oxide layer as a function of time. (b) Filament growth during voltage ramp. (c) Filament length evolution at different compliance currents and (d) Filament length at different compliance currents.

the filament length increases from 100 nA to 225 nA. From 225 nA to 275 nA, the filament length doesn't change much and increases slightly. Once the compliance current is changed from 275 nA to 300 nA, there is sudden increase in the filament length. And after 300 nA the filament length increases slightly and increases very slowly with a sigmoidal shape. This shape is due to the value of Vox that is limited by the effect of the current conservation (equation 3.9). When the filament length becomes as large as the oxide thickness one can consider that the capacitor is shunted which can be translated by a complete forming process.

3.4 From low compliance to high compliance (in μA range)

The memory effect was not observed at low compliance in nA range but at higher compliance current in μA range. As one can see in figure 3.11, both for high and low compliance current, I-V characteristics are plotted on the same log scale. The arrows and numbers in the figure are showing the direction of the ramp.

It can be clearly seen that for low compliance as the voltage ramp is applied in negative bias the current stays low till -2V and then starts increasing and reaches the compliance current. After it reaches the compliance current the ramp is reversed and

starts decreasing the applied voltage. The current stays in the range of compliance current and around 1V the current starts decreasing and returns back to almost zero around 0V. Once the polarity is reversed for the voltage ramp, the current stays low with increase in voltage, and starts increasing after 1V and reaches the compliance current around 3 V. After it reaches the compliance current, the ramp is reversed. The current stays constant with decreasing voltage until 1V and then it starts decreasing and goes to high resistance state around 0V. The same thing happens with the upcoming loops. This means there is no memory effect at lower compliance current.

But at high compliance current, shown in blue in figure 3.11, the current increases as the voltage increases and at around -2V it reaches the compliance current limit in order to SET the filament. Which means the high resistance state is switched to low resistance state. Once the ramp is applied in the opposite polarity the current still stays high and goes down after around 1.8 V switching the state from low resistance state to high resistance state by resetting the filament. Which shows a clear memory effect by setting and resetting the filament.

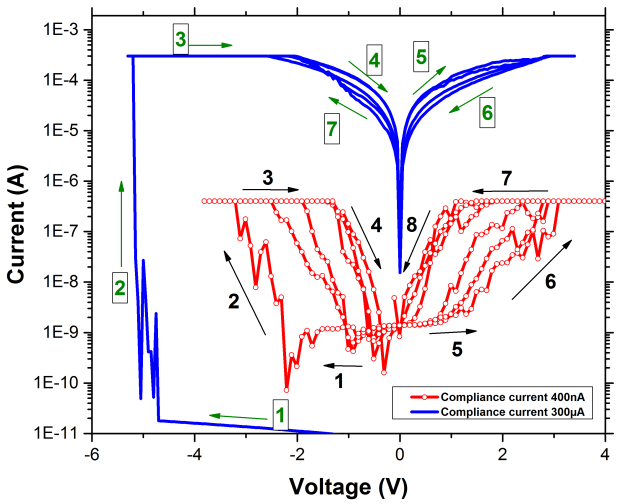

FIGURE 3.11: I-V characteristics at low compliance (in red) and at high compliance (in blue) for TiN/HfO_2 sample with full diamond tip in log scale.

According to the former paragraph interpretation at lower compliance current the filament is not completely formed so, when the voltage is decreased the filament also starts decreasing after some time because of this, the system returns to high resistance state.

But in case of high compliance, the filament is fully grown, which means bottom electrode is in contact with top electrode through filament. The driving mechanism at low compliance was the filament length as at high compliance it is the width of its cross section. This aspect will be treated in full details in the next chapter. However, one can roughly estimate the compliance current for which the transition occurs. Let's assume that the filament contains a region of narrowest section that limits the

current. In the nanometric range the conductance can be expressed via the Sharvin resistance whose expression is

$$G_{on} = \frac{2q^2}{h}\frac{k_F^2 S_c}{4\pi} \tag{3.10}$$

In equation 3.10 q is the absolute value of the electron charge, h the Plank constant, k_F the Fermi wave vector for the filament (one assumes Titanium filament as it will be discussed in the next chapter) and S_c is the area of the narrowest cross section of the filament. Now following the experimental linear relationship between the On-state conductance in the high compliance regime and the compliance current (see figure 3.6b) which reads:

$$G_{on} = V_c^{-1} I_c \tag{3.11}$$

With V_c = 0.35 V. From equation 3.10 and 3.11 one can obtain a linear relation between S_c and I_c:

$$S_C = V_c^{-1}\frac{2\pi h}{q^2 k_F^2} I_c \tag{3.12}$$

Since $k_F = 1.51810^{10} m^{-1}$ for Titanium, $S_c \sim 2 \times 10^{-15} I_c$. Assuming an atomic radius a_0 of 1.5 Å the number of atoms N in the narrowest part of the filament (for a circular cross section: $N = S_c/(\pi a_0^2)$) is $N \sim 2.85 \times 10^4 I_c$. Thus for 35$\mu$A one expects that S_c is reduced to the atomic size. At several hundred of nA the contention area is empty which means S_c is zero and the filament is not complete. For the low compliance experimental conditions of the former part, S_c is empty and the filament cross section area cannot account for the observed phenomenon consistently with the model of section 3.3.

3.5 Conclusion

In this chapter, C-AFM is used to characterize HfO_2 samples for OxRAM to study the resistive switching behavior. First of all, a preliminary study was performed to determine if the switching behavior is bipolar, unipolar or non-polar. It was found that the sample with TiN bottom electrode is showing bipolar resistive switching behavior and the sample with TiN/Ti bottom electrode is showing non-polar one. Different tip materials were used to see the impact on switching behavior and values for SET and RESET voltage as well as other parameters were determined.

After studying the switching behavior for different samples, a study of resistive switching at low compliance current in the range of nA was performed. I-V characteristics for both samples from 100nA to 400nA were performed by using boron doped full diamond tips as top electrode. It was found that in this compliance current range, the HfO_2 samples were not showing any memory effect. By comparing the experimental results with a model, it was found that at the low compliance current it was not possible to form a fully-grown filament, so the current was due to tunneling only.

To see the filament growth, the I-V characteristics were also performed at higher compliance current in the range of μA. Both samples were showing the memory effect. Even though at lower range in μA till 475μA for TiN/HfO_2 and 430μA for $TiN/Ti/HfO_2$ the On-state characteristics were not linear showing that the current is still due to tunneling. After forming with this threshold compliance, the on state current was linear, which means that the filament is completely grown and connecting both electrodes. A detailed study at high compliance current in the range of μA will be presented in chapter 4 for both HfO_2 based OxRAM samples.

Chapter 4

High Compliance Effect on Switching in OXRAM

4.1 Introduction

Recently the electric-field controlled resistive switching (RS) phenomenon in metal oxides has drawn tremendous attention for the development of next generation low power, high speed, high density and nonvolatile resistive random-access memory (RRAM) devices[175;300;301]. Resistive nonvolatile memory has been widely investigated recently due the scaling limitation of conventional flash technology for memory[302;303]. The resistive RAM are generally attributed to the formation and rupture of filament to change the resistance state. To increase the ratio of high resistance state and low resistance state is one of the challenges for the RRAM devices. It is reported in literature that the resistance state of RRAM devices are dependent on the current compliance[302;304]. During the forming the filament and during the measurements, a compliance current is required in order not to damage the devices. Larger compliance current gives rise to the possibility of permanent breakdown. The effect of a set compliance current on the resistance values of two states and their ration should be considered to further improvement of RRAM performance.

In the last chapter different studies were done to understand the switching mechanism. Studies at lower and higher compliance current were performed. It was found that at low compliance in the range on nA there was no memory effect. In the range of μA range the samples start showing the memory effect but still the filament was not completely formed until the compliance current reaches $300\mu A$ in the case of $TiN/Ti/HfO_2$ and $475\mu A$ in the case of TiN/HfO_2.

Many studies were done in literature at higher compliance current. However, no discussion about different AFM tip materials and the effect of polarity were found in the literature to our knowledge. So in this chapter, we will study the impact of the AFM tip nature and size, bottom electrode material and polarity of applied voltage on the switching characteristic as well the effect of compliance current ($600\mu A$) on ON state conductance. Moreover, a comparison with the 1T1R device will be discussed. In this chapter, we will describe the aforementioned experimental conditions in order to provide new insight in the resistive switching mechanism. The experimental data set will be discussed in detail using an existing model. Finally, we will give an interpretation and discuss the nature of resistive switching and the validity of above-mentioned ionic mechanism. Two different sample $Si-sub/TiN(20nm)/HfO_2(5nm)$ and$Si-sub/TiN(20nm)/Ti(10nm)/HfO_2(5nm)$ will be discussed to study the switching in OxRAM.

4.2 Experimental Observations

4.2.1 Effect of AFM tips

AFM Probe material effect

As discussed before, all the samples are without top electrode, so our AFM tips were used as a top electrode in MIM structure for OxRAM. Different tip materials had to tested in order to have similar conditions compared to metallic electrode electrical conductivity and thermal stability. Different AFM tips like PtSi coated, Pt coated, diamond coated and full diamond with boron doped will be used. Pt coated and diamond coated tips were not able to withstand currents in the range of mA and also the durability (after 10-15 loops in single measurement the coating was not there anymore) was not good. Furthermore, the tip resistance of Pt coated and diamond coated tips were in the order of several hundred $k\Omega$ as discussed in chapter 2, which was too high for our measurements. All these disadvantages led us to use full diamond and PtSi coated Si tips which have lower tip resistance in order to match the resistance of the metallic top electrode used in real devices.

The tip resistance of PtSi tip was in the order of 1-5 $k\Omega$, which was the best among the ones with Si bulk. Also, this tip was able to withstand currents in the mA range, but its durability was not good. After 3-4 measurements on the OxRAM sample the PtSi material went away, leading to contact between the Si bulk of the tip and the sample. Once the bulk Si of the tip comes to contact with the sample, the I-V characteristics became different because the work function and electrical conductivity of Si are different than the ones of the PtSi coating. To overcome these problems a new boron doped full diamond tip developed by IMEC[305;306] was studied. The tip resistance of this tip on HOPG was measured from around 500Ω to 1$k\Omega$, which corresponds to a resistivity similar to metal. As this tip is a full diamond one doped with high boron concentration to make it conductive, the durability is longer. It can withstand high current density without melting because of high thermal stability for diamond. According to these observations, PtSi and Full diamond tips were used to measure the switching behavior on HfO_2 OxRAM sample.

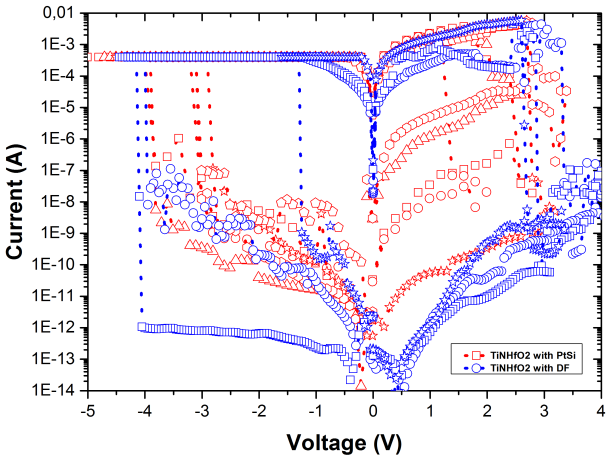

FIGURE 4.1: I-V characteristics for TiN/HfO_2 sample with sharp AFM tips (boron doped full diamond (in red) and PtSi (in blue))

In our setup we apply the voltage on the sample with grounded tip, which is different from studies in the literature. In literature, the voltage is applied to the top electrode in most cases which is difficult in our case due to complexity of the setup. So, in this work the voltage will always be applied to bottom electrode. For the sake of comparison with the most of the published results, we will apply negative voltage to SET, which would correspond to positive voltage on the tip with sample grounded, and the positive voltage on the sample to RESET which would correspond to negative voltage on the tip with sample grounded.

So, in our study the SET will occur for negative bias and RESET will occur for positive bias. To do the I-V measurement on HfO_2 sample we first apply a negative voltage ramp which means negative on the sample and positive on the tip to form the filament inside the oxide layer. The forming voltage was varying between $4.5V$ and $5.5V$. After the filament formation is done the positive ramp for RESET is applied which means positive on the sample and negative on the tip. Again, applying the negative ramp, we can SET the filament. The switching was observed by using both tips. All the electrical measurements are done by using a LabView program designed for these studies by using a Keithley 6430 sub-femtoampere source meter. Also, the overall I-V characteristics are similar for both tips as shown in figure 4.1. So, there is no prominent difference on switching characteristic for OxRAM with different tip material.

When the tips were new, the I-V characteristic reproducibility was poor, maybe because the tip was slightly shifting. The memory window which is large for the first cycle (On state/Off state ratio about 10^5) tends to decrease from cycle to cycle mainly because of an increase in HRS current. The On-state conductance and Off state conductance is almost similar for both tip states.

AFM tip size effect

In last section the I-V measurements were done by using two different types of tip (PtSi & Full Diamond). All the measurements were done when the tips were sharp. After doing measurement with sharp tip the measurement with blunt tips were also studied to see the effect on switching, which will be discussed in this section. The main motivation behind using the blunt AFM tip is to enlarge the apex and mimic the top electrode dimension as for devices which was first presented by Hou et al.(9) as discussed in CHAPTER 1. The AFM tips (Mainly Full diamond tips) were blunted by scanning them on the HfO_2 sample with higher contact force (100-150 nN) for 30 min to 1 hour on an area of $1\mu m^2$.

But in the case of PtSi tips, only measurements with a sharp tip were done because it was impossible to blunt the tip without removing the PtSi coating, leading to nonlinear I-V behavior on Highly Oriented Pyrolytic Graphite (HOPG). We have seen that there is no effect of the tip material on I-V characteristics when the tips were sharp. The I-V characteristics for different tips on the HOPG sample are presented in figure 4.2. Here, I-V characteristics are shown only for positive bias, but the same characteristics were found also for the negative bias. The resistance of the full diamond and PtSi sharp tip is almost the same, around 250Ω. To obtain the I-V characteristics of the AFM tip on HOPG, the maximum voltage was fixed to $2V$ in order to avoid tip destruction by Joule heating because the high conductivity leads to $8mA$ at $2V$.

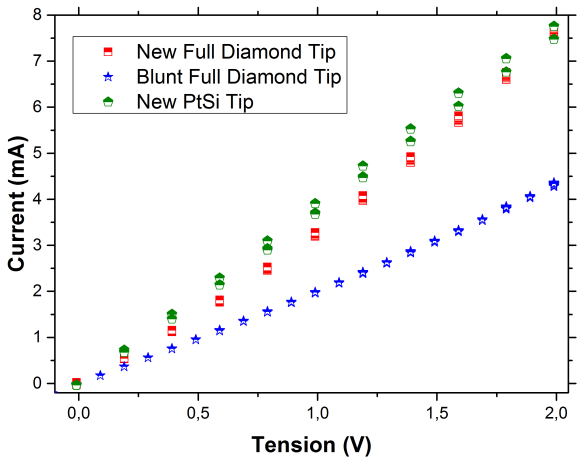

FIGURE 4.2: I-V characteristic for AFM tips on HOPG sample before and after blunting it on HfO_2 sample.

Even after making many measurements with the full diamond tip, its resistance did not change significantly. The resistance is higher for the blunt tip in figure 4.2 compared to the sharp tip because I-V characteristics were not obtained by the same full diamond tip. For different full diamond tips, resistance can vary in the range of few hundred ohms. It is almost the same as the one for the sharp tip.

By comparison, we found that the tip conductance is higher than the On state conductance of the HfO_2 layer. As it can be seen that the I-V characteristic reproducibility was poor when the tips were sharp, maybe because the tip was slightly shifting. But after blunting the full diamond tip, as it is shown in figure 4.3, the I-V switching characteristics were reproducible and SET voltage was also lower ($1.5V$) compared to the sharp tip ($2.8V$) but still higher compared to devices[143].

Same measurement procedure was adopted to the measurement with blunt tip. A negative ramp voltage is first applied on the bottom electrode in order to achieve the forming process. After forming the filament, a voltage ramp is applied towards the opposite polarity, (positive bias) on the bottom electrode to RESET the filament to return back to the high resistance state (HRS). After the RESET process, again negative bias is applied on the bottom electrode to SET the filament in order to get the low resistance state (LRS).

In figure 4.3a, the forming, RESET and SET for TiN/HfO_2 are shown as explained above. Arrows in figure 4.3a are showing the voltage ramp direction. For the first few cycles, the off state was varying little bit in the case of the blunt tip and getting constant with cycling. After few cycles, let us say, around 20 cycles, the off state was almost similar for every cycle, and this means that the tip is conditioning itself with cycles. However, the memory window is smaller compared to the sharp tip mainly because the Off-state current is much higher. The Off state current decreases with increasing voltage for voltages above $2V$ (Figure 4.3b), and the possible reason will be given in Sec. 4.4.

In figure 4.3c SET and RESET characteristic for $TiN/Ti/HfO_2$ are given. To get the characteristic shown in figure 4.3c, the forming step was done by using voltage

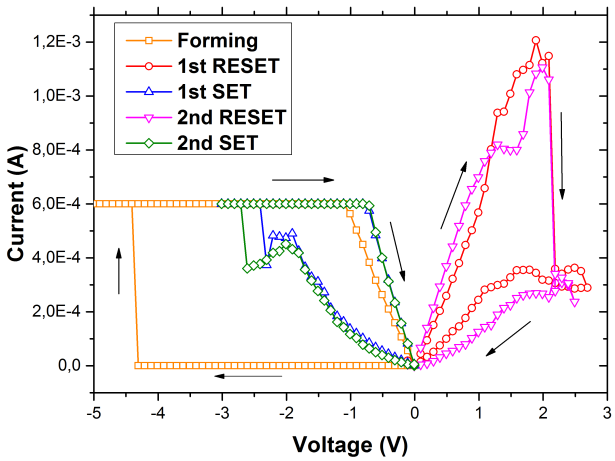

(A)

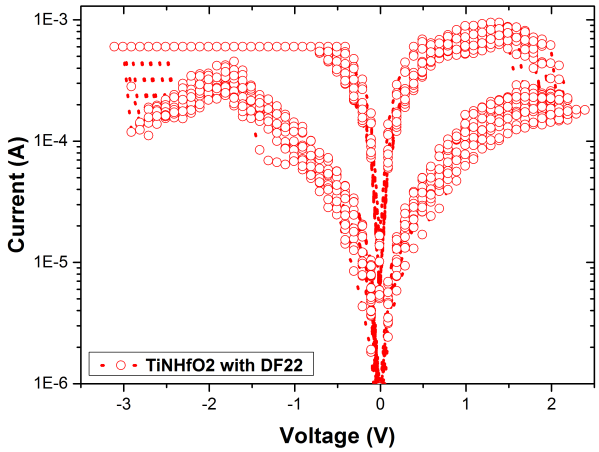

(B)

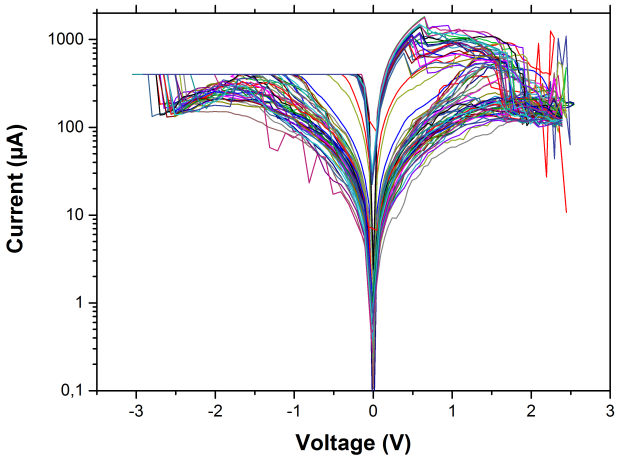

(C)

FIGURE 4.3: (a) Forming, SET and RESET steps on TiN/HfO_2 sample with blunt full diamond tip, (b) I-V characteristics with blunt full diamond AFM tip. Experimental data is the superposition of many loops, (c) I-V characteristics with blunt full diamond AFM tip for $TiN/Ti/HfO_2$ after forming the filament by using pulses.

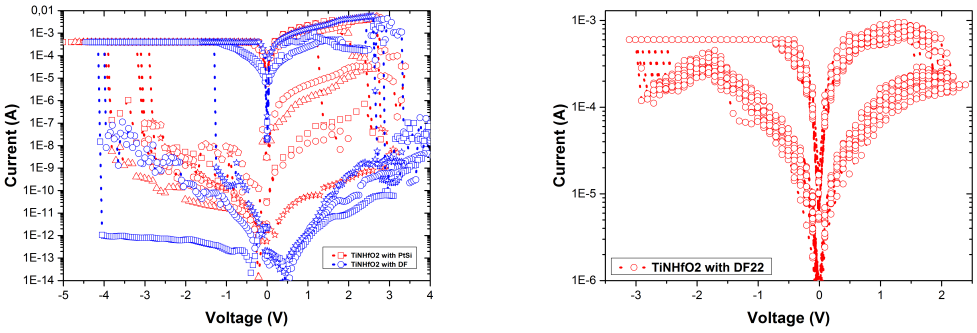

(A) (B)

FIGURE 4.4: I-V characteristics for TiN/HfO_2 sample with (a) sharp AFM tips, (b) blunt tip.

pulses. A pulse with a duration of $1\mu s$ and an amplitude of $5V$ was used to form the filament inside the oxide layer. The pulse count was 13. After forming the filament, normal voltage ramp was used to SET and RESET the filament by using Keithley. In figure 4.3c, more than 20 loops for SET and RESET are shown. The characteristics were the same as the one obtained after forming a filament by using voltage ramp. The SET and RESET voltages were also in the same order of range.

The difference in the I-V characteristics with sharp tips (PtSi coated and boron doped full diamond) and with blunt tip can be clearly seen in the figure 4.4. The memory window difference can also be seen. Also, the difference in SET and RESET voltage is clearly visible in the figure 4.4.

4.2.2 SEM-EDX Study

Before and after doing electrical measurement, topographical study was also done for each sample. Before doing the electrical measurement, we have to scan the sample on the area of $1 \times 1\mu m^2$ area to find the good place to do the measurements.

After installing the sample inside the ultra-high vacuum chamber, the tip and sample are transferred to the sample and tip stage of the AFM which also inside the ultra-high vacuum chamber. Once the tip and sample are installed the sample is approached manually by using remote control towards the tip to make the contact between tip and sample. Once the sample is in vicinity of the tip an automatic approach is used in order not to break the AFM tip by putting so much pressure on cantilever. After making the contact between sample and tip force curve is obtained to know if the contact force applied on the tip is enough to have good contact. After these steps a scan over the sample in contact mode is performed. The same scan is done 3-4 times to stabilize the tip over the sample surface and topographical images are recorded.

Electrical measurements were recorded for samples by using LabView program. The topography image before doing the electrical measurement is taken and it shows a very flat surface. Once the electrical measurements are done, one more topographical image was taken and hillock formation on the surface of the HfO_2 sample has been observed. The topographical images are shown in figure 4.5. The size of the

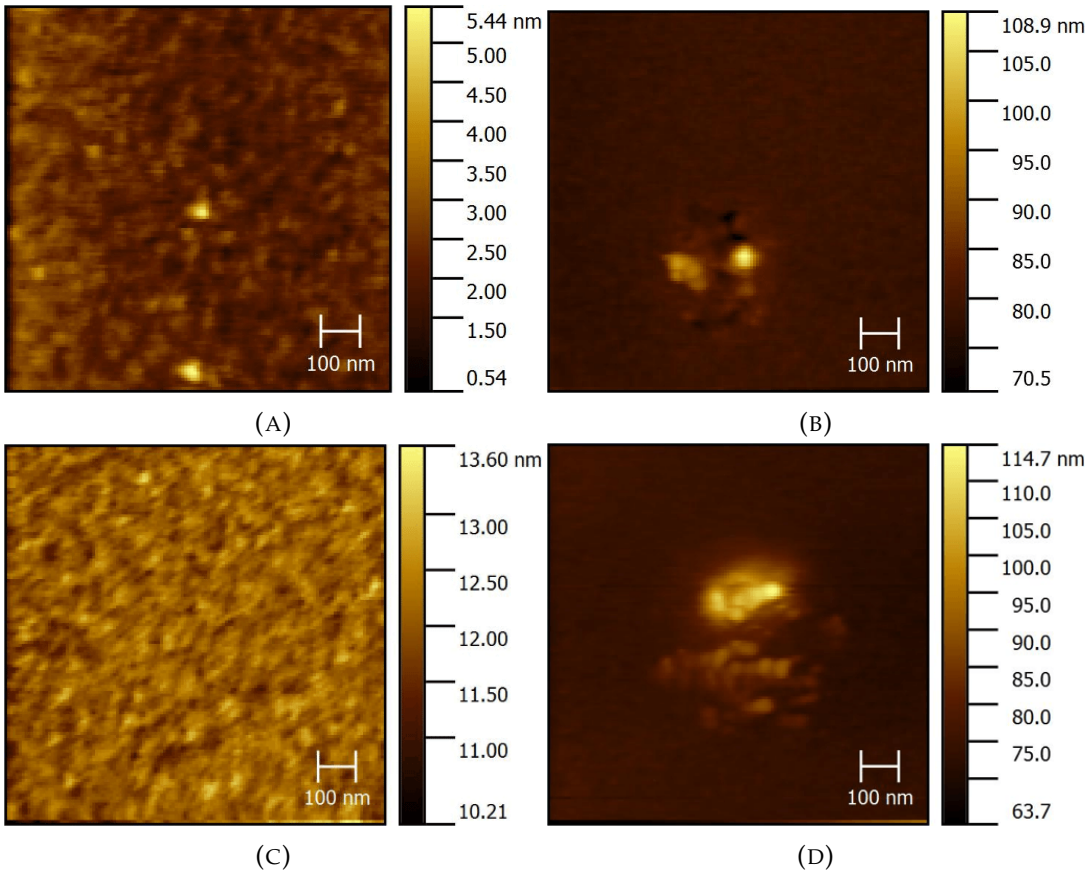

FIGURE 4.5: Topographical AFM images of HfO_2 surface (a) before I-V measurement with sharp tip, (b) after I-V measurement with sharp tip, (c) before I-V measurement with blunt tip & (d) after I-V measurements with blunt tip. A hillock like structure was detected after the I-V measurement.

hillock is around 30–50 *nm* as seen in figure 4.5b, but in the case of the blunt tip, it appears larger [Figure 4.5d]. Since the blunt tip is larger in diameter, the hillock width appears larger too. According to figures 4.5b and 4.5d, the hillock height is of the same size for both blunt tip and sharp tip cases. Thus, we can speculate that the hillock size does not depend too much on the tip apex area. This hillock like structure appears just after the filament formation. SET and RESET processes have no further impact on the hillock structure. Even after doing 80-100 loops for SET and RESET, there is no impact on hillock size.

The hillock formation was also studied with different compliance currents. Different compliance currents were fixed for filament formation and then, topographical images were taken for every current value. But we did not observe any impact of compliance current on the hillock structure.

In order to know the chemical composition of the hillock either one can use SEM EDX or TEM on the sample. But using SEM EDX on the sample maybe ineffective because of charge accumulation on the insulating HfO_2 layer. TEM analysis can only be performed after a long sample preparation procedure, but we tried it nevertheless. The results will be discussed in section 4.2.3.

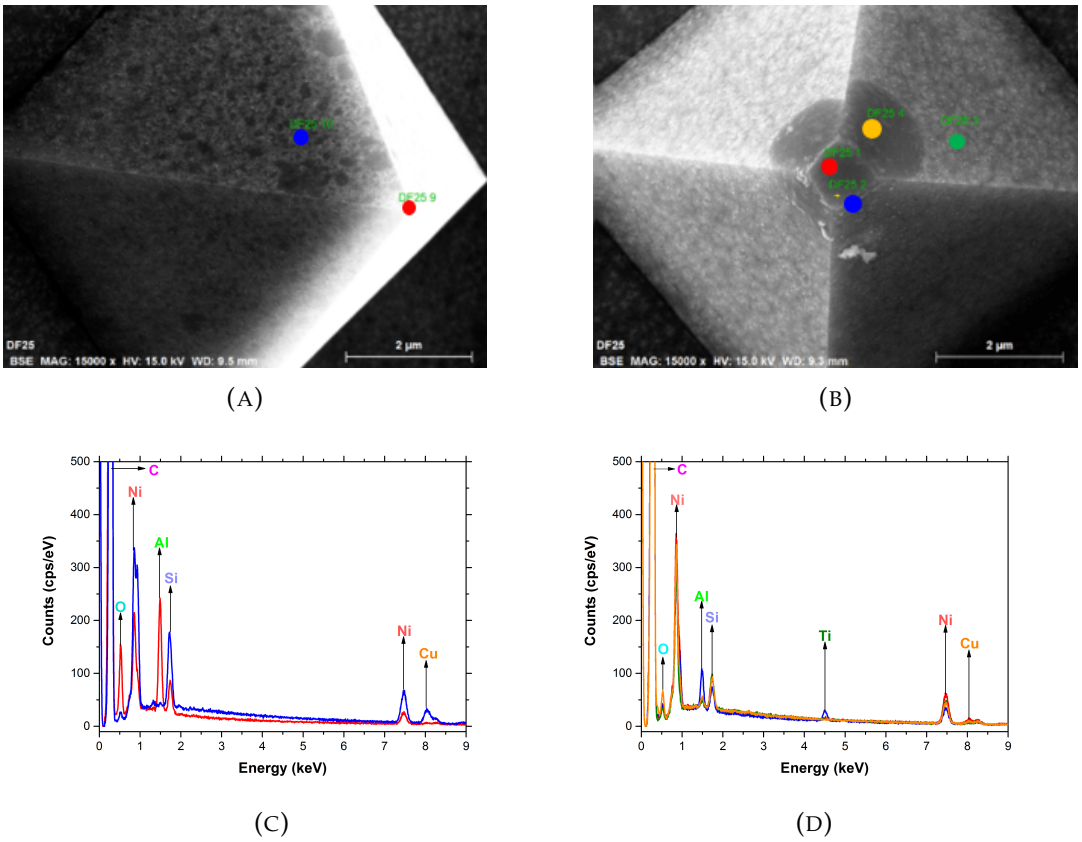

FIGURE 4.6: (a) & (b) SEM Images of sharp and used blunt full diamond tip, (c) & (d) EDX analysis of full diamond tip before and after electrical measurements on HfO_2 sample. The scan was done at two positions for the sharp tip before the electrical measurements as shown in the image by red and blue dots corresponding to the color in graph (c), and in the case of the blunt tip after the electrical measurements, the scan was performed at four different (red, blue, orange and green) positions corresponding to the color shown in graph (d)

However, one can obtain the chemical information using SEM EDX measurements on our AFM tips before and after electrical stresses.

SEM-EDX analysis of each tip was performed before and after the electrical measurement in order to know the chemical composition of the AFM tips. SEM-EDX spectra was obtained on a boron doped full diamond tip are shown in figure 4.6. As one can see in the graph that for the sharp unused tip, only Carbon, Oxygen, Nickel, and Silicon were found. Nickel is present because the cantilever of the AFM tip is composed of Ni. Also, some traces of Cu and Al were found. This is because of the sample stage which is used to hold the tips and SEM-EDX instrument.

But in figures 4.6b and 4.6d, which correspond to the tip used for the electrical measurement on the HfO_2 sample, some traces of Ti were found. Spectra at different positions of the tip were obtained, on the area which was in contact with sample and away from it. So, the green and yellow dots in figure 4.6b show the places far from the area which was in contact with sample like red and blue dots.

The spectra taken at the places which were in contact with sample show the presence of Ti and the places far away show no presence of Ti. In our overall structure

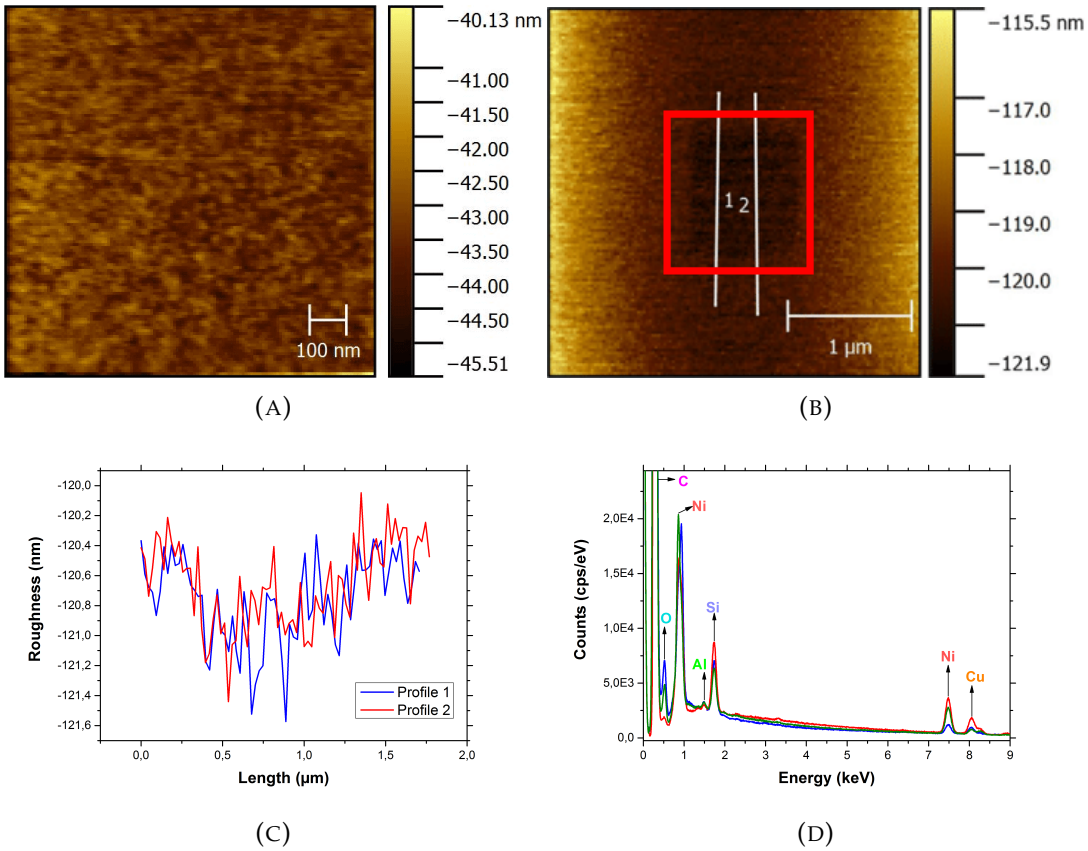

FIGURE 4.7: (a) Topographical AFM images of HfO_2 surface with new tip before blunting (b) Topographical AFM images of HfO_2 surface with blunt tip around the area where tip was blunted. The area where the tips was blunted is shown inside red rectangle and two white lines represent the profile taken to measure the roughness, (c) Roughness profiles over the surface where tip was blunted as shown in fig (b) by line 1 & 2, (d) SEM EDX measurement of full diamond tip, which was blunted on the $HfO-2$

Ti is only present in the bottom electrode which is composed of TiN as discussed in introduction part. Nowhere else in whole system Ti was present, it means that Ti is coming from the bottom electrode in some way. Thus, we can assume that Ti migrated through the HfO_2 layer from the TiN bottom electrode during electrical measurements.

Another study was done to confirm that presence of Ti on the tip is due to electrical measurements and not due to blunting. To be sure that Ti is not coming from anywhere else from the surface or because of some contamination at the HfO_2 surface, the new full diamond tip was blunted on HfO_2 surface without doing any electrical characterization. In order to see that tip is not scratching the HfO_2 layer and getting into contact with TiN after it was scanned over the surface for 90 minutes to blunt it at higher contact force (250 nN) compared to the contact force usually used for blunting.

In figure 4.7a we can see the topography image of the sample for an area $1 \times 1\mu m^2$ with new sharp full diamond AFM tip and this area was scanned for 90 minutes with 250 nN contact force. The topography image of the area where the tip was

scanned for long time was taken in bigger frame ($3 \times 3\mu m^2$) to see if the surface was scratched or not as shown in figure 4.7b. In figure 4.7c one can see a dark rectangle, which is the area where the tip was blunted. It seems that it got scratched but when two topographical profile were taken across the area, there was no difference in the roughness where the tip was blunted and the area where the tip was not blunted. As can be seen in figure 4.7c two profile for roughness are plotted and the roughness is constant over the surface. It means that there was no scratching in the HfO_2 layer.

After blunting the tip SEM-EDX measurements were performed to see the presence of Ti on the tip because of blunting the tip on HfO_2 surface or because of some contamination. As can be seen in the SEM-EDX spectra taken after blunting the tip in figure 4.7d, there is no peak recorded for Ti. The spectra after blunting is exactly the same as we obtained for the new unused tip (figure 4.6a). This proves that the Ti on the used tip (SEM-EDX spectra in figure 4.6 4.6d) is only coming after electrical characterization. It is not coming during the process of blunting or because of contamination.

4.2.3 TEM Analysis of Hillocks on TiN/HfO_2 surface

As already discussed about hillocks in previous section, it is really important to know the composition of hillocks. To understand the hillock appearance after forming the filament, TEM studies were performed. Although it is very difficult to make TEM studies to see the filament. There were many problems to solve to do TEM analysis. First of all, it is too difficult to find the exact localization of the hillock on the surface of HfO_2 as the sample is $1 \times 1cm^2$ and it is difficult to locate 50 nm size hillock.

With our setup it is not possible to have the top view of the sample because of the lack of cameras inside ultra-high vacuum chamber. We can only have the side view of the sample with the help of camera installed outside ultra-high chamber. This is why we used another AFM setup (Veeco AFM setup) with the same full diamond installed in primary vacuum.

As schematized in figure 4.8a the sample is glued on the sample holder and area on sample is marked with the help of marker. In second step, in selected area a matrix of 10×10 filaments was created, it means that there is an array of 10×10 hillocks. The filament formation was done by fixing the compliance current to 1 mA. After making the array of hillocks, sample was scratched at four places around the array. These scratch marks of $10 \times 10\mu m^2$ were done 40 μ m far away from the array. These scratch marks were done to easily find the array in the SEM to prepare the lamella for TEM.

We can see the array in the image taken by SEM in figure 4.8b. After locating the array, a lamella was prepared by using SEM-FIB. First carbon was deposited over two rows of the hillock and then platinum is deposited. After deposition the rest was etched and finally a lamella was prepared. There were many steps to form the lamella, the final lamella is shown in figure 4.8c.

After the lamella was prepared, it was transferred to TEM for analysis. A TEM image of the whole hillocks area is shown in figure 4.9a. In figure 4.9b, a zoom view of the single hillock is shown. One can see all the different layers (Si, TiN, HfO_2, and C). In the red circle in figure 4.9b one can see the rupture in HfO_2 layer. Here

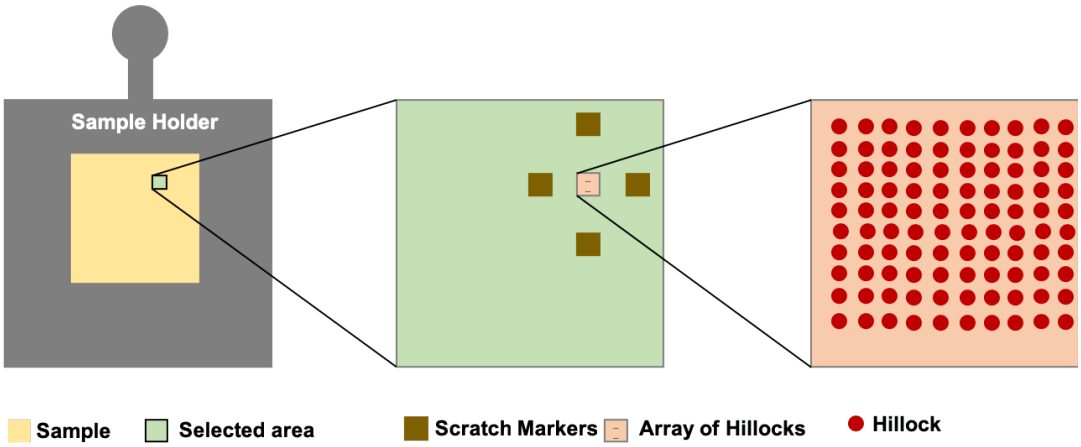

(A)

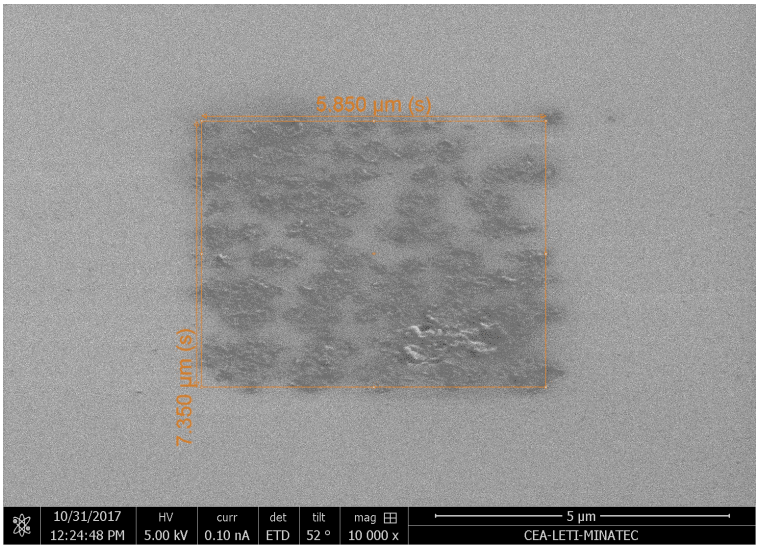

(B)

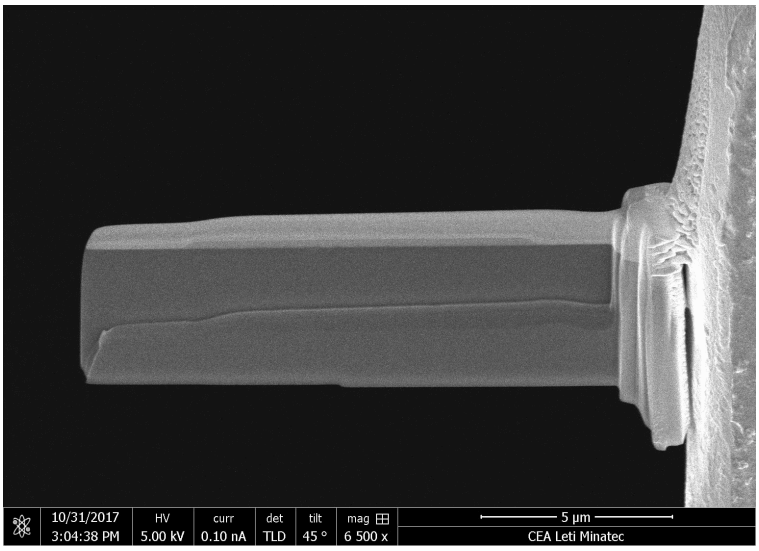

(C)

FIGURE 4.8: (a) Schematic representation of the array formation and its localization on TiN/HfO_2 sample by using AFM, (b) SEM image of the area where an array of hillocks is formed by forming the filament in TiN/HfO_2 sample, (c) Lamella of the array of hillocks for TEM measurement prepared by FIB-SEM.

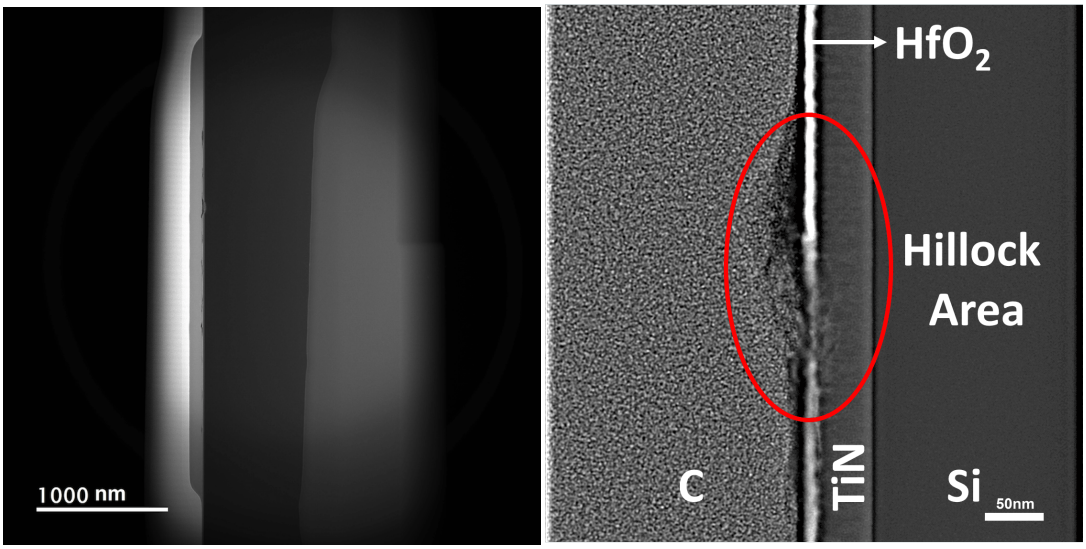

(A) (B)

FIGURE 4.9: (a) TEM image of the lamella, (b) TEM image of the hillock.

the HfO_2 layer is 5 nm and to form the filament $1mA$ compliance current was fixed. We think that because of such high current the HfO_2 layer got disrupted. Also, it is bit difficult to see the filament in 5 nm thick HfO2 layer. A detail study has to be done in future.

All the studies for TEM was done with the help of Tristan DEWOLF and G. AUDOIT. Tristan Dewolf studied switching in OxRAM in more detail by using TEM in his PhD in the same laboratory. He used C-AFM to form the filament and the prepared the lamella by using FIB and then transferred to TEM for analysis similar to us. He performed STEM- EELS measurement to know the composition of the filament. He observed that a *Ti*-rich region with a conical shape was clearly observed in the HfO_2 layer as shown in figure 4.10. This conical filament seems to connect the top and bottom electrode. With the help of STEM-EELS he showed the presence of different materials as shown in figure 4.11. So, from the studies done by Tristan DEWOLF it is clear that the filament is of *Ti*. We also took the same approach and considered the filament to be of *Ti*.

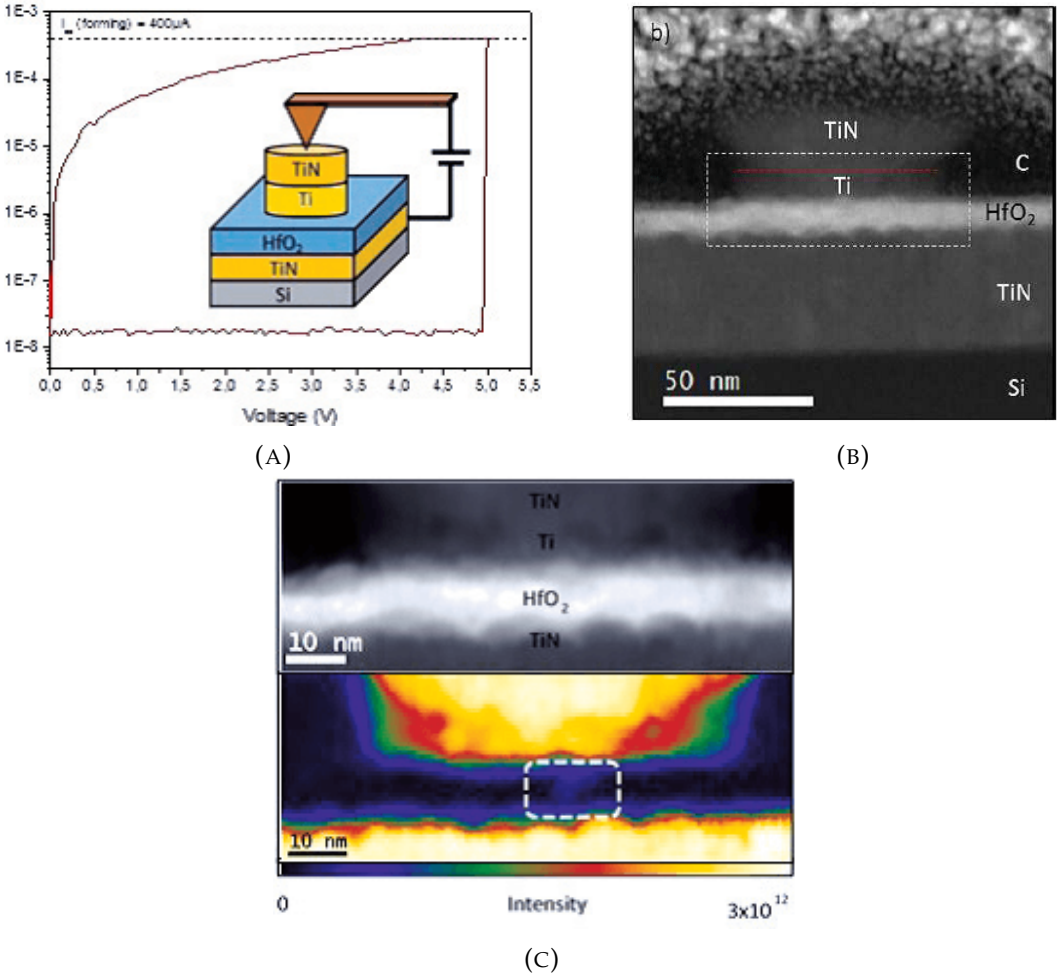

FIGURE 4.10: (a) Filament formation in HfO_2 based device by using C-AFM at 400 μA compliance current. (b) STEM image of the memory biased with C-AFM and (c) STEM-EELS map of extracted *Ti* signal after forming. *Ti* migration can be seen in blue in the area boxed with dashed line. The figure is taken from reference [307].

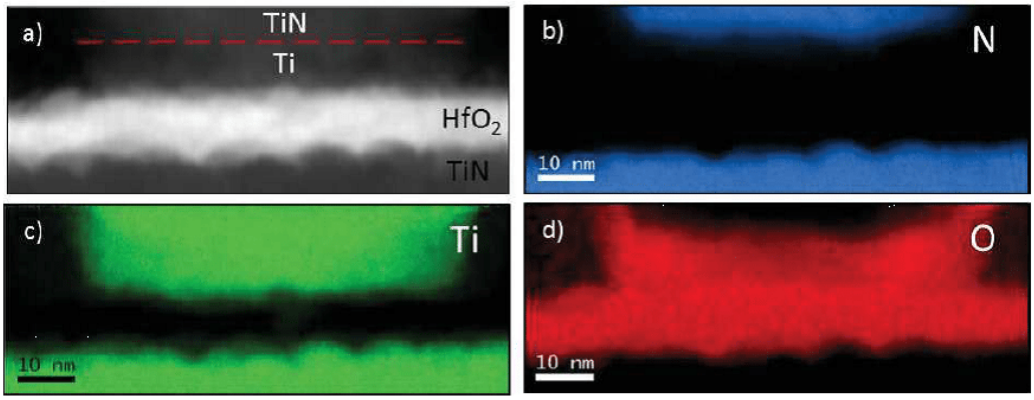

FIGURE 4.11: (a) STEM-HAADF image of the region where it is analyzed by EELS. STEM-EELS map of the polarized memory with a compliance current of 400 μA (b) for nitrogen, (c) for titanium (d) for oxygen. Small Ti migration can be seen in figure (c). The figure is taken from Tristan DEWOLF's PhD thesis [308].

4.2.4 Effect of bottom electrode

We have two different HfO_2 based oxide sample with two different bottom electrodes of Ti and TiN/Ti. The composition and thickness of the layers is given in section 4.1. I-V measurements were done on both samples by using the same AFM tip (blunt full diamond) as top electrode in secondary vacuum.

SET and RESET characteristics for both samples are shown in figure 4.12. The same steps for forming, SET, and RESET were performed as explained in section 4.2.1. For each measurement, 60-80 loops were performed at the same position. After 80 loops the tip sample contact was lost. One loop consists of one SET and one RESET characteristic. The compliance current for forming and SET was set to 600 μA in order to avoid overshoot and permanent breakdown. If we fix a higher compliance current in mA range it will be impossible to RESET the filament because of permanent breakdown.

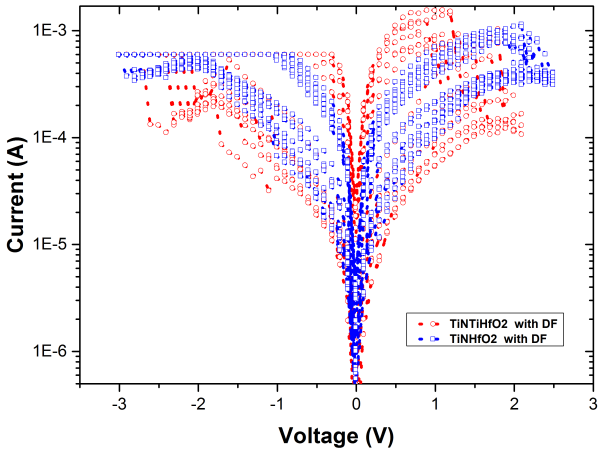

FIGURE 4.12: I-V characteristics and simulations for different bottom electrodes by using full diamond blunt tip as top electrode in both cases. Experimental data is the superposition of many (around 10) loops.

We observed that the memory window is larger with the TiN/Ti bottom electrode sample compared to the TiN bottom electrode sample. The ON state conductivity is higher, and off state conductivity is lower for the TiN/Ti bottom electrode. In figure 4.12, I-V characteristics after forming step with different bottom electrodes are shown. Around 10 loops per sample are shown in the figure.

4.2.5 G_{on} Variation with compliance

It is an established experiment fact that, on devices, the On-state conductance (G_{on}) increases with the compliance current. The dependence was also shown to be linear[309]. This dependence was explained by an effect of compliance current on the width of the filament and thus its electrical conductance. Here we will try to see if this effect of compliance current on the on-state conductance remains at a nanometric scale.

To see this effect the I-V characterization for each sample at different compliance currents was done. After doing the I-V characterization the mean value for On-state current conductance is calculated by averaging 20-30 loops. In particular, as it is shown in figure 4.13 (green stars), the variation of the ON state conductance (G_{on}) is proportional to the SET compliance current for devices[286].

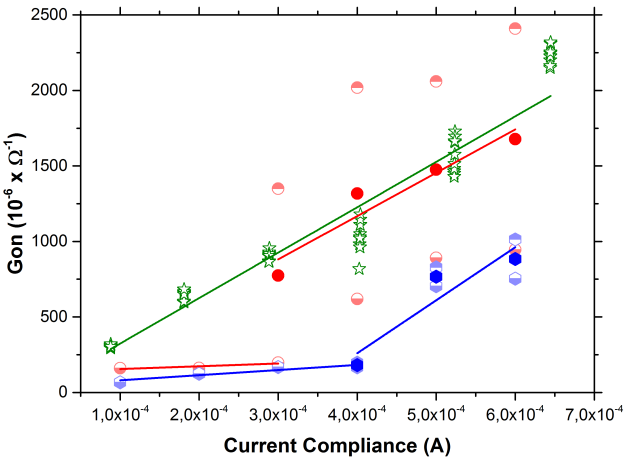

FIGURE 4.13: ON State conductivity (G_{on}) variation with different bottom electrodes at different compliance currents. (Red circle half down filled-Minimum value of G_{on} for $TiN/Ti/HfO_2$, Red circle half up filled-Maximum value of G_{on} for $TiN/Ti/HfO_2$, Red circle full filled -Mean value of G_{on} for $TiN/Ti/HfO_2$, Blue hexagonal half down filled -Minimum value of G_{on} for TiN/HfO_2, Blue hexagonal half up filled -Maximum value of G_{on} for TiN/HfO_2, Blue hexagonal full filled -Mean value of G_{on} for TiN/HfO_2, Green star unfilled-G_{on} for 1T1R device13) (The values of G_{on} for $TiN/Ti/HfO_2$ is in Red, the value of G_{on} for TiN/HfO_2 is in Blue and the values of G_{on} for 1T1R Devices are in Green

We have plotted characteristics obtained by an AFM blunt full diamond tip on the samples with different bottom electrodes. The highest and lowest value for On-state conductance are plotted in the graph for each compliance current for each sample. The compliance current range was 100–600 μA. In the case of the sample with TiN/Ti bottom electrode the linear behavior for On-state conductance with compliance current was obtained from 300 μA to 600 μA. Below 300 μA there is no increase in conductance current, this is may be because the compliance current was not high enough to form a complete filament.

We found that G_{on} is larger with TiN/Ti compared to the TiN bottom electrode and in the same order of magnitude as shown for devices in the literature. For the TiN/HfO_2 sample, we observed that below 475 μA compliance current (I_c), G_{on} does not increase linearly with I_c, and for higher compliance currents, G_{on} increases linearly with I_c. Also, with larger compliance current, the memory window is getting larger. We can see that the On-state conductivity for $TiN/Ti/HfO_2$ is almost the same as that for the 1T1R device, and for TiN/HfO_2, it is lower compared to that of the device. It appears that the linear relationship between the On-state conductance and the compliance current observed on devices remains basically at a nanometric

scale. The differences in figure 4.13 are explainable by tip position fluctuation and electrometer overshoot effect for the low compliance values.

4.2.6 Effect of Polarity

Polarity can play a very important role depending on the type of OxRAM (Unipolar or Bipolar). In Unipolar you can SET and RESET in the same polarity but for bipolar different polarity is used to RESET compared to the one used for SET. Here we already know that our samples have bipolar behavior so we are using different polarities for SET and RESET. The main aim here is to see the effect of polarity on SET and RESET if we change them. So, we want to see if the characteristic of the sample for SET obtained in positive bias will be similar to the characteristic obtained by doing SET in negative polarity. First of all, negative ramp voltage is applied on the bottom electrode to form a filament inside the oxide layer. After forming, opposite polarity (positive bias) is applied in order to RESET it. Again, the same polarity as we applied for the forming step is applied to SET, and many loops were recorded to study the distribution of SET and RESET voltages.

The same study was done for the opposite polarity. This time forming and SET are done with positive ramp voltage and RESET is performed in negative bias, and many loops were recorded. We performed the same experiment for both samples with different bottom electrodes by using the same blunt full diamond AFM tips as the top electrode. After doing all the measurements the characteristic for two different procedures were plotted on the same voltage scale to see the difference in I-V characteristic. As we can see in figure 4.14, there is no effect of polarity for both samples with different bottom electrodes. To see the effect of polarity on SET and RESET processes, all the curves are plotted on the same voltage scale as shown in figure 4.14c. The whole characteristic remains the same, no matter which polarity is used.

4.2.7 C-AFM experiments comparison with 1T1R Device

I-V characteristics for TiN/HfO_2 and $TiN/Ti/HfO_2$ samples taken by C-AFM are also compared with 1T1R device characteristics[310] in figures 4.15a and 4.15b, respectively. The On state and Off state currents and the memory window are in the same range of magnitude for the same compliance value in all cases. The On state current fluctuations are larger for CAFM measurements likely because of the better control of the compliance for 1T1R devices. It is worth noticing that the same current values for CAFM measurements and $1\mu m^2$ devices in figure 4.15 are consistent with a filamentary conduction mechanism. As we can see in the graph in figure 4.15 the voltage value for SET and RESET are larger than the values for device. For the device, SET and RESET voltages are around 0.8V, but for the TiN/HfO_2 sample, SET and RESET voltages are around $2V$–$2.8V$ and $1.5V$–$2V$, respectively. Those points will be discussed in section 4.3.2.

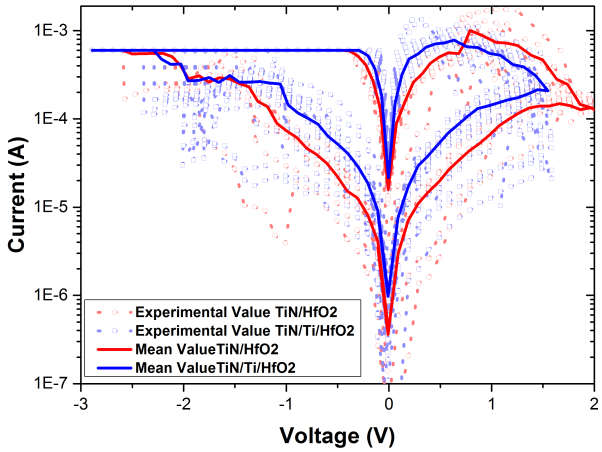

(A)

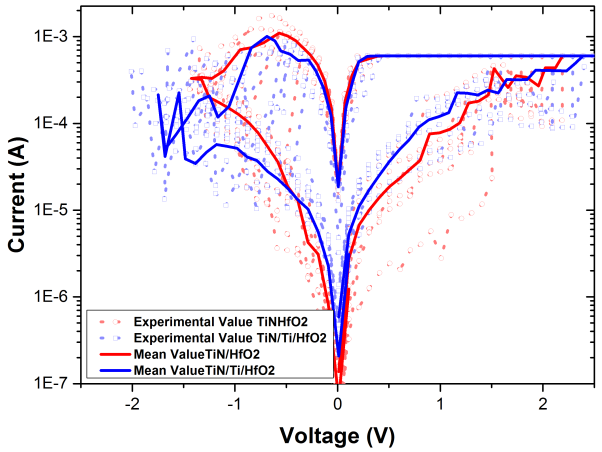

(B)

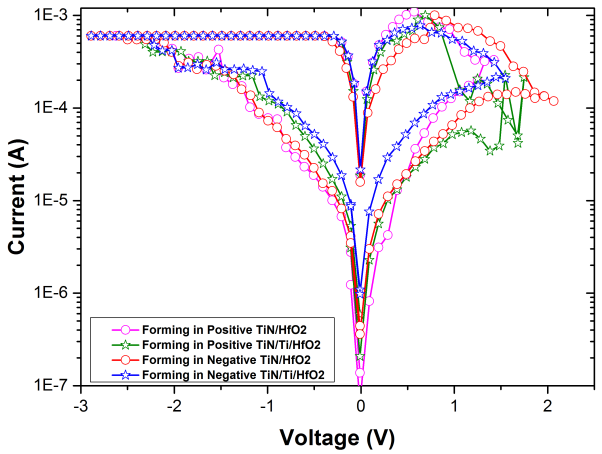

(C)

FIGURE 4.14: Polarity effect for different samples. (a) I-V characteristic with Forming and SET in negative bias and RESET in positive bias, (b) I-V characteristic with Forming and SET in positive bias and RESET in negative bias and (c) Both case (a) & (b) on same voltage. Experimental data is the superposition of many loops (10 loops)

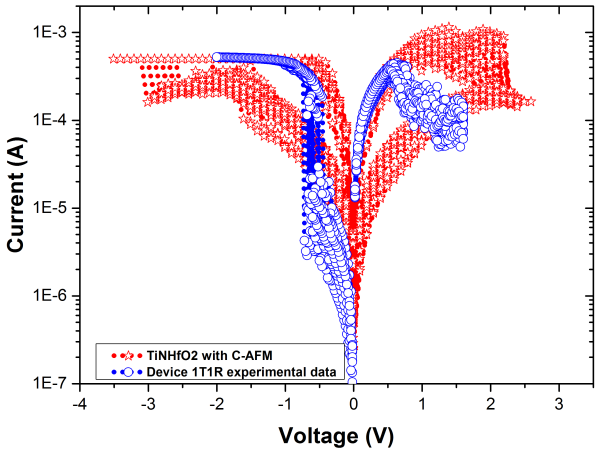

(A)

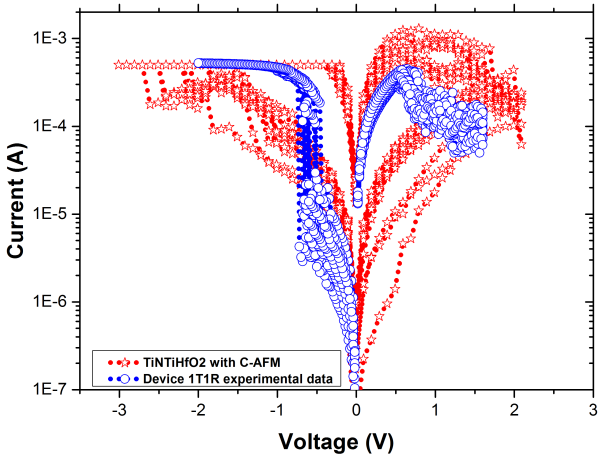

(B)

FIGURE 4.15: (a) AFM I-V characteristic comparison with 1T1R device characteristic for TiN/HfO_2 (b) Comparison of C-AFM and 1T1R device I-V characteristic obtained on $TiN/Ti/HfO_2$ sample. Experimental data is the superposition of many (around 10) loops.

4.2.8 Effect of Series Resistance on switching behavior

We did some measurements by putting a series resistance of 1.1 $k\Omega$ (we wanted to fix 1 $k\Omega$ but when the resistance measured with multimeter, it showed 1.1 $k\Omega$) in order to limit the current overshoot during the forming step. We used the same ramp steps as explained in previous sections. The compliance current was set to 600 μA for this experiment. First of all, the measurements with series resistance were done with $TiNHfO_2$ sample. In figure 4.16a, I-V characteristics with series resistance of 1.1 $k\Omega$ in green are shown. Only SET and RESET are shown in the figure. As we can see in the figure 4.16a that the memory window is very small for SET and RESET. It likely means that we are not able to form the filament completely and RESET it completely because of the series resistance.

In the same figure in blue it is the same characteristic as shown in green but we removed the series resistance from the measured characteristic by using divider bridge equation given below:

$$V_{ox} = V_{applied}\left(\frac{R_{ox}}{R_S + R_{ox}}\right) \tag{4.1}$$

where $V_{applied}$ is total voltage applied, V_{ox} is the voltage across the oxide layer, R_S is the series resistance and R_{ox} is the resistance of oxide layer.

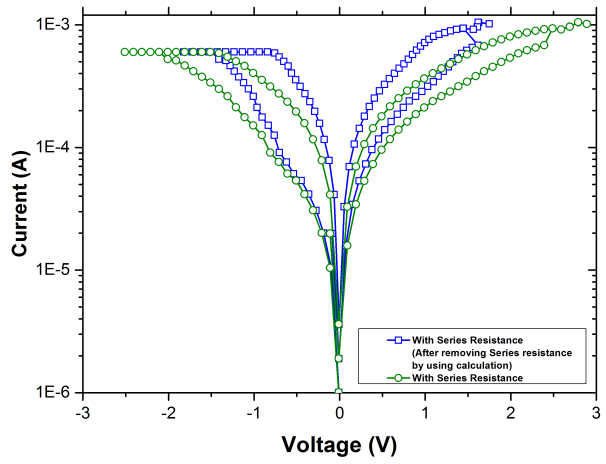

(A)

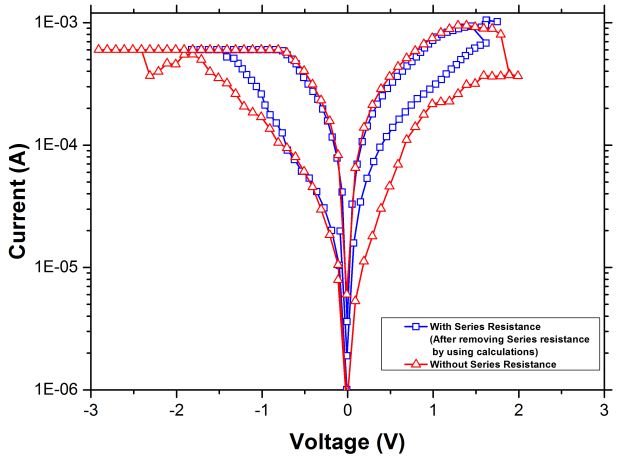

(B)

FIGURE 4.16: (a) Series resistance effect on I-V characteristic for TiN/HfO_2 with a series resistance of 1.1 $k\Omega$. (b) Comparison between the characteristic obtained with and without series resistance on the same sample with same conditions.

As one can see in the blue graph a little jump for setting and resetting exists. Also, the SET and RESET voltage is lower than the curve with series resistance, it

is because the voltage for the blue curve corresponds to the voltage droped across the oxide layer only and for green curve the voltage corresponds to the total voltage applied.

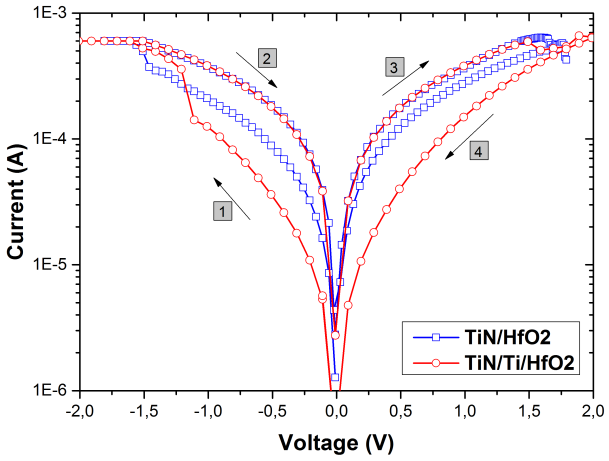

(A)

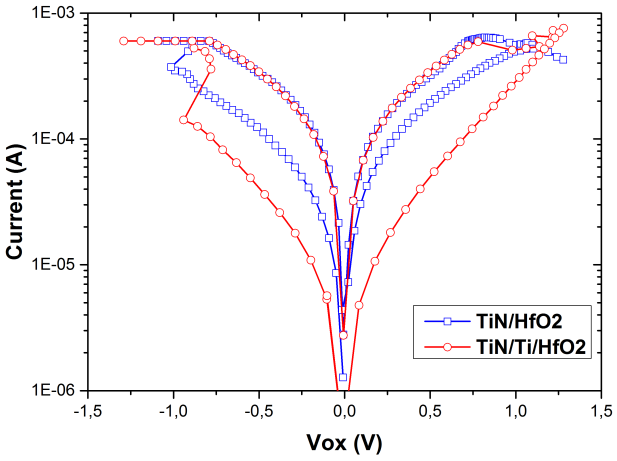

(B)

FIGURE 4.17: (a) I-V characteristics for TiN/HfO_2 and $TiN/Ti/HfO_2$ sample with series resistance of 1.1 $k\Omega$, (b) I-V characteristics for TiN/HfO_2 and $TiN/Ti/HfO_2$ sample after removing the series resistance of 1.1 $k\Omega$ by using calculations

We also did measurement without series resistance by using the same tip and same condition at the same time. In figure 4.16b, we plotted the characteristic with and without series resistance for the same sample and tip measured in the same conditions. As we can see the figure 4.16b the On-state current is exactly the same in both cases. The Off-state current is a bit lower in case of no series resistance and this is because we were able to achieve high enough current density to have enough joule heating to RESET the filament.

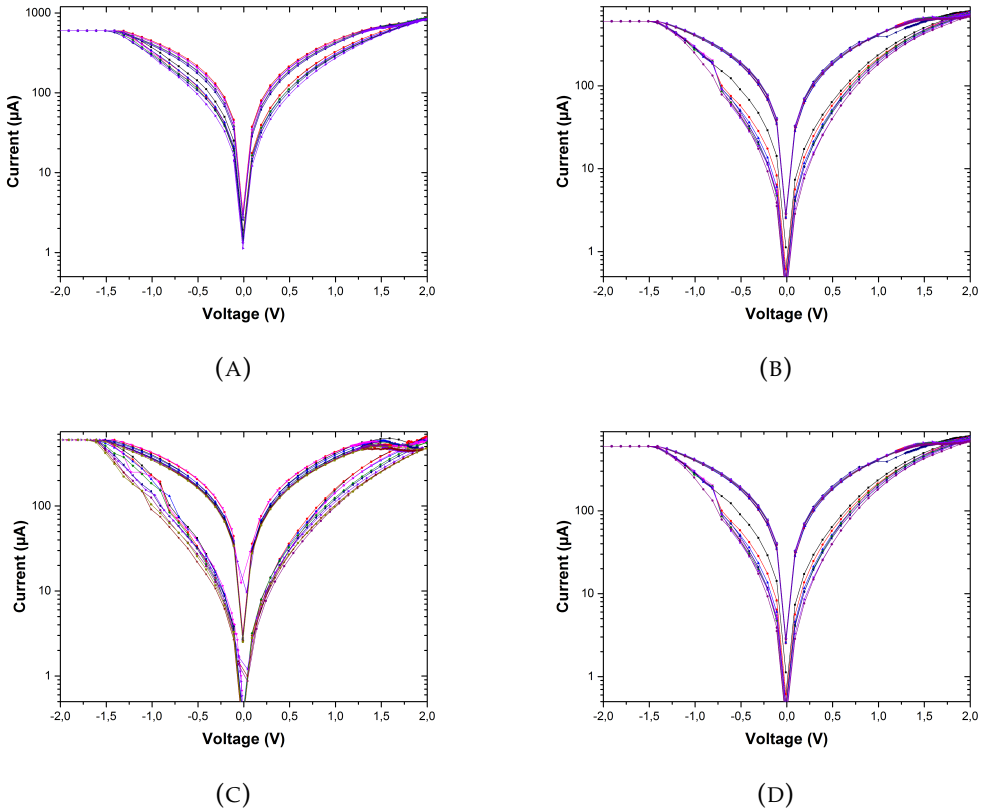

(A) (B)

(C) (D)

FIGURE 4.18: I-V characteristic for TiN/HfO_2 sample with series resistance. (a) First 20 loops for SET and RESET, (b) Next 10 loops with little bit larger memory window, (c) Next 10 loops with even larger window and becoming constant, (d) SET and RESET loops after around 40 loops with constant memory window with reproducible I-V characteristic, (e) Experimental result fitted by simulation.

This is the clear indication that the series resistance is playing the role in order not to RESET the filament completely. Also, we can see that the SET and RESET voltages are higher in case of no series resistance. The SET and RESET voltages in case of no series resistance are around $\sim 2.6V$ and $\sim 1.9V$ respectively. With series resistance SET and RESET voltages are around $\sim 1.5V$ and $\sim 1.3V$ respectively. This difference might be coming from a higher overshoot effect without series resistance.

Next step is to see the effect of bottom electrode with series resistance for two different samples we have for OxRAM. Same experimental procedure was adopted as mentioned before. The forming step was done by applying a negative ramp in order to form the filament. In figure 4.17a, the arrows and numbers are showing the direction of the voltage ramp. A series resistance of 1.1 $k\Omega$ is used in both cases. The on-state conductance is same for both samples. The off-state conductance is lower for the $TiN/Ti/HfO_2$ sample compared to the other sample. These characteristics are similar to the characteristics obtained without series resistance as shown in figure 4.12 and discussed in detail. SET voltage for $TiN/Ti/HfO_2$ is lower than TiN/HfO_2 but the RESET voltage is almost same in both cases. In the figure 4.17b same characteristics are shown as shown in figure 4.17a after removing the series resistance by using calculations.

We also studied the conditioning of the I-V characteristics with series resistance. After forming the filament in TiN/HfO_2 with full diamond tip as top electrode, many SET and RESET loops were recorded. In the beginning, the memory window (difference between on state and off state conductance) was very small at least for first 5-10 loops. With increasing number of loops, the memory window was also increasing. As we can see in figure 4.18a, the memory window is too low for first 20 loops. With increasing the number of loops, the memory window got better as can be seen in figure 4.18b for next 10 loops. In the coming next 10 loops the window gets even bigger and started becoming constant as can be seen in figure 4.18c. In figure 4.19a the I-V characteristics became really constant and reproducible after around 40 loops and for next 30 loops rested the same until the contact between AFM tip and the sample was lost.

In the beginning, after forming the filament was not completely formed and was unstable. With increasing the loop numbers, the filament started becoming stable and in the end after around 40 loops the filament is formed completely. Although the filament was not fully formed because of the high series resistance the current density was not obtained.

4.3 Discussion

In order to provide a better understanding of the experimental switching characteristics performed by C-AFM, we will use a phenomenological model that accounts well for $TiN/HfO_2/Ti/TiN$ 1T1R and 1R device switching characteristics in a wide range of temperatures[286]. In this phenomenological model we considered a filament and interpret the switching mechanism as a geometrical interpretation of the filament shape. In the following, we will examine the parameters that have to be modified to account for C-AFM measured characteristics knowing that the materials and thicknesses are the same as those of the devices (except the top electrode which is the C-AFM tip). The values of the fitted parameters will be used to interpret more thoroughly the experimental characteristics

4.3.1 Model Description

Many different models based on ionic drift diffusion[311], electron hopping transport[312] and whole filament enlargement and reduction based on redox reaction[313] were considered in literature. Here we have modelled the OxRAM by considering a conductive filament with a constriction surrounded by insulating oxide layer. In previous studies, for modelling the switching mechanism based on oxygen vacancies or ion diffusion from one part to opposite part of the oxide layer[314] was considered. In all the approaches mentioned before, the driving force of filament size variation is motion of the ions or oxygen vacancies under electric field. This can be understood in insulating layers but it seems difficult to understand in highly conductive regions. Also, it is difficult to understand the role of the diffusion mechanism in a reversible process since diffusion is irreversible. To avoid those discrepancies, we will use a model based on a nanometric conductive filament resulting from the forming process. The physical basis of the model used here is fully described in Ref[286] and was applied successfully to 1T1R and 1R OxRAM devices for a wide range of temperatures[286] in DC operation as well as in the pulse regime[309].

Here, for the sake of clarity, we will briefly describe this model. In literature, it was shown that the electromigration force is sufficient to break gold nanowires[315]. Some of the studies have even shown the resistive switching on the gold nanowires and explained it quantitatively by considering electromigration force[315]. The model used here assumes that the driving forces of resistive switching are the electromigration of Ti atoms and the Joule effect in a metallic nanowire.

An expression for electromigration force under an applied bias for gold nanowire is given by[316] :

$$F = 2mv_f \frac{\sigma}{q} J\eta \tag{4.2}$$

In equation 4.2, m is the electron mass, q the electron charge, v_F the Fermi velocity, σ an atomic cross section, J the current density and η the transmission factor. From equation 4.2 we can simply understand that when a current density J passes through the nanowire, the number of electrons by second transferring their kinetic energy to an atom in the nanowire is $\sim \frac{J\sigma}{q}$. Thus, the force acting on the atom is the electron kinetic momentum mv_F times $\frac{J\sigma}{q}$.

Considering the electromigration force whose direction is the one of the electron flux and that the OxRAM element consists of the metallic nanowire with a constriction in the oxide layer, the model is sketched in the figure 4.19[286]. The constriction area $S(t)$ is the time variable that describes the state of the OxRAM.

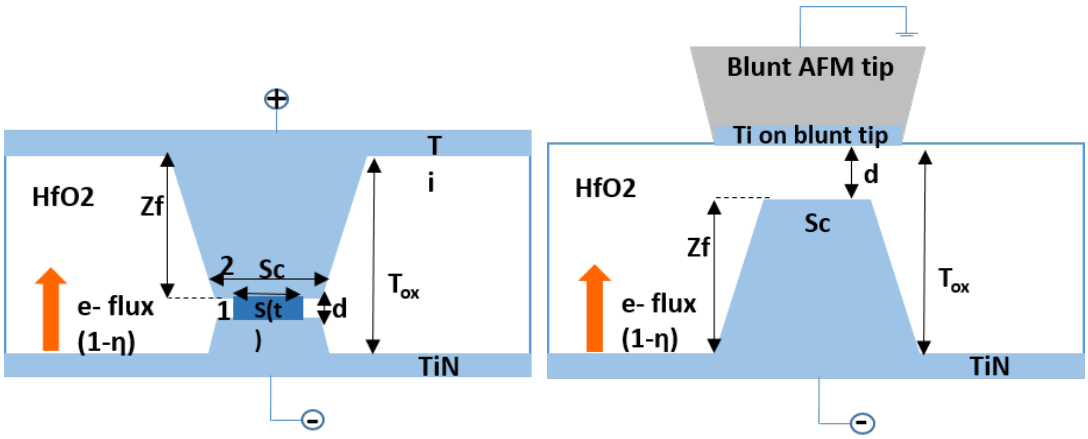

(A) (B)

FIGURE 4.19: Schematic description of the model[286] for (a) device, (b) CAFM measurements in the off state and polarized for set with blunt tip. T_{ox} is the HfO_2 thickness and S_c the constriction cross section. The other quantities are defined in the text and in table 4.1.

When the size of the contention is S_c it is in On state and if it is 0, it is in off state. This filament presents a constriction that can be filled or emptied with metal atoms (Figure 4.19a). As shown in figure 4.19a the atoms can be moved from region 1 to region 2. Region 1 is the contention and region 2 is filament. Let's consider the transfer rate of atoms from contention to filament is given by k_1 and filament to

contention by k_2. Also, let's assume the contention area $S(t)$ is proportional to the number of the metallic atoms in the contention. The evolution of contention area with time can be defined by:

$$\frac{dS}{dt} = k_2(S_c - S(t)) - k_1 S(t) \tag{4.3}$$

The state variable of the model is the constriction occupancy probability denoted by $P(t) = S(t)/S_c$ [Figure 4.19a], with S_c being the maximal constriction area[286], and is described by a simple balance equation that contains transfer rates

$$\frac{dP}{dt} = k_2(1 - P) - k_1 P \tag{4.4}$$

Those transfer rates k_1 , k_2 depend on electromigration, Joule heating and electron-phonon coupling in the constriction and are given by:

$$k_1 = \tau_o^{-1} e^{-\frac{V_1 + d.F_1}{k_b T(V_{ox} P, Ta)}} \tag{4.5}$$

$$k_2 = \tau_o^{-1} e^{-\frac{V_2 + d.F_2}{k_b T(V_{ox} P, Ta)}} \tag{4.6}$$

In equation 4.5 and 4.6, τ_o is the atomic vibration time (10^{-12} s), k_b is the Boltzmann constant,Ta is the external temperature (here 300K), V_1 and V_2 are the energies of the atomic potential well in the positions 1 and 2 respectively, d is the distance between the positions 1 and 2 (Figure 4.19a), F_1 and F_2 are the electromigration forces defined by equation 4.2.

$$F_{1,2} = 2mv_f \frac{\sigma}{q} J_{1,2} \eta_{1,2} \tag{4.7}$$

In equation 4.7 the current densities are $J_2 = -J_1 = -J$ and the electron transmission factors $\eta_2 = 1 - \eta_1 = 1 - \eta$ (since it is assumed that the transmission factor in one direction corresponds to the reflection factor in the opposite direction). v_F is the Fermi velocity, σ an atomic cross section m the electron mass and q the electron charge. The temperature depends on the applied voltage V because of Joule heating. As explained for the sake of simplicity the shape of filament and contention is considered as two cylindrical nanowires. The first one (filament) has the cross section of S_c and length of Z_f (contention location). The second cylindrical nanowire (the contention) has the cross-section area Sc and a length $d = T_{ox} - Z_f$. Now we can solve the steady heat equation for the geometry considered. The temperature due to Joule heating is given by:

$$T_J(P, V_{ox}, Ta, z_f) = Ta - \frac{I(P, V_{ox})^2}{2\kappa\sigma_c S_c}\left(2z_f^2 - \frac{z_f}{T_{ox}}(z_f^2 + T_{ox}^2)\right) - \frac{I(V)^2}{2\kappa\sigma_c S_o}\left(z_f^2(\frac{z_f}{T_{ox}} - 1))\right) \tag{4.8}$$

In equation 4.8, z_f, is the constriction location, T_{ox} the HfO_2 thickness, κ, σ_c the thermal and electrical conductivities of the filament, $I(P, V_{ox})$ the current as function of the applied voltage on OxRAM V_{ox}. When z_f increases the Joule heating temperature decreases for the same voltage or equivalently one needs a larger voltage to reset. However, when the constriction is open (i.e. when $P = 0$), we consider that the Joule heating is negligible. In that case the local electronic temperature in the constriction depends on the voltage with the following expression:

$$T_e(Ta, T_{ox}) = \frac{Ta}{1+\alpha} + \frac{\frac{qV_ox}{2k_B} coth \frac{qV_ox}{2k_B Ta}}{1+\alpha^{-1}} \tag{4.9}$$

In equation 4.9, α stands for the ratio of characteristic phonon and electron times. A larger value of α leads to a larger temperature for the same voltage or equivalently one needs a smaller voltage to set. So, in the intermediate state when the contention is partially filled according to probability P, we can calculate the temperature in the contention because of joule heating T_J (when $P = 1$) and local heating T_e (When $P = 0$). Thus, the total temperature is the interpolation between expressions 4.8 and 4.9:

$$T(V_{ox}, P) = T_J(V_{ox}, P, T) + T_e(V_{ox}, T)(1 - P) \tag{4.10}$$

The conductance in the mesoscopic system consisting in the constriction in a nanowire can be computed via Sharvin conductance, see[286] and references therein:

$$G_p(P) = \frac{2q^2}{h} \frac{k_F^2 S_c P}{4\pi} \left(1 + \gamma \frac{3T_{ox}}{4l}\right)^{-1} \tag{4.11}$$

In equation 4.11, h is the Plank constant, k_F the Fermi wave vector, l the electron mean free path and γ a geometric factor whose value is about 1. When $P = 1$, or $S_o = S_c$, $G(P) = G_{on}$:

$$G_{on} = \frac{2q^2}{h} \frac{k_F^2 S_c}{4\pi} \left(1 + \gamma \frac{3T_{ox}}{4l}\right)^{-1} \tag{4.12}$$

$$G_p(P) = G_{on}.P \tag{4.13}$$

When the constriction is empty (i.e when $P = 0$) the current is assumed to be due to tunneling or field assisted tunneling. For sake of simplicity we will approximate the tunneling current in order to retrieve the Fowler-Nordheim tunneling when V_{ox} > ϕ_b (the barrier height) and the direct tunneling when $V_{ox} < \phi_b$, ϕ_b being the barrier height between filament and constriction. The tunnel current takes the following form (for $V > 0$):

$$I_t(V) = S_c \frac{q^3}{8\pi h \phi_b} (E)^2 exp\left[\frac{-8\pi\sqrt{2m_{eff}}\phi_b^{\frac{3}{2}}}{3qhE} \cdot \left(1 - C(V_{ox})\left(1 - \frac{qV_{ox}}{\phi_b}\right)^{\frac{3}{2}}\right)\right] \tag{4.14}$$

In equation 4.14, E is the electric field in the constriction (V_{ox}/d), d being the constriction thickness and $C(V_{ox})$ a function which gives 1 when $qV_{ox} < \phi_b$ and zero otherwise, m_{eff} is the electron effective mass. Then, using the similar argument than the one used to evaluate the temperature in the constriction the current is given by the following interpolation:

$$I(P, V_{ox}) = G(P)V_{ox} + (1 - P)I_{tp} \tag{4.15}$$

The coupling with an external serial resistance or a MOSFET is given by:

$$V = V_o x + V_S \tag{4.16}$$

$$I(P, V) = I_S = \frac{V_S}{R_S} \tag{4.17}$$

In equation 4.16 and 4.17, V is the applied voltage, R_S and V_S are the serial resistance and the corresponding voltage drop. For 1T1R devices I_S has to be replaced by the drain current-drain voltage characteristic of the MOSFET and V_S by the drain voltage V_d. The self-consistent numerical resolution of equations 4.4, 4.16 and 4.17 allows to calculate P taking into account equations 4.5 - 4.13 as function of the voltage V_{ox}. Equation 4.15 allows to calculate in turn the current-voltage switching characteristics for any given time voltage dependence (voltage ramp which is the case here or voltage pulse for example).

Symbol	Quantity	Values
E_f	Fermi Energy	$8.8eV$
τ_o	Characteristic time	$10^{-12}s$
$\rho(Ti)$	Density	4500 Kgm^{-3}
$K(Ti)$	Filament thermal conductivity	21 $W(Km)^{-1}$
$\sigma_c(Ti)$	Filament conductivity	$2.5 \times 10^6(\Omega m)^{-1}$
α	Electron phonon couplinng factor	$MentionedinTable4.2$
ϕ_b	Barrier height	$MentionedinTable4.2$
γ	Geometric factor in conductance	1
l	Electron mean free path	$12.5nm$
d	Contention thickness	$MentionedinTable4.2$
V_1	Energy well of position 1	$MentionedinTable4.2$
V_2	Energy well of position 2	$MentionedinTable4.2$
σ	Electromigration force cross section	$2.9 \times 10^{-15}cm^2$
z_f	Contention localization	$MentionedinTable4.2$

TABLE 4.1: Parameters values used in the model in order to fit the experimental data.

4.3.2 Model comparison with experiments

In table 4.2 we have reported the fitted values corresponding to the calculated switching characteristics reported in figures 4.14, 4.21a, 4.21b, 4.22 and 4.23 together with the experimental characteristics. The metallic filament parameters (κ,σ_c,k_F) are those of Titanium[286] consistently with recent TEM EDX observations[307]. For sake of

consistency, we have fixed the same potential well energy values V_1 and V_2 in all cases since the materials are the same.

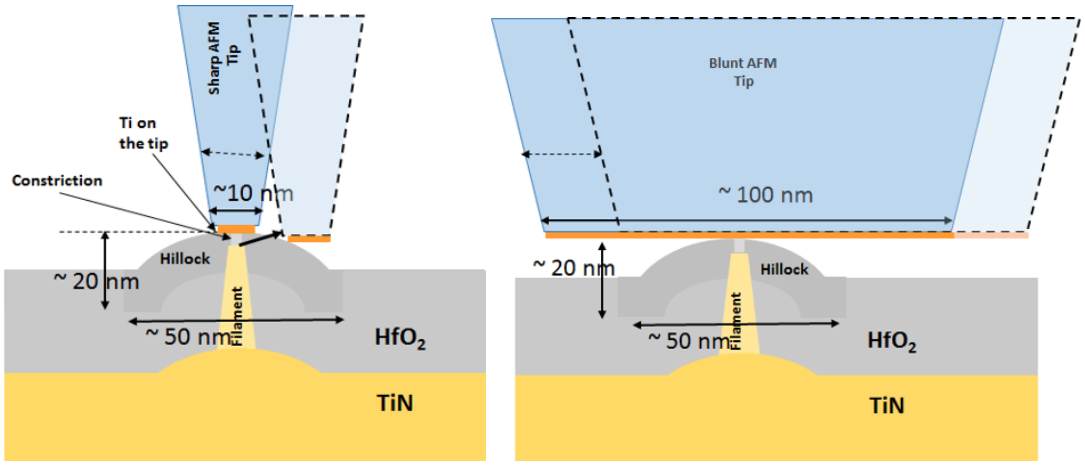

(A) (B)

FIGURE 4.20: Schematic description for shifting of AFM tip for (a) sharp full diamond tip, (b) blunt full diamond tip.

First, we will discuss the tip influence on switching current voltage characteristics, reported in figure 4.21a & 4.21b. For the sharp tips the off-state current is lower by several orders of magnitude compared to blunt tips. It increases from cycle to cycle which limits the practical interest. In the case of sharp tips, the fitted values in table 4.2 correspond to the curves plotted on figure 4.21a. Because of the cycling variability for sharp tips the values in table 4.1 correspond to the very first cycles and one can admit that they may fluctuate significantly.

As one can see in table 4.2, the differences between blunt and sharp tips fitted values are the barrier height and the tunneling distance. According to equation 4.12 this results in a larger tunneling barrier height and thickness for sharp tips than for blunt tips. It reflects the smaller Off state current observed for sharp tips compared to blunt tips. The other parameters are almost the same for both tips. In particular the filament constriction area (S_c) is almost the same whatever the tip. Its value is estimated using On state current value and equation 4.12 & 4.15 with $P = 1$ at $\sim 2.5nm^2$ (i.e. diameter $\sim 0.9nm$).

In order to understand the fitted barrier height value differences in table I it is worth comparing them with expected values $\Phi = W - \chi$ (W being the metal work function and χ is the electronic affinity, as it is illustrated in figure 4.21e). In the case of Pt/HfO_2 interface ϕ_1=5.3eV- 2.8eV=2.5 eV[317;318] and for C/HfO_2 interface ϕ_1=5eV-2.8 eV =2.2eV[317;318] and for Ti/HfO_2 ϕ_2=4.3 eV- 2.8 eV =1.5 eV[317;318]. Those values are consistent with the fitted values in table 4.2.

The high barrier height reported for sharp tips remains unclear. We assume that during the reset, the tip positions may slightly shift. In this situation, illustrated in figure 4.20a, the tunneling can take place in a pristine tip side/HfO_2 interface region leading to a $Ti/HfO_2/Tip$ interface with a larger tunneling distance than the one existing without tip shift. This may also explain the wide dispersion observed for the Off-state current with sharp tips. Conversely in the case of blunt tip since the tip diameter is very large compared to the filament constriction diameter, as it is sketched

Sample	**Top Electrode**	V_1**(ev)**	V_2**(ev)**	η	α	ϕ_1/ϕ_2 **(eV)**	$d(A)$	z_f **(ev)**
TiN/HfO_2	Full diamond (Blunt): Fig 4.21b	2.9	2.3	0.7	0.01	0.2/0.2	2-3	4.8-4.9
TiN/HfO_2	PtSi (Sharp) Fig 4.21a	2.9	2.3	∼0.8	∼0.01	∼2.5/1.3	∼7.5	2∼4.9
TiN/HfO_2	Full diamond (Sharp)Fig 4.21a	2.9	2.3	∼0.8	∼0.01	∼2.2/2	∼11	2∼4.9
$TiN/Ti/HfO_2$	Full diamond (Blunt) Fig 4.23	2.9	2.3	0.7	0.01	0.2/0.2	3-5	4.6
TiN/HfO_2 with series resistance	Full diamond (Blunt)Fig 4.24	2.9	2.3	0.55	0.01	0.2	3	4.65
$TiN/HfO_2/IT1R$	Ti/TiN Fig 4.22	2.9	2.3	0.1	0.1	0.2	4.5	4.3

TABLE 4.2: Fitting parameters values used to simulate the switching characteristics shown in figures 4.21a & 4.21b, 4.22, 4.23 & 4.24. The symbol ∼ indicates that the fitted values are less accurate because of the large cycling fluctuations observed for sharp tips.

on figure 4.20b a similar tip shift does not change the barrier nature $Ti/TiO_x/Ti$. Moreover, if the hillocks observed in section 4.2.2 and sketched in figure 4.20 were fully composed of Titanium one cannot expect tip effects on off state currents since the barrier height would be the same whatever the tip.

However, for blunt tips the barrier height is, according to table 4.2, the same as for devices $\phi_1 = \phi_2 = 0.2eV$ whatever the polarization. Because Ti is present on the blunt tip after measurements, one can then assume that the constriction's barrier is $Ti/MO_x/Ti$ (MO_x being an undetermined oxide) for blunt tips and devices. The barrier height for Ti/TiO_2 is ϕ=4.3eV - 3.9 eV =0.4 eV[317;318] (see figure 4.21f) which is very close to the $0.2eV$ in table 4.2. Since the electron affinity increases when the oxide becomes under-stoichiometric[319] one may explain the smaller $\phi_1 = \phi_2 = 0.2eV$ value for a $Ti/TiO_x/Ti$ barrier for blunt tips and devices. One can then assume that Ti has diffused in front of the Ti filament. This last barrier height evaluation is consistent with the EDX observation of section 4.2.2.

In figure 4.21 the difference between sharp tip and blunt tip in term of barrier height is shown by giving the different model for different tips. In figure 4.21a, the I-V characteristics with sharp tips are shown and in figure 4.21b the I-V characteristics with blunt tip are shown. We already discussed the possible reason in the previous paragraph for differences in the I-V characteristics in both cases. Figure 4.21c shows the model sketched for sharp tip when there is no Ti present on the tip. So, in this case we have Ti in the bottom electrode and in the filament and we have HfO_2 in the contention. Also, the filament length is shorter than in the case of blunt tip as mentioned previously.

Figure 4.21e shows the barrier height representation in the case of sharp tip. Here we have Pt or C for the AFM tip (top electrode), HfO_2 in the constriction gap and Ti for the filament. The barrier height for Pt/HfO_2 is higher than the barrier height of Ti/HfO_2. Here we considered the off state is due to the tunneling between tip and the filament. In figure 4.21d the model for blunt tip is presented showing lower contention size compared to sharp tip case. Also, in figure 4.21f the barrier height for this model is represented. In the case of blunt tip, we have Ti on the tip as confirmed by SEM EDX measurements. So, the barrier is composed of $Ti/TiO_x/Ti$.

One can also notice that in the case of measurements with blunt tips the off state current decreases with increasing voltage for voltages above typically $2V$ (Figure 4.21b). In order to reproduce this effect, we have introduced an ad-hoc variation of the barrier height for tunneling current with OxRAM element voltage (V_{ox}). To fit the experimental characteristic the empiric law was $\phi(V_{ox}) = \phi + 0.0015(V_{ox})^6$. In the experimental voltage range $\phi(V_{ox})$ rises from $0.2eV$ to $\sim 0.3eV$. This may be an indication that for high voltage more Ti atoms can be transferred to the tip increasing then the stoichiometry in oxygen in the gap, increasing in turn the barrier height. However, this explanation is somewhat speculative.

The most striking difference between devices characteristics and C-AFM measurement (illustrated in figure 4.22), are the set and reset voltage values that are much larger in the case of C-AFM ($\sim$3V vs $\sim$0.7V for the set voltage). The same trend was observed but with less extend by Hou et al.[143] for example. The model accounts for this effect (Figure 4.22) via the α(accounting for the set voltage, eq. 4.9)), the η parameters value (Table 4.2) and z_f (accounting for the reset voltage, equation 4.8). The electromigration force is proportional to the incident electron flux and to

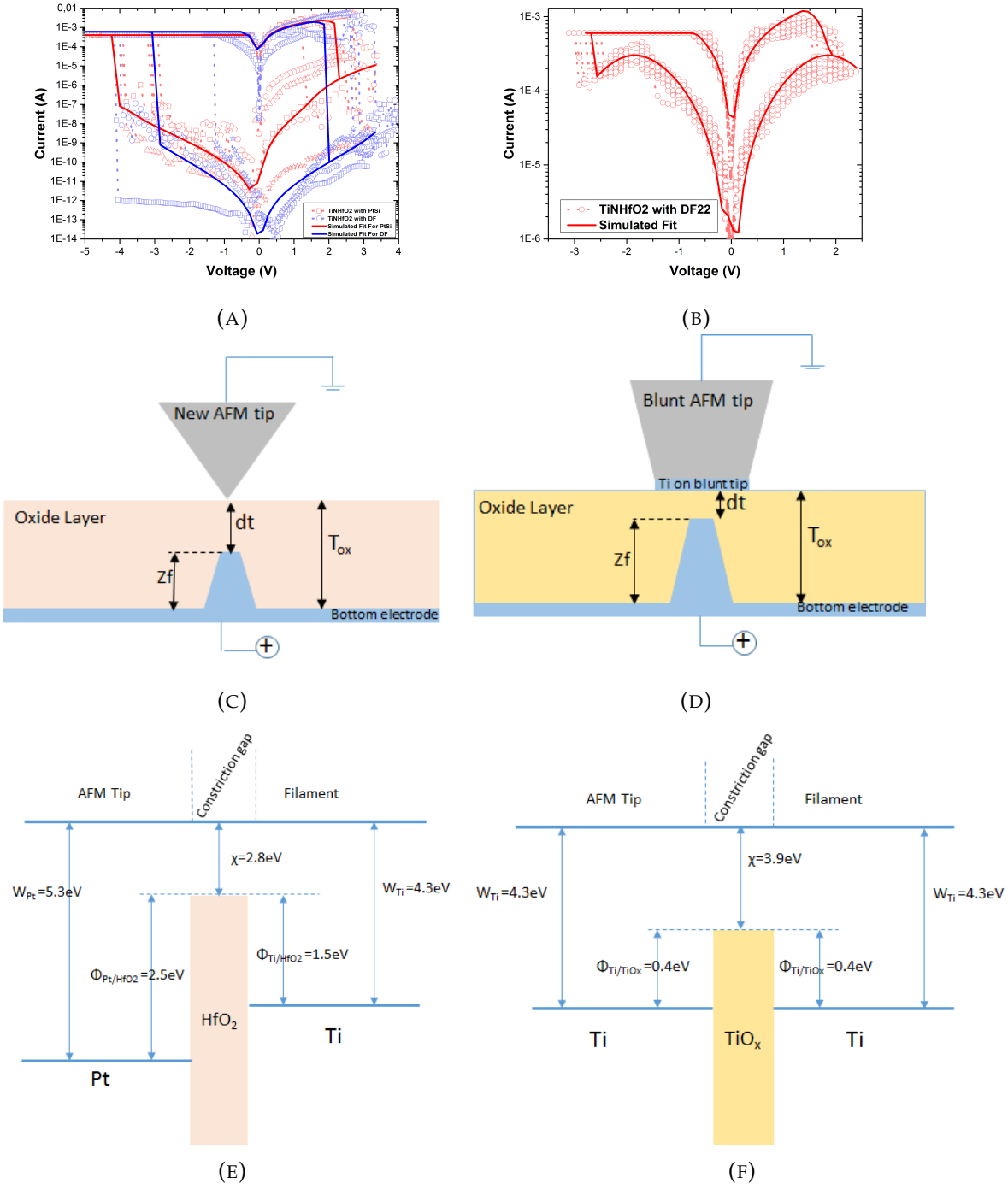

FIGURE 4.21: (a) I-V characteristics with (a) sharp AFM tip, (b) I-V characteristics with blunt full diamond AFM tip. Experimental data is the superposition of many loops. (c) Schematic description of the model for sharp tip, (d) Schematic description of the model for blunt tip, (e) Barrier height model for sharp tip, (f) Barrier height model for blunt tip.

the transmission factor. During the set the electron wind is directed from the tip to the filament and the transmission factor is $1-\eta$ (Figure 4.19). According to table 4.2 the transmission factor $(1-\eta)$ from the tip is 0.3 and smaller than the one accounting for devices characteristic (0.9).

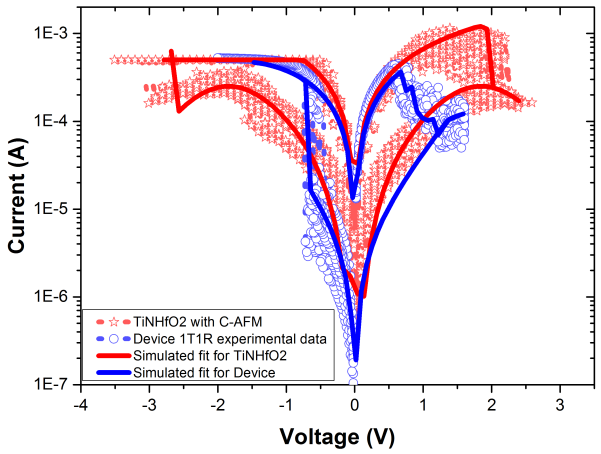

(A)

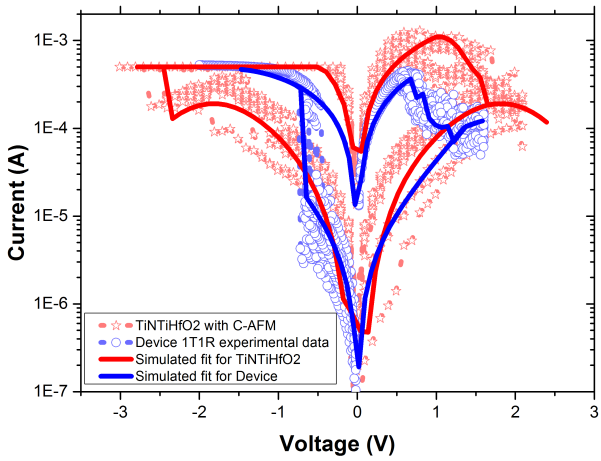

(B)

FIGURE 4.22: (a) AFM I-V characteristic comparison with 1T1R device characteristic for TiN/HfO_2 (b) Comparison of C-AFM and 1T1R device I-V characteristic obtained on TiN/Ti/HfO2 sample. Experimental data is the superposition of many (around 10) loops

As it is schematized on figure 4.19, before the set the electron flux comes from the bottom electrode for devices (Figure 4.19a) and it comes from the filament for C-AFM measurements (Figure 4.19b). The modification of η may likely be due to the geometric form of the filament's end surface which may be rougher than the contact with bottom electrode. The lower α (Equation 4.9) value reflects the lower electron-phonon coupling. This last is also proportional to the electron transmission factor and inversely proportional to the phonon density of states[320]. Thus, the reduction of $1-\eta$ is consistent with the reduction of α.

Moreover, to maintain the contact during measurement one has to apply a force of several tens of nano-Newton ($50nN$ the most of the time in our experiments). For a typical contact area of 10 nm^2 this force corresponds to a pressure of several GPa. For such a stress the phonon frequency spectra can shift[321] and may reduce also the coupling factor α. When α is larger the voltage necessary for set decreases because the electron phonon coupling is more efficient, resulting in a lower set voltage which is the case for 1T1R devices compared to C-AFM measurements.

From table 4.2 one can see that z_f is larger for C-AFM measurements than for devices. According to equation 4.8 when z_f increases the Joule heating temperature decreases and a larger voltage is necessary to achieve reset. The z_f values is likely induced by the forming process. In ref[286] it was speculatively assumed that the filament constriction location was limited by the power dissipated at breakdown by joule heating. When the constriction area increases the current density (at the compliance) decreases which decreases in turn the temperature and thus limits the filament growth. This assumption leads to an approximate analytical expression[286] $z_f \sim T_{ox} - \gamma(T_f - T)/Ebd$ where γ is a constant depending on the model parameters, T_f being the Titanium fusion temperature. For 1 μm^2 devices the breakdown field Ebd mean value is 3.8 MV/cm. For the CAFM experimental values is $Ebd = 11MV/cm$. The above-mentioned expression reproduces the z_f variation with Ebd trend. By the way the effect of device surface on Breakdown field is well known (see for instance[322]). Even if this approach is far too simple it is worth mentioning it.

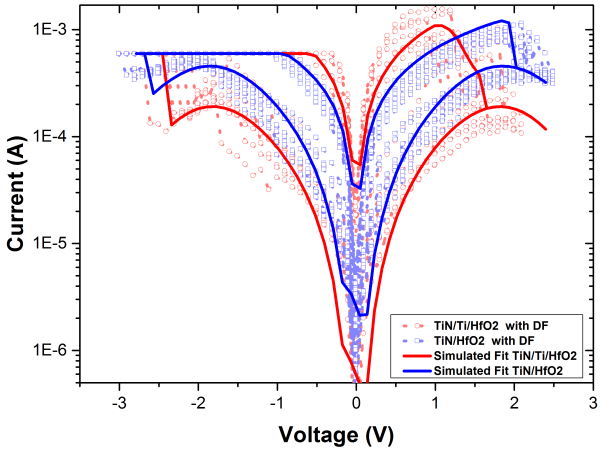

FIGURE 4.23: I-V characteristics and simulations for different bottom electrodes by using full diamond blunt tip as top electrode in both cases.

In the on state, since the filament's constriction is filled the conduction does not depend on the location of the constriction. It depends mostly on the area of the constriction (equation 4.12 & 4.15 with $P = 1$) and on the Fermi energy of the metallic filament which is assumed to be Ti in all the cases studied here. This is also the case with the C-AFM measurements and figures 4.22 shows that the On state current is similar for C-AFM and devices. The model is thus fully consistent with the

observation also for the On state. From ref[286] it was found experimentally and theoretically that the On state conductance depends mainly on the compliance current I_c with linear relation $G_{on} \sim V_c - 1.I_c$ where $V_c \sim 0.35$V for devices. This relation still exists for the C-AFM measurements even if a wide dispersion is observed as it is shown on figure 4.22. However the effect of overshoot in C-AFM precludes the observation of this law for the lowest compliance currents[323]. It seems that the effect of bottom electrode is only a slight lowering of the off-state conductance and of the memory window (figure 4.23) which was already observed on devices and may reflect a slight difference in constriction position and length according to table 4.2.

In figure 4.14 we have reported the effect of polarity. Changing the forming voltage polarity followed by the reset in the opposite polarity gives rise to very similar characteristics. This may indicate that the filament constriction location is not polarity dependent. It is worth noting that this conclusion has already been established in another context[324]. Since we observed *Ti* deposition on the tip after measurements we can infer that during forming Ti atoms migrate from the bottom electrode whatever is the polarity. This is not possible by electric field induced drift of ionized

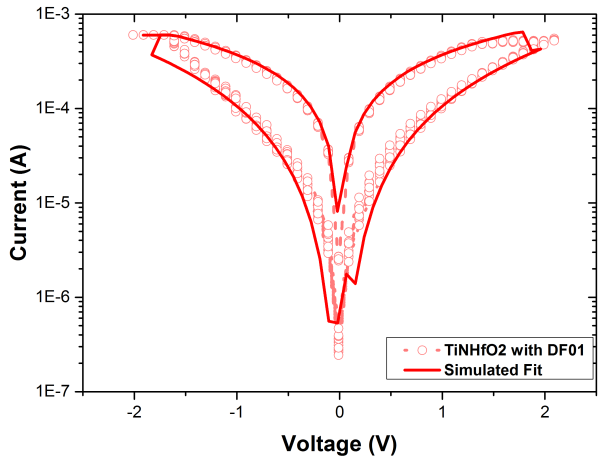

FIGURE 4.24: I-V characteristic for TiN/HfO2 sample with series resistance and simulated fit by using model.

Ti atoms or electromigration because those driving forces are polarity dependent. Thus, the *Ti* atoms driving force during the forming step could be the *Ti* atoms concentration gradient which is the same whatever the polarity. This is the case for the Fick law of diffusion which could be the mechanism in question during the forming step. However, during the forming process the temperature is likely non-uniform and could be very large in the first filamentary path of breakdown because of Joule heating. Thus, the diffusion which is a temperature activated process is mostly effective in this filamentary path and the diffusion takes place in its vicinity leading to the filament formation. The *Ti* atoms may migrate during forming from the *Ti* rich bottom electrode to the *Ti* poor top surface in this high temperature region. In the case of devices, the *Ti* atoms may diffuse from the *Ti* top electrodes leading to a constriction location nearer to the bottom electrode. This assumption seems to be consistent with all our observations. It is worth noting that the approach developed here may also explain the switching characteristics observed on *Pt* sputtered top electrodes on 1R devices[325] which share the same behavior as our measurement with sharp C-AFM tips.

The effect of adding a serial resistance on the fitting parameters of the model (whose result is plotted in figure 4.24 together with experiment data) is summarized in table 4.2. The effect of series resistance (R_S) is to reduce slightly the factor η or to enhance the factor α compared to the same experimental condition without R_S. More precisely to fit the SET voltage one needs to increase the electron flux $(1-\eta)$ or to increase the electron-phonon coupling (α). Both enhance the temperature at the same voltage favoring the SET. In other words, changing only R_S in the model is not sufficient to reproduce the SET voltage value. The values used to fit the R_S is effective in the forming step. It results in a better control of the compliance, which in turn affects the shape of the constriction.

4.4 Conclusion

In this chapter, we presented the resistive switching characteristics of HfO_2 based OxRAM by using C-AFM in vacuum environment in the context of high compliance regime. Samples with different bottom electrodes were studied by using AFM tips (Full diamond & PtSi) as top electrode for MIM structure. The results were analyzed using a phenomenological model assuming that the current is limited by a constriction in a conductive filament in the On-state after forming. In the Off state the constriction is open giving rise to a gap whose length and barrier height limit the tunneling current. The effect of different tip materials and size on switching characteristics was particularly studied. There was not much effect of tip material on the I-V switching characteristics although there was a strong effect of tip shape (sharp and blunt). With sharp tips one observed lower Off state currents and larger SET and RESET voltages which present large fluctuations with cycling.

With blunt tip the I-V characteristics presented higher Off state current comparable to devices and reproducible switching characteristics. SEM-EDX measurements on full diamond AFM tip have shown the presence of Ti on the blunt tips only after electrical measurements. Those facts consistently with the model-based analysis conducted us to assume that the differences between blunt and sharp tips may be explainable if the metallic filament constriction is located near the top electrode tip contact. For sharp tips the Off state tunneling current barrier is consistent with a $(PtorCtip)/HfO_2/Ti(filament)$ interface as for blunt tip and devices with $Ti/TiO_x/Ti$ interface. The difference in tunneling barrier characteristic was explained by the effect of slight tip shift effect.

For devices this constriction was assumed in the vicinity of the bottom electrode. This geometrical difference leads to variations of the electron flux transmission factor that accounts well for larger set voltages in the case of AFM tips compared to devices. The larger reset voltages observed for C-AFM were explained by the shallower filament constriction position and assumed to be linked to the higher breakdown electric field. Finally, we did not observe any significant effect of polarity on switching characteristics, including forming with C-AFM. Since Ti was present only in bottom electrodes the Titanium concentration gradient is likely the driving force in the forming process. Ti migration during forming from high Ti concentration electrodes to low Ti concentration in a preexisting hot breakdown percolation path might explain the differences in geometrical position and geometry of the filament constriction.

Chapter 5

Switching in Phase Change Materials

5.1 Introduction

The phase change memories (PCM) or phase change-Random access memory (PCRAM) is an emerging nonvolatile resistive memory technology which is based on the thermally induced phase transition of a thin film of chalcogenide material [193;201;326;327]. The PCM was introduced many decades ago but became more known in last 10-15 years becoming the most promising candidate for the next generation of nonvolatile memory [328].The phase change materials belong to the chalcogenides. The phase can be changed by current induced joule heating of the phase change material from amorphous to crystalline. By changing the phase of the chalcogenide material one can change the resistance of the layer because in amorphous state the resistivity is higher compared to the crystalline state. $Ge_2Sb_2Te_5$ (GST-225) is the commonly used chalcogenide material for phase change memory these days [236;242;244;326;329–332].

One can see in the figure 5.1, when the material is in amorphous state, the resistance of the layer is very high. When a voltage pulse is applied to the chalcogenide material, the resistivity of the amorphous phase decreases (threshold switching) and the current induced joule heating allows to crystallize the amorphous phase. Since the crystalline phase resistance is much lower, the PCM switches from high resistance state to low resistance state [333–335]. Again, a shorter pulse with higher amplitude is applied to melt the crystalline phase which becomes amorphous by quenching from the melted phase. This step changes the state from low resistance state to high resistance state.

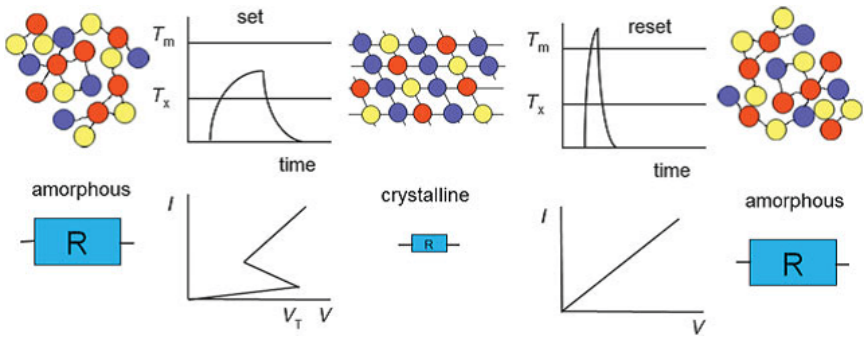

FIGURE 5.1: Schematic representation of phase change in phase change material for phase change memory [201].

In figure 5.2, the I-V characteristic for a phase change material (GST225) is shown.

In the amorphous state, when the voltage reaches the threshold voltage value V_{th} [142], it increases the conduction by an electronic process before the crystallization itself, which arises at the region denoted SET in the figure. The melting temperature corresponds to the region denoted RESET in the figure. Once in the crystalline phase and after the reset (where the material is in the liquid phase), a quick quench at room temperature allows the material to return in the amorphous state. This describes roughly the PCM operation. However, the crystallization temperature of GST, about 150°C precludes operation for automotive applications which are the industrial purpose of this work. To increase the crystallization temperature a germanium enrichment of GST was introduced. The optimized composition of this Ge-rich GST will be called GSTθ in the following and crystallize at about 350°C. For the same purpose, a nitrogen doping had also been introduced.

As it was mentioned in chapter 1 in section 1.5, CAFM has already been used to study GST 225 layers. Our main aim here is to study different materials for phase change memories i.e. stoichiometric GST as GSTθ. Also, we will study the effect of voltage ramp speed and effect of capping layer. Capping layer prevents the oxidation of GST layer. An attempt to give interpretations for our results will be given using simple conduction models and finite elements-based models which include growth simplified description.

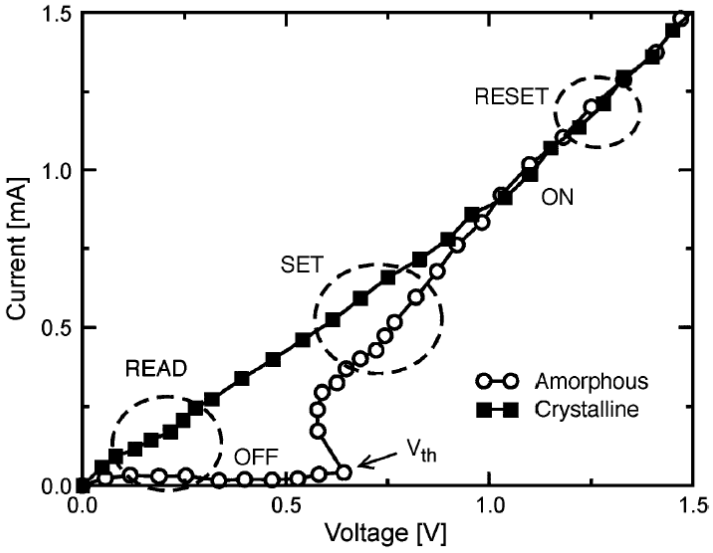

FIGURE 5.2: Typical current-voltage characteristic of GST-225 phase change material [195].

5.1.1 GST samples and experimental methods

Here we are going to study two different compositions of GST material. For each GST composition, we compare samples with and without capping layer. All the sample details are given in table 5.1. One composition is simply $Ge_2Sb_2Te_5$ (GST-225). The other one is germanium rich GST-225, called GSTheta (GSTθ). Phase transition for all the materials will be discussed in the coming section. The experimental setup is similar to the one used for OxRAM measurement. AFM tip (Boron doped full diamond) is used as top electrode as we don't have any top electrode deposited

on the sample. AFM tip is grounded and voltage is applied on the sample. Here we will apply positive voltage on the sample for all the measurements as shown in figure 5.3.

Sample	Substrate	Bottom Electrode nm	Phase Change Material (nm)	Capping Layer(nm)
1	Si Sub	TiN(20nm)	GST-225 (10nm)	-
2	Si Sub	TiN(20nm)	GST-225 (10nm)	GeN (3nm)
3	Si Sub	TiN(20nm)	GSTθ (10nm)	-
4	Si Sub	TiN(20nm)	GSTθ (10nm)	GeN (3nm)

TABLE 5.1: Phase change material sample description used to study the characteristic in this chapter.

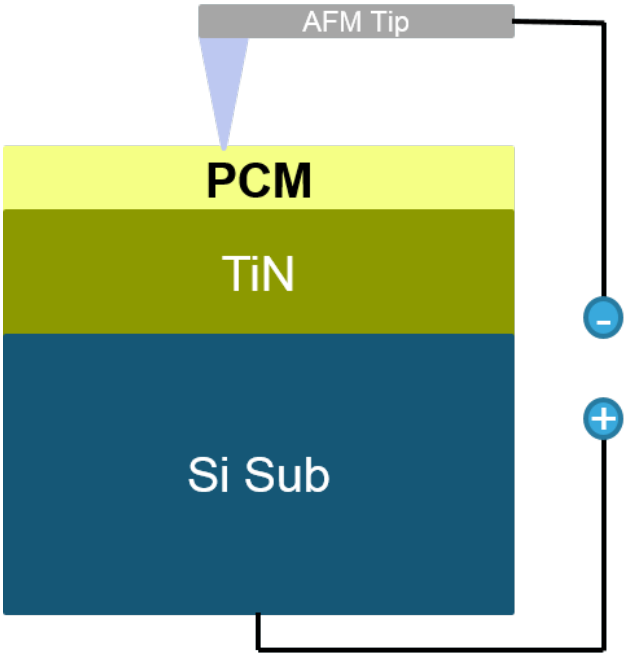

FIGURE 5.3: Schematic diagram representing the measurement setup with conductive atomic force microscope (C-AFM) for phase change memory

In figure 5.4, I-V characteristic of GST-225 is shown. As one can see in the beginning, the resistance of the GST is very high. The voltage ramp is applied and the voltage starts increasing. Once it reached the threshold voltage (Vth) which is around 0.8 V in the case of figure 5.4, the resistance starts decreasing. For voltages below threshold voltage, the conductance is higher than the conductance for voltages below the threshold voltage. Once the current reaches the compliance current value, the ramp is reversed and current starts decreasing with decreasing the voltage but the phase change material stays in On-state. It is difficult to RESET the PCM by using ramp because to RESET we need a pulse with higher amplitude and shorter duration to melt the material and then quench it very quickly to reverse the phase from crystalline to amorphous. Here we will only study the phase transition from amorphous to crystalline.

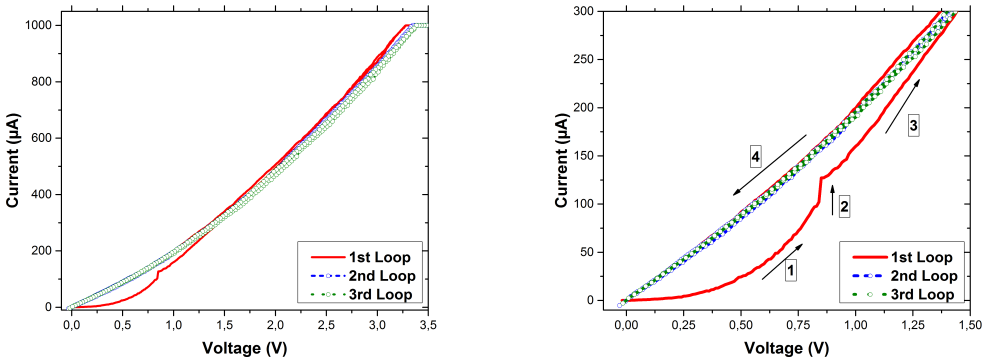

(A) (B)

FIGURE 5.4: (a) I-V characteristic for $Ge_2Sb_2Te_5$ (GST-225) sample by having full diamond AFM tip as top electrode. (b) Zoom in of (a) near the phase transition.

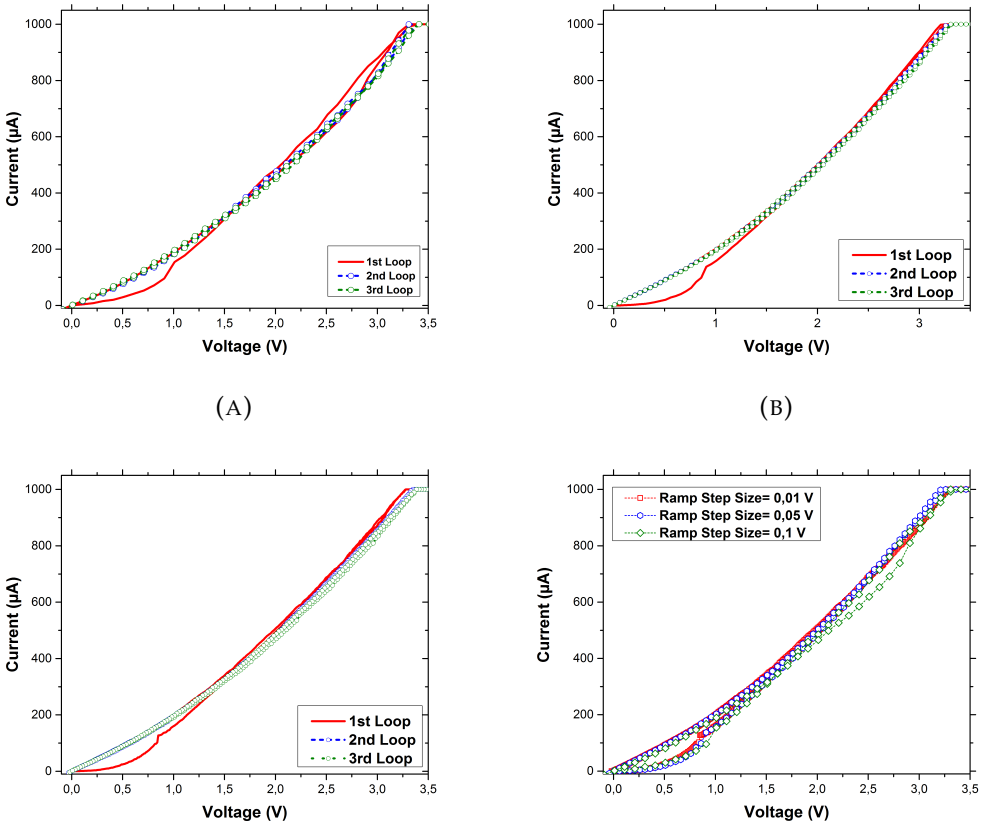

(A) (B)

(C) (D)

FIGURE 5.5: I-V characteristic for $Ge_2Sb_2Te_5$ (GST-225) sample by having full diamond AFM tip as top electrode at different ramp speed for different voltage step size. (a) at 0.1 V, (b) at 0.05 V, (c) at 0.01 V and (d) comparison of I-V characteristic at all the voltage step.

5.2 Experimental Observations

5.2.1 Ramp Speed effect

To know the effect of different ramp speeds on PCM I-V characteristics, different voltage step sizes were taken. 0.1V, 0.05V and 0.01V voltage sizes are used here to see the effect of ramp speed. For example, with 0.1V voltage step size the ramp speed was 0.125 V/sec. I-V characteristics for GST-225 for different voltage step sizes are shown in figure 5.5. In figure 5.5a the characteristic is shown for 0.1 V voltage step, in figure 5.5b the voltage step size is 0.05 V and in figure 5.5c the voltage step size is 0.01 V. The lower the voltage step size the lower the voltage ramp speed. With decreasing the step size one can have more points for the same characteristic.

In figure 5.5d, I-V characteristics for different voltage sizes are compared. One can see clearly that there is no effect of ramp speed in the I-V characteristic of GST-225. It can be seen that for all the voltage step size the threshold voltage is around 0.8 V. On state and off state conductance are also similar in both cases. We can conclude from the graph that there is no effect of ramp speed on the I-V characteristic of PCM material.

5.2.2 Capping Layer effect

As all the measurements were done by having AFM tip as top electrode, there was no top electrode deposited on top of the GST layer as can be seen in sample description in table 5.1. Because of the lack of top electrode deposition, it is possible to oxidize the sample and this is why all the measurements were done in ultra-high vacuum. Following the work of Tanaka et al.[244] a 3nm GeN capping layer is used to cover the GST layer in order to prevent the oxidation of the sample. So, measurements with and without capping layer for GST-225 and GSTθ were done to see its effect on I-V characteristic and phase transition.

I-V characteristics of GST-225 without capping layer are shown in figure 5.6a. The 1st loop represents the phase transition from amorphous to crystalline with a threshold voltage of 0.8 V. 2nd and 3rd loop represent the crystalline phase. Without capping layer, the current starts increasing slowly with increasing voltage until it reaches the threshold voltage of 0.8V. As soon as the voltage reaches the threshold voltage, there is a sudden increase of the current implying the phase transition from amorphous to crystalline. Once the phase changed, the current increases linearly with voltage and when the ramp is reversed, the current decreases in the same way almost linearly with decreasing voltage. Still the current is not completely linear with voltage after changing the phase, a possible reason can be because the phase change is not complete in all the volume below the tip.

In figure 5.6b the I-V characteristic with capping layer is shown. The 1st loop represents the change in the phase from amorphous to crystalline. The current stays almost zero as the voltage is increased and once it reaches around 1.75 V there is a breakdown and current increases abruptly and then starts increasing linearly. One can expect that this apparent threshold voltage increase is due to the capping layer. It is worth noting that the threshold values observed with CAFM by Bashkaran et al.[242] and Yang et al.[235] are also much larger than the expected values for similar reason. The apparent threshold voltage enhancement observed is likely due to the dielectric breakdown of the insulating capping layer. It is difficult to see the threshold voltage here because threshold voltage is around 0.8 V for this sample. When

the breakdown in capping layer happens, the breakdown voltage for capping layer is larger than the threshold voltage and this is why the threshold voltage is not observable. In figure 5.6c, both with and without capping layer sample's characteristics are compared. After the breakdown or the threshold, the current-voltage behavior is the same for both samples between 0 V and 1.75 V. For sample without capping layer, the current keeps increasing linearly with voltage but in the case of capping layer, the current increases more rapidly after its breakdown.

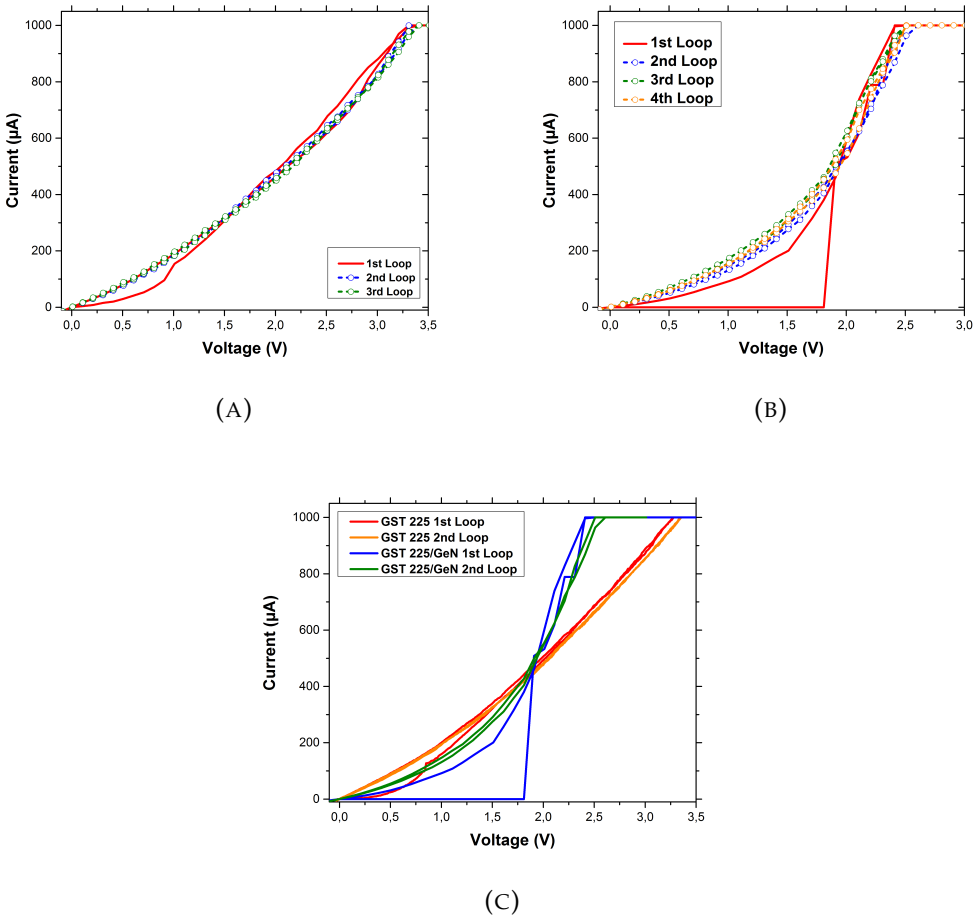

(A) (B)

(C)

FIGURE 5.6: I-V characteristic of $Ge_2Sb_2Te_5$ (GST-225) with full diamond AFM tip as top electrode. (a) without capping layer of GeN, (b) with capping layer of GeN and (c) comparison between both samples.

Same study was done for GSTθ sample with and without capping layer of GeN. A voltage ramp is applied to the sample in order to change the phase. I-V characteristic for sample without capping layer is given in figure 5.7a. One can see that the current stays almost negligible until 0.85 V. Then, there is a sudden increase followed by a continuous increase with increasing voltage. The threshold voltage (V_{th}) for GSTθ is around 0.85 V, which is almost similar to GST-225. Once the phase is changed, it stays crystalline for 2nd and 3rd loop. The current is not increasing linearly and one observes a large dispersion in successive current voltage characteristics compared to stoichiometric GST.

In figure 5.7b, one can see the I-V characteristic with capping layer. Again, there

is a breakdown in the capping layer around 1.5 V which is similar to the breakdown voltage in the case of GST-225 with capping layer. It seems there is two steps breakdown of the capping layer in the case of GSTθ. I-V characteristic for GSTθ with and without capping layer are compared in figure 5.7c.

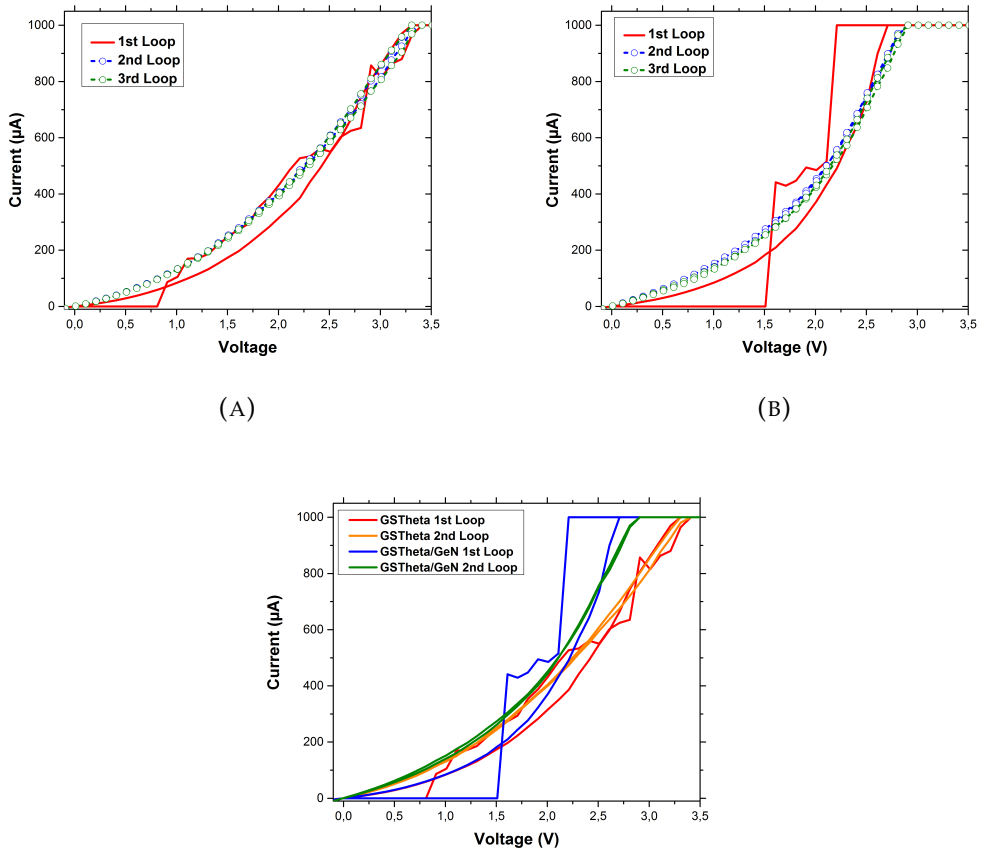

(A) (B)

(C)

FIGURE 5.7: I-V characteristic for GeSbTe-Theta (GSTθ) sample by having full diamond AFM tip as top electrode. (a) Without GeN capping layer, (b) with GeN capping layer and (c) comparison between both samples.

5.2.3 Topographical study for different PCM samples

Topographical study was also done for the sample with and without capping layer to see the effect on the surface of GST. It can be seen in figure 5.8a, that before the electrical characterization, the GST-225 surface is flat. But after doing electrical characterization, holes can be seen on the GST-225 surface as shown in figure 5.8b. I-V measurements for GST-225 were done at five different locations and the black spots in figure 5.8b represent the position of each measurement. Figure 5.8c shows the corresponding 3-D view. Same topographical study was done on the sample with GeN capping layer as shown in figure 5.9. The spots are wider than in the case without capping layer. As can be seen in the 3-D illustration, a pit kind structure is formed after electrical characterization in the GST layer. Because of the high contact force (50nN), the tip can penetrate the GST layer.

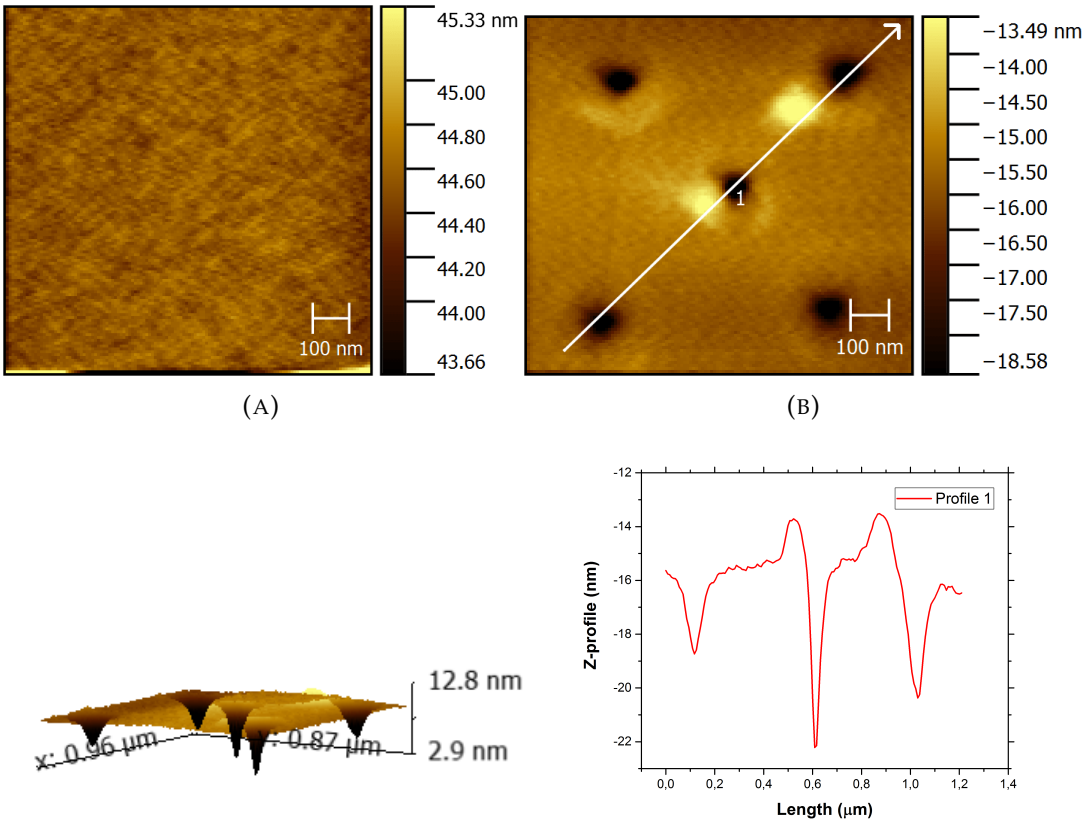

FIGURE 5.8: AFM topographical images of GST-225 without capping layer (a) before performing the electrical characterization, (b) after electrical characterizations, the white line represents the z-profile plotted in figure (d) and arrow represents the direction of the profile taken, (c) three-dimensional view of the image shown in figure (b), (d) the z-profile of the pit structures along the white line shown in figure (b).

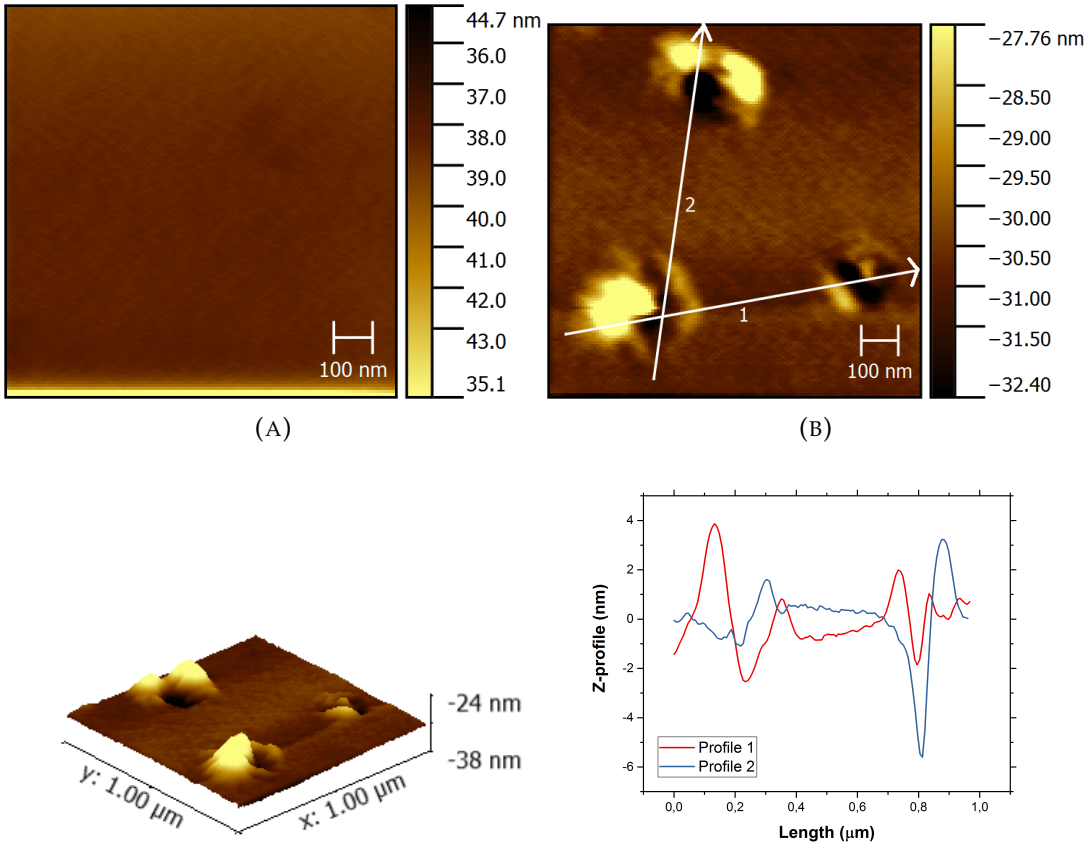

FIGURE 5.9: AFM topographical images of GST-225 with capping layer GeN (a) before performing the electrical characterization, (b) after electrical characterizations, the white line represents the z-profile plotted in figure (d) and arrow represents the direction of the profile taken, (c) three-dimensional view of the image shown in figure (b), (d) the z-profiles of the pit structures along the white line shown in figure (b).

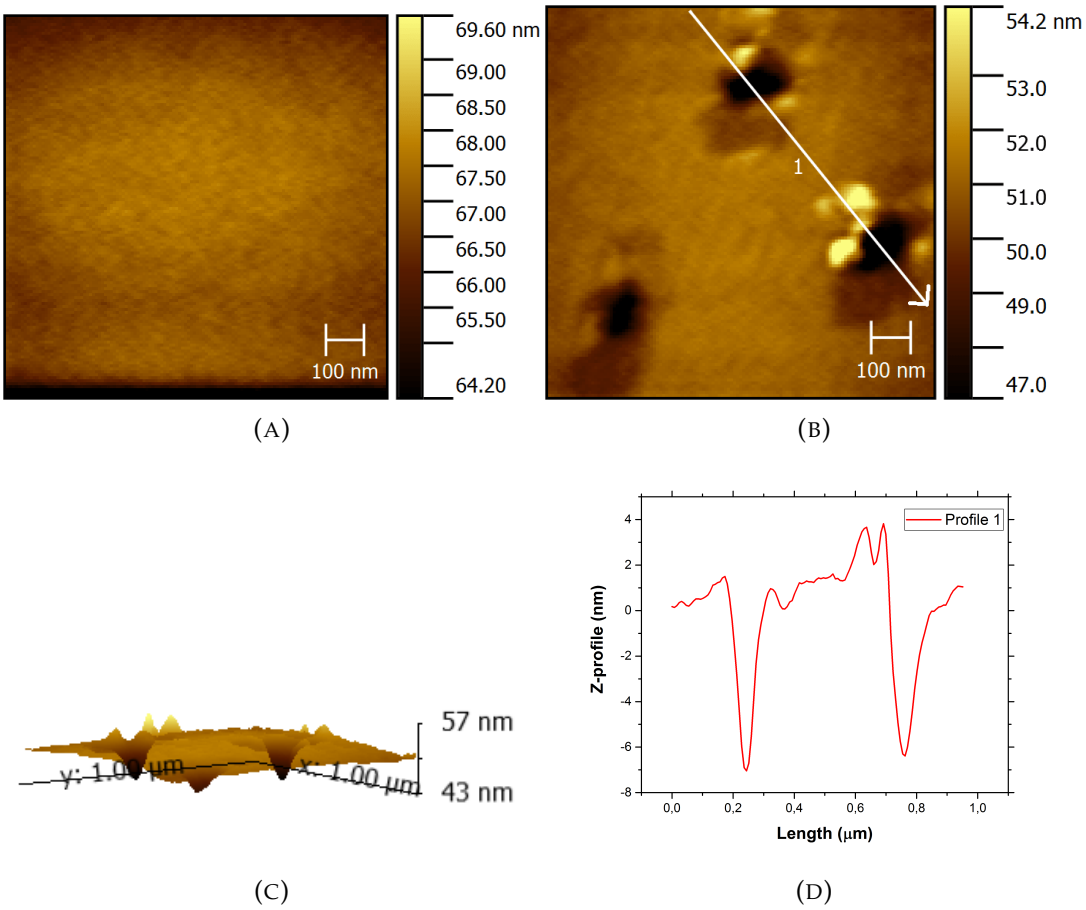

FIGURE 5.10: AFM topographical images of GSTθ without capping layer (a) before performing the electrical characterization, (b) after electrical characterizations, the white line represents the z-profile plotted in figure (d) and arrow represents the direction of the profile taken, (c) three-dimensional view of the image shown in figure (b), (d) the z-profile of the pit structures along the white line shown in figure (b).

Topographical images were taken for GSTθ with and without GeN capping layer before and after the electrical characterization as shown in figure 5.10 & 5.11 respectively. A pit structure can be seen for both samples. A possible reason for these pit structures will be discussed later.

5.2.4 GST 225 vs GSTθ

After comparing samples with and without capping layer, the GST-225 and GSTθ samples are compared. Let's start with the sample without capping layer. I-V characteristic for GST-225 and GSTθ are plotted on the same graph in figure 5.12a.

For the 1st loop, the current increases slowly with increasing voltage for GST-225 until it reaches the threshold voltage but in the case of GSTθ the current stays almost in pA range until it reaches the threshold voltage. The threshold voltage in the case of GST-225 is around 0.8 V and in the case of GSTθ is around 0.85V. The threshold voltage is not that different in both cases.

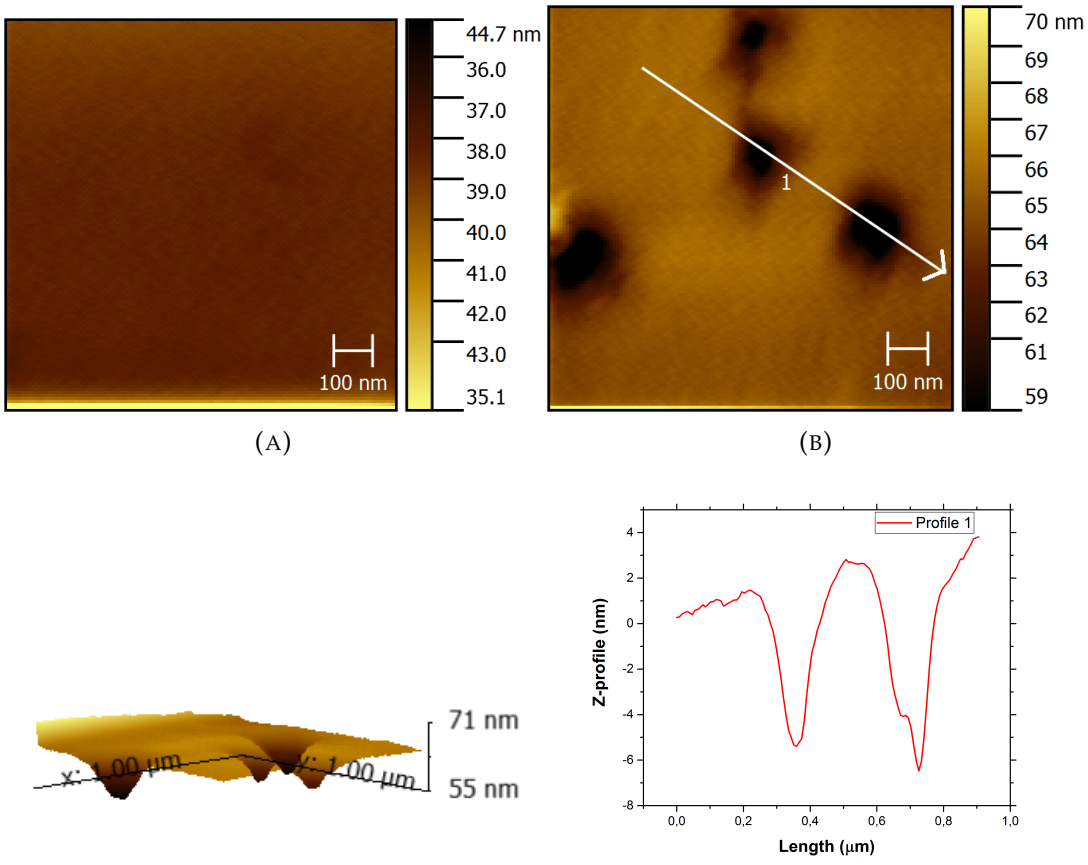

FIGURE 5.11: AFM topographical images of GSTθ with GeN capping layer (a) before performing the electrical characterization, (b) after electrical characterizations the white line represents the z-profile plotted in figure (d) and arrow represents the direction of the profile taken, (c) three-dimensional view of the image shown in figure (b), (d) the z-profile of the pit structures along the white line shown in figure (b).

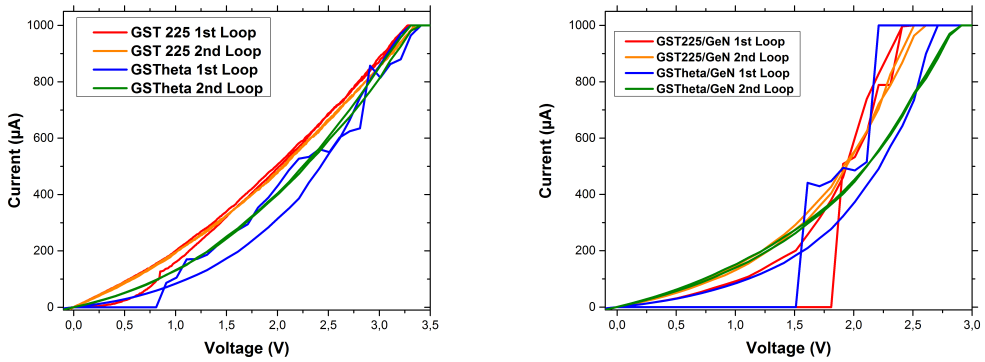

(A) (B)

FIGURE 5.12: Comparison for the I-V characteristic between GST-225 and GSTθ samples (a) without capping layer and (b) with capping layer.

The current in the case of GST-225 increases almost linearly with the voltage ramp implying that the phase is almost changed into crystalline and stays same for 2nd and 3rd loop also. But in the case of GSTθ, the current increases non-linearly with higher dispersion. Now GSTθ is a non-stoichiometric compound, implying that the material can crystallize in two crystalline phases i.e. roughly: Ge and GST 225. Thus, the conduction is likely the one of the compounds which is different from the GST 225 one alone. The conductance is higher in the case of GST-225 in crystalline state compared to the GSTθ.

I-V characteristic for the samples with capping layer is shown in the figure 5.12b. As can be seen, for the first loop the current stays almost zero in both cases. The breakdown for capping layer in the case of GST-225 happened around 1.75 V and 1.5V in the case of GSTθ. Once the breakdown occurred in capping layer, the voltage was enough to have a phase transition from amorphous to crystalline in both cases. 2nd loop in both cases is showing the I-V characteristic after changing the phase to crystalline. It can be seen from the figure 5.12b that the conductance stays same in the range of 0 V to 1.6 V for both samples. After 1.6 V, the conductance is lower in the case of GSTθ compared to GST-225. A discussion of phase transition for both samples will be given with the help of model in the discussion part.

5.3 Modeling

5.3.1 Analytic models for amorphous layers

To explain the experimental data two different models at device level were taken. Each model corresponds to different resistance states. For OFF state conductance a model was taken into account which is given by D. Ielmini et al.[198]. The model for ON state is taken from G. Navarro's thesis[199]. The model of each state will be discussed in brief here but can be found in more detail in respective references (ref). These models have been developed for the devices but we will take into account the same model for C-AFM measurements.

Off-state conductance model

Ielmini et al presented a model in their paper[198] based on the analysis of the Poole Frenkel mechanism. A simple one-dimensional analytical model was considered. They started the analysis by referring to the electron current at a specific trap energy E_T.

The electron velocity can be given by the average distance between two traps Δz divided by their average transfer time under the applied field. The transfer time in the same direction as the electrostatic force can be given by:

$$\tau_{\rightarrow} = \tau_o e^{\frac{E_C - E_T - qV_A\left(\frac{\Delta z}{2u_a}\right)}{k_B T}} \tag{5.1}$$

where τ_o is the characteristic escape time for a trapped electron, V_A is the applied voltage, q is the elementary charge, u_a is the amorphous chalcogenide thickness and $k_B T$ is thermal energy. The forward current is in the same direction as the electrostatic force and can be given by:

$$dI_{\rightarrow} = qAn_T(E_T)\frac{\Delta z}{\tau_{\rightarrow}}dE_T \tag{5.2a}$$

$$dI_{\rightarrow} = qAn_T(E_T)\frac{\Delta z}{\tau_o}e^{-\frac{\left[E_C - E_T - qV_A\left(\frac{\Delta z}{2u_a}\right)\right]}{k_B T}}dE_T \tag{5.2b}$$

where A is the area of the contact and $n_T(E_T)dE_T$ is the concentration of the electron in traps between E_T and $E_T + dE_T$. The reverse current is given similarly to equation 5.2 as

$$dI_{\leftarrow} = qAn_T(E_T)\frac{\Delta z}{\tau_o}e^{-\frac{\left[E_C - E_T + qV_A\left(\frac{\Delta z}{2u_a}\right)\right]}{k_B T}}dE_T \tag{5.3}$$

where the barrier lowering $-qV_A()\frac{\Delta z}{2u_a})$ is replaced by a barrier increase, by the same amount but opposite sign. The net current obtained from equation 5.2 and 5.3 is given by:

$$dI = qAn_T(E_T)\frac{\Delta z}{\tau_o}e^{-\frac{\left[E_C - E_F\right]}{k_B T}}sinh\left(\frac{qV_A}{k_B T}\frac{\Delta z}{2u_a}\right)dE_T \tag{5.4}$$

where the concentration of trapped electrons n_T has been replaced by

$$n_T(E_T) = N_T(E_T)e^{-\frac{(E_T - E_F)}{k_B T}} \tag{5.5}$$

which is the concentration of the traps $N_T(E_T)$ at energy level E_T multiplied by Maxwell-Boltzmann approximation of the Fermi distribution function at E_T.

From equation 5.4, the current can be obtained by integrating over the entire distribution of electron traps i.e., above E_F, leading to

$$I = 2qAN_{T,tot}\frac{\Delta z}{\tau_o}e^{-\frac{(E_C - E_F)}{k_B T}}sinh\left(\frac{qV_A}{k_B T}\frac{\Delta z}{2u_a}\right) \tag{5.6}$$

where $N_{T,tot}$ is the integral of the trap distribution in the gap above Fermi level. The real trap distribution in chalcogenide material is unknown. The inaccuracies of equation 5.4 are neglected for E_T close to E_F and to E_C and will treat $N_{T,tot}$ as an effective trap concentration.

On-state conductance model

G. Navarro in his thesis[199] explained about the On-state model for PCM at device level in detail but here a brief overview is presented. On-state electrical conductivity with the classical temperature activated equation for semiconductor materials is given by

$$\sigma_{on}(E,T) = \sigma_{o-on}(E,T)e^{-\frac{E_{cr}}{k_B T}} \tag{5.7}$$

where E_{cr} is the activation energy of the conduction of the crystalline phase. σ_o describes the conductivity at higher fields and higher current densities as given below:

$$\sigma_{o-on}(E,T) = \sigma_c \frac{e^{\sqrt{\frac{q|\vec{E}|\lambda}{k_B T}}}}{1 - e^{-\frac{W_{on}}{k_B T}}} \tag{5.8}$$

where σ_c is a constant, q is the elementary charge, λ is the percolation distance and W_{on} is the activation energy of the On-state. When the temperature increases by joule heating in the material, the temperature can be estimated by

$$T = \alpha_{th}\, \vec{J}.\vec{E} + T_o \tag{5.9}$$

where $T_o$is the ambient temperature and α_{th} the efficiency term ($\propto 1/k_{th}$). With temperature rise, the σ_o becomes:

$$\sigma_{on} = \frac{\sigma_c k_B}{W_{on}}(\alpha_{th}\, \vec{J}.\vec{E} + T_o) \tag{5.10}$$

By using Ohm's law from equation 5.10 we can say that:

$$\vec{J} = \frac{\sigma_c k_B}{W_{on}}(\alpha_{th}\, \vec{J}.\vec{E} + T_o)\,\vec{E} \tag{5.11}$$

And the current can be given in terms of σ_{on} with series resistance R_s.

$$I(V,T) = \frac{V}{R_s + \frac{d}{\sigma_{on}(V,T).S}} \tag{5.12}$$

5.3.2 Finite Elements Method (FEM) Approach

The physical mechanism for phase change for GST by using C-AFM involves the electrical, thermal and phase transformation process. A model for phase change in phase change material by using C-AFM was given by Wang et al.[336]. Here, also the same model is adopted by using COMSOL Multiphysics© as proposed by Wang et al and is described briefly. We consider that GST material is a semiconductor with traps in the gap[337] and its electrical conductivity is modeled through a field and

temperature dependent function. In addition, this model relies on a phase dependent electrical conductivity for the GST using the variable f_x which is the crystalline phase fraction:

$$\sigma_{GST} = \sigma_{am}(1 - f_x) + \sigma_{cryst} f_x \tag{5.13}$$

The electric conductivity of the crystalline GST is given by

$$\sigma_{cryst} = \sigma_c \frac{e^{\sqrt{\frac{q|\vec{E}|\lambda}{k_B T}}} e^{\left(\frac{-E_c}{k_B T}\right)}}{1 - e^{-\frac{W_{on}}{k_B T}}} \tag{5.14}$$

where σ_c is a constant and E_c is activation energy for crystallization. The electric conductivity of the amorphous GST ($\sigma_a m$) is given by considering the Poole-Frenkel Mechanism[338]:

$$\sigma_{am} = \left(\frac{2k_B T}{q j_o \Delta z} exp\left(\frac{E_A}{k_B T}\right) csh\left(\frac{qF\Delta z}{2k_B T}\right) \right)^{-1} \tag{5.15}$$

where F is the electric field, Δz is the average distance between localized state, E_A is the activation energy for Poole Frankel conduction, k_B is Boltzmann's constant, q is electron charge, j_o is the integral of the trap distribution in the gap above the fermi level and T is the temperature.

The classical heat transfer equation is taken into account for the temperature distribution inside GST. The resolution of the Laplace equation coupled to the heat equation gives the electric field distribution inside GST that can be used to calculate the joule heating source for the heat transfer equation. The classical heat transfer equation is taken into account for the temperature distribution inside GST. The thermal conductivity of GST exhibits the temperature dependence for crystalline GST. Wang et all gave thermal conductivity for crystalline GST by using power law:

$$K_{cryst} = 5 \times 10^{-4} exp\left(\frac{T}{100}\right) + 0.4 \tag{5.16}$$

where K_{cryst} is the thermal conductivity of the crystalline GST in W/(m.K). The generated temperature distribution is then used in the phase transforming using a phase change model. Wang et al gave a rate equation for evaluating the phase change process which enables the calculation of crystal fraction of GST medium (f_x) and given by

$$\frac{df_x}{dt} = (1 - f_x) k_x \tag{5.17}$$

where k_x is the thermally activated kinetic constant and can be given by

$$k_x = \left(t_{x1} exp\left(\frac{E_{x1}}{k_B T}\right) + t_{x2} exp\left(\frac{E_{x2}}{k_B T}\right) \right)^{-1} \tag{5.18}$$

where t_{x1} and t_{x2} are the preexponential factors and E_{x1} and E_{x2} the activation energies. The thermal conductivity K_{cryst} is considered phase dependent

$$K_{GST} = K_{am}(1 - f_x) + K_{cryst} f_x \tag{5.19}$$

where K_{am} is the thermal conductivity of amorphous GST considered constant. This model is implemented in COMSOL. A ramp voltage is considered similar to the one used for experiments. The AFM tip was grounded and voltage was applied on the sample. The values used for the COMSOL model for all the parameters mentioned above are given in table 5.2.

Parameter	Value
Δz	$3.3 \times 10^{-9}\ m$
j_o	$1 \times 10^{12}\ A/m^2$
E_A	$0.2\ eV$
E_C	$0.15\ eV$
σ_c	$2 \times 10^{5}\ S/m$
λ	$0.5 \times 10^{-9}\ m$
W_{on}	$0.5\ eV$
t_{x1}	$1.5 \times 10^{-29}\ s$
t_{x2}	$1 \times 10^{-14}\ s$
E_{x1}	$2.9\ eV$
E_{x1}	$1.1\ eV$
K_{am}	$0.2\ W/(m.K)$

TABLE 5.2: Different parameter values used for the GST-225 FEM model.

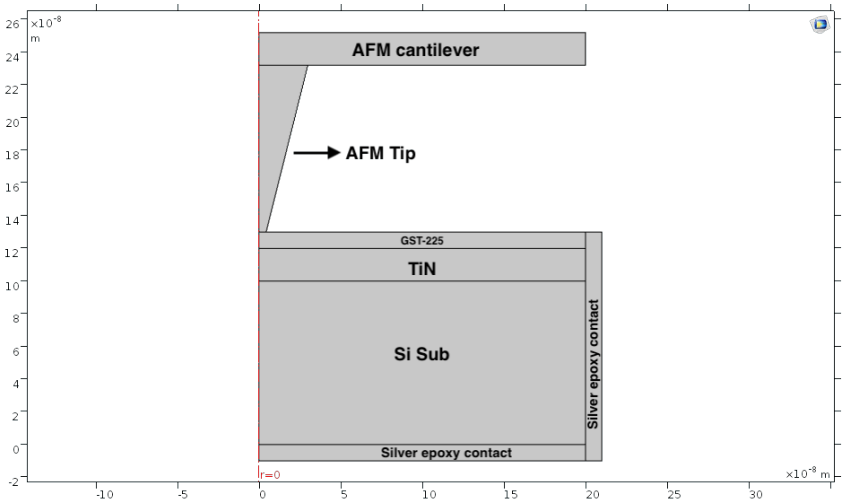

FIGURE 5.13: Schematic used for geometric modelling in the FEM approach for GST-225.

In figure 5.13, a typical C-AFM setup for phase change material designed by using COMSOL is shown. After designing the setup, the theoretical model explained above is applied. Different values for different parameters given in table 5.2 are used to run the simulations

5.4 Discussion

In this part we will use the above described models to interpret our measurements. In figure 5.14a for GST225, it can be seen that the experimental data is fairly well fitted by the analytical models for On-state and Off-state. The current in off state is calculated by using equation 5.6 given by Ielmini et al. And the current for On-state is calculated by using the equation 5.12 for the model given by G. Navarro. As we can see, the models with the parameter values of tables 5.3 and 5.4 fit correctly the experimental characteristics. The values in table 5.3 are completely similar to the values used for the devices. The tip- GST contact area radius in the calculations is 100nm (table 5.3) which is reasonable for blunt tips. Thus, the CAFM measurement at least for set experiment in voltage ramp regime is valid. The aforementioned models do not deal with the threshold field. The value measured here is 0.8V for 10nm thick layer of GST i.e. 0.8 MV/cm (figure 5.14a). Krebs et al.[339] measured it on devices with 1000 nm^2 area at 0.56 MV/cm which is really comparable. Finally, the On-state ohmic behavior is explained by the enhancement of On-state conductance with temperature that turns to limit the total current by the serial resistance R_s (equation 5.12).

Parameter	Value
Contact Surface Area(A)	$3 \times 10^{-14}\ m^2$
N_T	$\frac{3}{4\pi(\Delta z^3)}$
Δz	$2.9 \times 10^{-9}\ m$ for GST-225 $0.8 \times 10^{-9}\ m$ for GSTθ
τ_o	$1 \times 10^{-15}\ s$
u_a	$10 \times 10^{-9}\ m$
$E_C - E_F$	$0.3\ eV$

TABLE 5.3: Different parameters used for Ielmini et al model to model the OFF state of phase change materials.

Parameter	Value
σ_c	$2 \times 10^5\ S/m$
λ	$0.5 \times 10^{-9}\ m$
W_{on}	$0.5\ eV$
d	$10 \times 10^{-9}\ m$
S	$7 \times 10^{-18}\ m^2$
R_s	$5.16 \times 10^3\ \Omega$

TABLE 5.4: Different parameters used for Navarro et al. model to model the ON state of phase change materials.

In figure 5.14b for GSTθ, one can see that the experimental characteristics are only matching with the Ielmini et al model explaining that the amorphous phase was not completely changed into crystalline phase. Different values used for different parameters for ON state and OFF state simulation are given in table 5.3 and 5.4. As can it be seen in the table 5.3, the only difference for GST-225 and GSTθ for off state is the Δz value. For GST-225 it is 2.9 nm and for GSTθ it is 0.8 nm. This difference in the Δz is just a way to adapt the Ielmini model for GSTθ. It is difficult to really correlate

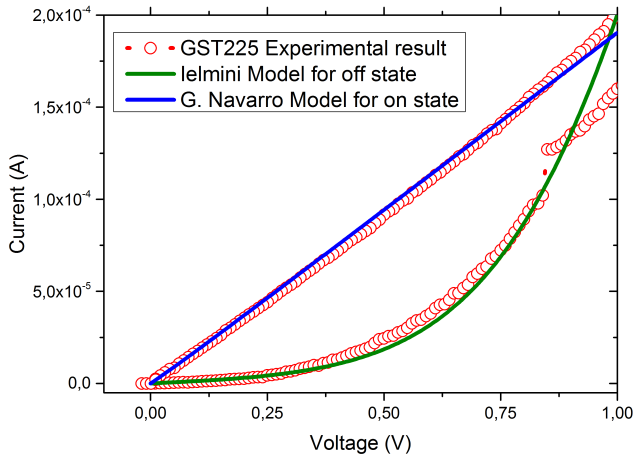

(A)

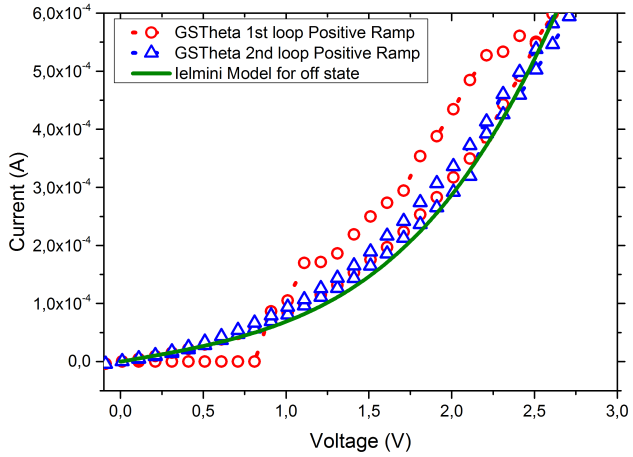

(B)

FIGURE 5.14: (a) I-V characteristic for phase change material with simulated fit obtained by different models for On-state and OFF state (a) for $Ge_2Sb_2Te_5$ (GST-225), (b) GSTθ.

the composition change with the Δz value. The model has to be reconsidered by implementing a multi-phase material with Ge and GST-225 conductivity mixing in an effective medium model for example, which is out of scope for this work.

Moreover, in figure 5.12a, a comparison between the I-V characteristic of GST-225 and GSTθ is also presented. It can be seen that the on-state conductance is higher for GST-225 compared to GSTθ. This is also observed for Off state amorphous phase. This behavior is consistent with the observation of Sousa et al.[340] reported in figure 5.15 which represent the resistance of GST layer as a function of temperature. The resistance is recorded first from low to high temperature. When the temperature increases the high resistance characteristic suddenly decreases which corresponds to the phase transition from amorphous to crystalline phase. The lower part of the curves corresponds to the cooling down in the crystalline phase. It can be seen in this

figure that the resistivity is higher for Ge enriched phases compared to stoichiometric GST-225. Moreover, one can see the enhancement of the transition temperature with Ge content in GST. Once the crystallization is achieved the resistance decreases with temperature for Ge rich samples (∼semiconducting behavior) conversely to GST 225 (∼metallic behavior). This is consistent with formation of separate Ge and GST 225 phases after Ge rich GST crystallization. This was confirmed [340] with the help of X-ray diffraction technique that the crystallization for Ge rich GST corresponds to the formation of Ge and GST-225 cubic phase which maybe the reason for difference in resistivity. This can be the reason for higher conductivity in GST-225 compared to GSTθ for the study presented in this thesis.

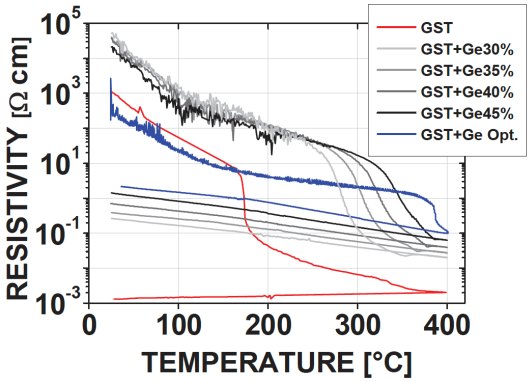

FIGURE 5.15: Resistivity versus temperature for GST-225 and Ge-rich GST (GSTθ) thin films, showing the increase of the crystallization temperature with increasing Ge content(taken from reference [340]).

We observed hillocks in the case of OxRAM as discussed in chapter 4 but in the case of GST material we observed pit like structures as shown in figure 5.7, 5.8, 5.10 & 5.11. The reason behind this may be that the HfO_2 layer for OxRAM has a higher hardness and young's modulus compared to GST for PCRAM. In literature, the young's modulus for HfO_2 is found around 153±13 GPa and hardness is around 8.4±04 GPa [341]. On the other hand, for GST, the value of young's modulus is found around 27.8±6.49 GPa for amorphous phase and 48.6±4.73 GPa for crystalline phase in literature [343]. And the value of hardness in literature for amorphous GST is found ∼1.5-2 GPa and for crystalline GST, it is ∼3-3.5 GPa [343]. Considering the radius of the tip ∼100nm a force of 50 nN gives rise to pressure in the order of magnitude of a few MPa. Thus, whatever the above-mentioned material Young modulus values, the deformation should be negligible. D'Arrigo et al. [344] studied the mechanical properties of as deposited GST-225 and presented the penetration depth as a function of the load force in indentation experiments. According to their work, a force of 50 nN would lead to a penetration depth of about 1 nm for a tip contact area of 50 nm^2 which is low compared to our case (∼ 10^4 nm^2 for blunt tips). Kim et al. [342] for nanolithography purpose also observed indented structures with C-AFM for high voltages (6-10 V) on as deposited GST-225, which can be seen in figure 5.16. This figure confirms that the effect is not purely mechanical, as no deformation on the surface was observed for low voltages. Thus, one may assume that the effect of phase change during the current voltage measurements and penetration of the tip when melting may be responsible for the observed pits.

The value of R_s is in the order of few $k\Omega$ as given in table 5.4. The high value of this serial resistance might be linked to the pit formation on the surface of the GST

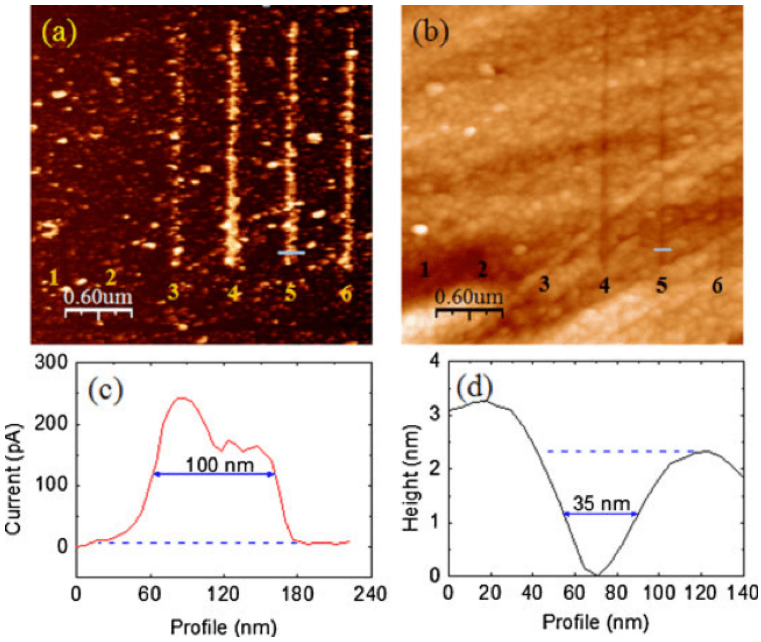

FIGURE 5.16: (a) AFM conductance image, (b) Topography image of crystallized wire-array on a-GST film. Wires 1, 2, 3, 4, 5, and 6 were fabricated with bias voltages, -1, -2, -4, -6, -8, and -10 V, respectively, (c) and (d) show line profiles along the solid lines of wire 5 in (a) and (b), respectively (taken from reference[342]).

during the electrical measurements.

Nevertheless, according to figure 5.14a it is not completely sure to observe any phase transition for GSTθ. However, as it was mentioned in the beginning of this chapter the crystallization temperature of GSTθ is about 350°C. Thus, we plot equation 5.9 in figure 5.17, to evaluate the temperature due to Joule heating. The crystallization temperature (°K) for GST-225 is plotted in green and the crystallization temperature for GSTθ is plotted in blue in figure 5.17. It can be seen that temperature calculated from equation 5.9 was lower than the crystallization temperature of GSTθ and this let us believe that the phase change is not observed in this case. However, a Multiphysics finite element approach taking into account the geometry of the problem may lead to a different conclusion.

In figure 5.18, FEM simulation for GST-225 crystallization are shown. For a ramp voltage applied between the AFM tip and the bottom electrode with a speed of 0.125 V/s. The color scale in figures 5.18 ranges from blue for the amorphous phase to dark red color for the crystalline phase for GST-225. Figure 5.18a is shown at 2 sec which corresponds to a mean voltage of 0.25 V. The following figures 5.18b-5.18f and 5.19a-5.19c are a zoom corresponding to the black box shown in figure 5.18a. So, figure 5.18b shows the zoomed area at 2s. It can be seen that there is no crystal fraction at 2s. Once it reaches 5s which means 0.625V, the phase starts changing from amorphous to crystalline and crystal fraction can be seen in figure 5.18c. Which means that 0.625V is the threshold voltage at which the phase starts changing. Also, the temperature distribution in GST layer at different voltages is shown in figure 5.19. At 2 sec when the voltage is 0.25V, the temperature is reaching around 300°K (see figure 5.19a) where the tip is in contact with the GST layer. With increasing time, the

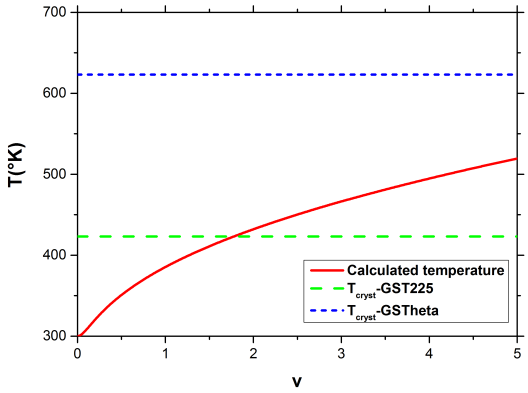

FIGURE 5.17: Temperature variation in the phase change material because of the joule heating is shown in red. In green the crystallization temperature of GST-225 and in blue the crystallization temperature of GSTθ are given.

joule heating increases due to increasing voltage and electric field. Because of this, increase in joule heating increases the temperature where tip is in contact with GST layer and is reaching around 900°K as can be seen in figure 5.19b. When the temperature is high, the crystalline fraction keeps growing with time and temperature. One can see in figure 5.19c that the temperature is still increasing with increasing the crystal fraction at 10 sec reaching around 1100°K. Now the melting temperature is 875°K (600°C). Thus, from FEM the temperature is high enough to melt a part of GST-225. From figure 5.18c to figure 5.18f, crystalline phase growth can be seen. It is much more difficult to implement such a simplified model for Ge rich material because of multiple phase crystallization. This is then out of scope for this work as the pit formation mechanism simulation, but deserve future numerical investigations. One can see that conversely to the unidimensional model (figure 5.17) the temperature is sufficient to crystallize even GSTθ.

5.5 Conclusion

In this chapter, we presented a C-AFM study of the electrical characteristics of phase change materials at nanoscale. The electrical measurements were recorded on GST-225 and GSTθ samples by using blunt full diamond tip. For GST-225 sample, the electronic threshold field is around 0.8 MV/cm which is comparable to values measured in devices. This is a progress compared to previous measurements done in literature that exhibit larger values. The current voltage characteristics in the set state are satisfactorily reproduced with classical models with the same parameters as for devices. This validates our method. Once the phase is changed from amorphous to crystalline it stayed in the same state for coming loops as it is difficult to switch back to amorphous by using voltage ramp by C-AFM. In fact, the reset process needs to follow the fusion by quenching and needs then a very short current pulse. This will be the object of forthcoming work. Other two samples with a capping layer of GeN were also studied. Because of the capping layer, it was difficult to see the threshold voltage because its breakdown voltage was around -1.5V - 1.75 V for both samples. This breakdown voltage is high enough to change the phase from amorphous to crystalline. For GSTθ, the threshold voltage is found around 0.85V.

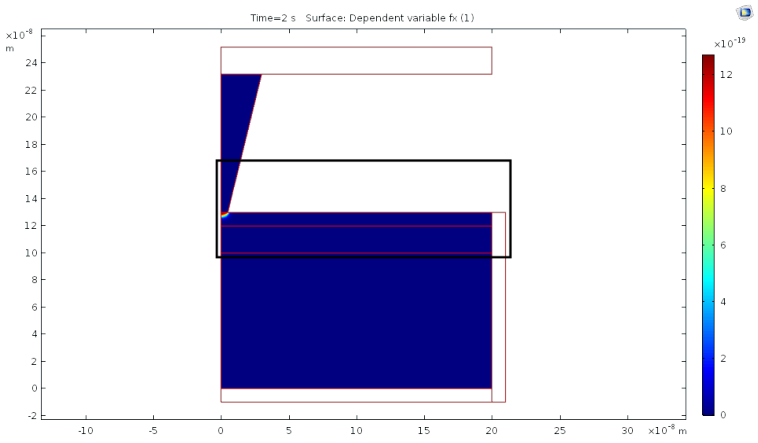
Time=2 s Surface: Dependent variable fx (1)
×10⁻⁸ m
×10⁻¹⁹

(A)

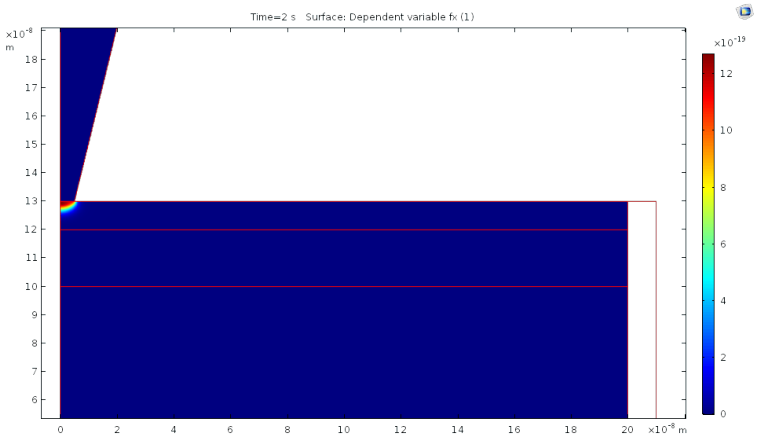
Time=2 s Surface: Dependent variable fx (1)
×10⁻⁸ m
×10⁻¹⁹

(B)

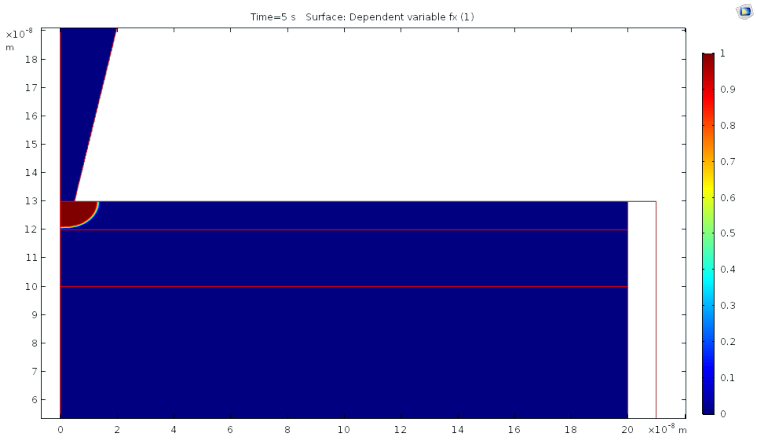
Time=5 s Surface: Dependent variable fx (1)
×10⁻⁸ m

(C)

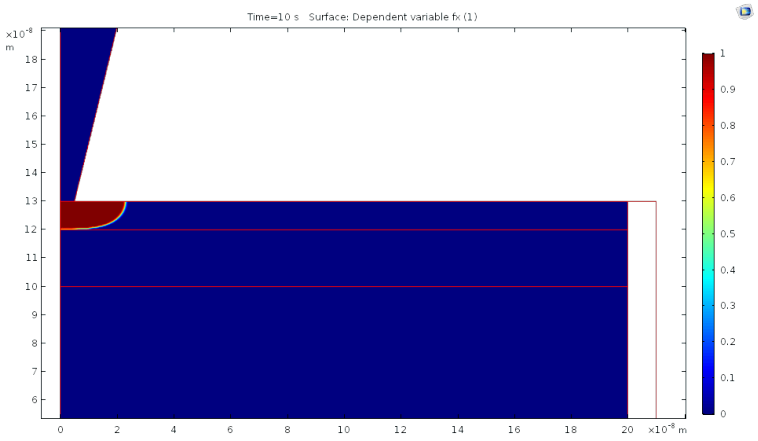
Time=10 s Surface: Dependent variable fx (1)
×10⁻⁸ m

(D)

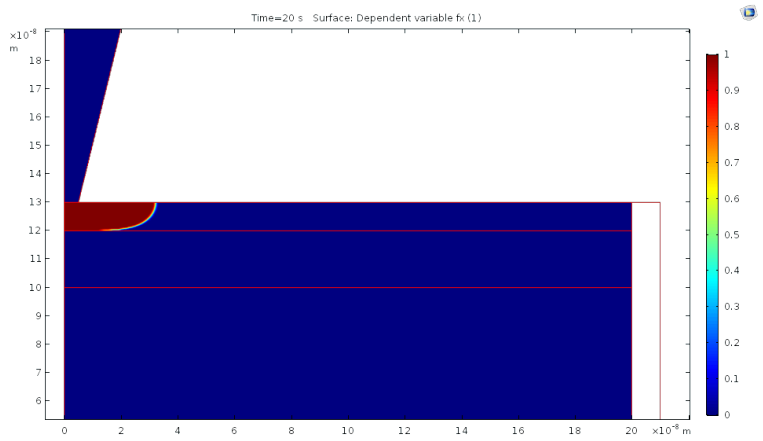

(E)

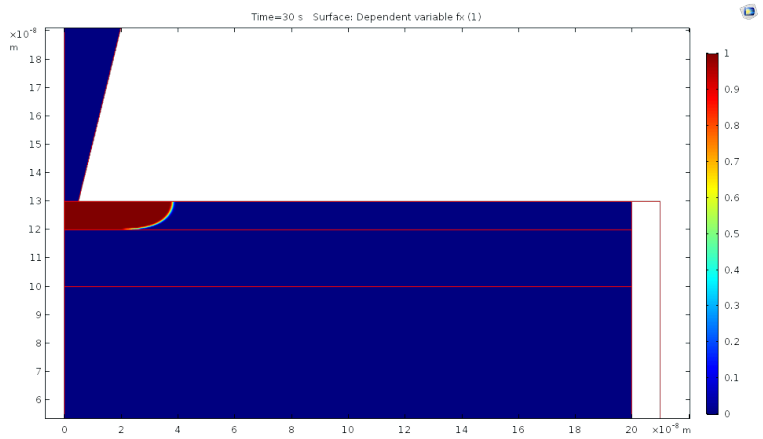

(F)

FIGURE 5.18: Simulation for GST-225 by using COMSOL Multiphysics© considering the model given by Wang et al. The model is showing the phase transition from amorphous to crystalline. Blue color for GST layer is showing amorphous phase and dark red color is showing crystalline phase. (a) Simulation for GST with voltage ramp speed of 0.125V/s is given at 2s, for showing the whole system. Simulation for GST at different times is shown (b) at 2s, (c) 5s, (d), 10s, (e) 20s, (f) 30s.

Topographic AFM images reveals important pits after measurements whatever the studied samples, which might be attributed to phase transform and melting combined with the tip pressure. A comparison between GST-225 and GSTθ is also presented. After changing the phase from amorphous to crystalline, the conductivity of on state is larger for GST-225 compared to GSTθ consistently with previous observations for the samples without capping layer and the GSTθ characteristic might likely be explained by a Ge & GST-225 phase separation after crystallization.

Finite element simulation were performed by using an approximate model given by Wang et al21. It was able to reproduce the switch of the phase from amorphous to crystalline and to show that although the tip narrowing the temperature reached in the GST layer is sufficient for crystallizing and even melt the PCM material. The reset step that needs short current pulses will be the object of further work.

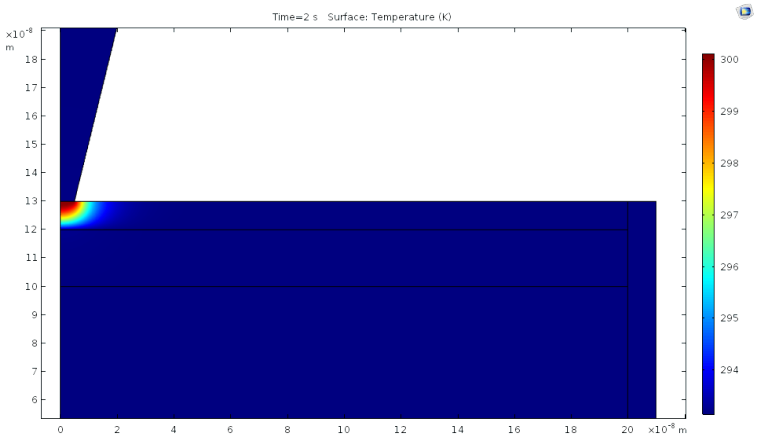

(A)

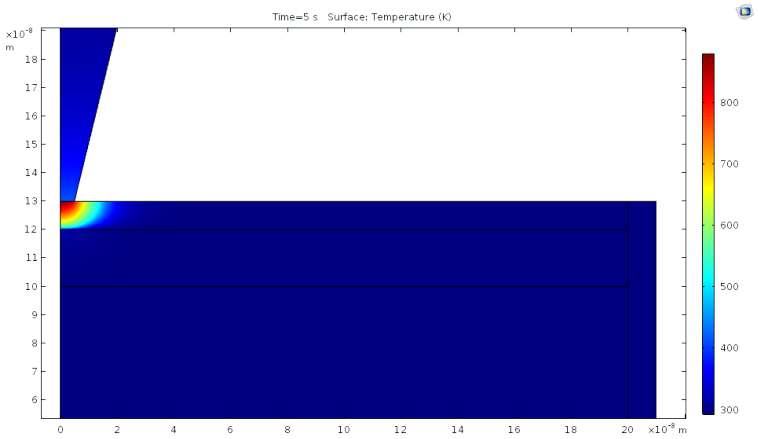

(B)

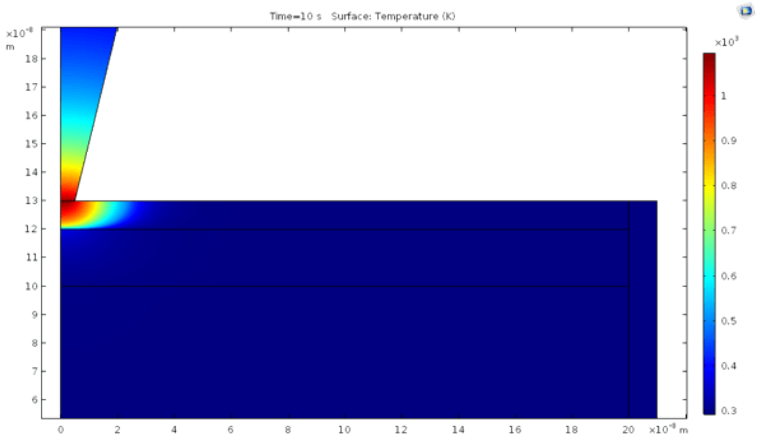

(C)

FIGURE 5.19: Temperature variation in GST-225 (a) at 2 sec, (b) at 5 sec and (c) at 10 sec.

Conclusion & Perspective

This manuscript addresses resistive switching mechanisms occurring in OxRAM and PCRAM memories. Both types of non-volatile memories were characterized by conductive atomic force microscopy (C-AFM) in ultra-high vacuum to avoid electrochemical reactions. As explained in the chapter 1, the switching mechanism in OxRAM is a debatable topic and many studies are ongoing to understand the nature and composition of the filament. In this work, we analyze the resistive switching and filament growth mechanism inside the oxide layer for OxRAM.

The OxRAM memory is based on conductive filament creation and disruption. The diameter of a filament is in the order of nm and it is necessary to study the characteristic of a single filament in the oxide layer in order to understand its nature. Normally in devices, the electrodes are much larger than the filament dimension, as it is difficult to go to few nm in size with the limitation of lithography. C-AFM is a very useful tool to overcome this problem, as a conductive AFM tip in nm range can be used as top electrode to study the switching mechanism of a single filament at nanoscale. Two different AFM tips (PtSi and boron doped full diamond tips) were used.

For OxRAM, two different HfO_2 based samples with different bottom electrodes (TiN and TiN/Ti) were studied by I-V characterization. First of all, a study of the switching behavior in OxRAM was performed. It was found that the TiN/HfO_2 sample is showing bipolar behavior with both AFM tips and the $TiN/Ti/HfO_2$ sample is showing non-polar switching behavior (both Unipolar and Bipolar).

Once the switching behavior is known for both samples, the effect of compliance current was studied in detail for both samples. First of all, I-V characteristics were performed in nA range and it was found that there was no memory effect but cycling between two reversible states was observed. The nonlinearity of the current and absence of memory effect at low compliance (nA) were discussed by comparison with a filament growth model. It was found that for this low compliance current it was not possible to form a fully-grown filament. The current cycling was assumed to be due to tunneling between the end of the filament and the CAFM tips. According to polarity, the filament height in the films evolves between to values that in turn fix the tunneling length, explaining quantitatively the cycling. In μA range, it was found that the on-state current is becoming linear with voltages if the compliance current is higher than a threshold current necessary for memory effect. The on-state conductance of $TiN/Ti/HfO_2$ stacks is found almost similar to 1T1R devices.

After comparing the resistive switching in low and high compliance current regime, a more detailed study was performed in high compliance current regime. First of all, the effect of different tips was studied on both samples. I-V characteristics were taken by using both sharp PtSi and boron doped full diamond tips. It was found that the ON state and OFF state do not depend on the tip material and that the I-V characteristics were not reproducible with the sharp tips. Then a blunt full

diamond tip was used to mimic the dimension of the electrodes in devices. It was found that the I-V characteristics were more reproducible than with a sharp tip.

After performing the electrical characterization, topographical images of HfO_2 surface were taken and hillock like structures were found at the place where electrical measurement was done. To understand the chemical composition of these hillocks, tip contamination after electrical measurements was analyzed by SEM-EDX. It was found that Ti was present on the tip, which could only come from the bottom electrode, meaning that the filament is formed by Ti migration through the oxide layer.

A model was adapted by considering a Ti filament inside the oxide layer and the simulated results were in good agreement with the experimental ones. The model was discussed for both sharp tip and blunt tips. For sharp tips, the Off-state tunneling current barrier is consistent with a (Pt or C tip) $/HfO_2/Ti(filament)$ interface and for blunt tips and devices, it is consistent with a $Ti/TiO_x/Ti$ interface, due to the migration of Ti from the bottom electrode to the tip, confirming that the filament is composed of Ti in our case. There was no effect of polarity on the resistive switching characteristics, meaning that Ti migrates through the layer in the vicinity of the dielectric breakdown path, where the temperature is very high, by diffusion rather than by drift.

The results obtained by C-AFM were compared to 1T1R devices and the on-state conductance was found almost similar for both. By modeling, we concluded that in Off-state, there is a difference in the geometry of the disrupted filament in both cases. This geometrical difference leads to variations of the electron flux transmission factor that accounts well for larger set voltages in the case of AFM tips compared to devices. The larger reset voltages observed for C-AFM were explained by a shallower filament constriction position and assumed to be linked to a higher breakdown electric field.

So, the final conclusion for OxRAM is that it is possible to scale it down and to have resistive switching at nanoscale by using C-AFM. Also, the switching is based on the formation and disruption of a Ti filament inside the oxide layer.

For PCRAM, two different compositions of GeSbTe material were used. One is $Ge_2Sb_2Te_5$ (GST-225) and the other one is Ge rich $GeSbTe(GST\theta)$ whi ch is suitable for automotive application thanks to its higher crystallization temperature. Both materials were studied with and without GeN capping layer. I-V characteristics were performed using the same setup and procedure as for OxRAM characterization. A threshold voltage for both samples was observed. For GST-225 it was found 0.8 V and for GSTθ it was found 0.85V for 10 nm thick samples which is very near to the observations on devices.

By comparison with analytical models for on state and off state in literature, the experimental results were discussed. We found out that in the case of GST-225 the current voltage characteristics are comparable to the observed one on standard devices. In particular, the amorphous Off-state conduction can be modelled with the same material parameters than the devices. The ratio between Off and On state resistances is more than one decade showing that the memory works at this scale. In the case of GSTθ, we were not able to model the state likely because of the phase separation between Ge and GST-225 during the crystallization which requires a proper approach even if we measure the threshold and observe the two resistive states. For

the samples with capping layer, it was difficult to see the threshold voltage because its breakdown voltage was in the range of -1.5V and - 1.75 V for both samples. This breakdown voltage is high enough to change the phase from amorphous to crystalline. Also, finite element method approach was considered by using COMSOL Multiphysics and phase transition in GST-225 was shown. Finally, topographical images after current voltage measurements revealed important pits whatever the material and capping layer. Those pits may be attributed to the combined effect of phase transform, melting and mechanical force of the CAFM tip.

For the perspective, it is necessary to study the PCRAM in detail. Here in this work the phase transition was studied by using a voltage ramp. Because the reset necessitates a melting and quenching step the use of short pulse is mandatory. A detailed study by using pulse with C-AFM setup is necessary and will be the object of future work. Also, a study related to different phase change materials at nanoscale is desirable. Different OTS materials for PCRAM and materials for interfacial phase change memory (iPCM) also need to be studied.

Bibliography

[1] An Chen. A review of emerging non-volatile memory (NVM) technologies and applications. *Solid-State Electronics*, 125:25–38, 2016. ISSN 00381101. doi: 10.1016/j.sse.2016.07.006. URL http://dx.doi.org/10.1016/j.sse.2016.07.006.

[2] Sreedhar Natarajan, Shine Chung, Lluis Paris, and Ali Keshavarzi. *Searching for the dream embedded memory*, volume 1. feb 2009. doi: 10.1109/MSSC.2009.933521.

[3] Mark H. Kryder and C Kim. *After Hard Drives—What Comes Next?*, volume 45. nov 2009. doi: 10.1109/TMAG.2009.2024163.

[4] Jagan Singh Meena, Simon Min Sze, Umesh Chand, and Tseung Yuen Tseng. Overview of emerging nonvolatile memory technologies. *Nanoscale Research Letters*, 9(1):1–33, 2014. ISSN 1556276X. doi: 10.1186/1556-276X-9-526.

[5] Livio Baldi, Roberto Bez, and Gurtej Sandhu. Solid-State Electronics Emerging memories. *Solid State Electronics*, 102:2–11, 2014. ISSN 0038-1101. doi: 10.1016/j.sse.2014.06.009. URL http://dx.doi.org/10.1016/j.sse.2014.06.009.

[6] Ming Jer Kao and E O L Itri. Emerging Non-volatile Memory. pages 109–113, 2010.

[7] D Kahng and S M Sze. A floating gate and its application to memory devices. *The Bell System Technical Journal*, 46(6):1288–1295, 1967. ISSN 0005-8580 VO - 46. doi: 10.1002/j.1538-7305.1967.tb01738.x.

[8] F Masuoka, M Asano, H Iwahashi, T Komuro, and S Tanaka. A new flash E²PROM cell using triple polysilicon technology. In *1984 International Electron Devices Meeting*, pages 464–467, 1984. ISBN VO -. doi: 10.1109/IEDM.1984.190752.

[9] F Masuoka, M Momodomi, Y Iwata, and R Shirota. New ultra high density EPROM and flash EEPROM with NAND structure cell. In *1987 International Electron Devices Meeting*, pages 552–555, 1987. ISBN VO -. doi: 10.1109/IEDM.1987.191485.

[10] Paolo Pavan, Roberto Bez, P Olivo, and Enrico Zanoni. *Flash Memory Cells—An Overview*, volume 85. sep 1997. doi: 10.1109/5.622505.

[11] R Bez, E Camerlenghi, A Modelli, and A Visconti. Introduction to flash memory. *Proceedings of the IEEE*, 91(4):489–502, 2003. ISSN 0018-9219 VO - 91. doi: 10.1109/JPROC.2003.811702.

[12] Boubacar Traor. Investigation of HfO2-based resistive RAM cells by electrical characterization and atomistic simulations Etude de cellules mémoires résistives RRAM à base de HfO 2 par caractérisation électrique et simulations atomistiques. 2015.

[13] K Takeuchi, Y Kameda, S Fujimura, H Otake, K Hosono, H Shiga, Y Watanabe, T Futatsuyama, Y Shindo, M Kojima, M Iwai, M Shirakawa, M Ichige, K Hatakeyama, S Tanaka, T Kamei, J Fu, A Cernea, Y Li, M Higashitani, G Hemink, S Sato, K Oowada, S Lee, N Hayashida, J Wan, J Lutze, S Tsao, M Mofidi, K Sakurai, N Tokiwa, H Waki, Y Nozawa, K Kanazawa, and S Ohshima. A 56-nm CMOS 99-mm2 8-Gb Multi-Level NAND Flash Memory With 10-MB/s Program Throughput. *IEEE Journal of Solid-State Circuits*, 42 (1):219–232, 2007. ISSN 0018-9200 VO - 42. doi: 10.1109/JSSC.2006.888299.

[14] D Nobunaga, E Abedifard, F Roohparvar, J Lee, E Yu, A Vahidimowlavi, M Abraham, S Talreja, R Sundaram, R Rozman, L Vu, C L Chen, U Chandrasekhar, R Bains, V Viajedor, W Mak, M Choi, D Udeshi, M Luo, S Qureshi, J Tsai, F Jaffin, Y Liu, and M Mancinelli. A 50nm 8Gb NAND Flash Memory with 100MB/s Program Throughput and 200MB/s DDR Interface. In *2008 IEEE International Solid-State Circuits Conference - Digest of Technical Papers*, pages 426–625, 2008. ISBN 0193-6530 VO -. doi: 10.1109/ISSCC.2008.4523239.

[15] C Trinh, N Shibata, T Nakano, M Ogawa, J Sato, Y Takeyama, K Isobe, B Le, F Moogat, N Mokhlesi, K Kozakai, P Hong, T Kamei, K Iwasa, J Nakai, T Shimizu, M Honma, S Sakai, T Kawaai, S Hoshi, J Yuh, C Hsu, T Tseng, J Li, J Hu, M Liu, S Khalid, J Chen, M Watanabe, H Lin, J Yang, K McKay, K Nguyen, T Pham, Y Matsuda, K Nakamura, K Kanebako, S Yoshikawa, W Igarashi, A Inoue, T Takahashi, Y Komatsu, C Suzuki, K Kanazawa, M Higashitani, S Lee, T Murai, K Nguyen, J Lan, S Huynh, M Murin, M Shlick, M Lasser, R Cernea, M Mofidi, K Schuegraf, and K Quader. A 5.6MB/s 64Gb 4b/Cell NAND Flash memory in 43nm CMOS. In *2009 IEEE International Solid-State Circuits Conference - Digest of Technical Papers*, pages 246–247,247a, 2009. ISBN 0193-6530 VO -. doi: 10.1109/ISSCC.2009.4977400.

[16] Boubacar Traore. Investigation of HfO2-based resistive RAM cells by electrical characterization and atomistic simulations Etude de cellules mémoires résistives RRAM à base de HfO 2 par caractérisation électrique et simulations atomistiques. 2015.

[17] ITRS. ITRS Roadmap for Semiconductors 2012 Update. 2012. URL http://www.itrs.net/links/2012ITRS/2012Chapters/2012Overview.pdf{%}5Cnhttp://www.itrs.net/links/2012ITRS/2012Tables/.

[18] E F Runnion, S M Gladstone, R S Scott, D J Dumin, L Lie, and J C Mitros. Thickness dependence of stress-induced leakage currents in silicon oxide. *IEEE Transactions on Electron Devices*, 44(6):993–1001, 1997. ISSN 0018-9383 VO - 44. doi: 10.1109/16.585556.

[19] G Molas, D Deleruyelle, B De Salvo, G Ghibaudo, M GelyGely, L Perniola, D Lafond, and S Deleonibus. Degradation of floating-gate memory reliability by few electron phenomena. *IEEE Transactions on Electron Devices*, 53(10):2610–2619, 2006. ISSN 0018-9383 VO - 53. doi: 10.1109/TED.2006.882284.

[20] Hiroshi Ishiwara. *Ferroelectric Random Access Memories*, volume 12. oct 2012. doi: 10.1166/jnn.2012.6651.

[21] H. Ishiwara. Current status and prospects of ferroelectric memories. 11:33.1.1–33.1.4, 2002. doi: 10.1109/iedm.2001.979615.

[22] Shu-Yau Wu. A new ferroelectric memory device, metal-ferroelectric-semiconductor transistor. *IEEE Transactions on Electron Devices*, 21(8):499–504, 1974. ISSN 0018-9383 VO - 21. doi: 10.1109/T-ED.1974.17955.

[23] K Sugibuchi, Y Kurogi, and N Endo. Ferroelectric field-effect memory device using Bi4Ti3O12 film. *Journal of Applied Physics*, 46(7):2877–2881, jul 1975. ISSN 0021-8979. doi: 10.1063/1.322014. URL https://doi.org/10.1063/1.322014.

[24] T Mikolajick, C Dehm, W Hartner, I Kasko, M J Kastner, N Nagel, M Moert, and C Mazure. FeRAM technology for high density applications. *Microelectronics Reliability*, 41(7):947–950, 2001. ISSN 0026-2714. doi: https://doi.org/10.1016/S0026-2714(01)00049-X. URL http://www.sciencedirect.com/science/article/pii/S002627140100049X.

[25] Ramtron Announces 8-Megabit Parallel Nonvolatile F-RAM Memory., 2009.

[26] J T Evans and R Womack. An experimental 512-bit nonvolatile memory with ferroelectric storage cell. *IEEE Journal of Solid-State Circuits*, 23(5):1171–1175, 1988. ISSN 0018-9200 VO - 23. doi: 10.1109/4.5940.

[27] T S Moise, S R Summerfelt, H McAdams, S Aggarwal, K R Udayakumar, F G Celii, J S Martin, G Xing, L Hall, K J Taylor, T Hurd, J Rodriguez, K Remack, M D Khan, K Boku, G Stacey, M Yao, M G Albrecht, E Zielinski, M Thakre, S Kuchimanchi, A Thomas, B McKee, J Rickes, A Wang, J Grace, J Fong, D Lee, C Pietrzyk, R Lanham, S R Gilbert, D Taylor, J Amano, R Bailey, F Chu, G Fox, S Sun, and T Davenport. Demonstration of a 4 Mb, high density ferroelectric memory embedded within a 130 nm, 5 LM Cu/FSG logic process. In *Digest. International Electron Devices Meeting,*, pages 535–538, 2002. ISBN VO -. doi: 10.1109/IEDM.2002.1175897.

[28] T. S. Böscke, J. Müller, D. Bräuhaus, U. Schröder, and U. Böttger. Ferroelectricity in hafnium oxide thin films. *Applied Physics Letters*, 99(10), 2011. ISSN 00036951. doi: 10.1063/1.3634052.

[29] Ricardo C. Sousa and I. Lucian Prejbeanu. Non-volatile magnetic random access memories (MRAM). *Comptes Rendus Physique*, 6(9):1013–1021, 2005. ISSN 16310705. doi: 10.1016/j.crhy.2005.10.007.

[30] Jun Yang, Hao Cai, You Wang, Lirida Naviner, Weisheng Zhao, and Wang Kang. High Performance MRAM with Spin-Transfer-Torque and Voltage-Controlled Magnetic Anisotropy Effects. *Applied Sciences*, 7(9):929, 2017. doi: 10.3390/app7090929.

[31] Claude Chappert, Albert Fert, and Frédéric Nguyen Van Dau. The emergence of spin electronics in data storage. *Nature Materials*, 6:813, nov 2007. URL https://doi.org/10.1038/nmat2024http://10.0.4.14/nmat2024.

[32] W J Gallagher and S S P Parkin. Development of the magnetic tunnel junction MRAM at IBM: From first junctions to a 16-Mb MRAM demonstrator chip. *IBM Journal of Research and Development*, 50(1):5–23, 2006. ISSN 0018-8646 VO - 50. doi: 10.1147/rd.501.0005.

[33] A V Khvalkovskiy, D Apalkov, S Watts, R Chepulskii, R S Beach, A Ong, X Tang, A Driskill-Smith, W H Butler, P B Visscher, D Lottis, E Chen, V Nikitin, and M Krounbi. Basic principles of STT-MRAM cell operation in memory

arrays. *Journal of Physics D: Applied Physics*, 46(7):74001, 2013. ISSN 0022-3727. doi: 10.1088/0022-3727/46/7/074001. URL http://dx.doi.org/10.1088/0022-3727/46/7/074001.

[34] B F Cockburn. Tutorial on magnetic tunnel junction magnetoresistive random-access memory. In *Records of the 2004 International Workshop on Memory Technology, Design and Testing, 2004.*, pages 46–51, 2004. ISBN 1087-4852 VO -. doi: 10.1109/MTDT.2004.1327983.

[35] W J Gallagher. Emerging nonvolatile magnetic memory technologies. In *2010 10th IEEE International Conference on Solid-State and Integrated Circuit Technology*, pages 1073–1076, 2010. ISBN VO -. doi: 10.1109/ICSICT.2010.5667548.

[36] G Prenat, G Di Pendina, C Layer, O Goncalves, K Jaber, B Dieny, R Sousa, I L Prejbeanu, and J P Nozieres. Magnetic memories: From DRAM replacement to ultra low power logic chips. In *2014 Design, Automation & Test in Europe Conference & Exhibition (DATE)*, page 1, 2014. ISBN 1530-1591 VO -. doi: 10.7873/DATE.2014.281.

[37] C Liaw, M Kund, D Schmitt-Landsiedel, and I Ruge. The conductive bridging random access memory (CBRAM): A non-volatile multi-level memory technology. In *ESSDERC 2007 - 37th European Solid State Device Research Conference*, pages 226–229, 2007. ISBN 1930-8876 VO -. doi: 10.1109/ESSDERC.2007.4430919.

[38] Wenhao Chen, Stefan Tappertzhofen, Hugh J Barnaby, and Michael N Kozicki. SiO2 based conductive bridging random access memory. *Journal of Electroceramics*, 39(1):109–131, 2017. ISSN 1573-8663. doi: 10.1007/s10832-017-0070-5. URL https://doi.org/10.1007/s10832-017-0070-5.

[39] C Gopalan, Y Ma, T Gallo, J Wang, E Runnion, J Saenz, F Koushan, P Blanchard, and S Hollmer. Demonstration of Conductive Bridging Random Access Memory (CBRAM) in logic CMOS process. *Solid-State Electronics*, 58(1):54–61, 2011. ISSN 0038-1101. doi: https://doi.org/10.1016/j.sse.2010.11.024. URL http://www.sciencedirect.com/science/article/pii/S0038110110004107.

[40] K Aratani, K Ohba, T Mizuguchi, S Yasuda, T Shiimoto, T Tsushima, T Sone, K Endo, A Kouchiyama, S Sasaki, A Maesaka, N Yamada, and H Narisawa. A Novel Resistance Memory with High Scalability and Nanosecond Switching. In *2007 IEEE International Electron Devices Meeting*, pages 783–786, 2007. ISBN 0163-1918 VO -. doi: 10.1109/IEDM.2007.4419064.

[41] Yooichi Hirose and Haruo Hirose. Polarity-dependent memory switching and behavior of Ag dendrite in Ag-photodoped amorphous As2S3 films. *Journal of Applied Physics*, 47(6):2767–2772, jun 1976. ISSN 0021-8979. doi: 10.1063/1.322942. URL https://doi.org/10.1063/1.322942.

[42] M Kund, G Beitel, C . Pinnow, T Rohr, J Schumann, R Symanczyk, K Ufert, and G Muller. Conductive bridging RAM (CBRAM): an emerging non-volatile memory technology scalable to sub 20nm. In *IEEE InternationalElectron Devices Meeting, 2005. IEDM Technical Digest.*, pages 754–757, 2005. ISBN 0163-1918 VO -. doi: 10.1109/IEDM.2005.1609463.

[43] Singh A Kozicki MN, Yun M, Hilt L. Applications of Programmable Resistance Changes in Metal-Doped Chalcogenides. In *Meeting; 195th, Electrochemical Society; 1999; Seattle; WA*, page 849. Electrochemical Society, 1999.

[44] Ilia Valov, Rainer Waser, John R Jameson, and Michael N Kozicki. Electrochemical metallization memories—fundamentals, applications, prospects. *Nanotechnology*, 22(25):254003, 2011. ISSN 0957-4484. doi: 10.1088/0957-4484/22/25/254003. URL http://dx.doi.org/10.1088/0957-4484/22/25/254003.

[45] Stephan Menzel, Stefan Tappertzhofen, Rainer Waser, and Ilia Valov. Switching kinetics of electrochemical metallization memory cells. *Physical Chemistry Chemical Physics*, 15(18):6945–6952, 2013. ISSN 1463-9076. doi: 10.1039/C3CP50738F. URL http://dx.doi.org/10.1039/C3CP50738F.

[46] K Terabe, T Hasegawa, T Nakayama, and M Aono. Quantized conductance atomic switch. *Nature*, 433:47, jan 2005. URL https://doi.org/10.1038/nature03190http://10.0.4.14/nature03190.

[47] Debanjan Jana, Sourav Roy, Rajeswar Panja, Mrinmoy Dutta, Sheikh Ziaur Rahaman, Rajat Mahapatra, and Siddheswar Maikap. Conductive-bridging random access memory: challenges and opportunity for 3D architecture. *Nanoscale Research Letters*, 10(1):188, 2015. ISSN 1556-276X. doi: 10.1186/s11671-015-0880-9. URL https://doi.org/10.1186/s11671-015-0880-9.

[48] Rainer Waser, Regina Dittmann, Georgi Staikov, and Kristof Szot. Redox-Based Resistive Switching Memories – Nanoionic Mechanisms, Prospects, and Challenges. *Advanced Materials*, 21(25-26):2632–2663, jul 2009. ISSN 0935-9648. doi: 10.1002/adma.200900375. URL https://doi.org/10.1002/adma.200900375.

[49] Simone Raoux and Matthis Wuttig. *Phase Change Materials: Science and Applications*, volume 1. 2009. ISBN 978-0-387-84873-0. doi: 10.1007/978-0-387-84874-7.

[50] R S Katiyar, J F Scott, Reji Thomas, H Kohlstedt, Cheol Seong Hwang, Doo Seok Jeong, and A Petraru. Emerging memories: resistive switching mechanisms and current status. *Reports on Progress in Physics*, 75(7):076502, 2012. ISSN 0034-4885. doi: 10.1088/0034-4885/75/7/076502.

[51] T W Hickmott. Low-Frequency Negative Resistance in Thin Anodic Oxide Films. *Journal of Applied Physics*, 33(9):2669–2682, sep 1962. ISSN 0021-8979. doi: 10.1063/1.1702530. URL https://doi.org/10.1063/1.1702530.

[52] Xiao Liang Hong, Desmond Jia Jun Loy, Putu Andhita Dananjaya, Funan Tan, Chee Mang Ng, and Wen Siang Lew. Oxide-based RRAM materials for neuromorphic computing. *Journal of Materials Science*, 53(12):8720–8746, 2018. ISSN 15734803. doi: 10.1007/s10853-018-2134-6. URL https://doi.org/10.1007/s10853-018-2134-6.

[53] J F Gibbons and W E Beadle. Switching properties of thin Nio films. *Solid-State Electronics*, 7(11):785–790, 1964. ISSN 0038-1101. doi: https://doi.org/10.1016/0038-1101(64)90131-5. URL http://www.sciencedirect.com/science/article/pii/0038110164901315.

[54] Simmons J G., Verderber R R., and Mott Nevill Francis. New conduction and reversible memory phenomena in thin insulating films. *Proceedings of the Royal Society of London. Series A. Mathematical and Physical Sciences*, 301(1464):77–102, oct 1967. doi: 10.1098/rspa.1967.0191. URL https://doi.org/10.1098/rspa.1967.0191.

[55] C J Varker and E M Juleff. Electron beam recording in SiO2with direct read-out using the electron beam induced current at a p-n junction. *Proceedings of the IEEE*, 55(5):728–729, 1967. ISSN 0018-9219 VO - 55. doi: 10.1109/PROC.1967.5671.

[56] G Dearnaley, A M Stoneham, and D V Morgan. Electrical phenomena in amorphous oxide films. *Reports on Progress in Physics*, 33(3):1129–1191, 1970. ISSN 0034-4885. doi: 10.1088/0034-4885/33/3/306. URL http://dx.doi.org/10.1088/0034-4885/33/3/306.

[57] L Chua. Memristor-The missing circuit element. *IEEE Transactions on Circuit Theory*, 18(5):507–519, 1971. ISSN 0018-9324 VO - 18. doi: 10.1109/TCT.1971.1083337.

[58] S. Q. Liu, N. J. Wu, and A. Ignatiev. Electric-pulse-induced reversible resistance change effect in magnetoresistive films. *Applied Physics Letters*, 76(19):2749–2751, 2000. ISSN 00036951. doi: 10.1063/1.126464.

[59] Ch. Gerber, C. Rossel, J. G. Bednorz, D. Widmer, and A. Beck. Reproducible switching effect in thin oxide films for memory applications. *Applied Physics Letters*, 77(1):139–141, 2002. ISSN 0003-6951. doi: 10.1063/1.126902.

[60] W W Zhuang, W Pan, B D Ulrich, J J Lee, L Stecker, A Burmaster, D R Evans, S T Hsu, M Tajiri, A Shimaoka, K Inoue, T Naka, N Awaya, A Sakiyama, Y Wang, S Q Liu, N J Wu, and A Ignatiev. Novel colossal magnetoresistive thin film nonvolatile resistance random access memory (RRAM). In *Digest. International Electron Devices Meeting,*, pages 193–196, 2002. ISBN VO -. doi: 10.1109/IEDM.2002.1175811.

[61] I G Baek, M S Lee, S Seo, M J Lee, D H Seo, D . Suh, J C Park, S O Park, H S Kim, I K Yoo, U . Chung, and J T Moon. Highly scalable nonvolatile resistive memory using simple binary oxide driven by asymmetric unipolar voltage pulses. In *IEDM Technical Digest. IEEE International Electron Devices Meeting, 2004.*, pages 587–590, 2004. ISBN VO -. doi: 10.1109/IEDM.2004.1419228.

[62] Dmitri B. Strukov, Gregory S. Snider, Duncan R. Stewart, and R. Stanley Williams. The missing memristor found. *Nature*, 453(7191):80–83, 2008. ISSN 00280836. doi: 10.1038/nature06932.

[63] C J Chevallier, C H Siau, S F Lim, S R Namala, M Matsuoka, B L Bateman, and D Rinerson. A 0.13m 64Mb multi-layered conductive metal-oxide memory. In *2010 IEEE International Solid-State Circuits Conference - (ISSCC)*, pages 260–261, 2010. ISBN 2376-8606 VO -. doi: 10.1109/ISSCC.2010.5433945.

[64] T Liu, T H Yan, R Scheuerlein, Y Chen, J K Lee, G Balakrishnan, G Yee, H Zhang, A Yap, J Ouyang, T Sasaki, A Al-Shamma, C Chen, M Gupta, G Hilton, A Kathuria, V Lai, M Matsumoto, A Nigam, A Pai, J Pakhale, C H Siau, X Wu, Y Yin, N Nagel, Y Tanaka, M Higashitani, T Minvielle, C Gorla,

T Tsukamoto, T Yamaguchi, M Okajima, T Okamura, S Takase, H Inoue, and L Fasoli. A 130.7-mm2 2-Layer 32-Gb ReRAM Memory Device in 24-nm Technology. *IEEE Journal of Solid-State Circuits*, 49(1):140–153, 2014. ISSN 0018-9200 VO - 49. doi: 10.1109/JSSC.2013.2280296.

[65] R Fackenthal, M Kitagawa, W Otsuka, K Prall, D Mills, K Tsutsui, J Javanifard, K Tedrow, T Tsushima, Y Shibahara, and G Hush. 19.7 A 16Gb ReRAM with 200MB/s write and 1GB/s read in 27nm technology. In *2014 IEEE International Solid-State Circuits Conference Digest of Technical Papers (ISSCC)*, pages 338–339, 2014. ISBN 0193-6530 VO -. doi: 10.1109/ISSCC.2014.6757460.

[66] Qing Luo, Xiaoxin Xu, Hongtao Liu, Hangbing Lv, Tiancheng Gong, Shibing Long, Qi Liu, Haitao Sun, Writam Banerjee, Ling Li, Jianfeng Gao, Nianduan Lu, and Ming Liu. Super non-linear RRAM with ultra-low power for 3D vertical nano-crossbar arrays. *Nanoscale*, 8(34):15629–15636, 2016. ISSN 20403372. doi: 10.1039/c6nr02029a.

[67] C. Cagli, J. Buckley, V. Jousseaume, T. Cabout, A. Salaun, H. Grampeix, J. F. Nodin, H. Feldis, A. Persico, J. Cluzel, P. Lorenzi, L. Massari, R. Rao, F. Irrera, F. Aussenac, C. Carabasse, M. Coue, P. Calka, E. Martinez, L. Perniola, P. Blaise, Z. Fang, Y. H. Yu, G. Ghibaudo, D. Deleruyelle, M. Bocquet, C. Müller, A. Padovani, O. Pirrotta, L. Vandelli, L. Larcher, G. Reimbold, and B. De Salvo. Experimental and theoretical study of electrode effects in HfO2based RRAM. *Technical Digest - International Electron Devices Meeting, IEDM*, 3:658–661, 2011. ISSN 01631918. doi: 10.1109/IEDM.2011.6131634.

[68] H Akinaga and H Shima. Resistive Random Access Memory (ReRAM) Based on Metal Oxides. *Proceedings of the IEEE*, 98(12):2237–2251, 2010. ISSN 0018-9219 VO - 98. doi: 10.1109/JPROC.2010.2070830.

[69] Byoungil Lee, Ming-Jinn Tsai, Pang-Shiu Chen, Shimeng Yu, Heng-Yuan Lee, Frederick T. Chen, Yi Wu, H.-S. Philip Wong, and Yu-Sheng Chen. Metal–Oxide RRAM. *Proceedings of the IEEE*, 100(6):1951–1970, 2012. ISSN 0018-9219. doi: 10.1109/jproc.2012.2190369.

[70] Helen Grampeix, Simon Jeannot, Yoshio Nishi, Boubacar Traore, Barbara De Salvo, Elisa Vianello, Luca Perniola, and Philippe Blaise. On the Origin of Low-Resistance State Retention Failure in HfO 2 -Based RRAM and Impact of Doping/Alloying . *IEEE Transactions on Electron Devices*, 62(12):4029–4036, 2015. ISSN 0018-9383. doi: 10.1109/ted.2015.2490545.

[71] Chao Xie, Biao Nie, Long Zhu, Long Hui Zeng, Yong Qiang Yu, Xian He Wang, Qun Ling Fang, Lin Bao Luo, and Yu Cheng Wu. High-performance nonvolatile Al/AlOx/CdTe:Sb nanowire memory device. *Nanotechnology*, 24(35), 2013. ISSN 09574484. doi: 10.1088/0957-4484/24/35/355203.

[72] Tseung-Yuen Tseng, Chenming Hu, Chung-Yi Wu, Chen-Yu Wu, and Chih-Yang Lin. Bistable Resistive Switching in Al2O3 Memory Thin Films. *Journal of The Electrochemical Society*, 154(9):G189, 2007. ISSN 00134651. doi: 10.1149/1.2750450.

[73] Ming Yang, Yang Liu, Wei Zhu, S. Fung, and T. P. Chen. Resistive Switching Behavior of Partially Anodized Aluminum Thin Film at Elevated Temperatures. *IEEE Transactions on Electron Devices*, 59(9):2363–2367, 2012. ISSN 0018-9383. doi: 10.1109/ted.2012.2205692.

[74] Min-Chen Chen, Ya-Hsiang Tai, Ya-Liang Yang, Tsung-Ming Tsai, Tai-Fa Young, J. C. Lou, Yin-Chih Pan, Rui Zhang, Yu-Ting Su, Chih-Cheng Shih, Kuan-Chang Chang, Chih-Hung Pan, Jian-Yu Chen, Simon M. Sze, Tian-Jian Chu, Jung-Hui Chen, Geng-Wei Chang, Ting-Chang Chang, and Yong-En Syu. Origin of Hopping Conduction in Graphene-Oxide-Doped Silicon Oxide Resistance Random Access Memory Devices. *IEEE Electron Device Letters*, 34(5): 677–679, 2013. ISSN 0741-3106. doi: 10.1109/led.2013.2250899.

[75] Yubao Li, Alexander Sinitskii, and James M. Tour. Electronic two-terminal bistable graphitic memories. *Nature Materials*, 7(12):966–971, 2008. ISSN 14764660. doi: 10.1038/nmat2331.

[76] Jubong Park, K. P. Biju, Seungjae Jung, Wootae Lee, Joonmyoung Lee, Seonghyun Kim, Sangsu Park, Jungho Shin, and Hyunsang Hwang. Multibit operation of TiOx-Based ReRAM by schottky barrier height engineering. *IEEE Electron Device Letters*, 32(4):476–478, 2011. ISSN 07413106. doi: 10.1109/LED.2011.2109032.

[77] Kuk Hwan Kim, Sung Hyun Jo, Siddharth Gaba, and Wei Lu. Nanoscale resistive memory with intrinsic diode characteristics and long endurance. *Applied Physics Letters*, 96(5), 2010. ISSN 00036951. doi: 10.1063/1.3294625.

[78] Chikako Yoshida, Kohji Tsunoda, Hideyuki Noshiro, and Yoshihiro Sugiyama. High speed resistive switching in PtTi O2 TiN film for nonvolatile memory application. *Applied Physics Letters*, 91(22), 2007. ISSN 00036951. doi: 10.1063/1.2818691.

[79] Kyung Jean Yoon, Young Jae Kwon, Xing Long Shao, Xi Wen Hu, Yu Min Kim, Dae Eun Kwon, Cheol Seong Hwang, Hae Jin Kim, Tae Hyung Park, Seul Ji Song, Jin Shi Zhao, Kyung Min Kim, and Jung Ho Yoon. A study of the transition between the non-polar and bipolar resistance switching mechanisms in the TiN/TiO 2 /Al memory . *Nanoscale*, 8(36):16455–16466, 2016. ISSN 2040-3364. doi: 10.1039/c6nr02800d.

[80] Shih Cheng Chen, Ting Chang Chang, Shih Yang Chen, Chi Wen Chen, Shih Ching Chen, S. M. Sze, Ming Jinn Tsai, Ming Jer Kao, and Fon Shan Yeh. Bipolar resistive switching of chromium oxide for resistive random access memory. *Solid-State Electronics*, 62(1):40–43, 2011. ISSN 00381101. doi: 10.1016/j.sse.2010.12.014. URL http://dx.doi.org/10.1016/j.sse.2010.12.014.

[81] Min Kyu Yang, Jae Wan Park, Tae Kuk Ko, and Jeon Kook Lee. Bipolar resistive switching behavior in Ti/ MnO2/Pt structure for nonvolatile memory devices. *Applied Physics Letters*, 95(4):1–4, 2009. ISSN 00036951. doi: 10.1063/1.3191674.

[82] Qin Wang, Qi Liu, Ming Liu, Sen Zhang, Shibing Long, and Weihua Guan. Resistive switching characteristics of MnO x -based ReRAM . *Journal of Physics D: Applied Physics*, 42(5):055112, 2009. ISSN 0022-3727. doi: 10.1088/0022-3727/42/5/055112.

[83] Y. S. Chen, B. Chen, B. Gao, F. F. Zhang, Y. J. Qiu, G. J. Lian, L. F. Liu, X. Y. Liu, R. Q. Han, and J. F. Kang. Anticrosstalk characteristics correlated with the set process for α -Fe2 O3 /Nb- SrTiO3 stack-based resistive switching device. *Applied Physics Letters*, 97(26):95–98, 2010. ISSN 00036951. doi: 10.1063/1.3532970.

[84] S. Muraoka, K. Osano, Y. Kanzawa, S. Mitani, S. Fujii, K. Katayama, Y. Katoh, Z. Wei, T. Mikawa, K. Arita, Y. Kawashima, R. Azuma, K. Kawai, K. Shimakawa, A. Odagawa, and T. Takagi. Fast switching and long retention Fe-O ReRAM and its switching mechanism. *Technical Digest - International Electron Devices Meeting, IEDM*, (1):779–782, 2007. ISSN 01631918. doi: 10.1109/IEDM.2007.4419063.

[85] Xu Gao, Hongxuan Guo, Yidong Xia, Jiang Yin, and Zhiguo Liu. Unipolar resistive switching characteristics in Co3O4 films. *Thin Solid Films*, 519(1):450–452, 2010. ISSN 00406090. doi: 10.1016/j.tsf.2010.07.075. URL http://dx.doi.org/10.1016/j.tsf.2010.07.075.

[86] June Sik Kwak, Young Ho Do, Yoon Cheol Bae, Hyunsik Im, and Jin Pyo Hong. Reproducible unipolar resistive switching behaviors in the metal-deficient CoOx thin film. *Thin Solid Films*, 518(22):6437–6440, 2010. ISSN 00406090. doi: 10.1016/j.tsf.2010.03.050.

[87] Hisashi Shima, Fumiyoshi Takano, Hidenobu Muramatsu, Hiro Akinaga, Yukio Tamai, Isao H. Inque, and Hidenori Takagi. Voltage polarity dependent low-power and high-speed resistance switching in CoO resistance random access memory with Ta electrode. *Applied Physics Letters*, 93(11):91–94, 2008. ISSN 00036951. doi: 10.1063/1.2982426.

[88] I. K. Yoo, B. S. Kang, Y. D. Park, M. J. Lee, and Y. Park. Interpretation of nanoscale conducting paths and their control in nickel oxide (NiO) thin films. *Applied Physics Letters*, 92(20):28–31, 2008. ISSN 00036951. doi: 10.1063/1.2936087.

[89] Yen Chun Huang, Po Yuan Chen, Tsung Shune Chin, Ru Shi Liu, Chao Yuan Huang, and Chih Huang Lai. Improvement of resistive switching in NiO-based nanowires by inserting Pt layers. *Applied Physics Letters*, 101(15), 2012. ISSN 00036951. doi: 10.1063/1.4758482.

[90] Sung In Kim, Young Ho Sa, Joo Hyung Kim, Young Wook Chang, Nanmee Kim, Heesang Kim, and Kyung Hwa Yoo. Scaling behaviors for resistive memory switching in NiO nanowire devices. *Applied Physics Letters*, 104(2), 2014. ISSN 00036951. doi: 10.1063/1.4862751.

[91] Yu Chao Yang, Feng Pan, Qi Liu, Ming Liu, and Fei Zeng. Fully room-temperature-fabricated nonvolatile resistive memory for ultrafast and high-density memory application. *Nano Letters*, 9(4):1636–1643, 2009. ISSN 15306984. doi: 10.1021/nl900006g.

[92] Fu Chien Chiu, Peng Wei Li, and Wen Yuan Chang. Reliability characteristics and conduction mechanisms in resistive switching memory devices using ZnO thin films. *Nanoscale Research Letters*, 7:1–9, 2012. ISSN 19317573. doi: 10.1186/1556-276X-7-178.

[93] S. Z. Rahaman, S. Maikap, W. S. Chen, H. Y. Lee, F. T. Chen, M. J. Kao, and M. J. Tsai. Repeatable unipolar/bipolar resistive memory characteristics and switching mechanism using a Cu nanofilament in a GeO x film. *Applied Physics Letters*, 101(7):1–6, 2012. ISSN 00036951. doi: 10.1063/1.4745783.

[94] C. H. Cheng, Albert Chin, and F. S. Yeh. Ultralow switching energy Ni/-GeOx/HfON/TaN RRAM. *IEEE Electron Device Letters*, 32(3):366–368, 2011. ISSN 07413106. doi: 10.1109/LED.2010.2095820.

[95] Chih-Yang Lin, Chen-Yu Wu, Chung-Yi Wu, Tzyh-Cheang Lee, Fu-Liang Yang, Chenming Hu, and Tseung-Yuen Tseng. Effect of Top Electrode Material on Resistive Switching Properties of ZrO2 Film Memory Devices. *IEEE Electron Device Letters*, 28(5):366–368, 2007. ISSN 0741-3106. doi: 10.1109/LED.2007.894652. URL http://ieeexplore.ieee.org/ielx5/55/4160006/04160030.pdf?tp={&}arnumber=4160030{&}isnumber=4160006{%}5Cnhttp://ieeexplore.ieee.org/document/4160030/.

[96] Tai-Yuen Huang, Jia-Woei Wu, Tseung-Yuen Tseng, Dai-Ying Lee, and Sheng-Yu Wang. Controllable oxygen vacancies to enhance resistive switching performance in a ZrO 2 -based RRAM with embedded Mo layer . *Nanotechnology*, 21(49):495201, 2010. ISSN 0957-4484. doi: 10.1088/0957-4484/21/49/495201.

[97] Weihua Guan, Shibing Long, Qi Liu, Ming Liu, and Wei Wang. Nonpolar nonvolatile resistive switching in Cu doped ZrO2. *IEEE Electron Device Letters*, 29(5):434–437, 2008. ISSN 07413106. doi: 10.1109/LED.2008.919602.

[98] Hyunhee Baek, Chanwoo Lee, Jungkyu Choi, and Jinhan Cho. Nonvolatile memory devices prepared from sol-gel derived niobium pentoxide films. *Langmuir*, 29(1):380–386, 2013. ISSN 07437463. doi: 10.1021/la303857b.

[99] M. Arita, H. Kaji, T. Fujii, and Y. Takahashi. Resistance switching properties of molybdenum oxide films. *Thin Solid Films*, 520(14):4762–4767, 2012. ISSN 00406090. doi: 10.1016/j.tsf.2011.10.174. URL http://dx.doi.org/10.1016/j.tsf.2011.10.174.

[100] Boubacar Traore. Investigation of HfO2-based resistive RAM cells by electrical characterization and atomistic simulations Etude de cellules mémoires résistives RRAM à base de HfO 2 par caractérisation électrique et simulations atomistiques. 2015.

[101] Yang Yin Chen, Sergiu Clima, Gouri Sankar Kar, Bogdan Govoreanu, Robin Degraeve, Guido Groeseneken, Ludovic Goux, Malgorzata Jurczak, Dirk J. Wouters, and Andrea Fantini. Endurance/Retention Trade-off on HfO2/Metal Cap 1T1R Bipolar RRAM. *IEEE Transactions on Electron Devices*, 60(3):1114–1121, 2013. ISSN 0018-9383. doi: 10.1109/ted.2013.2241064.

[102] H. Y. Lee, Y. S. Chen, P. S. Chen, P. Y. Gu, Y. Y. Hsu, S. M. Wang, W. H. Liu, C. H. Tsai, S. S. Sheu, P. C. Chiang, W. P. Lin, C. H. Lin, W. S. Chen, F. T. Chen, C. H. Lien, and M. J. Tsai. Evidence and solution of over-RESET problem for HfOX based resistive memory with sub-ns switching speed and high endurance. *Technical Digest - International Electron Devices Meeting, IEDM*, pages 7–10, 2010. ISSN 01631918. doi: 10.1109/IEDM.2010.5703395.

[103] Enrique A. Miranda, Christian Walczyk, Christian Wenger, and Thomas Schroeder. Model for the resistive switching effect in HfO2MIM structures based on the transmission properties of narrow constrictions. *IEEE Electron Device Letters*, 31(6):609–611, 2010. ISSN 07413106. doi: 10.1109/LED.2010.2046310.

[104] D. Walczyk, Ch Walczyk, T. Schroeder, T. Bertaud, M. Sowińska, M. Lukosius, M. Fraschke, B. Tillack, and Ch Wenger. Resistive switching characteristics of CMOS embedded HfO2-based 1T1R cells. *Microelectronic Engineering*, 88(7): 1133–1135, 2011. ISSN 01679317. doi: 10.1016/j.mee.2011.03.123.

[105] Shani Recher, Eilam Yalon, Dan Ritter, Ilan Riess, and Joseph Salzman. Solid-State Electronics Dual bipolar resistive switching in the sub-forming regime of HfO 2 resistive switching devices. *Solid State Electronics*, 111:238–242, 2015. ISSN 0038-1101. doi: 10.1016/j.sse.2015.04.002. URL http://dx.doi.org/10.1016/j.sse.2015.04.002.

[106] Francesca De Stefano, Michel Houssa, Valeri V. Afanas'Ev, Jorge A. Kittl, Małgorzata Jurczak, and Andre Stesmans. Nature of the filament formed in HfO2-based resistive random access memory, 2013. ISSN 00406090.

[107] Antonio C. Torrezan, John Paul Strachan, Gilberto Medeiros-Ribeiro, and R. Stanley Williams. Sub-nanosecond switching of a tantalum oxide memristor. *Nanotechnology*, 22(48), 2011. ISSN 09574484. doi: 10.1088/0957-4484/22/48/485203.

[108] Siddheswar Maikap, Debanjan Jana, Mrinmoy Dutta, and Amit Prakash. Self-compliance RRAM characteristics using a novel W/TaO x /TiN structure. *Nanoscale research letters*, 9(1):292, 2014. ISSN 1931-7573. doi: 10.1186/1556-276X-9-292. URL http://www.pubmedcentral.nih.gov/articlerender.fcgi?artid=4066319{&}tool=pmcentrez{&}rendertype=abstract.

[109] Masakazu Aono, Kazuya Terabe, Tsuyoshi Hasegawa, Toshitsugu Sakamoto, Naoki Banno, and Kevin Lister. Electronic transport in Ta2O5 resistive switch. *Applied Physics Letters*, 91(9):092110, 2007. ISSN 0003-6951. doi: 10.1063/1.2777170.

[110] F. Kurnia, Chunli Liu, C. U. Jung, and B. W. Lee. The evolution of conducting filaments in forming-free resistive switching Pt/TaOx/Pt structures. *Applied Physics Letters*, 102(15), 2013. ISSN 00036951. doi: 10.1063/1.4802263.

[111] Hsin Hung Huang, Wen Chieh Shih, and Chih Huang Lai. Nonpolar resistive switching in the Pt/MgO/Pt nonvolatile memory device. *Applied Physics Letters*, 96(19), 2010. ISSN 00036951. doi: 10.1063/1.3429024.

[112] H. F. Tian, Y. G. Zhao, X. L. Jiang, J. P. Shi, H. J. Zhang, and J. R. Sun. Resistance switching effect in LaAlO3/Nb-doped SrTiO3 heterostructure. *Applied Physics A: Materials Science and Processing*, 102(4):939–942, 2011. ISSN 09478396. doi: 10.1007/s00339-011-6276-5.

[113] Kou Chen Liu, Wen Hsien Tzeng, Kow Ming Chang, Jiun Jie Huang, Yun Ju Lee, Ping Hung Yeh, Pang Shiu Chen, Heng Yuan Lee, Frederick Chen, and Ming Jinn Tsai. Investigation of the effect of different oxygen partial pressure to LaAlO3 thin film properties and resistive switching characteristics. *Thin Solid Films*, 520(4):1246–1250, 2011. ISSN 00406090. doi: 10.1016/j.tsf.2011.04.205. URL http://dx.doi.org/10.1016/j.tsf.2011.04.205.

[114] X. T. Zhang, Q. X. Yu, Y. P. Yao, and X. G. Li. Ultrafast resistive switching in SrTiO3:Nb single crystal. *Applied Physics Letters*, 97(22):3–6, 2010. ISSN 00036951. doi: 10.1063/1.3524216.

[115] Min Yeong Song, Yujeong Seo, Yeon Soo Kim, Hee Dong Kim, Ho Myoung An, Bae Ho Park, Yun Mo Sung, and Tae Geun Kim. Realization of one-diode-type resistive-switching memory with Cr-SrTiO 3 film. *Applied Physics Express*, 5(9): 3–6, 2012. ISSN 18820778. doi: 10.1143/APEX.5.091202.

[116] Zhibo Yan, Yanyan Guo, Guoquan Zhang, and J. M. Liu. High-performance programmable memory devices based on Co-doped BaTiO 3. *Advanced Materials*, 23(11):1351–1355, 2011. ISSN 09359648. doi: 10.1002/adma.201004306.

[117] Xiliang He and Xiaomin Li. Field-induced resistive switching of (Ba0.6Sr0.4)TiO3thin films based on switching of conducting domains model. *Applied Physics Letters*, 102(22):0–3, 2013. ISSN 00036951. doi: 10.1063/1.4809532.

[118] Lu Liu, Shantao Zhang, Ying Luo, Guoliang Yuan, Junming Liu, Jiang Yin, and Zhiguo Liu. Coexistence of unipolar and bipolar resistive switching in BiFeO 3 and Bi 0.8Ca 0.2FeO 3 films. *Journal of Applied Physics*, 111(10):1–6, 2012. ISSN 00218979. doi: 10.1063/1.4716867.

[119] Mandar M. Shirolkar, Changshan Hao, Xiaolei Dong, Ting Guo, Lei Zhang, Ming Li, and Haiqian Wang. Tunable multiferroic and bistable/complementary resistive switching properties of dilutely Li-doped BiFeO3 nanoparticles: An effect of aliovalent substitution. *Nanoscale*, 6(9):4735–4744, 2014. ISSN 20403372. doi: 10.1039/c3nr05973a.

[120] T. Sakamoto, H. Sunamura, H. Kawaura, T. Hasegawa, T. Nakayama, and M. Aonob. Nanometer-scale switches using copper sulfide. *Applied Physics Letters*, 82(18):3032–3034, 2003. ISSN 00036951. doi: 10.1063/1.1572964.

[121] Jan Van Den Hurk, Ilia Valov, and Rainer Waser. Preparation and characterization of GeSx thin-films for resistive switching memories. *Thin Solid Films*, 527:299–302, 2013. ISSN 00406090. doi: 10.1016/j.tsf.2012.12.032. URL http://dx.doi.org/10.1016/j.tsf.2012.12.032.

[122] M. Morales-Masis, S. J. Van Der Molen, T. Hasegawa, and J. M. Van Ruitenbeek. Bulk and surface nucleation processes in Ag2S conductance switches. *Physical Review B - Condensed Matter and Materials Physics*, 84(11):1–7, 2011. ISSN 10980121. doi: 10.1103/PhysRevB.84.115310.

[123] Tsuyoshi Hasegawa, Alpana Nayak, Takeo Ohno, Kazuya Terabe, Tohru Tsuruoka, James K. Gimzewski, and Masakazu Aono. Memristive operations demonstrated by gap-type atomic switches. *Applied Physics A: Materials Science and Processing*, 102(4):811–815, 2011. ISSN 09478396. doi: 10.1007/s00339-011-6317-0.

[124] Michael N. Kozicki, Mira Park, and Maria Mitkova. Nanoscale memory elements based on solid-state electrolytes. *IEEE Transactions on Nanotechnology*, 4 (3):331–338, 2005. ISSN 1536125X. doi: 10.1109/TNANO.2005.846936.

[125] Hee Dong Kim, Ho Myoung An, Eui Bok Lee, and Tae Geun Kim. Stable bipolar resistive switching characteristics and resistive switching mechanisms observed in aluminum nitride-based ReRAM devices. *IEEE Transactions on Electron Devices*, 58(10):3566–3573, 2011. ISSN 00189383. doi: 10.1109/TED.2011.2162518.

[126] Hee Dong Kim, Ho Myoung An, Yujeong Seo, and Tae Geun Kim. Transparent resistive switching memory using ITO/AlN/ITO capacitors. *IEEE Electron Device Letters*, 32(8):1125–1127, 2011. ISSN 07413106. doi: 10.1109/LED.2011.2158056.

[127] Chao Chen, Guangsheng Tang, Cheng Song, Fei Zeng, Feng Pan, and Shuang Gao. Cu-Embedded AlN-Based Nonpolar Nonvolatile Resistive Switching Memory. *IEEE Electron Device Letters*, 33(12):1711–1713, 2012. ISSN 0741-3106. doi: 10.1109/led.2012.2220953.

[128] C. Chen, Y. C. Yang, F. Zeng, and F. Pan. Bipolar resistive switching in Cu/AlN/Pt nonvolatile memory device. *Applied Physics Letters*, 97(8):1–4, 2010. ISSN 00036951. doi: 10.1063/1.3483158.

[129] Hee Dong Kim, Ho Myoung An, Seok Man Hong, and Tae Geun Kim. Forming-free SiN-based resistive switching memory prepared by RF sputtering. *Physica Status Solidi (A) Applications and Materials Science*, 210(9):1822–1827, 2013. ISSN 18626300. doi: 10.1002/pssa.201329021.

[130] Hee Dong Kim, Ho Myoung An, Kyoung Chan Kim, Yujeong Seo, Ki Hyun Nam, Hong Bay Chung, Eui Bok Lee, and Tae Geun Kim. Large resistive-switching phenomena observed in Ag/Si3N 4/Al memory cells. *Semiconductor Science and Technology*, 25(6), 2010. ISSN 02681242. doi: 10.1088/0268-1242/25/6/065002.

[131] Hee Dong Kim, Ho Myoung An, Seok Man Hong, and Tae Geun Kim. Unipolar resistive switching phenomena in fully transparent SiN-based memory cells. *Semiconductor Science and Technology*, 27(12), 2012. ISSN 02681242. doi: 10.1088/0268-1242/27/12/125020.

[132] Di Fu, Dan Xie, Tingting Feng, Chenhui Zhang, Jiebin Niu, He Qian, and Litian Liu. Unipolar resistive switching properties of diamondlike carbon-based RRAM devices. *IEEE Electron Device Letters*, 32(6):803–805, 2011. ISSN 07413106. doi: 10.1109/LED.2011.2132750.

[133] Run-Wei Li, W. Dai, F. Zhuge, Y. W. Liu, M. Li, P. Cui, C. L. He, A. Y. Wang, and Y. H. Wu. Nonvolatile resistive switching memory based on amorphous carbon. *Applied Physics Letters*, 96(16):163505, 2010. ISSN 0003-6951. doi: 10.1063/1.3406121.

[134] Sung Hyun Jo and Wei Lu. CMOS compatible nanoscale nonvolatile resistance switching memory. *Nano Letters*, 8(2):392–397, 2008. ISSN 15306984. doi: 10.1021/nl073225h.

[135] S. Tappertzhofen, I. Valov, and R. Waser. Quantum conductance and switching kinetics of AgI-based microcrossbar cells. *Nanotechnology*, 23(14), 2012. ISSN 09574484. doi: 10.1088/0957-4484/23/14/145703.

[136] L. Chen, Z. G. Liu, H. X. Guo, B. Yang, J. Yin, K. B. Yin, and Y. D. Xia. Resistive switching devices based on nanocrystalline solid electrolyte (AgI)0.5(AgPO3)0.5. *Applied Physics Letters*, 91(24):243513, 2007. ISSN 0003-6951. doi: 10.1063/1.2825273.

[137] Byungjin Cho, Sunghoon Song, Yongsung Ji, and Takhee Lee. Organic resistive memory devices: Performance enhancement and advanced integration

architecture. *2011 IEEE Nanotechnology Materials and Devices Conference, NMDC 2011*, pages 295–296, 2011. ISSN 1616301X. doi: 10.1109/NMDC.2011.6155362.

[138] Su Ting Han, Ye Zhou, and V. A.L. Roy. Towards the development of flexible non-volatile memories. *Advanced Materials*, 25(38):5425–5449, 2013. ISSN 09359648. doi: 10.1002/adma.201301361.

[139] J. Joshua Yang, M. X. Zhang, John Paul Strachan, Feng Miao, Matthew D. Pickett, Ronald D. Kelley, G. Medeiros-Ribeiro, and R. Stanley Williams. High switching endurance in TaOx memristive devices. *Applied Physics Letters*, 97 (23):6–9, 2010. ISSN 00036951. doi: 10.1063/1.3524521.

[140] Chikako Yoshida, Kohji Tsunoda, Hideyuki Noshiro, and Yoshihiro Sugiyama. High speed resistive switching in PtTi O2 TiN film for nonvolatile memory application. *Applied Physics Letters*, 91(22), 2007. ISSN 00036951. doi: 10.1063/1.2818691.

[141] Chikako Yoshida, Kentaro Kinoshita, Takahiro Yamasaki, and Yoshihiro Sugiyama. Direct observation of oxygen movement during resistance switching in NiO/Pt film. *Applied Physics Letters*, 93(4):91–94, 2008. ISSN 00036951. doi: 10.1063/1.2966141.

[142] D. Ielmini, F. Nardi, and C. Cagli. Physical models of size-dependent nanofilament formation and rupture in NiO resistive switching memories. *Nanotechnology*, 22(25), 2011. ISSN 09574484. doi: 10.1088/0957-4484/22/25/254022.

[143] Y. Hou, U. Celano, L. Goux, L. Liu, A. Fantini, R. Degraeve, A. Youssef, Z. Xu, Y. Cheng, J. Kang, M. Jurczak, and W. Vandervorst. Sub-10 nm low current resistive switching behavior in hafnium oxide stack. *Applied Physics Letters*, 108(12):1–6, 2016. ISSN 00036951. doi: 10.1063/1.4944841.

[144] Liang Zhao, Zizhen Jiang, Hong Yu Chen, Joon Sohn, Kye Okabe, Blanka Magyari-Köpe, H. S.Philip Wong, and Yoshio Nishi. Ultrathin (2nm) HfOx as the fundamental resistive switching element: Thickness scaling limit, stack engineering and 3D integration. *Technical Digest - International Electron Devices Meeting, IEDM*, 2015-Febru(February):6.6.1–6.6.4, 2015. ISSN 01631918. doi: 10.1109/IEDM.2014.7046998.

[145] E. Vianello, O. Thomas, G. Molas, O. Turkyilmaz, N. Jovanović, D. Garbin, G. Palma, M. Alayan, C. Nguyen, J. Coignus, B. Giraud, T. Benoist, M. Reyboz, A. Toffoli, C. Charpin, F. Clermidy, and L. Perniola. Resistive Memories for Ultra-Low-Power embedded computing design. *Technical Digest - International Electron Devices Meeting, IEDM*, 2015-Febru(February):6.3.1–6.3.4, 2015. ISSN 01631918. doi: 10.1109/IEDM.2014.7046995.

[146] B. Govoreanu, G. S. Kar, Y. Y. Chen, V. Paraschiv, S. Kubicek, A. Fantini, I. P. Radu, L. Goux, S. Clima, R. Degraeve, N. Jossart, O. Richard, T. Vandeweyer, K. Seo, P. Hendrickx, G. Pourtois, H. Bender, L. Altimime, D. J. Wouters, J. A. Kittl, and M. Jurczak. 1010nm2Hf/HfOxcrossbar resistive RAM with excellent performance, reliability and low-energy operation. *Technical Digest - International Electron Devices Meeting, IEDM*, pages 31.6.1–31.6.4, 2011. ISSN 01631918. doi: 10.1109/IEDM.2011.6131652.

[147] Yang Yin Chen, Masanori Komura, Robin Degraeve, Bogdan Govoreanu, Ludovic Goux, Andrea Fantini, Naga Raghavan, Sergiu Clima, Leqi Zhang,

Attilio Belmonte, Augusto Redolfi, Gouri Sankar Kar, Guido Groeseneken, Dirk J. Wouters, and Malgorzata Jurczak. Improvement of data retention in HfO2/Hf 1T1R RRAM cell under low operating current. *Technical Digest - International Electron Devices Meeting, IEDM*, pages 10.1.1–10.1.4, 2013. ISSN 01631918. doi: 10.1109/IEDM.2013.6724598.

[148] H. Y. Lee, P. S. Chen, T. Y. Wu, Y. S. Chen, C. C. Wang, P. J. Tzeng, C. H. Lin, F. Chen, C. H. Lien, and M. J. Tsai. Low power and high speed bipolar switching with a thin reactive ti buffer layer in robust HfO2 based RRAM. *Technical Digest - International Electron Devices Meeting, IEDM*, pages 3–6, 2008. ISSN 01631918. doi: 10.1109/IEDM.2008.4796677.

[149] Woo-Young Yang and Shi-Woo Rhee. Effect of electrode material on the resistance switching of Cu2O film. *Applied Physics Letters*, 91(23):232907, dec 2007. ISSN 0003-6951. doi: 10.1063/1.2822403. URL https://doi.org/10.1063/1.2822403.

[150] Chih-Yang Lin, Sheng-Yi Wang, Dai-Ying Lee, and Tseung-Yuen Tseng. Electrical Properties and Fatigue Behaviors of ZrO[sub 2] Resistive Switching Thin Films. *Journal of The Electrochemical Society*, 155(8):H615, 2008. ISSN 00134651. doi: 10.1149/1.2946430.

[151] Z. Wei, T. Takagi, Y. Kanzawa, Y. Katoh, T. Ninomiya, K. Kawai, S. Muraoka, S. Mitani, K. Katayama, S. Fujii, R. Miyanaga, Y. Kawashima, T. Mikawa, K. Shimakawa, and K. Aono. Demonstration of high-density ReRAM ensuring 10-year retention at 85C based on a newly developed reliability model. *Technical Digest - International Electron Devices Meeting, IEDM*, pages 31.4.1–31.4.4, 2011. ISSN 01631918. doi: 10.1109/IEDM.2011.6131650.

[152] Myoung-Jae Lee, Chang Bum Lee, Dongsoo Lee, Seung Ryul Lee, Man Chang, Ji Hyun Hur, Young-Bae Kim, Chang-Jung Kim, David H. Seo, Sunae Seo, U-In Chung, In-Kyeong Yoo, and Kinam Kim. A fast, high-endurance and scalable non-volatile memory device made from asymmetric Ta2O5x/TaO2x bilayer structures. *Nature Materials*, 10(8):625–630, 2011. ISSN 1476-1122. doi: 10.1038/nmat3070. URL http://www.nature.com/doifinder/10.1038/nmat3070.

[153] Z. Wei, Y. Kanzawa, K. Arita, Y. Katoh, K. Kawai, S. Muraoka, S. Mitani, S. Fujii, K. Katayama, M. Iijima, T. Mikawa, T. Ninomiya, R. Miyanaga, Y. Kawashima, K. Tsuji, A. Himeno, T. Okada, R. Azuma, K. Shimakawa, H. Sugaya, T. Takagi, R. Yasuhara, KHoriba, H. Kumigashira, and M. Oshima. Highly reliable TaO x ReRAM and direct evidence of redox reaction mechanism. *Technical Digest - International Electron Devices Meeting, IEDM*, pages 1–4, 2008. ISSN 01631918. doi: 10.1109/IEDM.2008.4796676.

[154] Y. S. Chen, H. Y. Lee, P. S. Chen, P. Y. Gu, C. W. Chen, W. P. Lin, W. H. Liu, Y. Y. Hsu, S. S. Sheu, P. C. Chiang, W. S. Chen, F. T. Chen, C. H. Lien, and M. J. Tsai. Highly scalable hafnium oxide memory with improvements of resistive distribution and read disturb immunity. *Technical Digest - International Electron Devices Meeting, IEDM*, pages 105–108, 2009. ISSN 01631918. doi: 10.1109/IEDM.2009.5424411.

[155] Heng Yuan Lee, Frederick Chen, Tai-Yuan Wu, Yu Sheng Chen, Fred Chen, Ching-Chiun Wang, Pei-Jer Tzeng, C H Lin, Ming-Jinn Tsai, and Chenhsin

Lien. *HfOx Bipolar Resistive Memory With Robust Endurance Using AlCu as Buffer Electrode*, volume 30. aug 2009. doi: 10.1109/LED.2009.2021004.

[156] Shyh-Shyuan Sheu, Pei-Chia Chiang, Wen-Pin Lin, Heng-Yuan Lee, Pang-Shiu Chen, Yu-Sheng Chen, Tai-Yuan Wu, Frederick T. Chen, Keng-Li Su, Ming-Jer Kao, Kuo-Hsing Cheng, and Ming-Jinn Tsai. A 5ns Fast Write Multi-Level Non-Volatile 1 K Bits RRAM Memory with Advance Write Scheme. *IEEE Symposium on VLSI Circuits*, pages 82–83, 2009.

[157] Seunghyup Lee, Wan-Gee Kim, Shi-Woo Rhee, and Kijung Yong. Resistance Switching Behaviors of Hafnium Oxide Films Grown by MOCVD for Nonvolatile Memory Applications. *Journal of The Electrochemical Society*, 155(2): H92, 2007. ISSN 00134651. doi: 10.1149/1.2814153.

[158] A. Fantini, V. Jousseaume, S. Tirano, N. Rochat, P. Calka, J.F. Nodin, G. Auvert, H. Grampeix, R. Vignon, J.P. Barnes, B. De Salvo, A. Roule, S. Favier, H. Feldis, P. Gonon, A. Persico, C. Guedj, L. Perniola, S. Minoret, J. Buckley, P. Lorenzi, C. Vallee, and E. Martinez. Comparative study of non-polar switching behaviors of NiO- and HfO2-based Oxide Resistive-RAMs. pages 1–4, 2010. doi: 10.1109/imw.2010.5488316.

[159] Young Ho Do, June Sik Kwak, Yoon Cheol Bae, Kyooho Jung, Hyunsik Im, and Jin Pyo Hong. Hysteretic bipolar resistive switching characteristics in TiO 2/TiO2-x multilayer homojunctions. *Applied Physics Letters*, 95(9):2007–2010, 2009. ISSN 00036951. doi: 10.1063/1.3224179.

[160] J. Joshua Yang, Matthew D. Pickett, Xuema Li, Douglas A. A. Ohlberg, Duncan R. Stewart, and R. Stanley Williams. Memristive switching mechanism for metal/oxide/metal nanodevices. *Nature Nanotechnology*, 3(7):429–433, 2008. ISSN 1748-3387. doi: 10.1038/nnano.2008.160. URL http://www.nature.com/doifinder/10.1038/nnano.2008.160.

[161] Wei Wang, Shinobu Fujita, and S. Simon Wong. RESET mechanism of TiOx resistance-change memory device. *IEEE Electron Device Letters*, 30(7):733–735, 2009. ISSN 07413106. doi: 10.1109/LED.2009.2021001.

[162] Christina Rohde, Byung Joon Choi, Doo Seok Jeong, Seol Choi, Jin Shi Zhao, and Cheol Seong Hwang. Identification of a determining parameter for resistive switching of TiO2thin films. *Applied Physics Letters*, 86(26):1–3, 2005. ISSN 00036951. doi: 10.1063/1.1968416.

[163] S. C. Chae, J. S. Lee, W. S. Choi, S. B. Lee, S. H. Chang, H. Shin, B. Kahng, and T. W. Noh. Multilevel unipolar resistance switching in TiO2 thin films. *Applied Physics Letters*, 95(9):1–4, 2009. ISSN 00036951. doi: 10.1063/1.3224185.

[164] Articles You, M A Y Be, and Interested In. Resistive switching mechanism of thin films grown by atomic-layer deposition. 033715(June 2005), 2011. doi: 10.1063/1.2001146.

[165] S. Seo, M. J. Lee, D. H. Seo, E. J. Jeoung, D. S. Suh, Y. S. Joung, I. K. Yoo, I. R. Hwang, S. H. Kim, I. S. Byun, J. S. Kim, J. S. Choi, and B. H. Park. Reproducible resistance switching in polycrystalline NiO films. *Applied Physics Letters*, 85 (23):5655–5657, 2004. ISSN 00036951. doi: 10.1063/1.1831560.

[166] J. Y. Son and Y. H. Shin. Direct observation of conducting filaments on resistive switching of NiO thin films. *Applied Physics Letters*, 92(22):2006–2009, 2008. ISSN 00036951. doi: 10.1063/1.2931087.

[167] Articles You, M A Y Be, and Interested In. Resistive switching mechanism of thin films grown by atomic-layer deposition. 033715(June 2005), 2015. doi: 10.1063/1.2001146.

[168] G. Bersuker, D. C. Gilmer, D. Veksler, P. Kirsch, L. Vandelli, A. Padovani, L. Larcher, K. McKenna, A. Shluger, V. Iglesias, M. Porti, and M. Nafría. Metal oxide resistive memory switching mechanism based on conductive filament properties. *Journal of Applied Physics*, 110(12), 2011. ISSN 00218979. doi: 10.1063/1.3671565.

[169] Home Search, Collections Journals, About Contact, My Iopscience, and I P Address. Chemical and structural properties of conducting nanofilaments in TiN / HfO 2 -based resistive switching structures. 085706. doi: 10.1088/0957-4484/24/8/085706.

[170] Lifeng Liu, Xiao Sun, Dedong Han, Nuo Xu, Yi Wang, Ruqi Han, Bin Yu, Xiaoyan Liu, and Jinfeng Kang. Characteristics and mechanism of conduction/set process in TiNZnOPt resistance switching random-access memories. *Applied Physics Letters*, 92(23):232112, 2008. ISSN 0003-6951. doi: 10.1063/1.2945278.

[171] Krzysztof Szot, Wolfgang Speier, Gustav Bihlmayer, and Rainer Waser. Switching the electrical resistance of individual dislocations in single-crystalline SrTiO3. *Nature Materials*, 5(4):312–320, 2006. ISSN 1476-1122. doi: 10.1038/nmat1614. URL http://www.nature.com/doifinder/10.1038/nmat1614.

[172] M. Lanza, K. Zhang, M. Porti, M. Nafria, Z. Y. Shen, L. F. Liu, J. F. Kang, D. Gilmer, and G. Bersuker. Grain boundaries as preferential sites for resistive switching in the HfO2 resistive random access memory structures. *Applied Physics Letters*, 100(12):123508, 2012. ISSN 00036951. doi: 10.1063/1.3697648. URL http://scitation.aip.org/content/aip/journal/apl/100/12/10.1063/1.3697648.

[173] Liang Zhao, Jinyu Zhang, Yu He, Ximeng Guan, He Qian, and Zhiping Yu. Dynamic modeling and atomistic simulations of SET and RESET operations in TiO2-Based unipolar resistive memory. *IEEE Electron Device Letters*, 32(5):677–679, 2011. ISSN 07413106. doi: 10.1109/LED.2011.2115990.

[174] Doo Seok Jeong, Herbert Schroeder, Uwe Breuer, and Rainer Waser. Characteristic electroforming behavior in Pt/ TiO2 /Pt resistive switching cells depending on atmosphere. *Journal of Applied Physics*, 104(12), 2008. ISSN 00218979. doi: 10.1063/1.3043879.

[175] Rainer Waser and Masakazu Aono. Nanoionics-based resistive switching memories. *Nature materials*, 6(11):833–40, 2007. ISSN 1476-1122. doi: 10.1038/nmat2023. URL http://www.ncbi.nlm.nih.gov/pubmed/17972938.

[176] G. Bersuker, S. Privitera, P.D. Kirsch, B. Butcher, C. Bongiorno, S. Lombardo, R. Geer, A. Kalantarian, and D.C. Gilmer. Microscopy study of the conductive

filament in HfO2 resistive switching memory devices. *Microelectronic Engineering*, 109:75–78, 2013. ISSN 01679317. doi: 10.1016/j.mee.2013.03.145. URL http://dx.doi.org/10.1016/j.mee.2013.03.145.

[177] Umesh Chand, Chun Yang Huang, Jheng Hong Jieng, Wen Yueh Jang, Chen Hsi Lin, and Tseung Yuen Tseng. Suppression of endurance degradation by utilizing oxygen plasma treatment in HfO2resistive switching memory. *Applied Physics Letters*, 106(15), 2015. ISSN 00036951. doi: 10.1063/1.4918679.

[178] SHENG-YU WANG and TSEUNG-YUEN TSENG. INTERFACE ENGINEERING IN RESISTIVE SWITCHING MEMORIES. *Journal of Advanced Dielectrics*, 01(02):141–162, apr 2011. ISSN 2010-135X. doi: 10.1142/S2010135X11000306. URL https://doi.org/10.1142/S2010135X11000306.

[179] Kyung Min Kim, Cheol Seong Hwang, Seul Ji Song, Byung Joon Choi, and Gun Hwan Kim. Filamentary Resistive Switching Localized at Cathode Interface in NiO Thin Films. *Journal of The Electrochemical Society*, 156(12):G213, 2009. ISSN 00134651. doi: 10.1149/1.3240201.

[180] Kyooho Jung, Hongwoo Seo, Yongmin Kim, Hyunsik Im, Jin Pyo Hong, Jae Wan Park, and Jeon Kook Lee. Temperature dependence of high- and low-resistance bistable states in polycrystalline NiO films. *Applied Physics Letters*, 90(5):2005–2008, 2007. ISSN 00036951. doi: 10.1063/1.2437668.

[181] Myoung Jae Lee, Sun I. Kim, Chang B. Lee, Huaxiang Yin, Seung Eon Ahn, Bo S. Kang, Ki H. Kim, Jae C. Park, Chang J. Kim, Ihun Song, Sang W. Kim, Genrikh Stefanovich, Jung H. Lee, Seok J. Chung, Yeon H. Kim, and Youngsoo Park. Low-temperature-grown transition metal oxide based storage materials and oxide transistors for high- density non-volatile memory. *Advanced Functional Materials*, 19(10):1587–1593, 2009. ISSN 1616301X. doi: 10.1002/adfm.200801032.

[182] Kazuki Nagashima, Takeshi Yanagida, Masaki Kanai, Umberto Celano, Sakon Rahong, Gang Meng, Fuwei Zhuge, Yong He, Bae Ho Park, and Tomoji Kawai. Carrier type dependence on spatial asymmetry of unipolar resistive switching of metal oxides. *Applied Physics Letters*, 103(17), 2013. ISSN 00036951. doi: 10.1063/1.4826558.

[183] Kyung Min Kim, Byung Joon Choi, and Cheol Seong Hwang. Localized switching mechanism in resistive switching of atomic-layer-deposited Ti O2 thin films. *Applied Physics Letters*, 90(24), 2007. ISSN 00036951. doi: 10.1063/1.2748312.

[184] Myoung-Jae Lee, Ran-Ju Jung, Gyeong-Su Park, Dong-Chirl Kim, Sunae Seo, and Xiang-Shu Li. Observation of electric-field induced Ni filament channels in polycrystalline NiOx film. *Applied Physics Letters*, 91(22):222103, 2007. ISSN 0003-6951. doi: 10.1063/1.2813617.

[185] Deok-hwang Kwon, Kyung Min Kim, Jae Hyuck Jang, Jong Myeong Jeon, Min Hwan Lee, Gun Hwan Kim, Xiang-shu Li, Gyeong-su Park, Bora Lee, Seungwu Han, Miyoung Kim, and Cheol Seong Hwang. in TiO 2 resistive switching memory. *Nature Nanotechnology*, 5(2):148–153, 2010. ISSN 1748-3387. doi: 10.1038/nnano.2009.456. URL http://dx.doi.org/10.1038/nnano.2009.456.

[186] Jui Yuan Chen, Cheng Lun Hsin, Chun Wei Huang, Chung Hua Chiu, Yu Ting Huang, Su Jien Lin, Wen Wei Wu, and Lih Juann Chen. Dynamic evolution of conducting nanofilament in resistive switching memories. *Nano Letters*, 13(8): 3671–3677, 2013. ISSN 15306984. doi: 10.1021/nl4015638.

[187] Kyung Min Kim, Doo Seok Jeong, and Cheol Seong Hwang. Nanofilamentary resistive switching in binary oxide system; A review on the present status and outlook. *Nanotechnology*, 22(25), 2011. ISSN 09574484. doi: 10.1088/0957-4484/22/25/254002.

[188] F. Pan, S. Gao, C. Chen, C. Song, and F. Zeng. Recent progress in resistive random access memories: Materials, switching mechanisms, and performance. *Materials Science and Engineering R: Reports*, 83(1):1–59, 2014. ISSN 0927796X. doi: 10.1016/j.mser.2014.06.002. URL http://dx.doi.org/10.1016/j.mser.2014.06.002.

[189] Shimeng Yu, Ximeng Guan, and H. S.Philip Wong. Conduction mechanism of TiNHfOxPt resistive switching memory: A trap-assisted-tunneling model. *Applied Physics Letters*, 99(6):16–19, 2011. ISSN 00036951. doi: 10.1063/1.3624472.

[190] Stanford R Ovshinsky. Reversible Electrical Switching Phenomena in Disordered Structures. *Physical Review Letters*, 21(20):1450–1453, nov 1968. doi: 10.1103/PhysRevLett.21.1450. URL https://link.aps.org/doi/10.1103/PhysRevLett.21.1450.

[191] *Electronics*. McGraw-Hill Publication, 1970 edition.

[192] A.L. Lacaita, R. Bez, F. Pellizzer, A. Pirovano, and D. Ielmini. Analysis of Phase Distribution in Phase-Change Nonvolatile Memories. *IEEE Electron Device Letters*, 25(7):507–509, 2004. ISSN 0741-3106. doi: 10.1109/led.2004.831219.

[193] Geoffrey W. Burr, Matthew J. Breitwisch, Michele Franceschini, Davide Garetto, Kailash Gopalakrishnan, Bryan Jackson, Bulent Kurdi, Chung Lam, Luis A. Lastras, Alvaro Padilla, Bipin Rajendran, Simone Raoux, and Rohit S. Shenoy. Phase change memory technology. 223, 2010. ISSN 10711023. doi: 10.1116/1.3301579. URL http://arxiv.org/abs/1001.1164{%}0Ahttp://dx.doi.org/10.1116/1.3301579.

[194] A. Pirovano, F. Pellizzer, D. Ielmini, A.L. Lacaita, R. Bez, and A. Redaelli. Electronic Switching Effect and Phase-Change Transition in Chalcogenide Materials. *IEEE Electron Device Letters*, 25(10):684–686, 2004. ISSN 0741-3106. doi: 10.1109/led.2004.836032.

[195] Agostino Pirovano, Andrea L. Lacaita, Fabio Pellizzer, Sergey A. Kostylev, Augusto Benvenuti, and Roberto Bez. Low-field amorphous state resistance and threshold voltage drift in chalcogenide materials. *IEEE Transactions on Electron Devices*, 51(5):714–719, 2004. ISSN 00189383. doi: 10.1109/TED.2004.825805.

[196] D. Adler, M. S. Shur, M. Silver, and S. R. Ovshinsky. Threshold switching in chalcogenide-glass thin films. *Journal of Applied Physics*, 51(6):3289–3309, 1980. ISSN 00218979. doi: 10.1063/1.328036.

[197] David Adler, Heinz K. Henisch, and Sir Nevill Mott. The mechanism of threshold switching in amorphous alloys. *Reviews of Modern Physics*, 50(2):209–220, 1978. ISSN 00346861. doi: 10.1103/RevModPhys.50.209.

[198] Daniele Ielmini and Yuegang Zhang. Analytical model for subthreshold conduction and threshold switching in chalcogenide-based memory devices. *Journal of Applied Physics*, 102(5), 2007. ISSN 00218979. doi: 10.1063/1.2773688.

[199] Gabriele NAVARRO. *Reliability analysis of embedded phase change memories based on innovative materials*. PhD thesis, Université Grenoble Alpes, Grenoble France, 2013.

[200] Giovanni Betti Beneventi, Giovanni Betti, and Beneventi Characterization. *Characterization and modeling of Phase-Change Memories*. PhD thesis, 2012.

[201] Simone Raoux, Feng Xiong, Matthias Wuttig, and Eric Pop. Phase change materials and phase change memory. *MRS Bulletin*, 39(8):703–710, 2014. ISSN 08837694. doi: 10.1557/mrs.2014.139.

[202] Juarez L. F. Da Silva, Aron Walsh, and Hosun Lee. Insights into the structure of the stable and metastable (GeTe)m(Sb2Te3)n compounds. *Physical Review B*, 78(22):224111, 2008. ISSN 1098-0121. doi: 10.1103/PhysRevB.78.224111. URL https://link.aps.org/doi/10.1103/PhysRevB.78.224111.

[203] Huai Yu Cheng, Simone Raoux, and Jean L. Jordan-Sweet. Crystallization properties of materials along the pseudo-binary line between GeTe and Sb. *Journal of Applied Physics*, 115(9):1–6, 2014. ISSN 00218979. doi: 10.1063/1.4867045.

[204] G. Navarro, N. Pashkov, M. Suri, P. Zuliani, R. Annunziata, V. Sousa, L. Perniola, S. Maitrejean, A. Persico, A. Roule, A. Toffoli, and B. De Salvo. Electrical performances of tellurium-rich GexTe1-x phase change memories. *2011 3rd IEEE International Memory Workshop, IMW 2011*, pages 1–4, 2011. doi: 10.1109/IMW.2011.5873232.

[205] Milos Krbal, Alexander V Kolobov, Paul Fons, Junji Tominaga, S R Elliott, J Hegedus, A Giussani, K Perumal, R Calarco, T Matsunaga, N Yamada, K Nitta, and T Uruga. Crystalline GeTe-based phase-change alloys: Disorder in order. *Physical Review B*, 86(4):45212, jul 2012. doi: 10.1103/PhysRevB.86.045212. URL https://link.aps.org/doi/10.1103/PhysRevB.86.045212.

[206] S. Raoux, H. Y. Cheng, M. A. Caldwell, and H. S.P. Wong. Crystallization times of Ge-Te phase change materials as a function of composition. *Applied Physics Letters*, 95(7), 2009. ISSN 00036951. doi: 10.1063/1.3212732.

[207] C. Wiemer, A. Abrutis, J. Siegel, V. Plausinaitiene, W. Gawelda, and C. N. Afonso. Dynamics of laser-induced phase switching in GeTe films. *Journal of Applied Physics*, 109(12):123102, 2011. ISSN 0021-8979. doi: 10.1063/1.3596562.

[208] Matthias Wuttig and Noboru Yamada. Phase-change materials for rewriteable data storage. *Nature Materials*, 6:824, nov 2007. URL https://doi.org/10.1038/nmat2009http://10.0.4.14/nmat2009.

[209] K. L. Chopra and S. K. Bahl. Amorphous versus crystalline GeTe films. I. Growth and structural behavior. *Journal of Applied Physics*, 40(10):4171–4178, 1969. ISSN 00218979. doi: 10.1063/1.1657161.

[210] S. Maitrejean, C. Vallée, M. Armand, A. Roule, E. Gourvest, J. Kreisel, and S. Lhostis. Evidence of Germanium precipitation in phase-change Ge1xTex

thin films by Raman scattering. *Applied Physics Letters*, 95(3):031908, 2009. ISSN 0003-6951. doi: 10.1063/1.3186077.

[211] I. Friedrich, P. Franz, V. Weidenhof, W. Njoroge, and M. Wuttig. Structural transformations of Ge2Sb2Te5 films studied by electrical resistance measurements. *Journal of Applied Physics*, 87(9):4130–4134, 2002. ISSN 0021-8979. doi: 10.1063/1.373041.

[212] Hun Seo, Tae-Hee Jeong, Jeong-Woo Park, Cheong Yeon, Sang-Jun Kim, and Sang-Youl Kim. Investigation of Crystallization Behavior of SputterDeposited Nitrogen-Doped Amorphous Ge2Sb2Te5 Thin Films. *Japanese Journal of Applied Physics*, 39(Part 1, No. 2B):745–751, 2000.

[213] Hun Seo, Cheong Yeon, Myong R. Kim, Tae Hee Jeong, and Jeong Woo Park. Crystal Structure and Microstructure of NitrogenDoped Ge2Sb2Te5 Thin Film. *Japanese Journal of Applied Physics*, 39(Part 1, No. 5A):2775–2779, 2002. ISSN 0021-4922. doi: 10.1143/jjap.39.2775.

[214] Charles T. Rettner, Jean L. Jordan-Sweet, Andrew J. Kellock, Dolores C. Miller, Simone Raoux, Philip M. Rice, and Teya Topuria. Direct observation of amorphous to crystalline phase transitions in nanoparticle arrays of phase change materials. *Journal of Applied Physics*, 102(9):094305, 2007. ISSN 0021-8979. doi: 10.1063/1.2801000.

[215] J. A. Kalb, F. Spaepen, and M. Wuttig. Kinetics of crystal nucleation in undercooled droplets of Sb- and Te-based alloys used for phase change recording. *Journal of Applied Physics*, 98(5), 2005. ISSN 00218979. doi: 10.1063/1.2037870.

[216] M. H. R. Lankhorst, J. H. J. Roosen, A. E. T. Kuiper, M. van Schijndel, and L. van Pieterson. Phase-change recording materials with a growth-dominated crystallization mechanism: A materials overview. *Journal of Applied Physics*, 97 (8):083520, 2005. ISSN 0021-8979. doi: 10.1063/1.1868860.

[217] L. van Pieterson, M. van Schijndel, J. C. N. Rijpers, and M. Kaiser. Te-free, Sb-based phase-change materials for high-speed rewritable optical recording. *Applied Physics Letters*, 83(7):1373–1375, 2003. ISSN 0003-6951. doi: 10.1063/1.1604172.

[218] E G Yeo, L P Shi, R Zhao, and T C Chong. Investigation on Ultra-high Density and High Speed Non-volatile Phase Change Random Access Memory (PCRAM) by Material Engineering. *MRS Proceedings*, 918:905–918, 2006. ISSN 0272-9172. doi: DOI:10.1557/PROC-0918-H05-05-G06-05. URL https://www.cambridge.org/core/article/investigation-on-ultrahigh-density-and-high-speed-nonvolatile-phase-change-random-acc5992958DBBCCDFE8925B4E0496988308.

[219] Martijn H. R. Lankhorst, Bas W. S. M. M. Ketelaars, and R. A. M. Wolters. Low-cost and nanoscale non-volatile memory concept for future silicon chips. *Nature Materials*, 4(4):347–352, 2005. ISSN 1476-1122. doi: 10.1038/nmat1350.

[220] J.H. Yi, J.H. Park, H.S. Jeong, G.T. Jeong, C.W. Jeong, H. Horii, Y.N. Hwang, S.J. Ahn, S.Y. Lee, K.C. Ryoo, Y. Fai, B.I. Ryu, Y.J. Song, B.J. Kuh, Kinam Kim, J.M. Shin, S.H. Lee, Y.H. Ha, and G.H. Koh. Highly manufacturable high density phase change memory of 64Mb and beyond. pages 907–910, 2005. doi: 10.1109/iedm.2004.1419329.

[221] Simone Raoux, Martin Salinga, Jean L. Jordan-Sweet, and Andrew Kellock. Effect of Al and Cu doping on the crystallization properties of the phase change materials SbTe and GeSb. *Journal of Applied Physics*, 101(4), 2007. ISSN 00218979. doi: 10.1063/1.2654556.

[222] Y. C. Chen, C. T. Rettner, S. Raoux, G. W. Burr, S. H. Chen, R. M. Shelby, M. Salinga, W. P. Risk, T. D. Happ, G. M. McClelland, M. Breitwischt, A. Schrott, J. B. Philipps, M. H. Lee, R. Cheek, T. Nirschl, M. Lamorey, C. F. Chen, E. Joseph, S. Zaidi, B. Yee, H. L. Lung, R. Bergmann, and C. Lam. Ultra-thin phase-change bridge memory device using GeSb. *Technical Digest - International Electron Devices Meeting, IEDM*, pages 1–4, 2006. ISSN 01631918. doi: 10.1109/IEDM.2006.346910.

[223] Hong-Bay Chung, Kyung Shin, and Jae-Min Lee. Phase-change characteristics of chalcogenide Ge1Se1Te2 thin films for use in nonvolatile memories. *Journal of Vacuum Science & Technology A: Vacuum, Surfaces, and Films*, 25(1):48–53, 2007. ISSN 0734-2101. doi: 10.1116/1.2388956.

[224] K. Wang, C. Steimer, R. Detemple, D. Wamwangi, and M. Wuttig. Assessment of Se based phase change alloy as a candidate for non-volatile electronic memory applications. *Applied Physics A: Materials Science and Processing*, 81(8): 1601–1605, 2005. ISSN 09478396. doi: 10.1007/s00339-005-3358-2.

[225] Kyu-Jeong Choi, Myung-Jin Kang, M. Wuttig, Sung-Min Yoon, Byoung-Gon Yu, Sang-Ouk Ryu, Se-Young Choi, Y.-S. Park, Nam-Yeal Lee, and Seung-Yun Lee. Sb-Se-based phase-change memory device with lower power and higher speed operations. *IEEE Electron Device Letters*, 27(6):445–447, 2006. ISSN 0741-3106. doi: 10.1109/led.2006.874130.

[226] Hiroko Iwasaki, Makoto Harigaya, Osamu Nonoyama, Yoshiyuki Kageyama, Masaetsu Takahashi, Katsuyuki Yamada, Hiroshi Deguchi, and Yukio Ide. Completely Erasable Phase Change Optical Disc II: Application of Ag-In-Sb-Te Mixed-Phase System for Rewritable Compact Disc Compatible with CD-Velocity and Double CD-Velocity. *Japanese Journal of Applied Physics*, 32(Part 1, No. 11B):5241–5247, 1993. ISSN 0021-4922. doi: 10.1143/jjap.32.5241. URL http://dx.doi.org/10.1143/JJAP.32.5241.

[227] Bo Liu, Zhitang Song, Songlin Feng, and Bomy Chen. Characteristics of chalcogenide nonvolatile memory nano-cell-element based on Sb2Te3 material. *Microelectronic Engineering*, 82(2):168–174, 2005. ISSN 01679317. doi: 10.1016/j.mee.2005.07.007.

[228] Elisabetta Palumbo, Paola Zuliani, Massimo Borghi, and Roberto Annunziata. Forming operation in Ge-rich Ge x Sb y Te z phase change memories. *Solid-State Electronics*, 133(April 2018):38–44, 2017. ISSN 00381101. doi: 10.1016/j.sse.2017.03.016. URL http://dx.doi.org/10.1016/j.sse.2017.03.016.

[229] Y. L. Chen, J. Wang, C. M. Xiong, R. F. Dou, J. Y. Yang, and J. C. Nie. Scanning tunneling microscopy/spectroscopy studies of resistive switching in Nb-doped SrTiO 3. *Journal of Applied Physics*, 112(2), 2012. ISSN 00218979. doi: 10.1063/1.4733999.

[230] M. Trapatseli, D. Carta, A. Regoutz, A. Khiat, A. Serb, I. Gupta, and T. Prodromakis. Conductive atomic force microscopy investigation of switching thresholds in titanium dioxide thin films. *Journal of Physical Chemistry C*, 119(21): 11958–11964, 2015. ISSN 19327455. doi: 10.1021/acs.jpcc.5b01672.

[231] Y. Hou, U. Celano, L. Goux, L. Liu, R. Degraeve, Y. Cheng, J. Kang, M. Jurczak, and W. Vandervorst. Multimode resistive switching in nanoscale hafnium oxide stack as studied by atomic force microscopy. *Applied Physics Letters*, 109(2), 2016. ISSN 00036951. doi: 10.1063/1.4954258.

[232] You-lin Wu, Chun-wei Liao, and Jing-jenn Ling. Effect of current compliance and voltage sweep rate on the resistive switching of HfO 2 / ITO / Invar structure as measured by conductive atomic force microscopy. 242906(2014):2–6, 2014.

[233] Yuanmin Du, Amit Kumar, Hui Pan, Kaiyang Zeng, and Shijie Wang. The resistive switching in TiO2 films studied by conductive atomic force microscopy and Kelvin probe force microscopy The resistive switching in TiO 2 films studied by conductive atomic force microscopy and Kelvin probe force microscopy. 082107, 2013. doi: 10.1063/1.4818119.

[234] T. Diokh, E. Le-Roux, S. Jeannot, P. Candelier, L. Perniola, J. F. Nodin, V. Jousseaume, T. Cabout, H. Grampei, E. Jalaguier, and B. De Salvo. On the impact of the oxide thickness and reset conditions on activation energy of HfO2 based ReRAM extracted through disturb measurements. *IEEE International Integrated Reliability Workshop Final Report*, pages 106–109, 2013. doi: 10.1109/IIRW.2013.6804170.

[235] Fei Yang, Ling Xu, Li Fang, Yifan Jiang, Jun Xu, Weining Su, Yao Yu, Zhongyuan Ma, and Kunji Chen. Conductive Atomic Force Microscopy (C-AFM) observation of conducting nanofilaments formation in GeSbTe phase change materials. *Applied Physics A: Materials Science and Processing*, 112(3): 663–667, 2013. ISSN 09478396. doi: 10.1007/s00339-013-7623-5.

[236] Byeong-ju Bae, Sung-hoon Hong, Seon-Yong Hwang, Jae-yeon Hwang, Ki-Yeon Yang, and Heon Lee. Electrical characterization of Ge–Sb–Te phase change nano-pillars using conductive atomic force microscopy. *Semiconductor Science and Technology*, 24(7):075016, 2009. ISSN 0268-1242. doi: 10.1088/0268-1242/24/7/075016. URL http://stacks.iop.org/0268-1242/24/i=7/a=075016?key=crossref.7d3d6abd70ad84c3ffaaab0aad267904.

[237] Lei Wang, Wang Ren, Jing Wen, and Bangshu Xiong. Overview of Phase-Change Electrical Probe Memory. *Nanomaterials*, 8(10):772, 2018. doi: 10.3390/nano8100772.

[238] H. Satoh, K. Sugawara, and K. Tanaka. Nanoscale phase changes in crystalline Ge 2Sb 2Te 5 films using scanning probe microscopes. *Journal of Applied Physics*, 99(2), 2006. ISSN 00218979. doi: 10.1063/1.2163010.

[239] Ramanathaswamy Pandian, Bart J. Kooi, George Palasantzas, Jeff T M De Hosson, and Andrew Pauza. Nanoscale electrolytic switching in phase-change chalcogenide films. *Advanced Materials*, 19(24):4431–4437, 2007. ISSN 09359648. doi: 10.1002/adma.200700904.

[240] Anbarasu Manivannan, Santosh Kumar Myana, Kumaraswamy Miriyala, Smriti Sahu, and Ranjith Ramadurai. Low power ovonic threshold switching characteristics of thin GeTe6films using conductive atomic force microscopy. *Applied Physics Letters*, 105(24), 2014. ISSN 00036951. doi: 10.1063/1.4904412.

[241] Hiroyuki Kado and Takao Tohda. Nanometer-scale erasable recording using atomic force microscope on phase change media. *Japanese Journal of Applied Physics, Part 1: Regular Papers and Short Notes and Review Papers*, 36(1 B):523–525, 1997. ISSN 00214922. doi: 10.1143/JJAP.36.523.

[242] Harish Bhaskaran, Abu Sebastian, Andrew Pauza, Haralampos Pozidis, and Michel Despont. Nanoscale phase transformation in Ge2 Sb2 Te 5 using encapsulated scanning probes and retraction force microscopy. *Review of Scientific Instruments*, 80(8), 2009. ISSN 00346748. doi: 10.1063/1.3204449.

[243] Andriy Lotnyk, Bernd Rauschenbach, Ulrich Roß, Jürgen W. Gerlach, and Xinxing Sun. Nanoscale Bipolar Electrical Switching of Ge 2 Sb 2 Te 5 Phase-Change Material Thin Films . *Advanced Electronic Materials*, 3(12):1700283, 2017. doi: 10.1002/aelm.201700283.

[244] Keiji Tanaka. Smallest (10 nm) phase-change marks in amorphous and crystalline Ge2Sb2Te5 films. *Journal of Non-Crystalline Solids*, 353(18-21):1899–1903, 2007. ISSN 00223093. doi: 10.1016/j.jnoncrysol.2007.02.020.

[245] G. Binnig, H. Rohrer, Ch. Gerber, and E. Weibel. Surface studies by scanning tunneling microscopy. *Phys. Rev. Lett.*, 49:57–61, Jul 1982. doi: 10.1103/PhysRevLett.49.57. URL https://link.aps.org/doi/10.1103/PhysRevLett.49.57.

[246] G. Binnig, C. F. Quate, and Ch. Gerber. Atomic force microscope. *Phys. Rev. Lett.*, 56:930–933, Mar 1986. doi: 10.1103/PhysRevLett.56.930. URL https://link.aps.org/doi/10.1103/PhysRevLett.56.930.

[247] T. R. Albrecht and C. F. Quate. Atomic resolution imaging of a nonconductor by atomic force microscopy. *Journal of Applied Physics*, 62(7):2599–2602, 1987. doi: 10.1063/1.339435. URL https://doi.org/10.1063/1.339435.

[248] Jane Frommer. Scanning tunneling microscopy and atomic force microscopy in organic chemistry. *Angewandte Chemie International Edition in English*, 31(10):1298–1328, 1992. doi: 10.1002/anie.199212981. URL https://onlinelibrary.wiley.com/doi/abs/10.1002/anie.199212981.

[249] PK Hansma, VB Elings, O Marti, and CE Bracker. Scanning tunneling microscopy and atomic force microscopy: application to biology and technology. *Science*, 242(4876):209–216, 1988. ISSN 0036-8075. doi: 10.1126/science.3051380. URL http://science.sciencemag.org/content/242/4876/209.

[250] M Radmacher, RW Tillamnn, M Fritz, and HE Gaub. From molecules to cells: imaging soft samples with the atomic force microscope. *Science*, 257(5078):1900–1905, 1992. ISSN 0036-8075. doi: 10.1126/science.1411505. URL http://science.sciencemag.org/content/257/5078/1900.

[251] Q. Zhong, D. Inniss, K. Kjoller, and V.B. Elings. Fractured polymer/silica fiber surface studied by tapping mode atomic force microscopy. *Surface Science Letters*, 290(1):L688 – L692, 1993. ISSN 0167-2584. doi: https:

//doi.org/10.1016/0167-2584(93)90906-Y. URL http://www.sciencedirect.com/science/article/pii/016725849390906Y.

[252] B Drake, CB Prater, AL Weisenhorn, SA Gould, TR Albrecht, CF Quate, DS Cannell, HG Hansma, and PK Hansma. Imaging crystals, polymers, and processes in water with the atomic force microscope. *Science*, 243(4898): 1586–1589, 1989. ISSN 0036-8075. doi: 10.1126/science.2928794. URL http://science.sciencemag.org/content/243/4898/1586.

[253] Constant A. J. Putman, Kees O. Van der Werf, Bart G. De Grooth, Niek F. Van Hulst, and Jan Greve. Tapping mode atomic force microscopy in liquid. *Applied Physics Letters*, 64(18):2454–2456, 1994. doi: 10.1063/1.111597. URL https://doi.org/10.1063/1.111597.

[254] M. D. Kirk, T. R. Albrecht, and C. F. Quate. Low-temperature atomic force microscopy. *Review of Scientific Instruments*, 59(6):833–835, 1988. doi: 10.1063/1.1139788. URL https://doi.org/10.1063/1.1139788.

[255] T. Hantschel, C. Demeulemeester, P. Eyben, V. Schulz, O. Richard, H. Bender, and W. Vandervorst. Conductive diamond tips with sub-nanometer electrical resolution for characterization of nanoelectronics device structures. *physica status solidi (a)*, 206(9):2077–2081, 2009. doi: 10.1002/pssa.200982212. URL https://onlinelibrary.wiley.com/doi/abs/10.1002/pssa.200982212.

[256] T. Hantschel, M. Tsigkourakos, J. Kluge, T. Werner, L. Zha, K. Paredis, P. Eyben, T. Nuytten, Z. Xu, and W. Vandervorst. Overcoated diamond tips for nanometer-scale semiconductor device characterization. *Microelectronic Engineering*, 141:1 – 5, 2015. ISSN 0167-9317. doi: https://doi.org/10.1016/j.mee.2014.11.023. URL http://www.sciencedirect.com/science/article/pii/S0167931714005206. Micro/Nano Fabrication 2014.

[257] L.D. Landau and E. M. Lifshitz. *Theory of Elasticity*. Pergamon Press, 1970.

[258] Werner Frammelsberger, Guenther Benstetter, Janice Kiely, and Richard Stamp. C-afm-based thickness determination of thin and ultra-thin sio2 films by use of different conductive-coated probe tips. *Applied Surface Science*, 253 (7):3615 – 3626, 2007. ISSN 0169-4332. doi: https://doi.org/10.1016/j.apsusc.2006.07.070. URL http://www.sciencedirect.com/science/article/pii/S0169433206010348.

[259] Todd G. Ruskell, Richard K. Workman, Dong Chen, Dror Sarid, Sarah Dahl, and Stephen Gilbert. High resolution fowler-nordheim field emission maps of thin silicon oxide layers. *Applied Physics Letters*, 68(1):93–95, 1996. doi: 10.1063/1.116782. URL https://doi.org/10.1063/1.116782.

[260] R. Arinero, W. Hourani, A. D. Touboul, B. Gautier, M. Ramonda, D. Albertini, L. Militaru, Y. Gonzalez-Velo, C. Guasch, and F. Saigné. Toward a better understanding of the nanoscale degradation mechanisms of ultra-thin si02/si films: Investigation of the best experimental conditions with a conductive-atomic force microscope. *Journal of Applied Physics*, 110(1):014304, 2011. doi: 10.1063/1.3603037. URL https://doi.org/10.1063/1.3603037.

[261] Brandon L. Weeks, Mark W. Vaughn, and James J. DeYoreo. Direct imaging of meniscus formation in atomic force microscopy using environmental scanning electron microscopy. *Langmuir*, 21(18):8096–8098, 2005. doi: 10.1021/la0512087. URL https://doi.org/10.1021/la0512087. PMID: 16114907.

[262] W. Polspoel, W. Vandervorst, L. Aguilera, M. Porti, M. Nafria, and X. Aymerich. Nanometer-scale leakage measurements in high vacuum on de-processed high-k capacitors. *Microelectronics Reliability*, 48(8):1521 – 1524, 2008. ISSN 0026-2714. doi: https://doi.org/10.1016/j.microrel.2008.07.026. URL http://www.sciencedirect.com/science/article/pii/S0026271408002163. 19th European Symposium on Reliability of Electron Devices, Failure Physics and Analysis (ESREF 2008).

[263] P. Delcroix. *Etude à l'échelle nanométrique par sonde locale de la fiabilité de diélectriques minces pour l'intégration dans les composants microélectroniques du future*. PhD thesis, Université Joseph Fourrier, Grenoble, France, 2012.

[264] J. Sune, G. Mura, and E. Miranda. Are soft breakdown and hard breakdown of ultrathin gate oxides actually different failure mechanisms? *IEEE Electron Device Letters*, 21(4):167–169, April 2000. ISSN 0741-3106. doi: 10.1109/55.830970.

[265] S. Richter, M. Geva, J. P. Garno, and R. N. Kleiman. Metal–insulator–semiconductor tunneling microscope: two-dimensional dopant profiling of semiconductors with conducting atomic-force microscopy. *Applied Physics Letters*, 77(3):456–458, 2000. doi: 10.1063/1.127008. URL https://doi.org/10.1063/1.127008.

[266] K Shubhakar. Nanoscopic Study of HfO 2 Based HK Dielectric Stacks and Its Failure Analysis. *International Journal of Materials Science and Engineering Vol*, 2 (2):81–86, 2014. doi: 10.12720/ijmse.2.2.81-86.

[267] Mario Lanza. A review on resistive switching in high-k dielectrics: A nanoscale point of view using conductive atomic force microscope. *Materials*, 7(3):2155–2182, 2014. ISSN 1996-1944. doi: 10.3390/ma7032155. URL http://www.mdpi.com/1996-1944/7/3/2155.

[268] Cédric Sire, Serge Blonkowski, Michael J. Gordon, and Thierry Baron. Statistics of electrical breakdown field in hfo2 and sio2 films from millimeter to nanometer length scales. *Applied Physics Letters*, 91(24):242905, 2007. doi: 10.1063/1.2822420. URL https://doi.org/10.1063/1.2822420.

[269] Wouter Polspoel. High resolution study of high-k layers using c-afm. *Katholieke Universiteit Leuven – Faculty of Engineering*, 2012. URL $$Uhttps://lirias.kuleuven.be/retrieve/176233$$Dphdpublic.pdf[freelyavailable].

[270] Brice Gautier, Antoine Brugère, Wael Hourani, Octavian Ligor, Antonin Grandfond, Alexis Borowiak, David Albertini, Nanotechnologies De Lyon, and Insa De Lyon. Quelques bonnes raisons pour ne pas faire les mesures électriques par AFM à l'air . *Institut des Nanotechnologies de Lyon INSA*, 2012.

[271] S. Zafar, Q. Liu, and E. A. Irene. Study of tunneling current oscillation dependence on sio2 thickness and si roughness at the si/sio2 interface. *Journal of Vacuum Science & Technology A*, 13(1):47–53, 1995. doi: 10.1116/1.579442. URL https://doi.org/10.1116/1.579442.

[272] Alexander Olbrich, Bernd Ebersberger, and Christian Boit. Conducting atomic force microscopy for nanoscale electrical characterization of thin sio2. *Applied*

Physics Letters, 73(21):3114–3116, 1998. doi: 10.1063/1.122690. URL https://doi.org/10.1063/1.122690.

[273] Yuanmin Du, Amit Kumar, Hui Pan, Kaiyang Zeng, Shijie Wang, Ping Yang, and Andrew Thye Shen Wee. The resistive switching in tio2 films studied by conductive atomic force microscopy and kelvin probe force microscopy. *AIP Advances*, 3(8):082107, 2013. doi: 10.1063/1.4818119. URL https://doi.org/10.1063/1.4818119.

[274] Chia Min Chang, Yen Ju Liu, Ming Lun Tseng, Nien-Nan Chu, Ding-Wei Huang, Masud Mansuripur, and Din Ping Tsai. Characterization of ge2sb2te5 thin film alloys using conductive-tip atomic force microscopy. *physica status solidi (b)*, 249(10):1945–1950, 2012. doi: 10.1002/pssb.201200356. URL https://onlinelibrary.wiley.com/doi/abs/10.1002/pssb.201200356.

[275] M. J. Kim, I. G. Baek, Y. H. Ha, S. J. Baik, J. H. Kim, D. J. Seong, S. J. Kim, Y. H. Kwon, C. R. Lim, H. K. Park, D. Gilmer, P. Kirsch, R. Jammy, Y. G. Shin, S. Choi, and C. Chung. Low power operating bipolar tmo reram for sub 10 nm era. *Proceedings of the 2010 International Electron Devices Meeting (IEDM)*, pages 19.3.1–19.3.4, Dec 2010. ISSN 2156-017X. doi: 10.1109/IEDM.2010.5703391.

[276] Z. Zhang, Y. Wu, H. . P. Wong, and S. S. Wong. Nanometer-scalehfo$_x$rram. *IEEE Electron Device Letters*, 34(8):1005–1007, Aug 2013. ISSN 0741-3106. doi: 10.1109/LED.2013.2265404.

[277] Y. Hou, U. Celano, L. Goux, L. Liu, A. Fantini, R. Degraeve, A. Youssef, Z. Xu, Y. Cheng, J. Kang, M. Jurczak, and W. Vandervorst. Sub-10nm low current resistive switching behavior in hafnium oxide stack. *Applied Physics Letters*, 108 (12):123106, 2016. doi: 10.1063/1.4944841. URL https://doi.org/10.1063/1.4944841.

[278] A. Ranjan, N. Raghavan, J. Molina, S.J. O'Shea, K. Shubhakar, and K.L. Pey. Analysis of quantum conductance, read disturb and switching statistics in hfo2 rram using conductive afm. *Microelectronics Reliability*, 64:172 – 178, 2016. ISSN 0026-2714. doi: https://doi.org/10.1016/j.microrel.2016.07.112. URL http://www.sciencedirect.com/science/article/pii/S0026271416302566. Proceedings of the 27th European Symposium on Reliability of Electron Devices, Failure Physics and Analysis.

[279] Yong Cheol Shin, Min Hwan Lee, Kyung Min Kim, Gun Hwan Kim, Seul Ji Song, Jun Yeong Seok, and Cheol Seong Hwang. Bias polarity dependent local electrical conduction in resistive switching tio2 thin films. *physica status solidi (RRL) – Rapid Research Letters*, 4(5-6):112–114, 2010. doi: 10.1002/pssr.201004066. URL https://onlinelibrary.wiley.com/doi/abs/10.1002/pssr.201004066.

[280] J. Y. Son and Y.-H. Shin. Direct observation of conducting filaments on resistive switching of nio thin films. *Applied Physics Letters*, 92(22):222106, 2008. doi: 10.1063/1.2931087. URL https://doi.org/10.1063/1.2931087.

[281] D. McMullan. Scanning electron microscopy 1928–1965. *Scanning*, 17(3):175–185, 1995. doi: 10.1002/sca.4950170309. URL https://onlinelibrary.wiley.com/doi/abs/10.1002/sca.4950170309.

[282] VLADIMIR K. ZWORYKIN. The scanning electron microscope. *Scientific American*, 167(3):111–113, 1942. ISSN 00368733, 19467087. URL http://www.jstor.org/stable/24967890.

[283] Joseph I. Goldstein. *Scanning Electron Microscopy and X-Ray Microanalysis*. Springer, 4th edition, 2003.

[284] H. S.Philip Wong, Heng Yuan Lee, Shimeng Yu, Yu Sheng Chen, Yi Wu, Pang Shiu Chen, Byoungil Lee, Frederick T. Chen, and Ming Jinn Tsai. Metal-oxide RRAM. *Proceedings of the IEEE*, 100(6):1951–1970, 2012. ISSN 00189219. doi: 10.1109/JPROC.2012.2190369.

[285] A Ranjan, N Raghavan, J Molina, S J O Shea, K Shubhakar, and K L Pey. Microelectronics Reliability Analysis of quantum conductance , read disturb and switching statistics in HfO 2 RRAM using conductive AFM. *Microelectronics Reliability*, 64:172–178, 2016. ISSN 0026-2714. doi: 10.1016/j.microrel.2016.07.112. URL http://dx.doi.org/10.1016/j.microrel.2016.07.112.

[286] S Blonkowski and T Cabout. Bipolar resistive switching from liquid helium to room temperature. *Journal of Physics D: Applied Physics*, 48 (34):345101, 2015. ISSN 0022-3727. doi: 10.1088/0022-3727/48/34/345101. URL http://stacks.iop.org/0022-3727/48/i=34/a=345101?key=crossref.c49c80f2983e6cbe55cd7711e2352688.

[287] Ch. Walczyk, Ch. Wenger, D. Walczyk, M. Lukosius, I. Costina, M. Fraschke, J. Dabrowski, a. Fox, D. Wolansky, S. Thiess, E. Miranda, B. Tillack, and T. Schroeder. On the role of Ti adlayers for resistive switching in HfO[sub 2]-based metal-insulator-metal structures: Top versus bottom electrode integration. *Journal of Vacuum Science & Technology B: Microelectronics and Nanometer Structures*, 29(1):01AD02, 2011. ISSN 10711023. doi: 10.1116/1.3536524.

[288] T. Bertaud, D. Walczyk, Ch Walczyk, S. Kubotsch, M. Sowinska, T. Schroeder, Ch Wenger, C. Vallée, P. Gonon, C. Mannequin, V. Jousseaume, and H. Grampeix. Resistive switching of HfO2-based Metal-Insulator-Metal diodes: Impact of the top electrode material. *Thin Solid Films*, 520(14):4551–4555, 2012. ISSN 00406090. doi: 10.1016/j.tsf.2011.10.183. URL http://dx.doi.org/10.1016/j.tsf.2011.10.183.

[289] S. Blonkowski, T. Cabout, M. Azazz, C. Cagli, and E. Jalaguier. Fully Analytical Compact Model of OxRAM Based on Joule Heating and Electromigration for DC and Pulsed Operation. *2016 IEEE 8th International Memory Workshop, IMW 2016*, 2016. doi: 10.1109/IMW.2016.7495270.

[290] Mario Lanza. A Review on Resistive Switching in High-k Dielectrics: A Nanoscale Point of View Using Conductive Atomic Force Microscope. pages 2155–2182, 2014. doi: 10.3390/ma7032155.

[291] M. J. Kim. Low Power Operating Bipolar TMO ReRAM for Sub 10 nm Era. *Proceedings of the 2010 International Electron Devices Meeting (IEDM) (2010)*, 10: 441–447.

[292] Zhiping Zhang, Yi Wu, H. S. Philip Wong, and S. Simon Wong. Nanometer-scale HfOx RRAM. *IEEE Electron Device Letters*, 34(8):1005–1007, 2013. ISSN 07413106. doi: 10.1109/LED.2013.2265404.

[293] Yong Cheol Shin, Min Hwan Lee, Kyung Min Kim, Gun Hwan Kim, Seul Ji Song, Jun Yeong Seok, and Cheol Seong Hwang. Bias polarity dependent local electrical conduction in resistive switching TiO2 thin films. *Physica Status Solidi - Rapid Research Letters*, 4(5-6):112–114, 2010. ISSN 18626254. doi: 10.1002/pssr.201004066.

[294] S Brivio, G Tallarida, E Cianci, and S Spiga. Formation and disruption of conductive filaments in a HfO ₂ /TiN structure. *Nanotechnology*, 25(38):385705, 2014. ISSN 0957-4484. doi: 10.1088/0957-4484/25/38/385705. URL http://stacks.iop.org/0957-4484/25/i=38/a=385705?key=crossref.d5e1445ba79b046439c06f8f1c7d7763.

[295] Romain Foissac. *Etude à l'échelle nanométrique par sonde locale de la fiabilité et de la dégradation de films minces d'oxyde pour applications MOS et MIM*. PhD thesis, 2015.

[296] I V Karpov, M Mitra, D Kau, G Spadini, Y A Kryukov, and V G Karpov. Evidence of field induced nucleation in phase change memory. *Applied Physics Letters*, 92(17):173501, apr 2008. ISSN 0003-6951. doi: 10.1063/1.2917583.

[297] Charles Kittel. *Introduction to solid state physics / Charles Kittel*. Wiley, New York, 1976. ISBN 0471490245.

[298] C. Kachhava. *Solid State Physics,Solid State Device And Electronics*. New Age International, 2003.

[299] A Halimaoui, O Brière, and G Ghibaudo. Quasi-breakdown in ultrathin gate dielectrics. *Microelectronic Engineering*, 36(1):157–160, 1997. ISSN 0167-9317. doi: https://doi.org/10.1016/S0167-9317(97)00039-7. URL http://www.sciencedirect.com/science/article/pii/S0167931797000397.

[300] G I Meijer. Who Wins the Nonvolatile Memory Race? *Science*, 319(5870):1625 LP – 1626, mar 2008. doi: 10.1126/science.1153909. URL http://science.sciencemag.org/content/319/5870/1625.abstract.

[301] P. Misra, Y. Sharma, and R. S. Katiyar. Effect of Current Compliance on Resistive Switching Characteristics of Amorphous Ternary Rare Earth Oxide SmGdO3 Thin Films Grown by Pulsed Laser Deposition. *ECS Transactions*, 61 (6):133–138, 2014. ISSN 1938-6737. doi: 10.1149/06106.0133ecst.

[302] Yanfei Qi, Chun Zhao, Yuxiao Fang, Qifeng Lu, Chenguang Liu, Li Yang, and Ce Zhou Zhao. Compliance current effect on switching behavior of hafnium oxide based RRAM. *Proceedings of the International Symposium on the Physical and Failure Analysis of Integrated Circuits, IPFA*, 2017-July:1–4, 2017. doi: 10.1109/IPFA.2017.8060188.

[303] Meng Han Lin, Ming Chi Wu, Chen Hsi Lin, and Tseung Yuen Tseng. Effects of vanadium doping on resistive switching characteristics and mechanisms of SrZrO3-based memory films. *IEEE Transactions on Electron Devices*, 57(8):1801–1808, 2010. ISSN 00189383. doi: 10.1109/TED.2010.2050837.

[304] J. F. Kang, R. Q. Han, B. Gao, D. D. Han, B. Sun, L. F. Liu, X. Y. Liu, N. Xu, and Y. Wang. The Effect of Current Compliance on the Resistive Switching Behaviors in TiN/ZrO₂/Pt Memory Device. 7:1172–1173, 2015. doi: 10.7567/ssdm.2008.j-9-6.

[305] T. Hantschel, M. Tsigkourakos, J. Kluge, T. Werner, L. Zha, K. Paredis, P. Eyben, T. Nuytten, Z. Xu, and W. Vandervorst. Overcoated diamond tips for nanometer-scale semiconductor device characterization. *Microelectronic Engineering*, 141:1–5, 2015. ISSN 01679317. doi: 10.1016/j.mee.2014.11.023.

[306] T. Hantschel, C. Demeulemeester, P. Eyben, V. Schulz, O. Richard, H. Bender, and W. Vandervorst. Conductive diamond tips with sub-nanometer electrical resolution for characterization of nanoelectronics device structures. *Physica Status Solidi (A) Applications and Materials Science*, 206(9):2077–2081, 2009. ISSN 18626300. doi: 10.1002/pssa.200982212.

[307] Tristan Dewolf, Vincent Delaye, Nicolas Bernier, David Cooper, Nicolas Chevalier, Helen Grampeix, Christelle Charpin, Eric Jalaguier, Martin Kogelschatz, Sylvie Schamm-Chardon, and Guillaume Audoit. Nanocharacterization of switching mechanism in HfO2-based oxide resistive memories by TEM-EELS-EDS. *European Microscopy Congress 2016: Proceedings*, 21 (1):598–599, 2016. doi: 10.1002/9783527808465.EMC2016.5934. URL http://doi.wiley.com/10.1002/9783527808465.EMC2016.5934.

[308] Tristan Dewolf. *Nano-caractérisation des mécanismes de commutation dans les mémoires résistives à base d'HfO2*. PhD thesis, Université de Toulouse, 2018. URL http://thesesups.ups-tlse.fr/4134/.

[309] S. Blonkowski, T. Cabout, M. Azazz, C. Cagli, and E. Jalaguier. Fully Analytical Compact Model of OxRAM Based on Joule Heating and Electromigration for DC and Pulsed Operation. *2016 IEEE 8th International Memory Workshop, IMW 2016*, pages 0–3, 2016. doi: 10.1109/IMW.2016.7495270.

[310] Thomas CABOUT. *Optimisation technologique et caractérisation électrique de mémoires résistives OxRRAM pour applications basse consommation*. PhD thesis, UNIVERSITE D'AIX-MARSEILLE, 2014. URL https://www.theses.fr/188869557.

[311] Stefano Larentis, Federico Nardi, Simone Balatti, David C. Gilmer, and Daniele Ielmini. Resistive switching by voltage-driven ion migration in bipolar RRAMPart II: Modeling. *IEEE Transactions on Electron Devices*, 59(9):2468–2475, 2012. ISSN 00189383. doi: 10.1109/TED.2012.2202320.

[312] Peng Huang, Xiao Yan Liu, Bing Chen, Hai Tong Li, Yi Jiao Wang, Ye Xin Deng, Kang Liang Wei, Lang Zeng, Bin Gao, Gang Du, Xing Zhang, and Jin Feng Kang. A physics-based compact model of metal-oxide-based RRAM DC and AC operations. *IEEE Transactions on Electron Devices*, 60(12):4090–4097, 2013. ISSN 00189383. doi: 10.1109/TED.2013.2287755.

[313] Marc Bocquet, Damien Deleruyelle, Hassen Aziza, Christophe Muller, Jean Michel Portal, Thomas Cabout, and Eric Jalaguier. Robust compact model for bipolar oxide-based resistive switching memories. *IEEE Transactions on Electron Devices*, 61(3):674–681, 2014. ISSN 00189383. doi: 10.1109/TED.2013.2296793.

[314] R. Degraeve, A. Fantini, S. Clima, B. Govoreanu, L. Goux, Y. Y. Chen, D. J. Wouters, Ph Roussel, G. S. Kar, G. Pourtois, S. Cosemans, J. A. Kittl, G. Groeseneken, M. Jurczak, and L. Altimime. Dynamic 'hour glass' model for SET and RESET in HfO 2 RRAM. *Digest of Technical Papers - Symposium on VLSI*

Technology, (June):75–76, 2012. ISSN 07431562. doi: 10.1109/VLSIT.2012.6242468.

[315] S. L. Johnson, A. Sundararajan, D. P. Hunley, and D. R. Strachan. Memristive switching of single-component metallic nanowires. *Nanotechnology*, 21 (12), 2010. ISSN 09574484. doi: 10.1088/0957-4484/21/12/125204.

[316] Hiroshi Yasuda and Akira Sakai. Conductance of atomic-scale gold contacts under high-bias voltages. *Physical Review B - Condensed Matter and Materials Physics*, 56(3):1069–1072, 1997. ISSN 1550235X. doi: 10.1103/PhysRevB.56.1069.

[317] John Robertson. Band offsets of wide-band-gap oxides and implications for future electronic devices. *Journal of Vacuum Science & Technology B: Microelectronics and Nanometer Structures*, 18(3):1785, 2000. ISSN 0734211X. doi: 10.1116/1.591472. URL http://scitation.aip.org/content/avs/journal/jvstb/18/3/10.1116/1.591472.

[318] Herbert B Michaelson and Herbert B Michaelson. The work function of the elements and its periodicity The work function of the elements and its periodicity. 4729(1977):6–11, 2011. doi: 10.1063/1.323539.

[319] Andrey Sergeevich Sokolov, Yu-Rim Jeon, Sohyeon Kim, Boncheol Ku, Donghwan Lim, Hoonhee Han, Myeong Gyoon Chae, Jaeho Lee, Beom Gil Ha, and Changhwan Choi. Influence of oxygen vacancies in ALD HfO 2-x thin films on non-volatile resistive switching phenomena with a Ti/HfO 2-x /Pt structure. *Applied Surface Science*, 434:822–830, 2018. ISSN 01694332. doi: 10.1016/j.apsusc.2017.11.016. URL http://linkinghub.elsevier.com/retrieve/pii/S0169433217332397.

[320] Chen Z. and Sorbello R.S. Local heating in mesoscopic systems. *Physical Review B*, 47(20):527–534, 1993.

[321] Varghese Swamy, Alexei Kuznetsov, Leonid S. Dubrovinsky, Rachel A. Caruso, Dmitry G. Shchukin, and Barry C. Muddle. Finite-size and pressure effects on the Raman spectrum of nanocrystalline anatase Ti O2. *Physical Review B - Condensed Matter and Materials Physics*, 71(18):15–17, 2005. ISSN 10980121. doi: 10.1103/PhysRevB.71.184302.

[322] Cédric Sire, Serge Blonkowski, Michael J. Gordon, and Thierry Baron. Statistics of electrical breakdown field in Hf O2 and Si O2 films from millimeter to nanometer length scales. *Applied Physics Letters*, 91(24):2005–2008, 2007. ISSN 00036951. doi: 10.1063/1.2822420.

[323] H. J. Wan, P. Zhou, L. Ye, Y. Y. Lin, T. A. Tang, H. M. Wu, and M. H. Chi. In situ observation of compliance-current overshoot and its effect on resistive switching. *IEEE Electron Device Letters*, 31(3):246–248, 2010. ISSN 07413106. doi: 10.1109/LED.2009.2039694.

[324] E. Yalon, D. Kalaev, A. Gavrilov, S. Cohen, I. Riess, and D. Ritter. Detection of the conductive filament growth direction in resistive memories. *Device Research Conference - Conference Digest, DRC*, pages 299–300, 2014. ISSN 15483770. doi: 10.1109/DRC.2014.6872415.

[325] Cédric Mannequin, Alexandru Delamoreanu, Laurence Latu-Romain, Vincent Jousseaume, Helen Grampeix, Sylvain David, Caroline Rabot, Aziz Zenasni, Christophe Vallee, and Patrice Gonon. Graphene-HfO2-based resistive RAM memories. *Microelectronic Engineering*, 161:82–86, 2016. ISSN 01679317. doi: 10.1016/j.mee.2016.04.009. URL http://dx.doi.org/10.1016/j.mee.2016.04.009.

[326] Daniele Ielmini and Andrea L. Lacaita. Phase change materials in non-volatile storage. *Materials Today*, 14(12):600–607, 2011. ISSN 13697021. doi: 10.1016/S1369-7021(11)70301-7. URL http://dx.doi.org/10.1016/S1369-7021(11)70301-7.

[327] Christophe Vallée, Pierre Noé, Frédéric Fillot, Françoise Hippert, and Jean-Yves Raty. Phase-change materials for non-volatile memory devices: from technological challenges to materials science issues. *Semiconductor Science and Technology*, 33(1):013002, 2017. ISSN 0268-1242. doi: 10.1088/1361-6641/aa7c25.

[328] B C Lee, P Zhou, J Yang, Y Zhang, B Zhao, E Ipek, O Mutlu, and D Burger. Phase-Change Technology and the Future of Main Memory. *IEEE Micro*, 30 (1):143, 2010. ISSN 0272-1732 VO - 30. doi: 10.1109/MM.2010.24.

[329] Yoonjin Won, Jaeho Lee, Mehdi Asheghi, Thomas W. Kenny, and Kenneth E. Goodson. Phase and thickness dependent modulus of Ge2Sb2Te5 films down to 25nm thickness. *Applied Physics Letters*, 100(16):161905, 2012. ISSN 0003-6951. doi: 10.1063/1.3699227. URL http://aip.scitation.org/doi/10.1063/1.3699227.

[330] Tamihiro Gotoh, Kentaro Sugawara, and Keiji Tanaka. Nanoscale electrical phase-change in GeSb2Te4 films with scanning probe microscopes. *Journal of Non-Crystalline Solids*, 299-302(PART 2):968–972, 2002. ISSN 00223093. doi: 10.1016/S0022-3093(01)01061-4.

[331] Chia Min Chang, Yen Ju Liu, Ming Lun Tseng, Nien Nan Chu, Ding Wei Huang, Masud Mansuripur, and Din Ping Tsai. Characterization of Ge 2Sb 2Te 5 thin film alloys using conductive-tip atomic force microscopy. *Physica Status Solidi (B) Basic Research*, 249(10):1945–1950, 2012. ISSN 03701972. doi: 10.1002/pssb.201200356.

[332] Fei Yang, Ling Xu, Jing Chen, Jun Xu, Yao Yu, Zhongyuan Ma, and Kunji Chen. Nanoscale multilevel switching in Ge2Sb2Te5thin film with conductive atomic force microscopy. *Nanotechnology*, 27(3):35706, 2015. ISSN 13616528. doi: 10.1088/0957-4484/27/3/035706. URL http://dx.doi.org/10.1088/0957-4484/27/3/035706.

[333] S Hudgens and B Johnson. Overview of Chalcogenide Technology. *Current*, (November):1–4, 2004.

[334] D. Wamwangi, W. K. Njoroge, and M. Wuttig. Crystallization kinetics of Ge4Sb1Te5 films. *Thin Solid Films*, 408(1-2):310–315, 2002. ISSN 00406090. doi: 10.1016/S0040-6090(02)00062-7.

[335] V. Weidenhof, I. Friedrich, S. Ziegler, and M. Wuttig. Laser induced crystallization of amorphous Ge2Sb2Te5films. *Journal of Applied Physics*, 89(6):3168–3176, 2001. ISSN 00218979. doi: 10.1063/1.1351868.

[336] Lei Wang, Si Di Gong, Jing Wen, and Ci Hui Yang. An improved electrical switching and phase-transition model for scanning probe phase-change memory. *Journal of Nanomaterials*, 2016, 2016. ISSN 16874129. doi: 10.1155/2016/8078165.

[337] Qi Cao and Pengsheng Liu. Crystalline-amorphous phase transition of hyperbranched polyurethane phase change materials for energy storage. *Journal of Materials Science*, 42(14):5661–5665, 2007. ISSN 1573-4803. doi: 10.1007/s10853-006-0884-z. URL https://doi.org/10.1007/s10853-006-0884-z.

[338] Daniele Ielmini. Threshold switching mechanism by high-field energy gain in the hopping transport of chalcogenide glasses. *Physical Review B - Condensed Matter and Materials Physics*, 78(3):1–8, 2008. ISSN 10980121. doi: 10.1103/PhysRevB.78.035308.

[339] Daniel Krebs, Simone Raoux, Charles T Rettner, Geoffrey W Burr, Martin Salinga, and Matthias Wuttig. Threshold field of phase change memory materials measured using phase change bridge devices. *Applied Physics Letters*, 95(8):82101, aug 2009. ISSN 0003-6951. doi: 10.1063/1.3210792. URL https://doi.org/10.1063/1.3210792.

[340] V. Sousa, G. Navarro, N. Castellani, M. Coue, O. Cueto, C. Sabbione, P. Noe, L. Perniola, S. Blonkowski, P. Zuliani, and R. Annunziata. Operation fundamentals in 12Mb Phase Change Memory based on innovative Ge-rich GST materials featuring high reliability performance. *Digest of Technical Papers - Symposium on VLSI Technology*, 2015-Augus:T98–T99, 2015. ISSN 07431562. doi: 10.1109/VLSIT.2015.7223708.

[341] D. K. Venkatachalam, J. E. Bradby, M. N. Saleh, S. Ruffell, and R. G. Elliman. Nanomechanical properties of sputter-deposited HfO2 and Hf xSi1-xO2 thin films. *Journal of Applied Physics*, 110(4), 2011. ISSN 00218979. doi: 10.1063/1.3627155.

[342] Junho Kim. Nanoscale crystallization of phase change Ge2Sb 2Te5 film with AFM lithography. *Scanning*, 32(5):320–326, 2010. ISSN 01610457. doi: 10.1002/sca.20201.

[343] Il Mok Park, Jung Kyu Jung, Sang Ouk Ryu, Kyu Jeong Choi, Byoung Gon Yu, Young Bae Park, Seung Min Han, and Young Chang Joo. Thermomechanical properties and mechanical stresses of Ge2Sb2Te5 films in phase-change random access memory. *Thin Solid Films*, 517(2):848–852, 2008. ISSN 00406090. doi: 10.1016/j.tsf.2008.08.194. URL http://dx.doi.org/10.1016/j.tsf.2008.08.194.

[344] G. D'Arrigo, A. Mio, G. Favaro, M. Calabretta, A. Sitta, A. Sciuto, M. Russo, M. Calì, M. Oliveri, and E. Rimini. Mechanical properties of amorphous Ge2Sb2Te5 thin layers. *Surface and Coatings Technology*, 355(October 2017):227–233, 2018. ISSN 02578972. doi: 10.1016/j.surfcoat.2018.02.050. URL https://doi.org/10.1016/j.surfcoat.2018.02.050.

Resistive non-volatile memories characterization by conductive atomic force microscopy (C-AFM) in ultra-high vacuum environment

The ongoing research in the field of non-volatile memories aims to overcome the limitation of flash memories in terms of scalability. Several emerging memory technologies especially OxRAMs and PCRAMs are being explored as potential successors due to many advantages like good scalability, long data retention time, fast read & write speed and low power consumption. In MIM structures for OxRAM, forming and disruption of the nanometer sized conductive filament is commonly accepted as the physical phenomenon for the switching, but still a debate is going on to understand the nature and characteristics of the conductive filament. Hence, in this thesis work we studied mechanisms related to the conductive filament based resistive switching at nanoscale. To do the electrical characterization, a new technique using conductive atomic force microscopy (C-AFM) in ultra-high vacuum is proposed. It is found that in the case of HfO2 based OxRAM, the filament is formed by Ti diffusion from the bottom electrode through the oxide layer. Also, phase transition in phase change materials for PCRAM is investigated for GST-225 and Ge rich GST. It was found that the phase transition from amorphous to crystalline is possible at nanoscale. Finally, the threshold for GST-225 is observed at values nearer to those observed on devices than former observations with standard C-AFM.

Keywords: *Non-Volatile Memories, OxRAM, PCRAM, Conductive atomic force microscopy (C-AFM), Nanoelectronics, Microelectronics, Ultra-high vacuum, Electrical characterization, Filament, Simulation.*

Caractérisation des mémoires non volatiles résistives par microscopie à force atomique en mode conduction (C-AFM) sous ultravide

Les recherches en cours dans le domaine des mémoires non-volatiles visent à dépasser la limitation des mémoires flash en termes d'évolutivité. Plusieurs technologies de mémoires émergentes, en particulier les mémoires OxRAM et les mémoires PCRAM sont à l'étude en tant que successeurs potentiels en raison de leurs nombreux avantages, tels qu'une bonne évolutivité, une longue durée de conservation des données, une vitesse de lecture et d'écriture rapide et une faible consommation d'énergie. Dans les structures MIM pour OxRAM, la formation et la rupture d'un filament conducteur de taille nanométrique sont communément acceptées comme étant le phénomène physique de la commutation, mais un débat est toujours en cours pour comprendre la nature et les caractéristiques du filament conducteur. Par conséquent, dans cette thèse, nous étudions les mécanismes liés à la commutation résistive à base de filaments conducteurs à l'échelle nanométrique. Pour effectuer la caractérisation électrique, une nouvelle technique utilisant la microscopie à force atomique en mode conduction (C-AFM) sous ultravide est proposée. Il s'avère que dans les mémoires OxRAM à base de HfO2, le filament est créé par diffusion de Ti de l'électrode inférieure à travers l'oxyde. En outre, la transition de phase dans les matériaux pour PCRAM est étudiée pour le GST riche en Ge et le GST-225. Il a été constaté que la transition de phase dans les matériaux à changement de phase est possible à l'échelle nanométrique. Enfin, la tension de seuil observée dans le cas du GST-225 est bien plus proche des valeurs mesurées sur dispositifs que celles obtenues avec un CAFM standard.

Mots-clés: *Mémoires non volatiles, OxRAM, PCRAM, Microscopie à force atomique conductrice (C-AFM), nanoélectronique, microélectronique, ultravide, caractérisation électrique, filament, simulation.*